

DISSERTATION

DIRECT FLUORINATION OF $K_2B_{12}H_{12}$ AND SYNTHESIS AND
CHARACTERIZATION OF METAL SALTS OF $B_{12}F_{12}^{2-}$

Submitted by

Dmitry V. Peryshkov

Department of Chemistry

In partial fulfillment of the requirements

For the Degree of Doctor of Philosophy

Colorado State University

Fort Collins, Colorado

Spring 2011

Doctoral Committee:

Advisor: Steven H. Strauss

Elliot R. Bernstein

C. Michael Elliott

Anthony K. Rappe

John R. Ridley

ABSTRACT

DIRECT FLUORINATION OF $K_2B_{12}H_{12}$ AND SYNTHESIS AND CHARACTERIZATION OF METAL SALTS OF $B_{12}F_{12}^{2-}$

A significantly improved large-scale (10 g) perfluorination of $K_2B_{12}H_{12}$ is described. The advantages of the new procedure are: (i) a ten-fold increase in the scale of the reaction with no sacrifice in yield or product purity; (ii) acetonitrile is used as the solvent instead of anhydrous HF; and (iii) a glass reaction vessel is used instead of a Monel reactor. DFT calculations and experimental data are reported that suggest that the absence of acidity significantly increased the rate and improved the efficiency of the reaction.

Number of salts of Li^+ ; Na^+ ; K^+ ; Rb^+ ; Cs^+ ; NH_4^+ , Ag^+ ; Mg^{2+} ; Ca^{2+} ; Ba^{2+} ; Co^{2+} ; Ni^{2+} ; and Zn^{2+} and the $B_{12}F_{12}^{2-}$ anion were prepared and 24 crystal structures (some compounds were prepared by others) were determined. The thermal stabilities of the $M_m(L)_nB_{12}F_{12}$ salts were studied by thermogravimetric analysis (TGA) and differential scanning calorimetry (DSC). It was found that $Cs_2B_{12}F_{12}$ is stable up to 600 °C under an inert atmosphere, which is the highest temperature among weakly coordinating fluoroanions. The compounds $K_2B_{12}F_{12}$, $Rb_2B_{12}F_{12}$, $Cs_2B_{12}F_{12}$, and $Ag_2B_{12}F_{12}$ were prepared as ligand-free solids.

It was found that the $K_2(H_2O)_{0,2,4}B_{12}F_{12}$ system of compounds can undergo rapid interconversion among the three crystalline phases, two of them reversibly in presence of water vapor. The reversible interconversion was found to be a reconstructive (i.e., topotactic) solid-state reaction and, when carried out very slowly, a single-crystal-to-

single-crystal transformation. The exchange of $\text{H}_2\text{O}(g)$ with either D_2O or H_2^{18}O in crystalline $\text{K}_2(\text{D}_2\text{O})_2\text{B}_{12}\text{F}_{12}$ or $\text{K}_2(\text{H}_2^{18}\text{O})_2\text{B}_{12}\text{F}_{12}$ at 25 °C was also rapid. The new concept of latent porosity, as ligands rapidly enter a lattice and displace some of the weak and non-directional $\text{M}\cdots\text{F}(\text{B})$ bonds in salts of the large, highly-symmetric, superweak anion $\text{B}_{12}\text{F}_{12}^{2-}$, is presented and discussed.

TABLE OF CONTENTS

CHAPTER 1. INTRODUCTION	1
Justification for the Research	1
Structures of High-Symmetry Weakly-Coordinating Anions.....	4
Brief Review of Relevant Solid-State Structures.....	5
Abbreviations and Terminology Used in this Dissertation	6
CHAPTER 2. DIRECT PERFLUORINATION OF $K_2B_{12}H_{12}$ IN ACETONITRILE. AN EFFICIENT LARGE-SCALE SYNTHESIS OF $K_2B_{12}F_{12}$ AND $Cs_2B_{12}F_{12}$	14
Introduction	14
Experimental	15
I. Reagents and Solvents.....	15
II. Large-Scale Preparation of $K_2B_{12}F_{12}$ and $Cs_2B_{12}F_{12}$	15
III. Spectroscopic measurements.....	16
IV. DFT calculations.	17
Results and discussion.....	17
I. General Comments About $B_{12}H_{12}^{2-}$ Fluorination and Determining $B_{12}H_{12-x}F_x^{2-}$ Mol% Values. Optimization of Fluorination Reaction Conditions.	17
II. Fluorination of $B_{12}H_{12-x}F_x^{2-}$ Ions in Acetonitrile at the Gas-Bubble/Solution Interface.	26
III. Inhibition of F_2 Fluorination of $B_{12}H_{12-x}F_x^{2-}$ Anions by Protic Acids	29
IV. The Solvation of $B_{12}H_{12-x}F_x^{2-}$ Anions.....	31
V. Minimizing the Formation of BF_4^- During $B_{12}H_{12}^{2-}$ Fluorination.	33
CHAPTER 3. MONOVALENT METAL-ION SALTS OF $B_{12}F_{12}^{2-}$, INCLUDING $Ag(H_2O)_4B_{12}F_{12}$ AND $[NH_4 \cdot H_2O]_2B_{12}F_{12}$	50
Introduction	50
Experimental Section	50

I. Reagents and Solvents.....	50
II. Preparation and Crystallization of Monovalent Cation Salts of $B_{12}F_{12}^{2-}$	51
III. Characterization.....	53
Results and Discussion.....	53
I. Synthesis and Crystallization.	53
II. X-ray Crystallography.	55
III. Thermal Stabilities of Monovalent Metal-Ion Salts of $B_{12}F_{12}^{2-}$	70
CHAPTER 4. SILVER(I) SALTS OF $B_{12}F_{12}^{2-}$ ANION	99
Introduction.....	99
Experimental	99
I. Reagents and Solvents.....	99
II. Preparation and Crystallization of $Ag_2(L)_nB_{12}F_{12}$ salts.	100
III. Single-Crystal X-ray Diffraction.....	101
IV. Thermogravimetric Analysis (TGA).....	101
V. Infrared spectroscopy (FTIR).....	102
Results and Discussion.....	102
I. Synthesis and Thermal Stability of $Ag_2(L)_nB_{12}F_{12}$	102
II. X-ray crystallography	104
III. Confirming the Superweak Nature of $B_{12}F_{12}^{2-}$	107
CHAPTER 5. DIVALENT METAL-ION SALTS OF $B_{12}F_{12}^{2-}$	121
Introduction.....	121
Experimental Section	121
I. Reagents and Solvents.....	121
II. Preparation and Crystallization of Divalent Metal-Ion Salts of $B_{12}F_{12}^{2-}$	122
III. Characterization.....	123
Results and Discussion.....	124
I. Synthesis and Crystallization.	124
II. X-ray Crystallography.	124
III. Thermogravimetric Analysis.	127
CHAPTER 6. REVERSIBLE HYDRATION/DEHYDRATION AND LATENT POROSITY OF $K_2B_{12}F_{12}$	144

Introduction	144
Experimental	145
I. Reagents and Solvents.....	145
II. Thermogravimetric Analysis (TGA) and Differential Scanning Calorimetry (DSC).....	145
III. Powder X-ray Diffraction (PXRD).....	145
IV. Infrared spectroscopy (FTIR).....	145
V. Scanning Electron Microscopy (SEM).....	146
VI. DFT calculations.	146
Results and discussion.....	146
I. The Comparison of Ionic Lattices in $K_2(H_2O)_nB_{12}F_{12}$ ($n = 0, 2, 4$)	146
II. The $K_2(H_2O)_2^{2+}$ and $K_2(H_2O)_4^{2+}$ Dimers.	148
III. Dehydration/Rehydration Reactions.....	151
CHAPTER 7. FUTURE WORK.....	184

CHAPTER 1. INTRODUCTION

Justification for the Research Described Herein

Interest in the $B_{12}F_{12}^{2-}$ anion derives from its high-symmetry (I_h , the highest possible symmetry of any chemical species other than atoms or atomic ions) and its expected weakly-coordinating nature. (The applications of weakly-coordinating anions are numerous and have been the subject of a number of excellent reviews.¹⁻⁶) Although it is true that an F atom forms very strong bonds to most elements other than an O atom, an N atom, or another F atom, it only forms one strong bond at a time. Furthermore, fluorine is the most electronegative element, so the lone pairs on an F atom bonded to another element are very tightly held and are not readily shared. For both reasons, the F atom in a strong B–F bond should be very weakly basic as far as forming a bridge bond to a metal ion. Weak $BF\cdots M^{n+}$ interactions should lead to reactive M^{n+} metal ions; this has been shown to be the case when metal ions have a number of weak $CF\cdots M^{n+}$, $EF\cdots M^{n+}$ ($E = P, As, Sb$), and $TeF\cdots M^{n+}$ bonds.¹⁻⁶ Thus, the metal ions in solvent-free/ligand-free $M_2(B_{12}F_{12})_n$ salts may be the closest approach to the reactivity of the corresponding gas-phase M^{n+} metal ion one can achieve in a crystalline compound. If the metal ions in $M_2(B_{12}F_{12})_n$ salts were accessible to gaseous reagents (i.e., if the gaseous reagents could diffuse through the lattice), then catalytic activity might be realized that would be reminiscent of microporous zeolites containing ion-exchanged catalytically-active metal ions. The rapid and reversible absorption/desorption of gaseous reagents by rigid⁷⁻¹¹ or flexible (breathable)¹²⁻¹⁵ microporous solids such as zeolites is a historically important¹⁶⁻¹⁸ as well as a current area of fundamental and applied research. In addition to technological applications, rapid and reversible absorption reactions involving crystalline

materials can serve as model systems for studying the mechanisms of solid-state reactions, whether or not those reactions involve single-crystal-to-single-crystal transformations.^{7-10,19-27} The difficulties of combining the frequently incompatible features of thermal stability, porosity, reversible dynamic motion, and crystallinity in solids has been recently discussed.²⁷

One goal of the work described in this dissertation was to scale up the literature synthesis²⁸ of $\text{K}_2\text{B}_{12}\text{F}_{12}$, using commercially available $\text{K}_2\text{B}_{12}\text{H}_{12}$ as a starting material and elemental fluorine (i.e., 20% F_2 in N_2) as the fluorinating reagent, without sacrificing the purity and yield of the product, and without using much more than the stoichiometric amount of elemental fluorine. In addition, significantly decreasing the amount of time needed for a given synthesis/purification was also an important goal. The figures of merit for the literature synthesis, published in 2003 by the Strauss research group,²⁸ are that ca. 1.3 g of $\text{K}_2\text{B}_{12}\text{F}_{12}$ could be made with 99+% purity in 72% recrystallized yield starting with 0.9 g of $\text{K}_2\text{B}_{12}\text{H}_{12}$; this procedure, including recrystallization of the product, took a total of six days to complete. In the work described in Chapter 2 of this dissertation, a new procedure was developed that resulted in the synthesis of 99.5+% pure $\text{K}_2\text{B}_{12}\text{F}_{12}$ in 74% yield in a total of two days (ca. 15 g of recrystallized $\text{K}_2\text{B}_{12}\text{F}_{12}$ was isolated starting with 10 g of $\text{K}_2\text{B}_{12}\text{H}_{12}$) using only 14 equivalents of F_2 , a modest 16.7% excess. The work described in Chapter 2 has already been published in a full paper in *J. Am. Chem. Soc.*²⁹ In addition to Prof. Strauss and our DFT collaborator Dr. Alexey A. Popov, the author of this dissertation is the only other co-author of this paper.

The reason for scaling up the synthesis of $\text{K}_2\text{B}_{12}\text{F}_{12}$ was so that a large number of $\text{M}_2(\text{B}_{12}\text{F}_{12})_n$ or $[\text{M}(\text{L})_m]_2(\text{B}_{12}\text{F}_{12})_n$ salts (L = a volatile ligand) could be prepared in gram quantities and studied by a battery of physicochemical techniques (note that two-thirds of all elements in the periodic table are metals). In many cases it was envisioned that the ligand L would be the solvent from which the $\text{M}_2(\text{B}_{12}\text{F}_{12})_n$ salt was crystallized. This was the second goal of this work, and it was essentially exploratory in nature. Before the work

carried out in this dissertation was performed, only two compounds, $(\text{CPh}_3)_2\text{B}_{12}\text{F}_{12}$ ²⁸ and $\text{Cs}_2(\text{H}_2\text{O})\text{B}_{12}\text{F}_{12}$ ³⁰, had been structurally characterized. It was not known if ligand-free $\text{M}_2(\text{B}_{12}\text{F}_{12})_n$ could be prepared (i.e., if they were stable under the conditions necessary for their synthesis). During the course of this work, one ligand-free salt, $\text{K}_2\text{B}_{12}\text{F}_{12}$, was isolated and characterized by single-crystal X-ray diffraction. In addition, salts of the following metal ions, containing one or more ligands, were also isolated and structurally characterized by X-ray diffraction: Li^+ ; Na^+ ; K^+ ; Rb^+ ; Cs^+ ; NH_4^+ ; Ag^+ ; Mg^{2+} ; Ca^{2+} ; Ba^{2+} ; Co^{2+} ; Ni^{2+} ; and Zn^{2+} . In some cases the compounds were prepared and crystallized by other members of the Strauss Research Group, and this will be clearly indicated. However, with the exception of the diffraction data collection for crystals of $\text{K}_2(\text{HF})_3\text{B}_{12}\text{F}_{12}$ and $\text{Cs}_2(\text{HF})\text{B}_{12}\text{F}_{12}$, all crystallographic work was performed by the author (the data for these two compounds were collected by Mr. Roland Friedemann in Prof. Dr. Konrad Seppelt's laboratory at the Free University Berlin, Berlin, Germany). A total of 24 compounds were structurally characterized by the author, and analyses of their structures constitute the largest parts of Chapters 3, 4, and 5 of this dissertation.

Finally, the thermal stabilities of the ligated metal-ion salts studied in this work were investigated by thermogravimetric analysis (TGA) and differential scanning calorimetry (DSC). Conditions were developed to prepare a number of new ligand-free metal-ion salts of $\text{B}_{12}\text{F}_{12}^{2-}$, although only one of them, $\text{K}_2\text{B}_{12}\text{F}_{12}$, could be isolated as single crystals suitable for X-ray diffraction. Nevertheless, in addition to $\text{K}_2\text{B}_{12}\text{F}_{12}$, the ligand-free salts $\text{Rb}_2\text{B}_{12}\text{F}_{12}$, $\text{Cs}_2\text{B}_{12}\text{F}_{12}$, and $\text{Ag}_2\text{B}_{12}\text{F}_{12}$ were also isolated and characterized. The reversible and extremely rapid hydration and dehydration of $\text{K}_2\text{B}_{12}\text{F}_{12}$ proved to be especially interesting, and an in-depth study of it became a major focus of the final part of the author's Ph.D. research. This study is discussed in detail in Chapter 6. Most of this work, in which the "latent porosity" of $\text{K}_2\text{B}_{12}\text{F}_{12}$ was discovered, has recently been published in a full paper in *J. Am. Chem. Soc.*³¹ In addition to Prof. Strauss and Dr. Popov, the author of this dissertation is the only other co-author of this paper. It is significant that the latent

porosity of metal salts of $B_{12}F_{12}^{2-}$, and its possible application to problems in mechanistic solid-state chemistry and catalysis, has become the primary boron-chemistry focus in the Strauss Research Group. The fact that it was not anticipated at the outset of the author's Ph.D. research underscores the value of exploratory research.

Structures of High-Symmetry Weakly-Coordinating Anions

For reasons outlined above, some of the most effective weakly-coordinating anions contain multiple F atoms strongly bonded to one or another element.¹⁻⁶ The most weakly-coordinating of these have been termed superweak anions,⁵ invoking the concept that the weakest base would be expected to be the conjugate base (conjugate anion) of a neutral superacid (the term superacid is defined by the IUPAC as a compound "having a high acidity, generally greater than that of 100-weight% sulfuric acid"³²).

The icosahedral (I_h) superweak anion $B_{12}F_{12}^{2-}$ was chosen as the subject of this research in part because of its high symmetry, since this would simplify the study of the structural chemistry of its salts. For example, an isotropic polyatomic anion such as $B_{12}F_{12}^{2-}$ would allow comparisons to be made with salts of monoatomic anions (e.g., the structures of $M_2B_{12}F_{12}$ could be compared with the structures of K_2O or Cs_2S and the structures of $MB_{12}F_{12}$ could be compared with the structures of $NaCl$, $CsCl$, or $NiAs$). Alternative superweak anions such as $1-R-CB_{11}F_{11}^-$ ³³ and $R_3NB_{12}F_{11}^-$,³⁴ although based on an idealized icosahedral CB_{11} or B_{12} core, have C_{5v} or C_s symmetry for $R = H$ and even lower symmetry for $R = CH_3$, C_2H_5 , etc. The structures of the $B_{12}F_{12}^{2-}$,³⁵ $1-CH_3-CB_{11}F_{11}^-$,³⁶ and $(CH_3)NB_{12}F_{11}^-$ ³⁴ anions are shown in Figure 1.1. Other I_h -symmetry anions include $B_{12}H_{12}^{2-}$ and $B_{12}Cl_{12}^{2-}$, which are not expected to be as weakly-coordinating as $B_{12}F_{12}^{2-}$. Ligand-free/solvent-free salts of these anions include $Li_2B_{12}H_{12}$,³⁷ $Cs_2B_{12}H_{12}$,³⁸ $Ag_2B_{12}Cl_{12}$,³⁹ and $Cs_2B_{12}Cl_{12}$.⁴⁰ An icosahedral anion that may be as weakly coordinating or more weakly coordinating than $B_{12}H_{12}^{2-}$ is $B_{12}(CH_3)_{12}^{2-}$,⁴¹

but very few salts of this anion are known. The pseudo-spherical nature of the $B_{12}F_{12}^{2-}$ anion is shown in Figure 1.2. Fluoroanions such as tetrahedral BF_4^- and BeF_4^{2-} and octahedral PF_6^- , AsF_6^- , SbF_6^- , SiF_6^{2-} , MnF_6^{2-} , GeF_6^{2-} , etc., also have high symmetry. Relevant ligand-free/solvent-free metal-ion salts of these anions include $LiBF_4$,⁴² $NaBF_4$,⁴³ KBF_4 ,^{44,45} $RbBF_4$,⁴⁶ $CsBF_4$,⁴⁷ $LiPF_6$,⁴⁸ $KAsF_6$,⁴⁹ K_2BeF_4 ,⁵⁰ K_2SiF_6 ,⁵¹ K_2MnF_6 ,⁵² and K_2GeF_6 .⁵³

Brief Review of Relevant Solid-State Structures

There are a few very common structures of MX and M_2X salts (i.e., ionic compounds) containing monoatomic ions.⁵⁴ As far as cubic unit cells are concerned, there is the NaCl (B1) structure, which is an expanded cubic close-packed (CCP) array of Cl^- anions with Na^+ cations in all of the O_h holes. There is the cubic ZnS structure (B3; sphalerite), which is an expanded CCP array of S^{2-} anions with Zn^{2+} cations in half of the T_d holes. There is the antifluorite structure (C1) exhibited by, among other compounds, Na_2O , which is an expanded CCP array of O^{2-} anions with Na^+ cations in all of the T_d holes. There is also the CsCl structure (B2), with an expanded simple cubic array of Cl^- anions with Cs^+ cations in the centers of the Cl_8 cubes. Fragments of these structures are shown in Figure 1.2.

As far as hexagonal unit cells are concerned, there is the NiAs (B8₁) structure, which is an expanded hexagonal close-packed (HCP) array of As atoms with Ni atoms in all of the O_h holes. There is the hexagonal ZnS structure (B4; wurtzite), which is an expanded HCP array of S^{2-} anions with Zn^{2+} cations in half of the T_d holes. There is also the Cs_2S structure (C23, anticotunnite), which is an expanded HCP array of S^{2-} anions with Cs^+ cations in half of the T_d holes and all of the O_h holes. Note that there is no HCP analog of the antifluorite structure, because the centers of pairs of T_d holes on either side of a close-packed layer of anions (i.e., T_d holes sharing the same triangle of anions in a close-packed

layer) are too close for both of them to contain cations. A common structure for intermetallic compounds, but rare for ionic compounds at 1 atm and 25 °C, is the Ni₂In structure (B8₂), which is an expanded HCP array of In atoms with Ni atoms in all of the *O_h* holes and half of the *D_{3h}* holes within the close-packed layers. Fragments of these four structures are shown in Figure 1.3.

Binary salts with 99+% ionic character are generally limited to alkali metal halides and oxides,⁵⁵ but the interactions between alkali metal cations and high-symmetry fluoroanions such as BeF₄²⁻, SiF₆²⁻, MnF₆²⁻, etc. are also predominantly ionic in nature. A variety of structure types are exhibited when the aforementioned fluoroanions are paired with a given alkali metal ion to form A₂X salts. For example, there are at least two polymorphs of K₂MnF₆. One has the antifluorite structure⁵⁶ and one has the Cs₂S-type structure⁵⁷ (in this discussion the packing arrangement of EF_{*n*}²⁻ anions is being equated to the packing arrangement of the central atoms E, not to the packing arrangement of their F atoms). Similarly, K₂SiF₆ and K₂GeF₆ each exhibit two polymorphs. For K₂SiF₆, the situation is similar to K₂MnF₆: one polymorph has the antifluorite structure⁵⁸ and the other, which is a naturally occurring mineral recently found in the La Fossa crater on Volcano Island near Sicily, has the Cs₂S-type structure.⁵¹ However, one polymorph of K₂GeF₆ has the Cs₂S-type structure⁵⁹ and the other has an unusual hexagonal structure consisting of superimposed close-packed layers of anions with K⁺ ions significantly off-center in half of the trigonal-prismatic holes.⁵³

Abbreviations and Terminology Used in this Dissertation

Table 1.1 contains a list of abbreviations and definitions used in this dissertation. In any discussion of structures containing metal ions and weakly-coordinating fluoroanions such as B₁₂F₁₂²⁻, it is necessary, albeit difficult, to define when a bond is a bond:^{2,3} as M···F distances become longer and longer, there must be a point at which the two atoms

are so weakly bonded that it is not sensible to connect them with a line, whether a solid line (typically used in chemical drawings to denote primary bonding interactions) or a dotted line (typically used to denote secondary, weaker bonding interactions such as hydrogen bonding and outer-sphere interactions in transition-metal complexes). In this dissertation bond valences⁶⁰ are calculated, whenever possible, for all interactions with metal ions that might be considered bonding (e.g., all interactions less than 4 Å). Any bond valence less than 0.03 (i.e., 3%) is considered to be a non-bonding interaction.

Non-bonded interactions are easy to calculate for solid-state organic compounds and even for many solid-state metal complexes by comparing the distance between two atoms with the sum of their van der Waals radii. However, this is not a good definition for ionic compounds for the simple reason that van der Waals radii for metal ions are poorly defined, if defined at all. The value for potassium in Bondi's classic work is 2.75 Å.⁶¹ If this is added to the van der Waals radius for a F atom, 1.47 Å,⁶¹ the sum is 4.22 Å, which is much too long to be of significance as far as bonding (even ionic bonding) is concerned: the bond valence for K and F at this distance is only 0.002. Using the 3% definition, K···F interactions longer than 3.3 Å will not be considered bonding in this work, and if any drawing includes a K···F interaction longer than 3.3 Å, it will deserve a specific comment as to why it has been included. The same will be true for any M···X interaction with a bond valence less than 3%. Bond valence parameters for all relevant pairs of atoms used throughout this dissertation are listed in Table 1.2.

The concept of primary and secondary bonding interactions (i.e., a clear demarcation between them) also breaks down for some, if not most, of the compounds described in this dissertation. In compounds such as Cs₂(H₂O)B₁₂F₁₂, the *only* bonds to the Cs¹⁺ ions are eleven relatively long Cs···F interactions, which range from 3.049(1) Å (bond valence = 0.143) to 3.443(1) Å (bond valence = 0.049). There is no sensible way to group the eleven distances into primary interactions and secondary interactions.

Finally, for consistency, interactions between metal ions and F atoms will be written as $M\cdots F$, and interactions between metal ions and C, N, and O atoms will be written as $M-X$. This distinction will not necessarily imply that the $M-X$ interactions are stronger, or even shorter, than any of the $M\cdots F$ interactions in a particular compound.

Table 1.1 Abbreviations and Definitions Used in this Dissertation

DSC	differential scanning calorimetry
TGA	thermogravimetric analysis
ITGA	isothermal gravimetric analysis
NMR	nuclear magnetic resonance
FTIR	Fourier-transform infrared
XRD	X-ray diffraction (generic)
SC-XRD	single-crystal X-ray diffraction
PXRD	powder X-ray diffraction
NI-ESI-MS	negative-ion electrospray ionization mass-spectrometry
esd	estimated standard deviation (standard error) in XRD derived results
⊙	the centroid of B ₁₂ clusters in a B ₁₂ X ₁₂ ²⁻ anion
dd-H ₂ O	distilled deionized water
a-HF	anhydrous HF
a-CH ₃ CN	anhydrous CH ₃ CN
w-CH ₃ CN	acetonitrile as received, containing less than 0.3% water according to the manufacturers analysis
DFT	density functional theory

Table 1.2. Bond Valence Parameters⁶² for the M···F and M–X Interactions for the Crystal Structures Described in the Dissertation.^a

cation	F	O	N
Li ⁺	1.360	1.466	1.61
Na ⁺	1.677	1.80	1.93
K ⁺	1.992	2.13	2.26
Rb ⁺	2.16	2.26	2.37
Cs ⁺	2.33	2.42	2.53
Mg ²⁺	1.581	1.693	1.85
Ca ²⁺	1.842	1.967	2.14
Ba ²⁺	2.19	2.29	2.47
Ag ⁺	1.80	1.805	1.85
Co ²⁺	1.64	1.692	1.84
Ni ²⁺	1.599	1.654	1.75
Zn ²⁺	1.62	1.704	1.77
Pd ²⁺	1.74	1.792	1.81

^a The bond valence contribution of each interaction is calculated using the formula $BV = \exp[(R_{MX} - d_{MX})/0.37]$,⁶² where R_{MX} is a bond valence parameter listed in the table and d_{MX} is an M–X (M···F) distance.

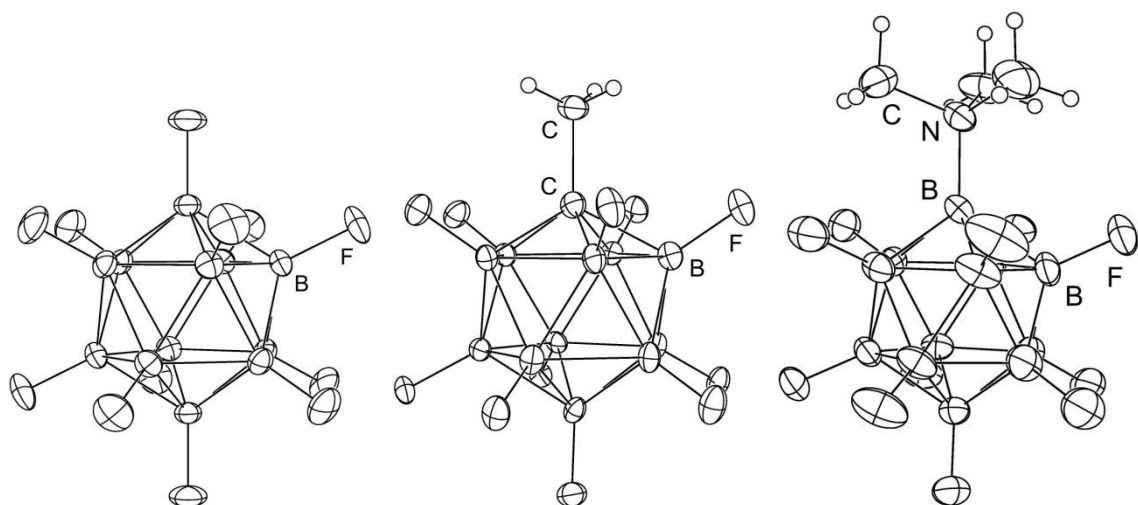


Figure 1.1. Structures of the $B_{12}F_{12}^{2-}$ (left), $1\text{-CH}_3\text{-CB}_{11}\text{F}_{11}^-$ (middle), and $(\text{CH}_3)\text{NB}_{12}\text{F}_{11}^-$ (right) anions (50% probability ellipsoids except for H atoms, which are shown as spheres of arbitrary size). These structures were reported in references 35, 36, and 34, respectively.

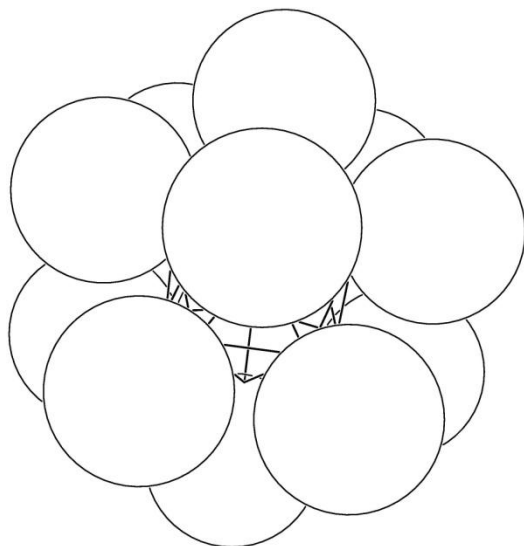


Figure 1.2. The pseudo-spherical nature of the $B_{12}F_{12}^{2-}$ anion. The coordinates for this drawing of the anion were taken from the structure of $\text{K}_2(\text{H}_2\text{O})_4\text{B}_{12}\text{F}_{12}$, which is presented in Chapter 3. The radius of each F atom was set to 1.47 \AA , which is the van der Waals radius of an F atom.

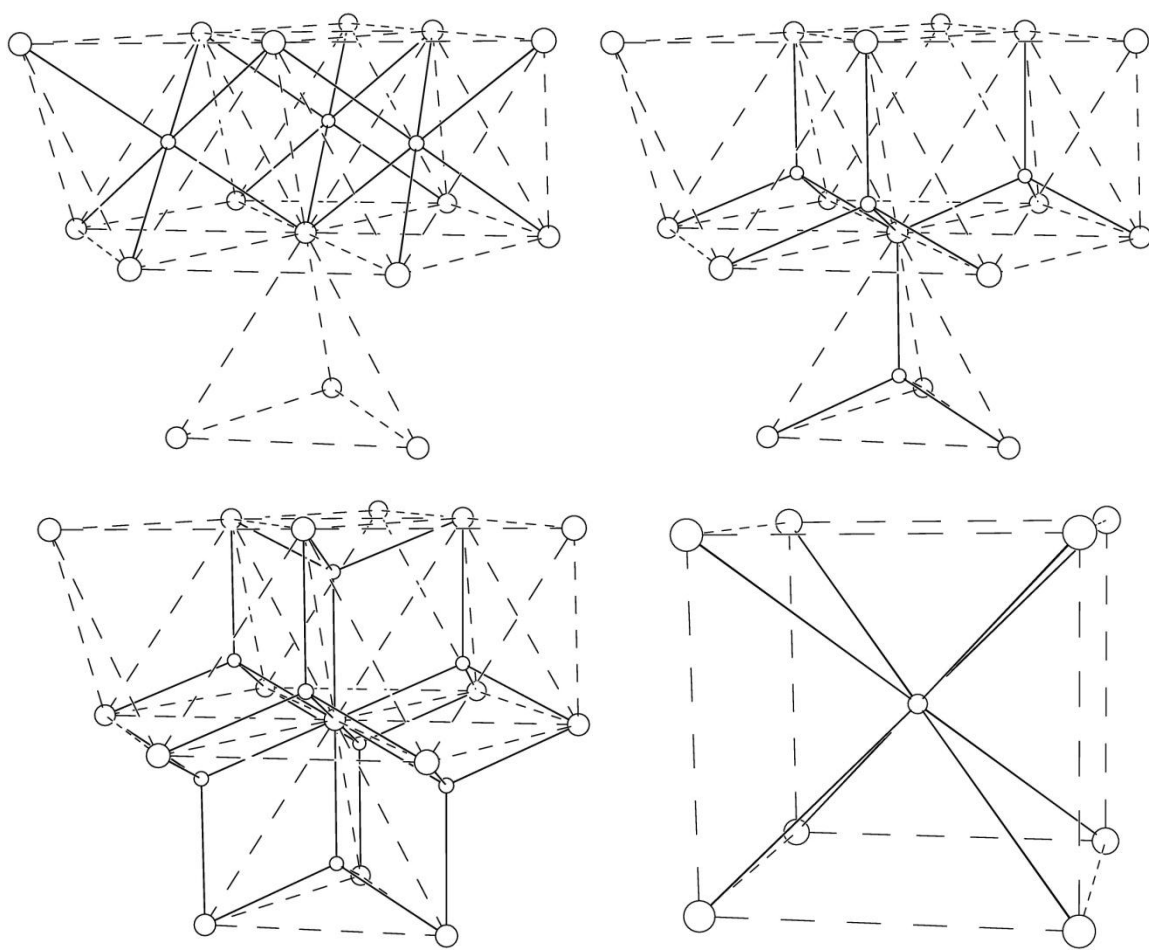


Figure 1.3. Fragments of the structures of NaCl (top left), cubic ZnS (sphalerite; top right), Na₂O (antifluorite; bottom left), and CsCl (bottom right). The larger spheres are anions and the smaller spheres are cations.

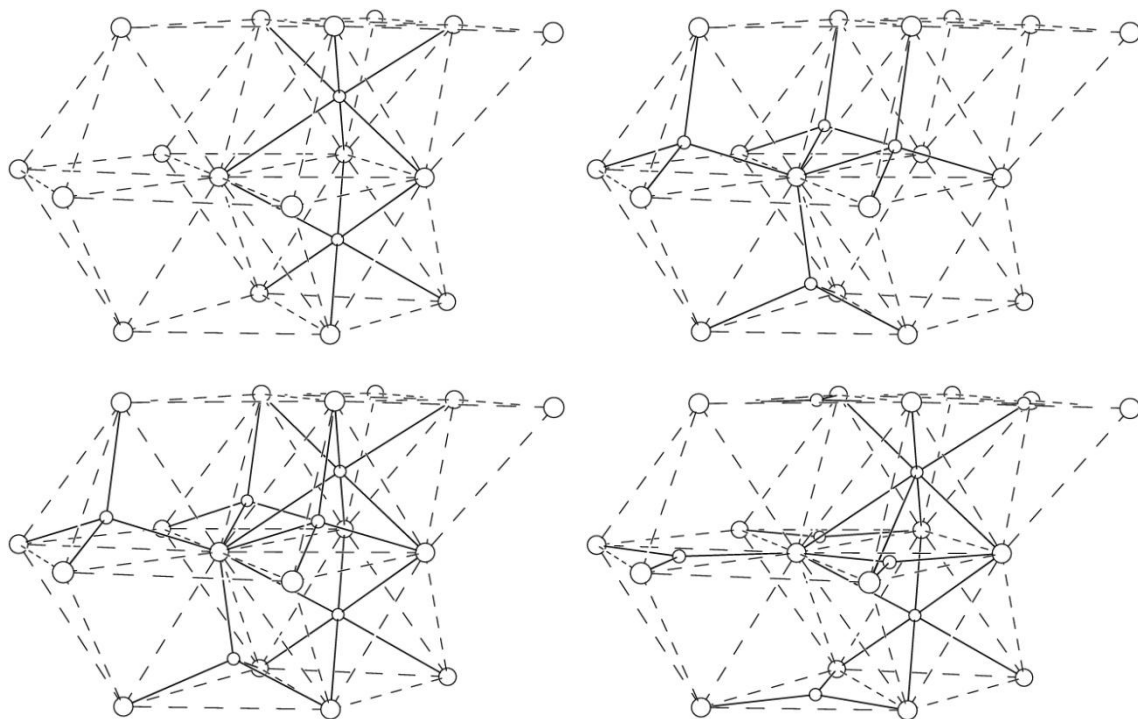


Figure 1.4. Fragments of the structures of NiAs (top left), hexagonal ZnS (wurtzite; top right), Cs₂S (anticotunnite; bottom left), and Ni₂In (bottom right). The larger spheres are anions and the smaller spheres are cations.

CHAPTER 2. DIRECT PERFLUORINATION OF $K_2B_{12}H_{12}$ IN ACETONITRILE. AN EFFICIENT LARGE-SCALE SYNTHESIS OF $K_2B_{12}F_{12}$ AND $Cs_2B_{12}F_{12}$

Introduction

In 2003 the Strauss group, in collaboration with Solntsev, reported an improved synthesis of $K_2B_{12}F_{12}$ (72% recrystallized yield) in a one-pot reaction that required first heating $K_2B_{12}H_{12}$ in anhydrous HF to 70 °C and then treating the reaction mixture with 20/80 F_2/N_2 at 25 °C (see Scheme 2.1).^{28,63} However, the scale of the reaction was limited to ca. 1 g of $K_2B_{12}H_{12}$ starting material in order to obtain the highest yield with the fewest by-products. In addition, a Monel reaction vessel was required because the pressure of F_2/N_2 typically used was 50 psi or higher, too high for routine use of large-volume fluoropolymer reaction vessels. Furthermore, the fluorination took nearly a week to complete (nominally five to six days, and one additional day for workup and recrystallization of the product). In 2004 Casteel and Ivanov reported in a patent that $B_{12}H_{12}^{2-}$ salts could be polyfluorinated with F_2 not only in anhydrous HF but also in aqueous HF, formic acid, and acetic acid.⁶⁴ However, complete conversion of $B_{12}H_{12}^{2-}$ to $B_{12}F_{12}^{2-}$ was not achieved in any solvent other than anhydrous HF, and neither reaction times nor isolated yields of purified $B_{12}F_{12}^{2-}$ salts were reported. Note that all previous preparations of $K_2B_{12}F_{12}$ or attempts to prepare $B_{12}F_{12}^{2-}$ salts were performed in acidic media.

In this chapter, a new procedure is described that was used for the preparation of 99.5+ mol% $K_2B_{12}F_{12}$ in 74% recrystallized yield or 99.5+ mol% $Cs_2B_{12}F_{12}$ in 76% recrystallized yield using up to 10 g of $K_2B_{12}H_{12}$ as the starting material, acetonitrile as the solvent, and an ordinary Pyrex flask with standard-taper joints as the reaction vessel.

When the partially fluorinated mixture of compounds $\text{K}_2\text{B}_{12}\text{H}_8\text{F}_4/\text{K}_2\text{B}_{12}\text{H}_7\text{F}_5$ was used instead of $\text{K}_2\text{B}_{12}\text{H}_{12}$ as the starting material, the yield of $\text{K}_2\text{B}_{12}\text{F}_{12}$ was 92%. The development of this procedure was carried out in parallel with DFT calculations, which helped to explain why rigorous *exclusion* of any protic acid was the key to an efficient F_2 perfluorination of $\text{K}_2\text{B}_{12}\text{H}_{12}$.

Experimental

I. Reagents and Solvents.

The salt $\text{K}_2\text{B}_{12}\text{H}_{12}$ (KatChem) was used as received. Potassium fluoride (Mallinckrodt) was ground to a fine powder in a mortar and pestle and dried at 250 °C. The mixture of gaseous fluorine (20%) and nitrogen (80%) was obtained from Air Products and Chemicals, Inc. and used as received. Anhydrous AlCl_3 (Mallinckrodt) was sublimed under vacuum. The compounds KI, KHSO_4 , KHCO_3 , K_2CO_3 , and CaH_2 (Mallinckrodt) were Reagent Grade or better and were used as received. Acetonitrile (Aldrich; ACS grade) was purified as follows:⁶⁵ (i) the as-received solvent was refluxed over anhydrous AlCl_3 for 1 h, then distilled; (ii) the distillate was refluxed over KMnO_4 and K_2CO_3 for 15 min, then distilled again; (iii) the second distillate was refluxed over KHSO_4 for 1h, then distilled a third time; (iv) the third distillate was refluxed over CaH_2 for 4–6 h, then distilled for the fourth and last time and was stored under nitrogen.

II. Large-Scale Preparation of $\text{K}_2\text{B}_{12}\text{F}_{12}$ and $\text{Cs}_2\text{B}_{12}\text{F}_{12}$.

The compound $\text{K}_2\text{B}_{12}\text{H}_{12}$ (10.1 g, 46 mmol) was dissolved in a mixture of *w*- CH_3CN (490 mL) and H_2O (12 mL) in a three-neck one-liter Pyrex round-bottom flask to give a colorless solution. Finely-ground KF (22.7 g, 390 mmol) was added, most of which did not dissolve. A 20/80 F_2/N_2 mixture was bubbled through the reaction mixture at the rate of 115–125 mL min^{-1} for 6 h with vigorous stirring. The reaction mixture became pale yellow after 3 h of fluorination. The gas flow was stopped after 6 h and the reaction mixture was bubbled with N_2 for 30 min to remove traces of F_2 . The mixture was filtered

and the filtrate was evaporated to dryness under vacuum. The solid residue was re-dissolved in 500 mL of a-CH₃CN and filtered. Finely-ground KF (27.3 g, 470 mmol) was added to the filtrate. The 20/80 F₂/N₂ mixture was bubbled through the reaction mixture at a slightly lower rate, 100–110 mL min⁻¹, for 7 h, again with vigorous stirring. The reaction was judged to be complete when an aqueous KI solution in a trap connected to the outlet of the reaction flask changed color from colorless or light yellow to brown. The reaction mixture was filtered and the filtrate was neutralized to pH 7 with aqueous KHCO₃. All volatiles were removed under vacuum. The pale-yellow solid residue was mixed with 100 mL of w-CH₃CN and filtered. The filtrate was evaporated to dryness under vacuum. The resulting pale-yellow solid was dissolved in 6% hydrogen peroxide (50 mL) and heated to 80 °C for 2 h, after which time the solution was colorless. In order to isolate K₂B₁₂F₁₂, the colorless solution was evaporated to dryness and the white solid residue was recrystallized from w-acetonitrile and dried at 60 °C under vacuum. Yield: 14.84 g (34 mmol K₂B₁₂F₁₂, 74% based on K₂B₁₂H₁₂). In order to isolate Cs₂B₁₂F₁₂, the colorless solution was treated with aqueous CsCl (18.1 g, 106 mmol) and cooled to 0°C. The colorless needle-shaped crystals of Cs₂B₁₂F₁₂·H₂O were isolated by filtration, washed twice with ice-cold water (2 × 10 mL), and dried in air. Yield: 22.42 g (34.9 mmol Cs₂B₁₂F₁₂·H₂O, 76% yield based on K₂B₁₂H₁₂).

III. Spectroscopic Measurements.

Samples for ¹¹B and ¹⁹F{¹¹B} NMR spectroscopy were acetonitrile-*d*₃ solutions in 5-mm glass tubes and were recorded on a Bruker WP-300 spectrometer operating at 96.2 and 282.2 MHz, respectively. Chemical shifts (δ scale) are relative to external BF₃(OEt₂) for ¹¹B (δ 0.0 ppm) and external C₆F₆ for ¹⁹F (δ -164.9 ppm). Samples for negative-ion electrospray-ionization mass spectrometry (NI-ESI-MS) were solutions in w-CH₃CN or w-CH₃CN containing 2.4% H₂O and were recorded on a Fisons VG Quattro-SQ mass spectrometer. Samples for thermogravimetric analysis were analyzed using a TA Instruments TGA-2950 instrument (platinum sample pans; *ca.* 10 mg sample size; 25–

650 °C temperature range; heating rate 3 °C min⁻¹). Samples for infrared spectroscopy were Nujol mulls between KBr windows for K₂B₁₂H₁₂ or a mixture of K₂B₁₂HF₁₁ and K₂B₁₂F₁₂.⁶⁶ Spectra were recorded on a Nicolet FTIR spectrometer at 2 cm⁻¹ resolution. Solution conductivities of K₂B₁₂H₁₂ and K₂B₁₂F₁₂ were measured in w-CH₃CN containing 2.4% H₂O using a YSI model 32 conductivity bridge operated at 1 kHz with a YSI model 3403 conductivity cell ($k = 0.9964 \text{ cm}^{-1}$).

IV. DFT calculations.

All DFT calculations were performed by Dr. Alexey Popov (Leibniz Institute for Solid State and Materials Research, Dresden, Germany) using the ORCA code.⁶⁷ The PBE0 functional^{68,69} and def2-TZVP(-f) basis set,⁷⁰ with {311/1} contraction scheme for H and {62111/411/11} for B and F atoms, was employed throughout the calculations. Electrostatic contributions to solvation energies were computed using the conductor-like screening model (COSMO) approach as implemented in ORCA.⁷¹ Symmetry restrictions were not used in the course of optimization.

Results and Discussion

I. General Comments About B₁₂H₁₂²⁻ Fluorination and Determining B₁₂H_{12-x}F_x²⁻ Mol% Values. Optimization of Fluorination Reaction Conditions.

Whether the fluorinating agent is anhydrous HF,^{28,30} F₂,^{28,63,64} or F-TEDA(BF₄)₂,⁷² the fluorination of B₁₂H₁₂²⁻ almost certainly involves electrophilic attack on the icosahedral borane dianion.⁷³ The DFT-predicted HOMO of B₁₂H₁₂²⁻ is shown in Figure 2.1. The electrophile probably forms a Lewis acid–base complex with one of the triangular B₃ faces of the B₁₂H_{12-x}F_x²⁻ icosahedron in much the same way that the 11th H atom (i.e., H⁺) in B₁₀H₁₁⁻ caps a triangular face of B atoms in the B₁₀H₁₀²⁻ anion⁷⁴ or the 13th H atom (i.e., H⁺) in B₁₂H₁₃⁻ is predicted to cap a triangular face of the B₁₂H₁₂²⁻ anion.⁷⁵

In order to optimize the conditions for F₂ fluorination, a way to reliably measure the mol% of each B₁₂H_{12-x}F_x²⁻ anion in the reaction mixture over time was needed. Negative-ion electrospray-ionization mass spectrometry (NI-ESI-MS) was used for this purpose (the virtues of NI-ESI-MS for analyzing borane and carborane cluster anions in general have been discussed by Hop et al.^{76,77}). A typical intermediate-fluorination-stage NI-ESI mass spectrum is shown in Figure 2.2. A control experiment using a 50:50 mol% mixture of K₂B₁₂H₁₂ and K₂B₁₂F₁₂ as the sample revealed that the sensitivity coefficient of B₁₂F₁₂²⁻ is 3.1 times as large as that of B₁₂H₁₂²⁻. Therefore, all mass-spectral intensities were scaled according to their relative sensitivity coefficients, assuming that the relative change in sensitivity coefficient per unit increment in *x* is constant. For simplicity, the sum of the scaled intensities of the most abundant isotopomers for a given B₁₂H_{12-x}F_x²⁻/KB₁₂H_{12-x}F_x⁻ pair was used as an index of the relative amount of B₁₂H_{12-x}F_x²⁻ present for each observed value of *x* (only occasionally were peaks due to NaB₁₂H_{12-x}F_x⁻ present, usually when the sample inlet system was not rinsed sufficiently before use).

It was not possible to measure the relative concentrations of B₁₂H_{12-x}F_x²⁻ anions in complex mixtures by ¹⁹F{¹¹B} NMR spectroscopy because multiple isomers with overlapping resonances were present for 4 ≤ *x* ≤ 10. However, only one isomer is possible for *x* = 11 and 12. For a sample containing B₁₂HF₁₁²⁻ and B₁₂F₁₂²⁻, the NI-ESI-MS B₁₂F₁₂²⁻/B₁₂HF₁₁²⁻ mole ratio was 7.3 and the ¹⁹F{¹¹B} NMR mole ratio was 6.9, a relative error of ca. 6%. In another sample containing these two anions, the NI-ESI-MS B₁₂F₁₂²⁻/B₁₂HF₁₁²⁻ mole ratio was 1.47 and the ¹⁹F{¹¹B} NMR mole ratio was 1.43, a relative error of ca. 3%. Although larger errors in mole ratios or mol% values determined by the NI-ESI-MS procedure for other mixtures of B₁₂H_{12-x}F_x²⁻ anions cannot be ruled out, that was not an important issue in this study because, for two reasons, there was no intent to determine rate constants from the changes in mol% values over time (i.e., only qualitative estimations of mol% values were needed). The first reason is that the 20/80

F_2/N_2 flow rate was not kept constant from experiment to experiment or even during a given experiment (see below). The second reason is that no attempt was made to keep the size of the bubbles of F_2/N_2 gas or the size and shape of the reaction vessel constant from experiment to experiment (the scale of the syntheses discussed below varied by a factor of 10; however, the same reaction vessel *was* used for reactions with the same amount of $K_2B_{12}H_{12}$ starting material). The solubility of F_2 in HF and organic solvents is very low,^{78,79} and most F_2 fluorinations in organic solvents are believed to occur at the gas-bubble/solution interface.^{79,80} Therefore, it was expected that the fluorination reactions would be heterogeneous in nature, and for this reason only qualitative estimations of relative rates of reaction were determined.

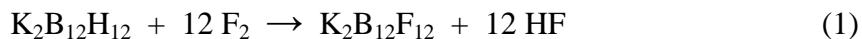
In principle, it should not be possible for the average value of x (i.e., \bar{x}) to be higher than the number of equivalents of F_2 that have been added to the reaction mixture. However, during the early stages of the reaction, the percentages of various $B_{12}H_{12-x}F_x^{2-}$ anions are more difficult to estimate precisely than at latter stages of the reaction. This is because the ratio of NI-ESI-MS sensitivity coefficients is somewhat concentration dependent, and the NI-ESI-MS samples did not all have the same concentration. Therefore, \bar{x} for a narrow range of x values is more precise than for a wide range of x values. Most significantly, \bar{x} near the end of the reaction is relatively precise.

The F_2/N_2 flow rate was not kept constant because there was less interest in *minimizing* the reaction time (although *shortening* the reaction time was one of the goals) than in minimizing the $F_2/K_2B_{12}H_{12}$ mole ratio necessary for efficient perfluorination. In general, the flow rate was set at a level that resulted in only a small amount of unreacted F_2 leaving the reaction vessel over time (this was monitored by bubbling the gas leaving the reaction vessel through a solution of KI in H_2O , which was changed periodically). In many experiments, it was necessary to decrease the flow rate as the reaction progressed because the uptake of F_2 by the reaction mixture decreased over time. For the most efficient reactions reported below, the flow rates used resulted in negligible amounts of

unreacted F₂ leaving the reaction vessel until a short time before the perfluorinations were complete.

The first goal of this work was to significantly improve the synthesis of B₁₂F₁₂²⁻ salts relative to our 2003 procedure that is depicted in Scheme 2.1.^{28,63} The goal was to develop an alternative procedure that would allow one to (i) scale up the reaction so that at least 10 g of K₂B₁₂H₁₂ starting material could be used without sacrificing the purity or yield of the final product (the benchmark for the recrystallized yield of 99+% pure K₂B₁₂F₁₂ was 72%)²⁸, (ii) shorten the reaction time, including recrystallization of the final product, from ca. 1 week to no more than two days, (iii) use as little excess F₂ as possible, and (iv) replace anhydrous HF (a-HF) with a less-reactive and less-volatile solvent so that a fluoropolymer or possibly a Pyrex reaction vessel could be used and so that the F₂/N₂ mixture could be continuously bubbled through the reaction mixture until the reaction was complete.

Acetonitrile has been used for F₂ fluorinations of organic substrates⁸¹⁻⁸³ because it is fluorinated very slowly at 0 °C.^{84,85} It is also a polar solvent in which K₂B₁₂H₁₂ is soluble (the solubility of K₂B₁₂H₁₂ was determined to be 0.035 M in "wet" acetonitrile (i.e., ACS-grade acetonitrile as received, containing less than 0.3% water according to the manufacturers analysis; abbreviated as w-CH₃CN); the solubility was determined to be only 0.008 M in anhydrous acetonitrile (a-CH₃CN)). Therefore, acetonitrile was chosen as the most suitable replacement for a-HF in the F₂ fluorination of K₂B₁₂H₁₂. The balanced net reaction is given by Eqn. 1:



Reaction mixtures consisting of K₂B₁₂H₁₂ vigorously stirred in w-CH₃CN at 0 °C, were treated with a continuous flow of atmospheric-pressure 20/80 F₂/N₂ that was slowly bubbled through the stirred mixtures (note: atmospheric pressure in Fort Collins is ca.

0.8 atm). The nominal initial concentrations of $\text{K}_2\text{B}_{12}\text{H}_{12}$ anions that were used for the reactions varied from 0.05 to 0.5 M (these are "nominal" concentrations because all of the starting material did not dissolve until several boron vertexes had been fluorinated). The results for two typical reactions are listed in Table 2.1 as Exps. 1 and 2. The mol% values listed were determined by NI-ESI-MS. It can be seen that these reaction conditions are not suitable for an efficient large-scale synthesis. For example, in Exp. 2 a significant excess of F_2 was required, and even then the fluoroborane product contained 6% $\text{B}_{12}\text{HF}_{11}^{2-}$. In addition, the reaction took 52 h to reach that point, far longer than our goal of less than 24 h for the fluorination phase of the targeted two-day synthesis. Furthermore, the limited solubility of $\text{K}_2\text{B}_{12}\text{H}_{12}$ and $\text{K}_2\text{B}_{12}\text{H}_{12-x}\text{F}_x$ with $x \leq 3$ in w- CH_3CN resulted in significant amounts of undissolved solid remaining in the reaction mixture for the first seven hours of F_2 bubbling, and this is certainly one of the causes of the long reaction time.

Nevertheless, the results of Exps. 1 and 2 were encouraging: $\text{B}_{12}\text{H}_{12}^{2-}$ can be perfluorinated with F_2 in acetonitrile *without* the formation of by-products that are difficult to remove from $\text{K}_2\text{B}_{12}\text{F}_{12}$. For example, the potential by-products KF , KHF_2 , and KBF_4 have extremely low solubilities in CH_3CN and therefore are easy to remove from $\text{K}_2\text{B}_{12}\text{F}_{12}$. Furthermore, although it has proven difficult to separate the by-product $\text{K}_2\text{B}_{12}\text{HF}_{11}$ from $\text{K}_2\text{B}_{12}\text{F}_{12}$ by fractional recrystallization, the presence of 6% $\text{B}_{12}\text{HF}_{11}^{2-}$ was not considered a problem in the long run because a more efficient set of reaction conditions would transform it into $\text{B}_{12}\text{F}_{12}^{2-}$ (just like the other 94% of $\text{B}_{12}\text{HF}_{11}^{2-}$ that had been transformed into $\text{B}_{12}\text{F}_{12}^{2-}$). The problem was that under these conditions the final fluorination of $\text{B}_{12}\text{HF}_{11}^{2-}$ was apparently very slow.

To mitigate the problem of undissolved solids at early stages of fluorination, a series of experiments exemplified by Exp. 3 in Table 2.1 were performed (see Scheme 2). The same amount of $\text{K}_2\text{B}_{12}\text{H}_{12}$ was used for Exps. 2 and 3, but the solvent for Exp. 3 was w- CH_3CN to which 1% H_2O had been added and the concentration of $\text{K}_2\text{B}_{12}\text{H}_{12}$ was

reduced by a factor of 10. These changes resulted in a homogeneous solution of $\text{K}_2\text{B}_{12}\text{H}_{12}$ at the start of fluorination. At various intervals, the reaction solution was purged with N_2 and small samples were withdrawn, worked up, and analyzed by NI-ESI-MS. The results are displayed as the blue curves in the panels shown in Figure 2.3. The x axis in each plot is the $n(\text{F}_2)/n(\text{K}_2\text{B}_{12}\text{H}_{12})$ mole ratio (i.e., the ratio of the molar amount of F_2 added at that point in time to the molar amount of $\text{K}_2\text{B}_{12}\text{H}_{12}$ *starting material* (i.e., $n(\text{K}_2\text{B}_{12}\text{H}_{12})$ is *not* the number of moles of $\text{B}_{12}\text{H}_{12}^{2-}$ remaining at that time; it is constant for a given synthesis)). The y axes are, from top to bottom, the average x value for all $\text{B}_{12}\text{H}_{12-x}\text{F}_x^{2-}$ anions in the reaction mixture, the mol% $\text{B}_{12}\text{H}_{12}^{2-}$ remaining in the reaction mixture, and the mol% $\text{B}_{12}\text{F}_{12}^{2-}$ in the reaction mixture at that point in time.

At first glance, the blue curves for Exp. 3 appear unremarkable: they show an increase in \bar{x} , an increase in the mol% $\text{B}_{12}\text{F}_{12}^{2-}$, and a decrease in the mol% $\text{B}_{12}\text{H}_{12}^{2-}$ over time. However, mass spectra of samples withdrawn after 30 min and after 7 h, which are shown in Figure 2.4, revealed a critical detail that cannot be discerned from the plots in Figure 2.3 (the peaks due to $\text{KB}_{12}\text{H}_{12-x}\text{F}_x^-$ monoanions other than $\text{KB}_{12}\text{H}_{12}^-$ are not shown in the spectra in Figure 2.4, but that does not affect the conclusions that follow because their intensities are roughly proportional to the intensities of the peaks of the corresponding $\text{B}_{12}\text{H}_{12-x}\text{F}_x^{2-}$ anions; the full spectra are shown in Figures 2.2 and 2.5). Consider the 30 min spectrum. The most abundant $\text{B}_{12}\text{H}_{12-x}\text{F}_x^{2-}$ anion is the starting material, $\text{B}_{12}\text{H}_{12}^{2-}$. Also present are small amounts of anions with $x = 1-7$ and a significantly larger amount of the final product, $\text{B}_{12}\text{F}_{12}^{2-}$ (the amount of $\text{B}_{12}\text{F}_{12}^{2-}$ present is ca. 4% of the amount of $\text{B}_{12}\text{H}_{12}^{2-}$ present; for comparison, the amount of $\text{B}_{12}\text{H}_5\text{F}_7^{2-}$ present is ca. 2.1% of the amount of $\text{B}_{12}\text{H}_{12}^{2-}$). Conspicuously absent ($\ll 1\%$) are anions with $x = 8-11$, which means that *they were converted to $\text{B}_{12}\text{F}_{12}^{2-}$ faster than they were formed*. Now consider the 7 h spectrum. Along with $\text{B}_{12}\text{F}_{12}^{2-}$, anions with $x = 9-11$ are the dominant species. In fact, the anions with $x = 9-11$ are collectively ca. 3 times as abundant as $\text{B}_{12}\text{F}_{12}^{2-}$. The \bar{x} value for Exp. 3 was 9.3 after 12.7 equiv. of F_2 had been

passed through the solution, but only increased to 11.6 after another 9.1 equiv. of F_2 has been used (see Figure 2.3). Thirty minutes into the F_2 fluorination, a significant amount of $B_{12}F_{12}^{2-}$ had been formed and the concentration of $B_{12}HF_{11}^{2-}$ was so low it could not be detected by NI-ESI-MS. However, after 21.8 equiv. of F_2 had been added, the ratio $\text{mol}(B_{12}F_{12}^{2-})/\text{mol}(B_{12}HF_{11}^{2-})$ was only 4 (see Table 2.1). How could $B_{12}F_{12}^{2-}$ be formed rapidly from $B_{12}HF_{11}^{2-}$ at the beginning of the reaction but formed only slowly in the middle of the reaction and even slower at the time when the reaction was stopped?

Several factors were considered. To a first approximation, the total concentration of all B_{12} species, and hence the ionic strength, remained constant throughout the reaction, so that was probably not an issue (control experiments showed that only a few percent of the solvent CH_3CN evaporated during 18 h of F_2/N_2 bubbling at 0 °C). Later experiments (e.g. Exps. 7–11) proved that CH_3CN is not fluorinated fast enough under the conditions of our reactions to account for final $n(F_2)/n(K_2B_{12}H_{12})$ ratios much greater than 12. Some B_{12} clusters were destroyed during the fluorinations, producing KBF_4 , which is only sparingly soluble in acetonitrile, but the formation of a modest amount of fine precipitate during the reaction did not seem like a plausible explanation for the inhibition of F_2 fluorination of $B_{12}HF_{11}^{2-}$ as the reaction progressed.

The only possible explanation that remained was that the buildup of HF in the reaction mixture was slowing down the F_2 fluorination, especially for the $x = 9-11$ anions. At first this possibility was doubted, because the Casteel and Ivanov patent contains the statement "The improvement in the liquid phases process resides in effecting the $[F_2]$ fluorination of said borohydride salts [including $K_2B_{12}H_{12}$] in the presence of a reaction medium having an acidity between that of water and anhydrous HF. More specifically, the reaction medium should have a Hammett acidity, H_0 , between $0 > H_0 > -11$."⁶⁴ In Example 20 of the patent, the solvent was aqueous $NaHCO_3$. This is the only example with a reaction medium that was not acidic, and the poor results caused the

inventors to state "The results show that reaction media which remain below the desired level [of acidity] throughout the reaction give very inefficient fluorination."⁶⁴

Using the final mol% values for the $x = 9-12$ anions in Exp. 3 and assuming that no HF was swept out of the reaction vessel by the F_2/N_2 gas, the final concentration of HF was calculated to be 0.53 M. After the Exp. 3 reaction mixture was filtered, it was neutralized with aqueous KOH. From the amount of KOH used, the concentration of HF (i.e., active H^+) in the final reaction mixture was determined to be 0.49 M, more than 90% of the theoretical amount. To demonstrate more conclusively that the presence of HF inhibits the F_2 fluorination of $B_{12}H_{12}^{2-}$ in $w-CH_3CN$, several syntheses were performed such as Exp. 4, which was similar to Exp. 3 except that the solvent consisted of $w-CH_3CN$ to which 2% H_2O and 2% anhydrous HF had been added, as shown in Scheme 2.2. This reaction was also monitored by NI-ESI-MS over time (see the black curves in Figure 2.3) but was stopped after only 9.5 h because the $n(F_2)/n(K_2B_{12}H_{12})$ ratio had already reached 29 (see Table 2.1). At that point, \bar{x} was only 10.5. In addition, very little $B_{12}F_{12}^{2-}$ was formed during the first 30 min. The Air Products patent notwithstanding, it was now clear that HF *inhibits* the F_2 perfluorination of $K_2B_{12}H_{12}$, and the buildup of HF in the reaction mixture over time had to be avoided to achieve the goal of a rapid and efficient large-scale synthesis of $K_2B_{12}F_{12}$. It is ironic that HF inhibits F_2 fluorination in our reactions because it can slowly fluorinate $B_{12}H_{12}^{2-}$ by itself in $w-CH_3CN$ at 0 °C (as well as in $a-HF$ at higher temperatures^{28,30}). An identical solution to the one used for Exp. 4 was prepared but was not treated with F_2/N_2 gas. Within 35 min, 6% of the first fluorination intermediate, $B_{12}H_{11}F^{2-}$, was detected by NI-ESI-MS.

The discovery that HF inhibits the F_2 fluorination of $B_{12}H_{12}^{2-}$ in acetonitrile led to Exps. 5–11 in Table 2.1. The addition of insoluble KF to sequester HF in the form of insoluble KHF_2 proved to be the key to the development of a rapid and efficient F_2 fluorination of $K_2B_{12}H_{12}$. The red curves in Figure 2.3 correspond to Exp. 11 (to demonstrate reproducibility, two data points from Exp. 9 ("+") and one data point from

Exp. 8 ("x") are superimposed on the red curve in the top panel of the figure). The curves in the top panel, which are graphs of \bar{x} as a function of the $n(\text{F}_2)/n(\text{K}_2\text{B}_{12}\text{H}_{12})$ mole ratio, clearly show that F_2 fluorination is faster as well as more efficient in the absence of the protic acid HF, especially in the latter stages of the reaction. For example, for $\bar{x} \approx 7.3$, the $n(\text{F}_2)/n(\text{K}_2\text{B}_{12}\text{H}_{12})$ values for the red (KF added), blue (neither KF nor HF added), and black (HF added) curves are ca. 7, 10, and 16, respectively; for $\bar{x} \approx 11.5$, the $n(\text{F}_2)/n(\text{K}_2\text{B}_{12}\text{H}_{12})$ values are 12, 20, and >30 , respectively. The difference between the red and blue curves for $\bar{x} \approx 7.3$ is only three equiv. F_2 , but adding the next four F atoms to the B_{12} cages required only five additional equiv. F_2 when KF was added but ten additional equiv. F_2 when neither KF nor HF was added. The differences between the red and black curves are even larger.

The middle and bottom panels of Figure 2.3 show that both (i) the disappearance of $\text{B}_{12}\text{H}_{12}^{2-}$ at the beginning of the reaction and (ii) the appearance of $\text{B}_{12}\text{F}_{12}^{2-}$ towards the end of the reaction are faster in the absence of acid than in the presence of acid. For example, at $n(\text{F}_2)/n(\text{K}_2\text{B}_{12}\text{H}_{12}) \approx 5$, $\text{B}_{12}\text{H}_{12}^{2-}$ had virtually disappeared when KF had been added to the reaction mixture (red curve) but was still at one-third of its original concentration when HF had been added to the reaction mixture (black curve). Furthermore, when neither KF nor HF had been added (blue curve), the disappearance of $\text{B}_{12}\text{H}_{12}^{2-}$ became slower and slower as the reaction progressed.

The experiments described above eventually led to a set of conditions that produced either 15 g of 99.5+% pure $\text{K}_2\text{B}_{12}\text{F}_{12}$ (74% yield based on $\text{K}_2\text{B}_{12}\text{H}_{12}$) or 22 g of 99.5% pure $\text{Cs}_2\text{B}_{12}\text{F}_{12}$ (76% yield) in less than two days using ordinary Pyrex reaction vessels and acetonitrile containing an excess of KF, as shown in Scheme 2. These optimized syntheses correspond to Exps. 10 and 11 in Table 2.1, respectively. It was found that in order to shorten the reaction time as much as possible, it was necessary to add ca. half the F atoms using *w*- CH_3CN to which 2.4% H_2O had been added as the solvent, after which the reaction mixture was filtered (to remove KF, KHF_2 , and KBF_4) and the solvent was

stripped by rotary evaporation. The residue was redissolved in a-CH₃CN containing an excess of KF and the remaining F atoms were added. This procedure used 14.0 equiv. F₂, which is only a 16.7% excess based on the amount of K₂B₁₂H₁₂ starting material. The purity of isolated K₂B₁₂F₁₂ and Cs₂B₁₂F₁₂·H₂O was judged to be 99.5+% based on their NMR and NI-ESI mass spectra, representative examples of which are shown in Figure 2.6. The new procedure is compared with other literature B₁₂H₁₂²⁻ fluorination procedures in Table 2.2. It represents a ten-fold increase in the scale of the reaction over our previous procedure without sacrificing yield or purity. In addition, it can be performed in an ordinary Pyrex reaction vessel and it is very efficient in terms of the amount of excess F₂ that is required. Finally, the ten-fold increase in scale was achieved in one-third of the time necessary for the previously reported procedure.

II. Fluorination of B₁₂H_{12-x}F_x²⁻ Ions in Acetonitrile at the Gas-Bubble/Solution Interface.

As stated earlier, it is generally assumed that F₂ fluorinations in organic solvents occur at the interface of bubbles of F₂/N₂ gas and the solution.^{79,80} Figure 2.7 shows a reaction scheme consistent with this hypothesis. It also shows F₂ acting as an electrophile and forming a Lewis acid–base complex with one of the 20 triangular faces of the B₁₂H₁₂²⁻ anion prior to the B–H → B–F transformation, which occurs with the concomitant formation of a molecule of HF. Furthermore, the B₁₂H₁₂²⁻ and B₁₂H₁₁F²⁻ anions depicted at the gas-bubble/solution interface are shown, for simplicity, half in solution and half in the gas phase. Although there was no intent to investigate the interfacial nature of this reaction at the beginning of this study, several observations were made that strongly suggested that the F₂ fluorination of B₁₂H₁₂²⁻ did not occur in a homogeneous phase, and experiments were then designed and carried out to test this hypothesis.

If the fluorination of B₁₂H_{12-x}F_x²⁻ anions occurred in homogeneous solution, where all twenty triangular faces were simultaneously exposed to the dissolved fluorinating

agent, and if the equilibrium binding of F_2 to an anion and the rate of fluorination of an individual B–H vertex were both independent of the value of x , a statistical factor would cause the first fluorination step, $B_{12}H_{12}^{2-} \rightarrow B_{12}H_{11}F^{2-}$, to be 12 times faster than the last fluorination step, $B_{12}HF_{11}^{2-} \rightarrow B_{12}F_{12}^{2-}$. Given that $B_{12}H_{12-x}F_x^{2-}$ anions become weaker Lewis bases as x increases, and given that the remaining B–H bonds in a $B_{12}H_{12-x}F_x^{2-}$ anion become shorter, and presumably stronger, as x increases (see the FTIR spectra of $K_2B_{12}H_{12}$ and a mixture of $K_2B_{12}HF_{11}$ and $K_2B_{12}F_{12}$ in Figure 2.8), one might expect the difference in rates for the first and last steps to be greater than a factor of 12. However, the red curve in the top panel in Figure 2.3 shows that this is definitely not the case: the slopes of all of the lines connecting two consecutive data points do not differ by more than a factor of two. This means that *the substitution of H atoms by F atoms occurs at approximately the same rate for all values of x* under “red curve” conditions.

This is further demonstrated by comparing the average rate of disappearance of $B_{12}H_{12}^{2-}$ at the beginning of the reaction (see the red curve in the middle panel of Figure 2.3) with the average rate of disappearance of $B_{12}HF_{11}^{2-}$ at the end of the reaction, which is equal in magnitude and opposite in sign to the rate of appearance of $B_{12}F_{12}^{2-}$ at the end of the reaction (see the red curve in the bottom panel of Figure 2.3). The absolute value of the slope of the first red line in the middle panel is 38% per equiv. F_2 ; the slope of the last red line in the bottom panel is 30% per equiv. F_2 , only 21% smaller.

Roughly equal rates of fluorination for all values of x strongly suggest a heterogeneous reaction involving the gas-bubble/solution interface. The model shown in Figure 2.7 can be refined in the following way. If one assumes that only *one* triangular face of the anion (i.e., three B–X vertexes) penetrates the gas bubble *and* that the anions are preferentially oriented so that the triangular face that penetrates has the maximum number of B–H vertexes that remain on the anion, then at least one B–H bond would penetrate into the F_2/N_2 bubble for $x < 12$ and an F_2 molecule would bind to and react with that triangular face in the bubble regardless of how many other faces have B–H

vertexes (i.e., in this model, every anion that penetrated the bubble with $x < 12$ would have at least one B–H vertex that can react with F_2).

If these assumptions are valid, there would be essentially no statistical factor that favors the fluorination of anions with low values of x . Based on the extensive literature on the partitioning of inorganic anions at the air/water interface⁸⁶⁻⁹⁰ (and a less extensive but still significant literature on anion partitioning at gas/nonaqueous-solution interfaces^{91,92}), it can be proposed that the aforementioned assumptions are reasonable and therefore provide an explanation for the qualitatively similar relative rates of F_2 fluorination of $B_{12}H_{12}^{2-}$ and $B_{12}HF_{11}^{2-}$. For example, it is well known that soft, polarizable anions, which generally have large ionic radii, are present, and their concentrations are even enhanced, at the surface of polar liquids, including air bubbles in polar liquids.⁸⁶⁻⁹³ It has been shown that BH_4^- is a softer Lewis base than BF_4^- .⁹⁴ Is it possible that $B_{12}H_{12}^{2-}$ is also softer (i.e., more polarizable) than $B_{12}F_{12}^{2-}$? To estimate the relative polarizabilities, α , of $B_{12}H_{12}^{2-}$ and $B_{12}F_{12}^{2-}$, they were calculated using DFT methods in a dielectric-continuum-model for acetonitrile. The polarizabilities of Br^- , BH_4^- , and BF_4^- were also calculated under the same conditions (the literature values for Br^- (computational)⁹⁵ and BH_4^- (experimental, in KBH_4)⁹⁶ are 4.5 and 4.0 \AA^3 , respectively). The results are: $\alpha(B_{12}H_{12}^{2-}) = 36.5 \text{ \AA}^3$; $\alpha(B_{12}F_{12}^{2-}) = 26.4 \text{ \AA}^3$; $\alpha(Br^-) = 3.6 \text{ \AA}^3$; $\alpha(BH_4^-) = 5.9 \text{ \AA}^3$; $\alpha(BF_4^-) = 3.4 \text{ \AA}^3$. Thus, $B_{12}H_{12}^{2-}$ is significantly more polarizable, and therefore softer, than $B_{12}F_{12}^{2-}$. According to reported second-harmonic-generation and sum-frequency-generation experiments and molecular dynamics calculations on inorganic anions at the surface of polar liquids,⁸⁶⁻⁹³ the softer $B_{12}H_{12}^{2-}$ anion should have a greater propensity than $B_{12}F_{12}^{2-}$ or $B_{12}HF_{11}^{2-}$ to partition to the gas-bubble/solution interface. It is even possible that $B_{12}H_{12}^{2-}$ and $B_{12}H_{12-x}F_x^{2-}$ anions with low values of x could exclude $B_{12}HF_{11}^{2-}$ from the gas-bubble/solution interface and, therefore, exclude it from access F_2 .

To test this possibility, the following experiments were performed. A solution of $B_{12}HF_{11}^{2-}$ and $B_{12}F_{12}^{2-}$ was prepared in w- CH_3CN containing 2.4% added H_2O . The mole ratio $[B_{12}HF_{11}^{2-}]/[B_{12}F_{12}^{2-}]$ was determined by ^{19}F NMR integration to be 1.43. The solution was divided into two equal parts, to which either $K_2B_{12}H_{12}$ or $K_{12}B_{12}F_{12}$ was added. The ratios $[B_{12}HF_{11}^{2-}]/[B_{12}H_{12}^{2-}]$ and $[B_{12}HF_{11}^{2-}]/(\text{added } [B_{12}F_{12}^{2-}])$ were both 1.53. The total concentration of B_{12} clusters and the concentration of K^+ was therefore the same in the two solutions. Each solution was bubbled with 20/80 F_2/N_2 at the same rate used for Exps. 10 and 11 for a given period of time. The results are shown in Figure 2.9. In the absence of $B_{12}H_{12}^{2-}$, $B_{12}HF_{11}^{2-}$ was converted to $B_{12}F_{12}^{2-}$ with only 1.1 equiv. F_2 (based on $B_{12}HF_{11}^{2-}$), similar to the final red-curve line segment in Figure 2.3. However, in the presence of $B_{12}H_{12}^{2-}$, only 2% of the $B_{12}HF_{11}^{2-}$ present was converted to $B_{12}F_{12}^{2-}$, even after 3.2 equiv. F_2 (based on $B_{12}HF_{11}^{2-}$; this amount is 4.0 equiv. based on added $B_{12}H_{12}^{2-}$) was bubbled through the solution. During the addition of F_2/N_2 , $B_{12}H_{12}^{2-}$ was converted to a mixture of $B_{12}H_{12-x}F_x^{2-}$ anions with $x = 0$ (0.24%), 1 (2.08%), 1 (3.61%), 3 (5.58%), 4 (15.01%), 5 (3.24%), and 6 (1.18%); no $B_{12}HF_{11}^{2-}$ was produced from the added $B_{12}H_{12}^{2-}$. Therefore, $B_{12}H_{12}^{2-}$ and $B_{12}H_{12-x}F_x^{2-}$ anions with low values of x significantly inhibited the fluorination of $B_{12}HF_{11}^{2-}$, which is consistent with the hypothesis that the harder anion $B_{12}HF_{11}^{2-}$ is excluded from the gas-bubble/solution interface when the softer anions $B_{12}H_{12}^{2-}$, $B_{12}H_{11}F^{2-}$, $B_{12}H_{10}F_2^{2-}$, etc. are present. When only $B_{12}HF_{11}^{2-}$ and $B_{12}F_{12}^{2-}$ are present, such as during the final stage of Exps. 10 and 11, $B_{12}HF_{11}^{2-}$ is not excluded from the bubble surface and is fluorinated quickly.

III. Inhibition of F_2 Fluorination of $B_{12}H_{12-x}F_x^{2-}$ Anions by Protic Acids.

In order to investigate whether the inhibition of F_2 fluorination of $B_{12}H_{12-x}F_x^{2-}$ anions by HF is due to the unique properties of HF dissolved in acetonitrile or to general-acid inhibition, Exps. 12 and 13 listed in Table 2.1 were performed. The solvents were 50/50 (v/v) w- CH_3CN/HCO_2H and 88/12 (v/v) HCO_2H/H_2O , respectively. No KF was added, so HF also built up in the reaction mixtures over time. In both cases, the presence of a

significant amount of formic acid inhibited F_2 fluorination even more than in Exp. 1, in which the only acid present was the fluorination by-product HF. These results imply that there is general-acid inhibition of F_2 fluorination.

The experiments discussed in the previous section not only support the hypothesis that $B_{12}H_{12-x}F_x^{2-}$ anions with low values of x are more likely to be present at the gas-bubble/solution interface than anions with high values of x , they also suggest that the B–H vertexes of $B_{12}H_{12-x}F_x^{2-}$ anions at the interface are more likely to extend into the bubble of F_2/N_2 than the B–F vertexes of these anions (this is because excess $B_{12}F_{12}^{2-}$ did not prevent the rapid fluorination of $B_{12}HF_{11}^{2-}$ even as the concentration of the latter anion approached zero). When HF is present during the fluorination, it almost certainly solvates $B_{12}H_{12-x}F_x^{2-}$ anions more strongly than does CH_3CN . Even though the dipole moments of gas-phase HF and CH_3CN are 1.80 and 3.92 D, respectively, the H–F bond is considerably more polar than the C–H bonds of CH_3CN . Furthermore, the dielectric constants of neat HF and CH_3CN are 83.6 (0 °C) and 37.6 (15 °C), respectively. It can be proposed that HF preferentially solvates $B_{12}H_{12-x}F_x^{2-}$ anions at triangular B_3 faces with B–H vertexes. If this is true, it would explain the inhibition of F_2 fluorination by the steadily increasing amount of HF byproduct as $B_{12}H_{12}^{2-}$ is converted to $B_{12}F_{12}^{2-}$ (i.e., in the absence of KF(s)). For one thing, HF solvation (i.e., formation of an acid-base complex between the anion and HF) would affect the equilibrium binding of F_2 to the anion. For another thing, it would make the portions of the $B_{12}H_{12-x}F_x^{2-}$ anions with soft B–H vertexes less soft, which would affect the extent to which the B–H vertexes extend into the F_2/N_2 bubble (note that the polarizability of HF, 0.83 \AA^3 ,⁹⁷ is exceptionally low).

DFT calculations were performed to test this proposal. Because DFT is not very reliable for describing weak intermolecular interactions, the relative energies of monoprotonated adducts of the hypothetical intermediate anion 1,2,3,4,5,6- $B_{12}H_6F_6^{2-}$ and the known intermediate $B_{12}HF_{11}^{2-}$ were calculated. For each anion, a single H^+ ion was added to different triangular faces and the resulting monoanions were optimized in a

dielectric continuum that is a model for an acetonitrile solution. The DFT-predicted relative energies, which are shown next to each DFT-optimized structure in Figure 2.10, demonstrate that protonation of $1,2,3,4,5,6\text{-B}_{12}\text{H}_6\text{F}_6^{2-}$ on a triangular face that includes B12 is favored by 47.0 kJ mol^{-1} relative to a triangular face that includes B1. This is in spite of the charge distribution that results in negative charge density accumulating at the "F₆" end of the $1,2,3,4,5,6\text{-B}_{12}\text{H}_6\text{F}_6^{2-}$ anion (see below). The differences for the four types of triangular faces of the last fluorination intermediate, $\text{B}_{12}\text{HF}_{11}^{2-}$, are smaller but still favor a triangular face that includes the last remaining B–H vertex (i.e., the B12–H12 moiety). Based on these results, it was concluded that HF and other protic acids inhibit the F₂ fluorination of $\text{B}_{12}\text{H}_{12-x}\text{F}_x^{2-}$ anions by competing with the Lewis acid F₂ for the most basic triangular faces, namely those with the remaining B–H vertexes. The rate of F₂ fluorination becomes slower as HF is formed in the reaction because the concentration of *vacant* triangular faces with B–H vertexes becomes lower. As more HF accumulates in solution, the five triangular faces of $\text{B}_{12}\text{HF}_{11}^{2-}$ that include B12–H12 are, presumably, all solvated by HF molecules, significantly decreasing the rate of the final fluorination step $\text{B}_{12}\text{HF}_{11}^{2-} \rightarrow \text{B}_{12}\text{F}_{12}^{2-}$.

The isomer $1,2,3,4,5,6\text{-B}_{12}\text{H}_6\text{F}_6^{2-}$ was chosen for the DFT study described above because of its high symmetry and because the computational results would be easier to interpret than those of a lower-symmetry species. It may not be an actual intermediate in the F₂ fluorination of $\text{B}_{12}\text{H}_{12}^{2-}$. In fact, it was not one of the $\text{B}_{12}\text{H}_6\text{F}_6^{2-}$ intermediates observed during the high-temperature HF fluorination of $\text{B}_{12}\text{H}_{12}^{2-}$.^{30,98}

IV. The Solvation of $\text{B}_{12}\text{H}_{12-x}\text{F}_x^{2-}$ Anions.

Interestingly, the difference in DFT-predicted energies for the B1,B2,B3 and B7,B8,B12 isomers of protonated $\text{H}(\text{B}_{12}\text{H}_6\text{F}_6)^{-}$ shown in Figure 2.10 in the absence of a dielectric continuum (i.e., in vacuum), 36.3 kJ mol^{-1} , is *smaller* than the difference in the dielectric continuum, 47.0 kJ mol^{-1} . This is because the charge asymmetry in $\text{H}(\text{B}_{12}\text{H}_6\text{F}_6)^{-}$ is larger when the added proton is on the B7–B8–B12 face than when it is

on the B1–B2–B3 face, and a higher dielectric medium will stabilize the more polar species relative to the less polar species. This explanation can also be used to understand the energy differences for two $\text{K}(\text{B}_{12}\text{H}_6\text{F}_6)^-$ ion pairs that were also calculated and which are shown in Figure 2.11. The DFT-predicted energies were lower, both in vacuum and in the dielectric medium, when the K^+ ion was closest to F1, F2, and F3 rather than when it was closest to H7, H8, and H12, and the difference between them in the dielectric medium, 17.8 kJ mol^{-1} , was *much* smaller than the 70.0 kJ mol^{-1} difference in vacuum. In this case, the more stable ion pair has a lower charge asymmetry than the less stable ion pair.

The greater stability of the F1,F2,F3 isomer of $\text{K}(\text{B}_{12}\text{H}_6\text{F}_6)^-$ relative to the H7,H8,H12 isomer does not mean that K^+ forms a stronger ion pair with $\text{B}_{12}\text{F}_{12}^{2-}$ than with $\text{B}_{12}\text{H}_{12}^{2-}$. In fact, just the opposite must be true. The NI-ESI mass spectrum of a 50/50 mixture of $\text{K}_2\text{B}_{12}\text{H}_{12}$ and $\text{K}_2\text{B}_{12}\text{F}_{12}$ displayed peaks for the $\text{B}_{12}\text{H}_{12}^{2-}$ and $\text{KB}_{12}\text{H}_{12}^-$ ions with an intensity ratio $I(\text{B}_{12}\text{H}_{12}^{2-})/I(\text{KB}_{12}\text{H}_{12}^-)$ of ca. 1 as shown in Figure 2.12. In contrast, the ratio $I(\text{B}_{12}\text{F}_{12}^{2-})/I(\text{KB}_{12}\text{F}_{12}^-)$ was ca. 15. This is consistent with the observation that ion pairing for NaBH_4 dissolved in poly(ethylene oxide) is more extensive than for NaBF_4 dissolved in the same polymer.⁹⁹ Furthermore, the conductivities (σ) of 0.092 M solutions of $\text{K}_2\text{B}_{12}\text{H}_{12}$ and $\text{K}_2\text{B}_{12}\text{F}_{12}$ in *w*- CH_3CN containing 2.4% H_2O were measured (this solvent corresponded to the solvents used in Exps. 10 and 11). The results are: $\sigma(\text{K}_2\text{B}_{12}\text{H}_{12}) = 9.95(5) \text{ mS cm}^{-1}$; $\sigma(\text{K}_2\text{B}_{12}\text{F}_{12}) = 13.02(4) \text{ mS cm}^{-1}$. Based on all of these results, it is almost certain that ion pairing between K^+ and $\text{B}_{12}\text{H}_{12}^{2-}$ is more extensive than between K^+ and $\text{B}_{12}\text{F}_{12}^{2-}$. It therefore follows that the $\text{K}_2\text{B}_{12}\text{H}_{12}$ lattice energy should be significantly larger than the $\text{K}_2\text{B}_{12}\text{F}_{12}$ lattice energy.

The electrostatic contribution to the acetonitrile solvation energy difference between $\text{B}_{12}\text{H}_{12}^{2-}$ and $\text{B}_{12}\text{F}_{12}^{2-}$ can be estimated by comparing the difference in DFT-predicted total energies of $\text{B}_{12}\text{H}_{12}^{2-}$ in vacuum and in the dielectric continuum with the

corresponding difference in total energies of $B_{12}F_{12}^{2-}$. The net result is that the electrostatic contribution to the acetonitrile solvation energy is 115 kJ mol^{-1} larger for $B_{12}H_{12}^{2-}$. Since $K_2B_{12}H_{12}$ is much less soluble in acetonitrile than $K_2B_{12}F_{12}$, the difference in lattice energies must be greater than the difference in anion solvation energies.

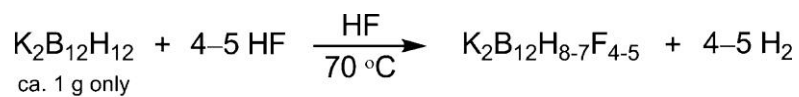
V. Minimizing the Formation of BF_4^- During $B_{12}H_{12}^{2-}$ Fluorination.

One way to further improve the yield of salts of $B_{12}F_{12}^{2-}$ would be to reduce the amount of BF_4^- formed by F_2 -induced degradation of $B_{12}H_{12-x}F_x^{2-}$ ions. In the previously reported synthesis, it was demonstrated that most BF_4^- formation occurred when $x = 0-3$.²⁸ To further test the efficiency of the new F_2 fluorination procedure, a mixture of $K_2B_{12}H_8F_4$ and $K_2B_{12}H_7F_5$ (ca. 80:20 molar ratio) was used as the starting material instead of $K_2B_{12}H_{12}$ (this recrystallized and NI-ESI-MS-analyzed mixture was prepared as previously described²⁸). The reaction conditions were: $0 \text{ }^\circ\text{C}$; $[B_{12}H_{8,7}F_{4,5}^{2-}] = 0.045 \text{ M}$; solvent = a- CH_3CN (because these partially-fluorinated compounds were soluble without added water); 113 mmol KF; 3.5 h; and F_2/B_{12} mole ratio = 8.3 (6% excess). The yield of 99.5+% $K_2B_{12}F_{12}$ was 92% based on the amount of B_{12} starting material (cf. 74% for Exp. 10). Since the yield of the recrystallized sample of $K_2B_{12}H_8F_4$ and $K_2B_{12}H_7F_5$ was 80% based on $K_2B_{12}H_{12}$, the overall yield of $K_2B_{12}F_{12}$ prepared this way was only 74% based on $K_2B_{12}H_{12}$. However, the overall yield can potentially be higher, because it is probably not necessary to recrystallize the partially-fluorinated mixture.

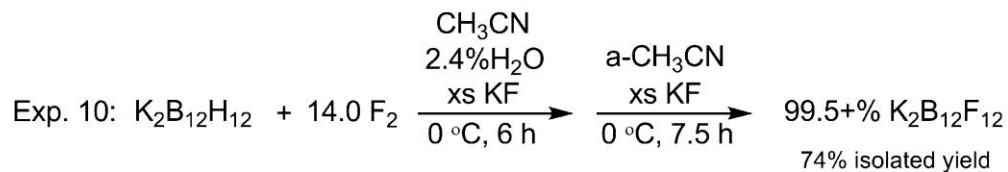
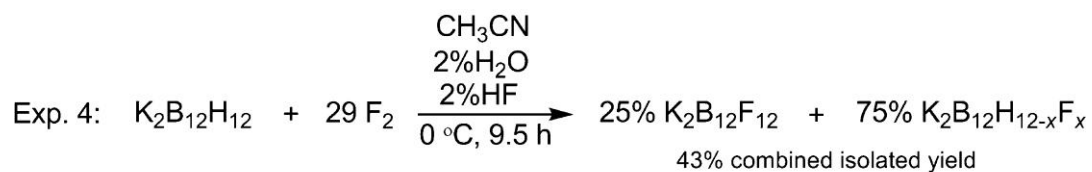
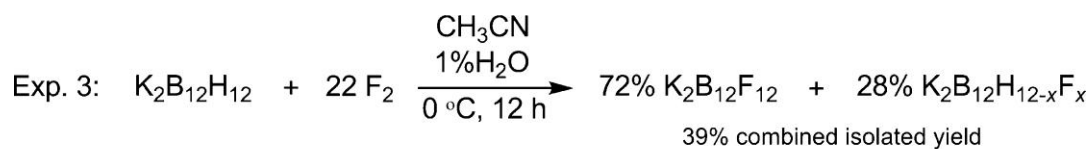
Two additional pairs of experiments were performed to test the stability of $B_{12}H_{12-x}F_x^{2-}$ anions in the presence of F_2 . A sample of anhydrous $K_2B_{12}H_{12}$ powder was treated with 0.68 atm of dry F_2 (50 psia of 20/80 F_2/N_2) for 10 h at 23(1) $^\circ\text{C}$. The resulting solid did not all dissolve in water, indicating that some oligomeric B_{12} -containing species may have formed. The soluble species were unreacted $B_{12}H_{12}^{2-}$ (51 mol%), BF_4^- (5 mol%), and $B_{12}F_{12}^{2-}$ (44 mol%), indicating that at least 6.2% of the original $B_{12}H_{12}^{2-}$ had been degraded to BF_4^- . (It is interesting that anions with $x = 1-11$

were *not* observed.) When a sample of anhydrous $\text{K}_2\text{B}_{12}\text{F}_{12}$ powder was treated the same way, no insoluble products were produced, and the mole ratio of unreacted $\text{B}_{12}\text{F}_{12}^{2-}$ to BF_4^- observed by $^{19}\text{F}\{^{11}\text{B}\}$ NMR indicated that only 1.8% of the original amount of $\text{B}_{12}\text{F}_{12}^{2-}$ had been degraded to BF_4^- .

The second additional pair of experiments consisted of treating 0.046 M $\text{K}_2\text{B}_{12}\text{F}_{12}$ in *w*- CH_3CN with 5.0 equiv. F_2 (as 20/80 F_2/N_2) bubbled through the solution during two hours, with and without 2% added HF. There was no precipitate in either case. In the solution without added HF, only $\text{B}_{12}\text{F}_{12}^{2-}$ and a barely detectable amount of BF_4^- was observed by $^{19}\text{F}\{^{11}\text{B}\}$ NMR, corresponding to $\ll 0.1\%$ cluster degradation. In contrast, when the solution contained 2% HF, 0.5% of the original amount of $\text{B}_{12}\text{F}_{12}^{2-}$ was converted to BF_4^- . Therefore, not only does HF slow down the F_2 fluorination of $\text{B}_{12}\text{H}_{12}^{2-}$ to $\text{B}_{12}\text{F}_{12}^{2-}$, it also promotes the degradation of the product by F_2 .



Scheme 2.1. Fluorination of $\text{K}_2\text{B}_{12}\text{H}_{12}$ reported in ref 28.



Scheme 2.2. Fluorination of $\text{K}_2\text{B}_{12}\text{H}_{12}$ in Experiments 3, 4, and 10 (Table 2.1).

Table 2.1. Fluorination of $\text{K}_2\text{B}_{12}\text{H}_{12}$ by 20/80 F_2/N_2 in Organic Solvents

Exp.	scale, mmol $\text{K}_2\text{B}_{12}\text{H}_{12}$	conc., M^b	solvent	Additive (v/v)	F_2/B_{12} mol ratio	time, h	mol% anionic product(s) ^c
1	5.0 ^d	0.10	w- CH_3CN	H_2O (< 0.3%)	> 12	12.0	80% $\text{B}_{12}\text{F}_{12}^{2-}$, 20% $\text{B}_{12}\text{HF}_{11}^{2-}$ [54%]
2	23 ^e	0.50	w- CH_3CN	H_2O (< 0.3%)	27	52.0	94% $\text{B}_{12}\text{F}_{12}^{2-}$, 6% $\text{B}_{12}\text{HF}_{11}^{2-}$
3	23	0.046	w- CH_3CN	H_2O (1.0%)	22	12.0	72% $\text{Cs}_2\text{B}_{12}\text{F}_{12}$, 18% $\text{Cs}_2\text{B}_{12}\text{HF}_{11}$, 7% $\text{Cs}_2\text{B}_{12}\text{H}_2\text{F}_{10}$ 3% $\text{Cs}_2\text{B}_{12}\text{H}_3\text{F}_9$ [39%]
4	5.2	0.052	w- CH_3CN	H_2O (2.0%), a/HF (2.0%)	29	9.5	25% $\text{Cs}_2\text{B}_{12}\text{F}_{12}$, 31% $\text{Cs}_2\text{B}_{12}\text{HF}_{11}$, 23% $\text{Cs}_2\text{B}_{12}\text{H}_2\text{F}_{10}$ 12% $\text{Cs}_2\text{B}_{12}\text{H}_3\text{F}_9$ 5% $\text{Cs}_2\text{B}_{12}\text{H}_4\text{F}_8$ [43%]
5	23	0.046	w- CH_3CN	H_2O (1.0%), KF (400 mmol)	17	11.8	$\text{Cs}_2\text{B}_{12}\text{F}_{12}$ [68%]
6	18	0.038	(1) w- CH_3CN	(1) H_2O (1.7%), KF (180 mmol)	(1) 8.9	(1) 6.5	(1) 12% $\text{B}_{12}\text{F}_{12}^{2-}$
			(2) a- CH_3CN	(2) KF (74 mmol)	(2) 5.2	(2) 4.5	(2) $\text{K}_2\text{B}_{12}\text{F}_{12}$ [68%]
7	18	0.030	(1) w- CH_3CN	(1) H_2O (1.3%), KF (130 mmol)	(1) 8.7	(1) 8.3	(1) 14% $\text{B}_{12}\text{F}_{12}^{2-}$
			(2) a- CH_3CN	(2) KF (93 mmol)	(2) 4.4	(2) 3.5	(2) $\text{K}_2\text{B}_{12}\text{F}_{12}$ [71%]

Table 2.1., continued

8	23	0.046	(1) w-CH ₃ CN (2) a-CH ₃ CN	(1) H ₂ O (2.4%), KF (220 mmol) (2) KF (100 mmol)	(1) 6.4 (2) 6.4	(1) 6.0 (2) 6.0	(1) 10% B ₁₂ F ₁₂ ²⁻ (2) K ₂ B ₁₂ F ₁₂ [70%]
9	47	0.094	(1) w-CH ₃ CN (2) a-CH ₃ CN	(1) H ₂ O (2.5%), KF (450 mmol) (2) KF (240 mmol)	(1) 11 (2) 4.2	(1) 22 (2) 8.0	(1) 26% B ₁₂ F ₁₂ ²⁻ (2) K ₂ B ₁₂ F ₁₂ [72%]
10	46	0.092	(1) w-CH ₃ CN (2) a-CH ₃ CN	(1) H ₂ O (2.4%), KF (390 mmol) (2) KF (470 mmol)	(1) 6.8 (2) 7.2	(1) 6.0 (2) 7.5	(1) 7% B ₁₂ F ₁₂ ²⁻ (2) K ₂ B ₁₂ F ₁₂ [74%]
11	46	0.092	(1) w-CH ₃ CN (2) a-CH ₃ CN	(1) H ₂ O (2.4%), KF (390 mmol) (2) KF (470 mmol)	(1) 6.8 (2) 7.2	(1) 6.0 (2) 7.5	(1) 6% B ₁₂ F ₁₂ ²⁻ (2) Cs ₂ B ₁₂ F ₁₂ [76%]
12	4.5 ^f	0.25	w-CH ₃ CN	HCO ₂ H (50%)	—	12.0	29% B ₁₂ F ₁₂ ²⁻ , 41% B ₁₂ HF ₁₁ ²⁻ , 30% B ₁₂ H ₂ F ₁₀ ²⁻
13	5.5	0.55	HCO ₂ H	H ₂ O (12%)	28	14.0	39% B ₁₂ F ₁₂ ²⁻ , 44% B ₁₂ HF ₁₁ ²⁻ , 17% B ₁₂ H ₂ F ₁₀ ²⁻

^a All results from this work. ^b The nominal initial concentration of K₂B₁₂H₁₂. ^c Isolated recrystallized yield. ^d The amount of time necessary for all solids to dissolve in the reaction mixture was not recorded for this experiment. ^e All solids dissolved in the reaction mixture only after 7 h. ^f All solids dissolved in the reaction mixture after 20 min.

Table 2.2. Literature Syntheses of $B_{12}F_{12}^{2-}$

refs	M^+	scale, mmol	solvent	conc., M	additive	[F] reagent ^b	flow or batch ^c	temp., °C	time	mol% major anionic product(s) [isolated yield] ^d
100,101	K^+	40	H_2O	0.2		20/80 F_2/N_2	flow	0	50 h	$B_{12}(OH)F_{11}^{2-}$ [39%]
98	Cs^+	n/r	HF	not reported		HF	n/a	70	14 h	$B_{12}H_8F_4^{2-}$
30	Cs^+	n/r	HF	not reported		HF	n/a	550	5 h	$B_{12}F_{12}^{2-}$ [38%]
28	K^+	4	HF	0.08		20/80 F_2/N_2	batch	25	72 h	21% $B_{12}F_{12}^{2-}$, BF_4^- , $B_{24}F_{22}^{4-}$
28	K^+	4	HF	0.08		(1) HF; (2) 20/80 F_2/N_2	(1) n/a; (2) batch	(1) 70; (2) 25	(1) 14 h; (2) 72 h	(1) $B_{12}H_8F_4^{2-}$ (2) $B_{12}F_{12}^{2-}$ [72%]
64	K^+	12	HCOOH	2	O_2	10/10/80 $F_2/O_2/N_2$	flow	0–20	n/r	5% $B_{12}F_{12}^{2-}$, 35% $B_{12}HF_{11}^{2-}$, 60% $B_{12}H_2F_{10}^{2-}$
64	K^+	12	(1) HCOOH; (2) HCOOH/HF	(1) 2 (2) 1	O_2	10/10/80 $F_2/O_2/N_2$	flow	0–20	n/r	60% $B_{12}F_{12}^{2-}$, 35% $B_{12}HF_{11}^{2-}$
64	K^+	8	CH_3COOH	0.8	O_2	10/10/80 $F_2/O_2/N_2$	flow	20	n/r	75% $B_{12}F_{12}^{2-}$, 18% $B_{12}HF_{11}^{2-}$, 7% $B_{12}H_2F_{10}^{2-}$

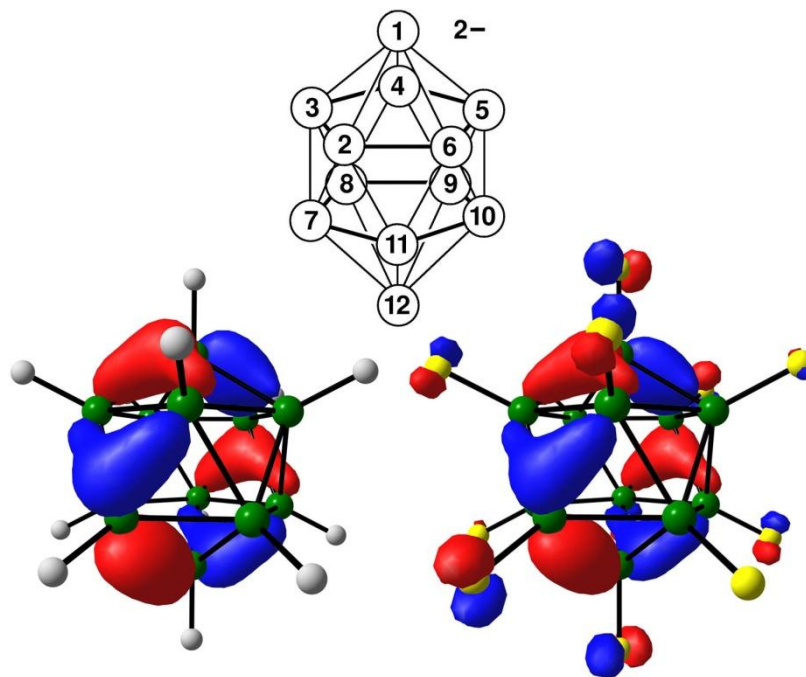


Figure 2.1. The IUPAC-approved numbering of the B_{12} icosahedron in species such as $B_{12}H_{12}^{2-}$ and $B_{12}F_{12}^{2-}$ (top) and one of the DFT-predicted quadruply-degenerate HOMOs of $B_{12}H_{12}^{2-}$ (bottom left) and $B_{12}F_{12}^{2-}$ (bottom right).

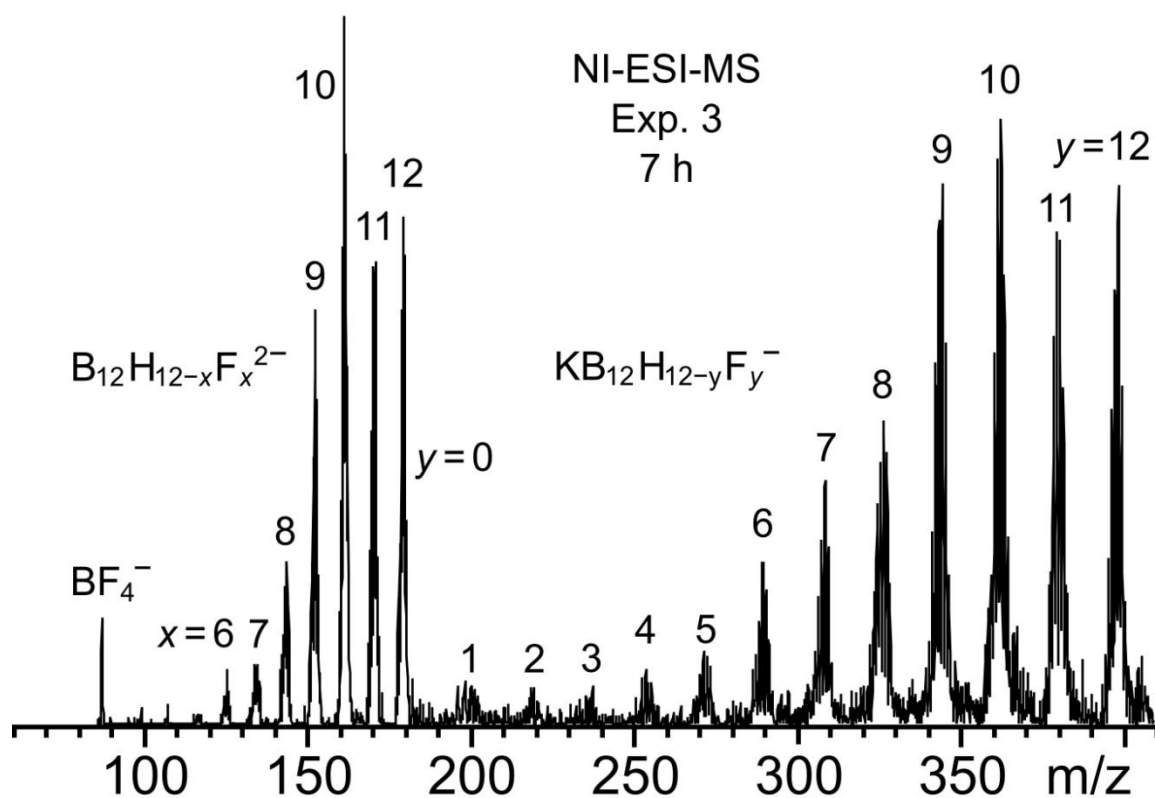


Figure 2.2. Full-scale negative-ion electrospray-ionization mass spectrum of a sample of the reaction mixture in Experiment 3 taken after 7 h of fluorination.

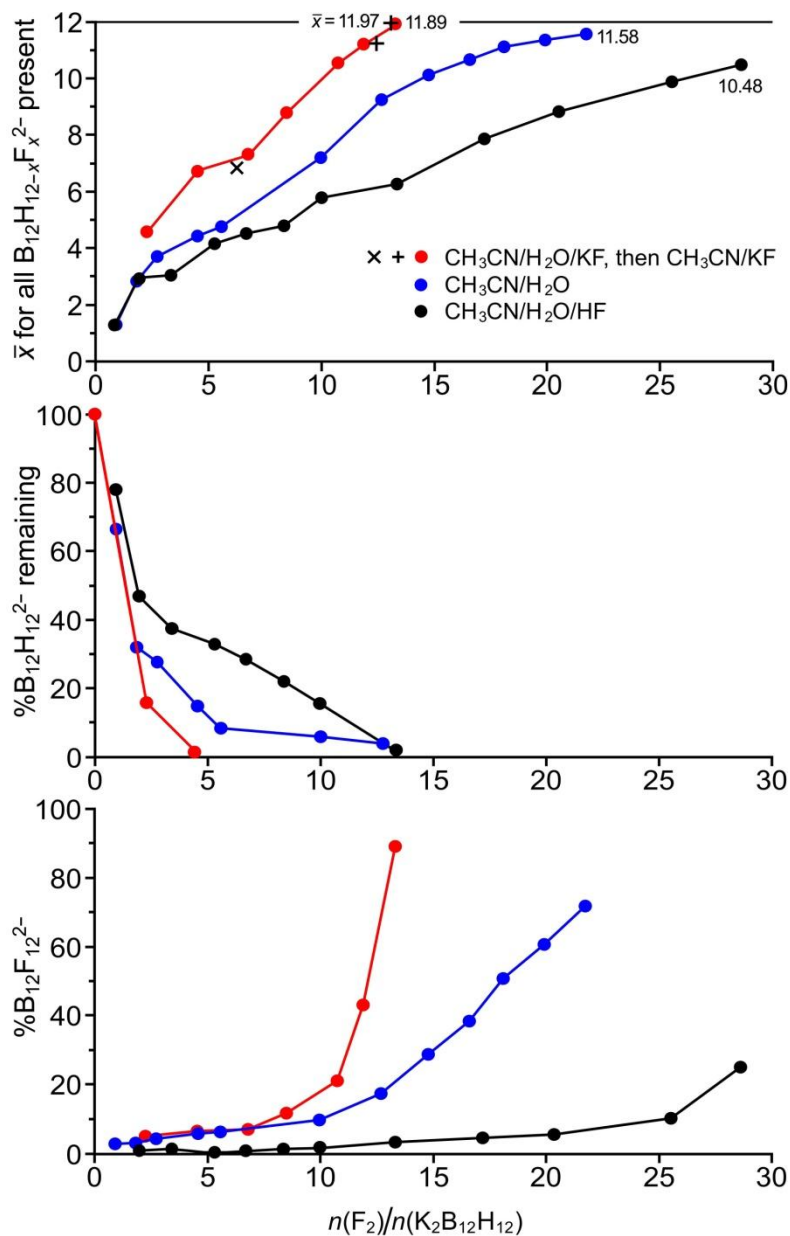


Figure 2.3. Plots of average x values for all $B_{12}H_{12-x}F_x^{2-}$ anions present, % $B_{12}H_{12}^{2-}$ remaining, and $B_{12}F_{12}^{2-}$ formed during fluorination Experiments 3, 4, and 11 vs. the number of equivalents of F_2 bubbled through the solution per mole of $K_2B_{12}F_{12}$.

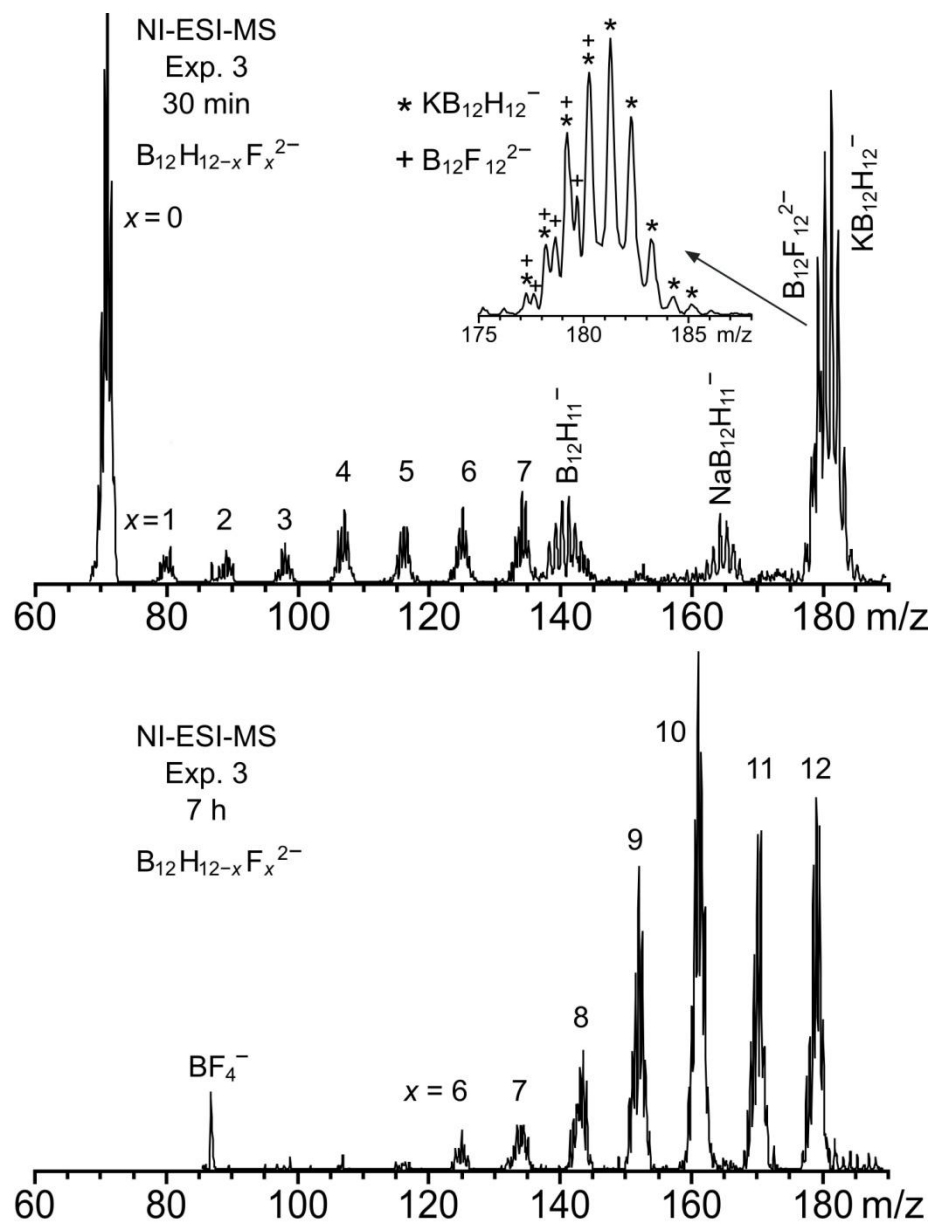


Figure 2.4. Abbreviated-scale negative-ion electrospray-ionization mass spectrum of samples of the reaction mixture in Experiment 3 taken after 30 min (top) and 7 h (bottom) of fluorination.

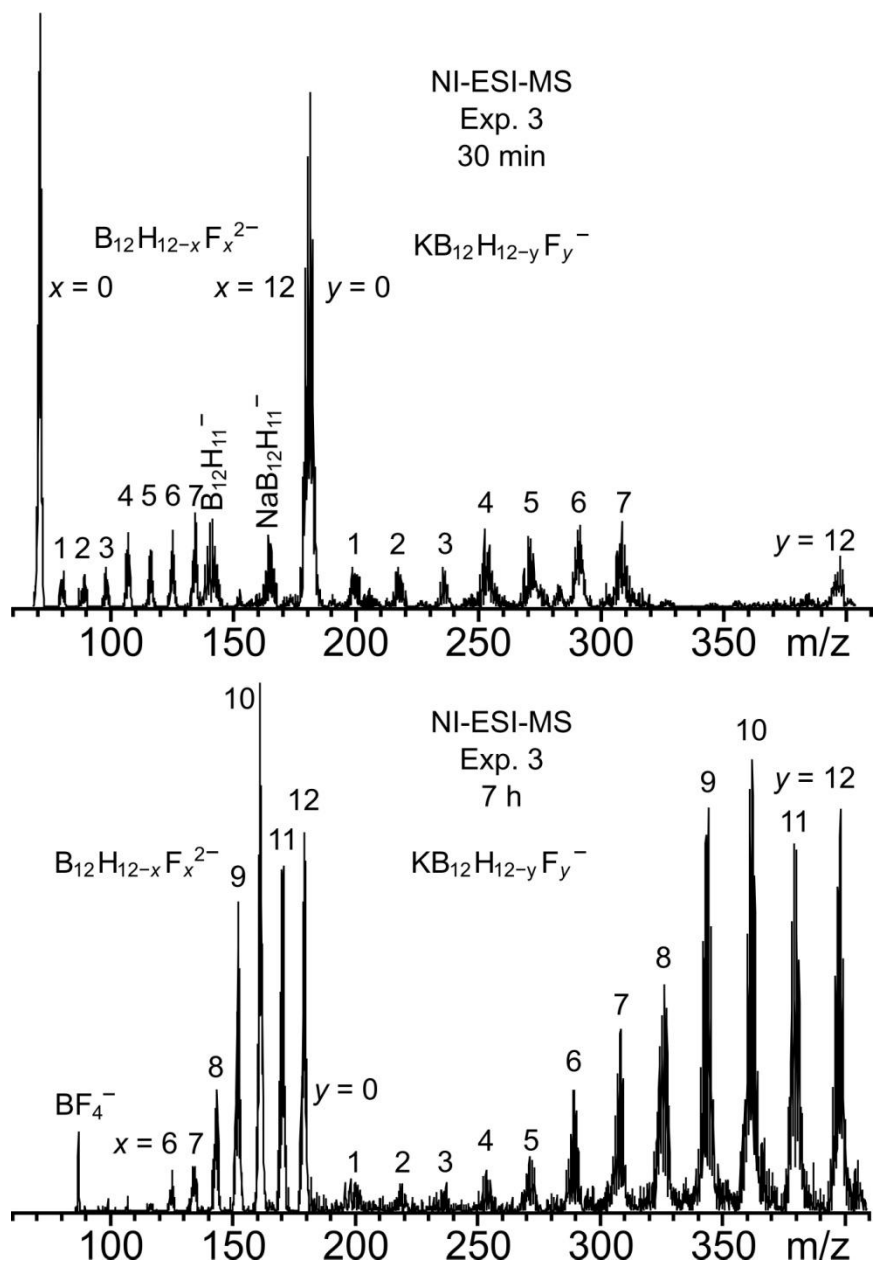


Figure 2.5. NI-ESI mass spectra of 30 min and 7 h samples from Exp. 3.

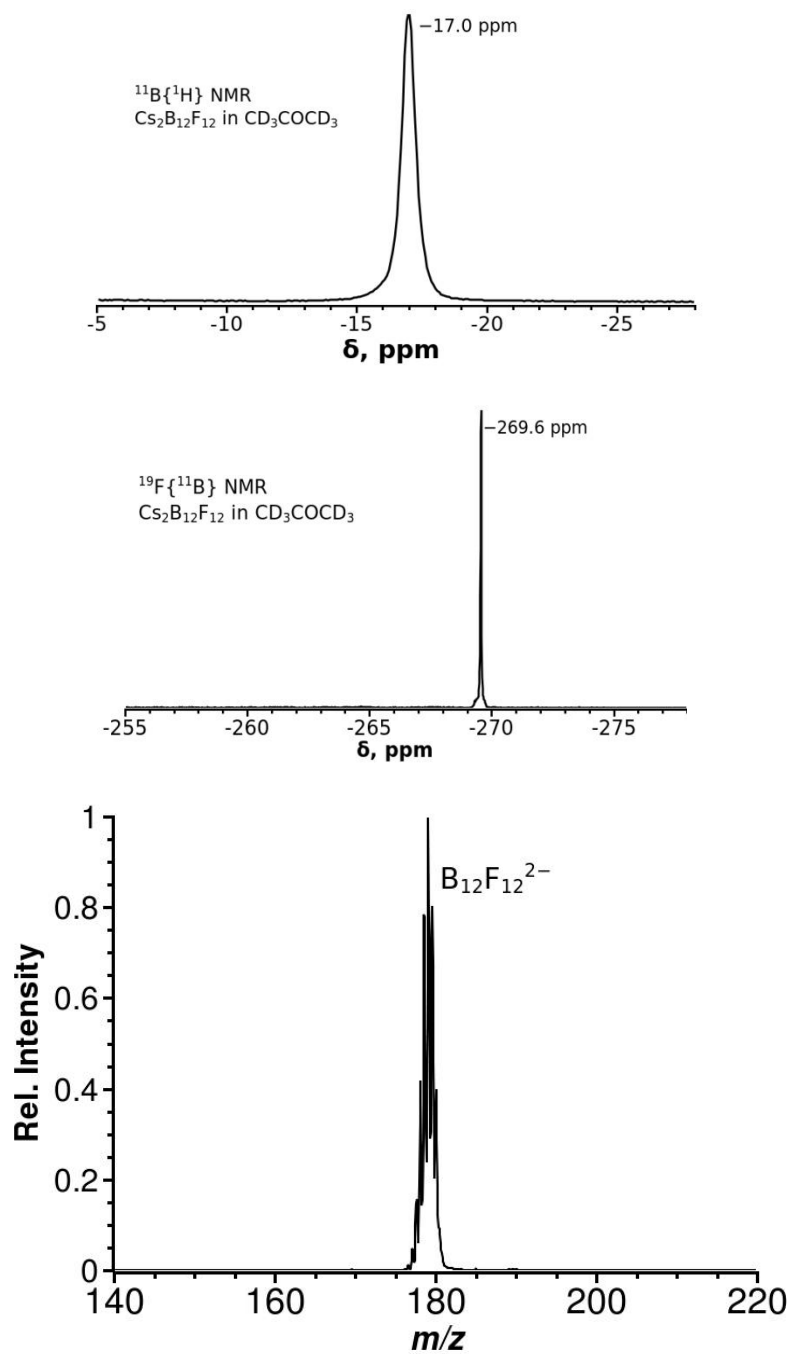


Figure 2.6. NMR spectra of recrystallized $\text{Cs}_2(\text{H}_2\text{O})\text{B}_{12}\text{F}_{12}$ and a negative-ion electrospray-ionization mass spectrum of recrystallized $\text{K}_2\text{B}_{12}\text{F}_{12}$ from large-scale preparations.

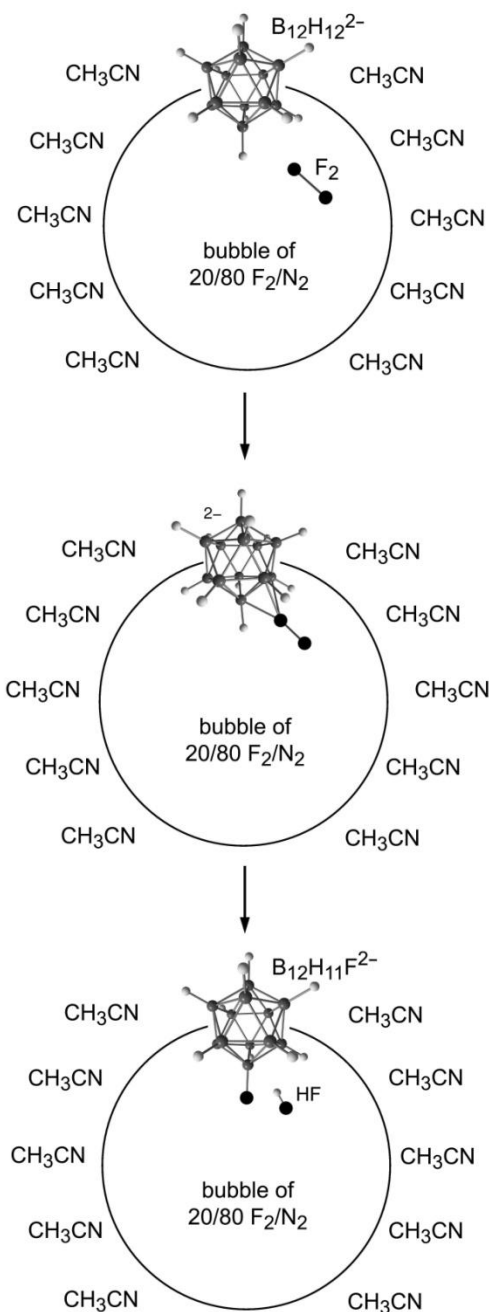


Figure 2.7. Proposed reaction scheme for the fluorination of $B_{12}H_{12}^{2-}$ on the surface of a bubble of F_2/N_2 gas in acetonitrile. The size of the bubble is not to scale. The fraction of the anion that extends into the bubble is arbitrary.

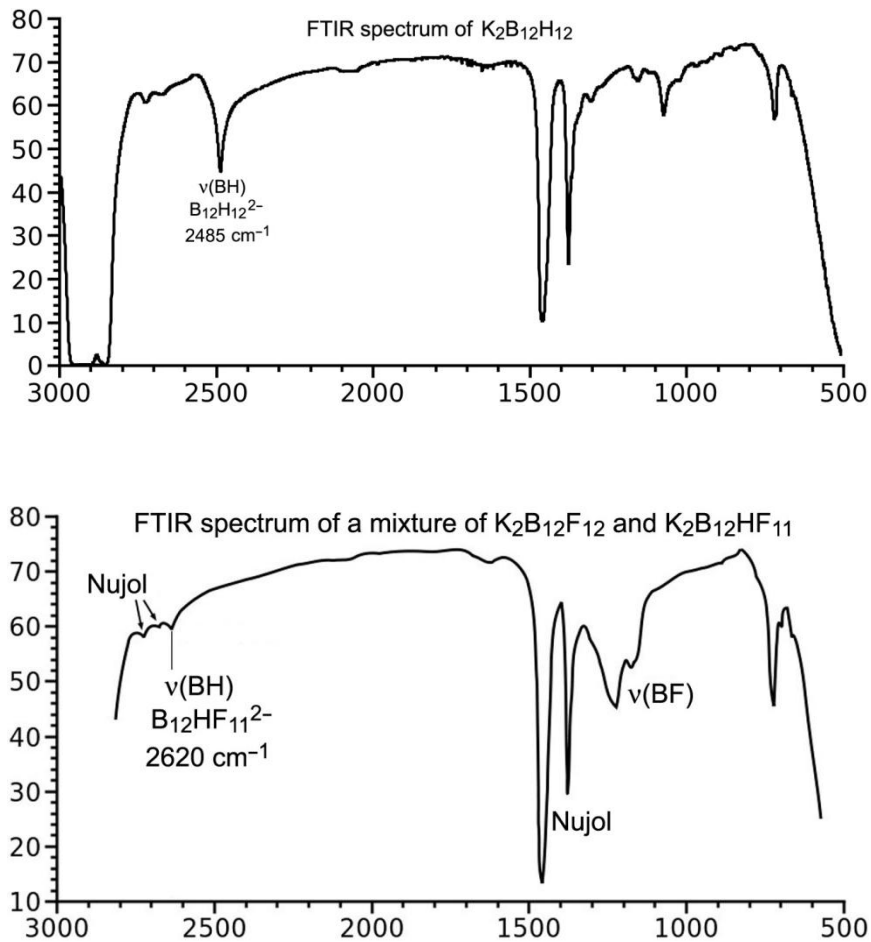


Figure 2.8. Nujol mull FTIR spectra of $K_2B_{12}H_{12}$ (top) and a mixture of $K_2B_{12}HF_{11}$ and $K_2B_{12}F_{12}$ (bottom). Note that the $\nu(BH)$ band for the $B_{12}HF_{11}^{2-}$ anion is at a much higher energy than the T_{1u} $\nu(BH)$ band of $B_{12}H_{12}^{2-}$, suggesting that the B–H bond in $B_{12}HF_{11}^{2-}$ is considerably stronger than the B–H bonds in $B_{12}H_{12}^{2-}$.

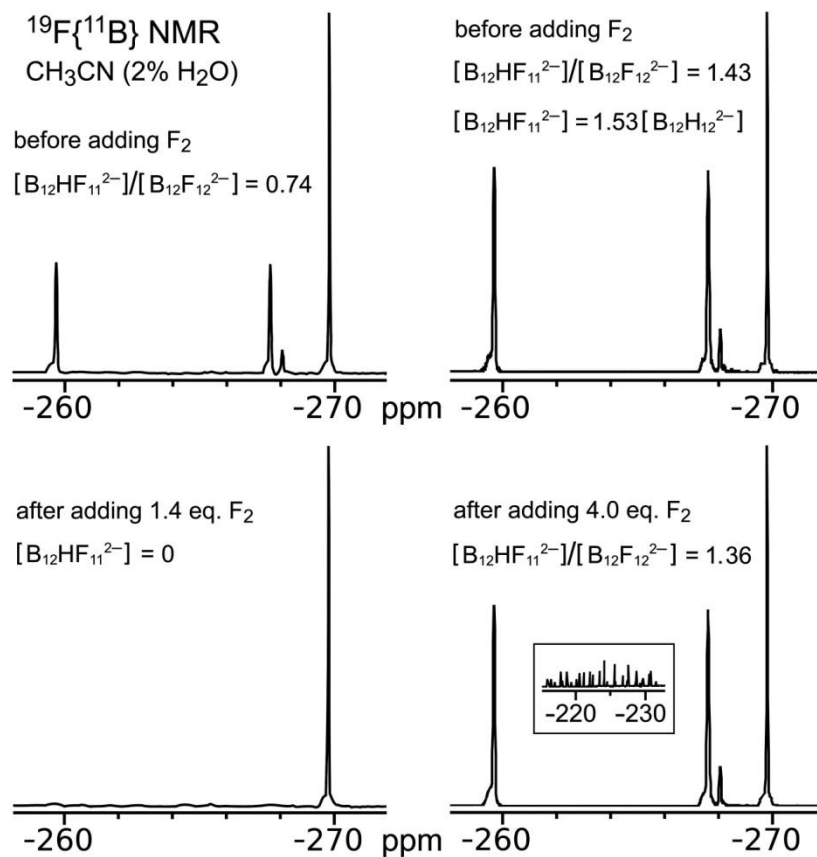


Figure 2.9. Boron-11 decoupled ^{19}F NMR spectra of mixtures of $\text{K}_2\text{B}_{12}\text{H}_{12}$, $\text{K}_2\text{B}_{12}\text{HF}_{11}$, and $\text{K}_2\text{B}_{12}\text{F}_{12}$ in CD_3CN containing 2.4% H_2O before and after fluorination with 20/80 F_2/N_2 gas.

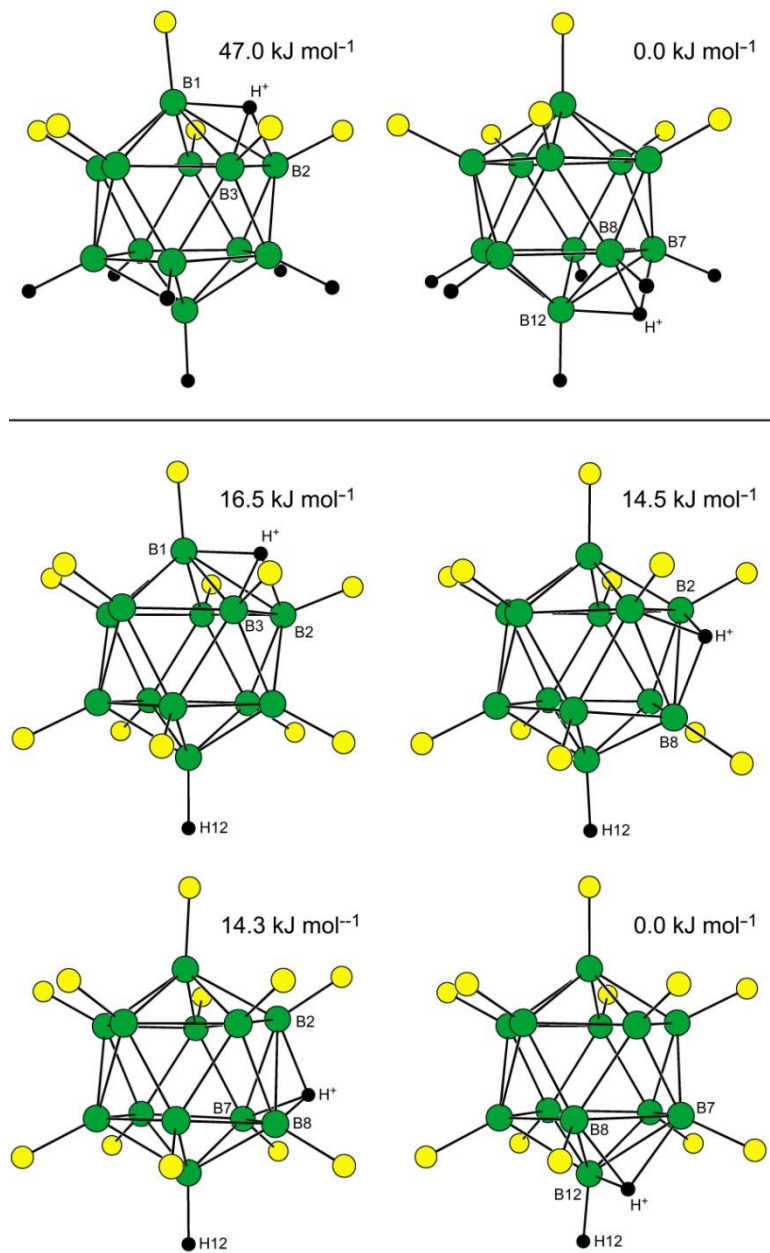
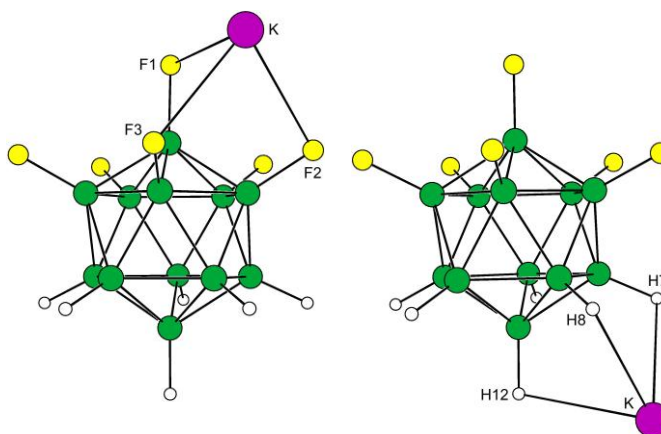


Figure 2.10. DFT-optimized structures and relative energies for isomers of $\text{HB}_{12}\text{H}_6\text{F}_6^-$ (above the line) and $\text{HB}_{12}\text{HF}_{11}^-$ (below the line).

dielectric continuum: 0.0 kJ/mol

+17.8 kJ/mol



vacuum: 0 kJ/mol

+70.0 kJ/mol

Figure 2.11. DFT-predicted relative energies for two isomers of $[\text{KB}_{12}\text{H}_6\text{F}_6]^-$.

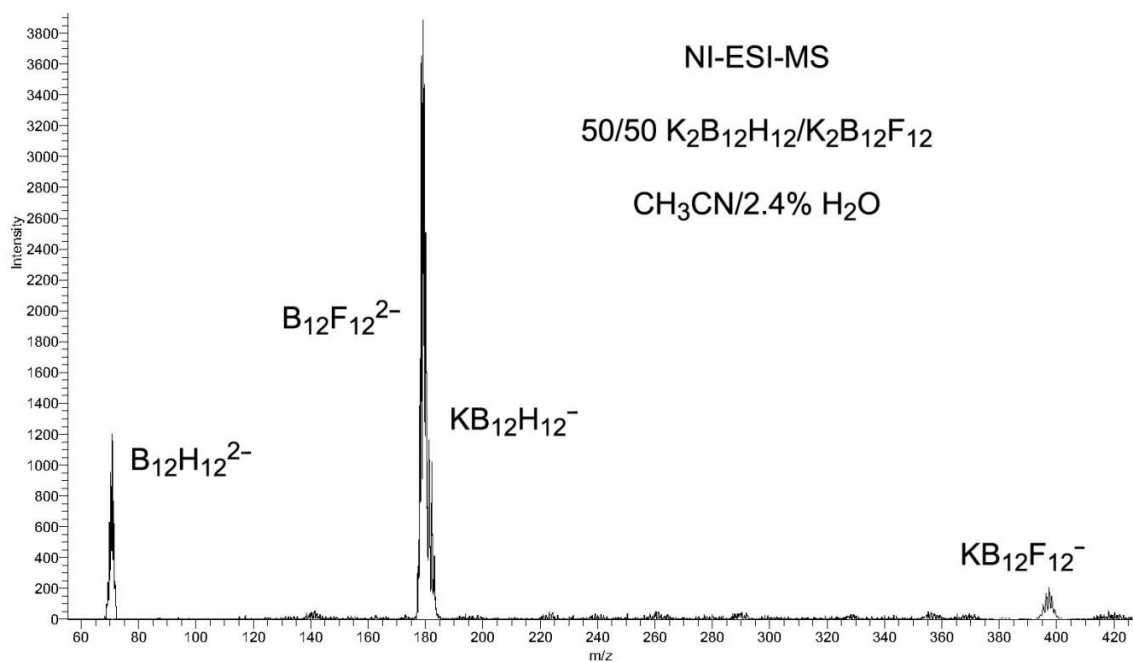


Figure 2.12. Negative-ion electrospray-ionization mass spectrum of a 50/50 mixture of $\text{K}_2\text{B}_{12}\text{H}_{12}$ and $\text{K}_2\text{B}_{12}\text{F}_{12}$ in acetonitrile containing 2.4% water.

CHAPTER 3. MONOVALENT METAL-ION SALTS OF $B_{12}F_{12}^{2-}$, INCLUDING $Ag(H_2O)_4B_{12}F_{12}$ AND $[NH_4 \cdot H_2O]_2B_{12}F_{12}$

Introduction

The purpose of this study was to investigate the types of structures that monovalent cation salts of $B_{12}F_{12}^{2-}$ would form. This study was exploratory in nature and was not intended to support or refute any particular hypothesis other than that the variety of structures observed, if indeed a variety of structures was observed, would be interesting from a purely scientific point of view.

Experimental Section

I. Reagents and Solvents.

Acetonitrile (Fisher Scientific) was dried as described in Chapter 2 and 30% aqueous H_2O_2 (Fisher Scientific) was used as received. The deionized distilled water had a resistivity of at least $18 \text{ M}\Omega$ and will be referred to as dd- H_2O . The anhydrous salt $K_2B_{12}F_{12}$ was prepared as described in Chapter 2. The silver salt $Ag_2(CH_3CN)_4B_{12}F_{12}$ was prepared as described in Chapter 4. Anhydrous $LiCl$ (Aldrich) and $LiClO_4$ (Sigma-Aldrich) were dried at $110 \text{ }^\circ\text{C}$ in air and stored in a purified N_2 -filled glovebox. Anhydrous NH_4Cl (Sigma-Aldrich), $NaCl$ (Fisher Scientific), and $CsCl$ (Fisher Scientific) were used as received. Single crystals of $Rb_2(H_2O)_4B_{12}F_{12}$, were prepared by Mr. Matic Lozinšek, co-worker in the Strauss research group. Single crystals of $K_2(HF)_3B_{12}F_{12}$ and $Cs_2(HF)B_{12}F_{12}$ were prepared by Roland Friedemann at the Free

University, Berlin, Germany, from samples of $\text{K}_2\text{B}_{12}\text{F}_{12}$ and $\text{Cs}_2\text{B}_{12}\text{F}_{12}$ supplied by the author.

II. Preparation and Crystallization of Monovalent Cation Salts of $\text{B}_{12}\text{F}_{12}^{2-}$.

A. $\text{Li}_2(\text{H}_2\text{O})_4\text{B}_{12}\text{F}_{12}$. A solution of $\text{Ag}_2(\text{CH}_3\text{CN})_4\text{B}_{12}\text{F}_{12}$ (200 mg; 0.271 mmol) in anhydrous acetonitrile (a- CH_3CN ; 5 mL) was added quickly to a solution of anhydrous LiCl (23.0 mg; 0.542 mmol) in dd- H_2O (5 mL) and vigorously stirred for 10 min. After removing the white precipitate of AgCl , the filtrate was allowed to slowly evaporate. Colorless crystals of $\text{Li}_2(\text{H}_2\text{O})_4\text{B}_{12}\text{F}_{12}$ were formed and were characterized by TGA and single-crystal X-ray diffraction (SC-XRD).

B. $\text{Na}_2(\text{H}_2\text{O})_4\text{B}_{12}\text{F}_{12}$. A solution of $\text{Ag}_2(\text{CH}_3\text{CN})_4\text{B}_{12}\text{F}_{12}$ (200 mg; 0.271 mmol) in a- CH_3CN (5 mL) was added quickly to a solution of anhydrous NaCl (31.7 mg; 0.542 mmol) in dd- H_2O (5 mL) and vigorously stirred for 10 min. After removing the white precipitate of AgCl , the filtrate was allowed to slowly evaporate in a desiccator containing a saturated solution of MgCl_2 ($P(\text{H}_2\text{O}) = 7$ torr). Colorless crystals of $\text{Na}_2(\text{H}_2\text{O})_4\text{B}_{12}\text{F}_{12}$ were formed and were characterized by TGA and SC-XRD.

C. $\text{LiK}(\text{H}_2\text{O})_4\text{B}_{12}\text{F}_{12}$. A solution of $\text{K}_2\text{B}_{12}\text{F}_{12}$ (150 mg; 0.344 mmol) in a- CH_3CN (5 mL) was added quickly to a solution of anhydrous LiClO_4 (36.6 mg; 0.344 mmol) in a- CH_3CN (5 mL) at 0 °C and left to react for 24 h. After removing a white precipitate (presumably KClO_4) by filtration, dd- H_2O (10 mL) was added to the filtrate and the solution was allowed to evaporate slowly. Colorless crystals of $\text{LiK}(\text{H}_2\text{O})_4\text{B}_{12}\text{F}_{12}$ were formed and were characterized by SC-XRD.

D. $\text{K}_2\text{B}_{12}\text{F}_{12}$. This compound was prepared as described in Chapter 2. An aqueous solution of $\text{K}_2\text{B}_{12}\text{F}_{12}$ in dd- H_2O was allowed to evaporate slowly in a desiccator containing concentrated H_2SO_4 . Small colorless crystals of $\text{K}_2\text{B}_{12}\text{F}_{12}$ were formed and were characterized by SC-XRD.

E. $K_2(H_2O)_2B_{12}F_{12}$. An aqueous solution of $K_2B_{12}F_{12}$ was allowed to evaporate slowly, but not to dryness. Colorless crystals of $K_2(H_2O)_2B_{12}F_{12}$ were formed, separated from the mother liquor, and characterized by SC-XRD.

F. $K_2(H_2O)_4B_{12}F_{12}$. An saturated aqueous solution of $K_2B_{12}F_{12}$ was slowly cooled to 0 °C. Colorless crystals of $K_2(H_2O)_2B_{12}F_{12}$ were formed, separated from the mother liquor, and characterized by SC-XRD.

G. $K_2(CH_3CN)_2B_{12}F_{12}$. A solution of $K_2B_{12}F_{12}$ in a- CH_3CN was allowed to evaporate slowly, yielding colorless crystals of $K_2(CH_3CN)_2B_{12}F_{12}$ characterized by SC-XRD.

H. $Cs_2(H_2O)B_{12}F_{12}$. An aqueous solution of $K_2B_{12}F_{12}$ (500 mg, 1.15 mmol) was treated with aqueous CsCl (387 mg, 2.30 mmol) and cooled to 0 °C. The colorless, needle-shaped crystals of $Cs_2B_{12}F_{12}\cdot H_2O$ were isolated by filtration, washed twice with of ice-cold water (2×10 mL), dried in air, and characterized by TGA and SC-XRD.

I. $Cs_2(CH_3CN)B_{12}F_{12}$. A solution of $Cs_2B_{12}F_{12}$ in a- CH_3CN was allowed to evaporate slowly, yielding colorless crystals of $Cs_2(CH_3CN)B_{12}F_{12}$ characterized by SC-XRD.

J. $Ag_2(H_2O)_4B_{12}F_{12}$. The compound $Ag_2(CH_3CN)_4B_{12}F_{12}$ (50 mg, 0.068 mmol) was dissolved in dd- H_2O (10 mL). The solution was evaporated to dryness under vacuum at 60 °C. The white solid residue was dissolved in dd- H_2O (10 mL) and the solution was allowed to slowly evaporate in a dessicator. Colorless crystals of $Ag_2(H_2O)_4B_{12}F_{12}$ were formed and were characterized by TGA and SC-XRD.

K. $[NH_4\cdot H_2O]_2B_{12}F_{12}$. A solution of $Ag_2(CH_3CN)_4B_{12}F_{12}$ (100 mg; 0.136 mmol) in anhydrous acetonitrile (5 mL) was added quickly to a solution of NH_4Cl (14.5 mg; 0.272 mmol) in dd- H_2O (5 mL) and vigorously stirred for 10 min. After removing the white precipitate of $AgCl$, the filtrate was allowed to slowly evaporate. Colorless crystals of $[NH_4\cdot H_2O]_2B_{12}F_{12}$ were formed and were characterized by TGA and SC-XRD.

III. Characterization.

A. Single-Crystal X-ray Diffraction. Unit cell parameters were obtained from least-squares fits to the angular coordinates of all reflections, and intensities were integrated from a series of frames (ω and φ rotation) covering more than a hemisphere of reciprocal space. Absorption and other corrections were applied using SADABS.¹⁰² The structures were solved using direct methods and refined (on F^2 , using all data) by a full-matrix, weighted least squares process. Standard Bruker control and integration software (APEX II) was employed,¹⁰³ and Bruker SHELXTL software was used for structure solution, refinement, and molecular graphics.¹⁰⁴ The crystallographic and data-collection parameters for all compounds are listed in Table 3.1.

The B₁₂ centroid–centroid ($\odot \cdots \odot$) distances are listed without the corresponding esd's. Individual B–B bond distance esd's are in the range 0.001–0.005 Å for the reported structures. The position of each \odot is derived from the positions of the twelve boron atoms, and therefore the esd's of the \odot coordinates are generally one order of magnitude smaller than those of the atoms that make up the B₁₂ cluster (i.e., the esd's of the \odot coordinates are ca. 0.0001–0.0005 Å for the structures described in this dissertation).

B. Thermogravimetric Analysis (TGA). Samples for TGA were analyzed using a TA Instruments TGA-2950 instrument (platinum sample pans; ca. 10 mg samples; 25–650 °C temperature range; heating rate 3 °C min⁻¹). The carrier gas was dry He.

Results and Discussion

I. Synthesis and Crystallization.

The crystalline compounds described in this chapter other than Ag₂(H₂O)₄B₁₂F₁₂ were prepared in metathesis reactions of NH₄Cl or the corresponding metal chlorides and Ag₂(CH₃CN)₄B₁₂F₁₂ (Equation 1). Even though the reactions involved the use of water as a co-solvent, the anhydrous chlorides were used to insure that the desired 2.00:1.00

$\text{NH}_4^+:\text{B}_{12}\text{F}_{12}^{2-}$ or $\text{M}^+:\text{B}_{12}\text{F}_{12}^{2-}$ mole ratios were precise to at least three significant figures (i.e., to assure that NH_4Cl or the metal chloride being weighed was free of traces of coordinated or lattice water molecules).



The silver salt $\text{Ag}_2(\text{CH}_3\text{CN})_4\text{B}_{12}\text{F}_{12}$ was used as a solution in acetonitrile. The $\text{M}_2(\text{H}_2\text{O})_n\text{B}_{12}\text{F}_{12}$ hydrates were crystallized from water-acetonitrile solvent mixtures. An evaporation of acetonitrile or anhydrous HF solutions of anhydrous $\text{M}_2\text{B}_{12}\text{F}_{12}$ salts resulted in the crystallization of CH_3CN or HF solvates, respectively (the HF solvates were prepared by R. Friedemann; see above). The compound $\text{Cs}_2(\text{H}_2\text{O})\text{B}_{12}\text{F}_{12}$ exhibited low solubility in water at 0 °C and was crystallized by slowly cooling a hot aqueous solution of $\text{Cs}_2\text{B}_{12}\text{F}_{12}$ to 0 °C. The compound $\text{K}_2(\text{H}_2\text{O})_4\text{B}_{12}\text{F}_{12}$ was found to be unstable with respect to dehydration to $\text{K}_2(\text{H}_2\text{O})_2\text{B}_{12}\text{F}_{12}$ unless the solid was kept in contact with liquid water at sub-ambient temperatures. Slow evaporation of an aqueous solution of $\text{K}_2\text{B}_{12}\text{F}_{12}$ at 25 °C produced single crystals of $\text{K}_2(\text{H}_2\text{O})_2\text{B}_{12}\text{F}_{12}$, not single crystals of $\text{K}_2(\text{H}_2\text{O})_4\text{B}_{12}\text{F}_{12}$. In this work, the only solvent-free salt that could be isolated as single-crystals suitable for X-ray diffraction was $\text{K}_2\text{B}_{12}\text{F}_{12}$, and it was obtained by slow evaporation of water from an aqueous solution of $\text{K}_2\text{B}_{12}\text{F}_{12}$ in a dessicator. Crystals of $\text{K}_2(\text{H}_2\text{O})_2\text{B}_{12}\text{F}_{12}$ formed initially and were subsequently dehydrated in what proved to be a topotactic transformation of crystalline $\text{K}_2(\text{H}_2\text{O})_2\text{B}_{12}\text{F}_{12}$ into crystalline $\text{K}_2\text{B}_{12}\text{F}_{12}$. Most of the sample after drying was a microcrystalline powder, but several small single crystals of $\text{K}_2\text{B}_{12}\text{F}_{12}$ suitable for SC-XRD were also isolated. This indicates that the topotactic reaction shown in Equation 2 can also be a single-crystal-to-single-crystal transformation when carried out extremely slowly.



It is noteworthy that an aqueous solution containing Li^+ , K^+ , and $\text{B}_{12}\text{F}_{12}^{2-}$ deposited crystals of the mixed cation compound $\text{LiK}(\text{H}_2\text{O})_4\text{B}_{12}\text{F}_{12}$ but an aqueous solution containing K^+ , Cs^+ , ClO_4^- , and $\text{B}_{12}\text{F}_{12}^{2-}$ deposited crystals of $\text{Cs}_2(\text{H}_2\text{O})\text{B}_{12}\text{F}_{12}$, not $\text{KCs}(\text{H}_2\text{O})_n\text{B}_{12}\text{F}_{12}$. Another example of this phenomenon is that an a-HF solution containing K^+ , Cs^+ , AsF_6^- , and $\text{B}_{12}\text{F}_{12}^{2-}$ deposited crystals of $\text{K}_3(\text{AsF}_6)\text{B}_{12}\text{F}_{12}$ and not crystals of a mixed metal salt.³⁵ Nevertheless, crystalline salts containing both K^+ and Cs^+ are known, including $\text{KCs}(\text{ClO}_4)_2$,¹⁰⁵ $\text{KCs}[\text{Pd}(\text{NO}_3)_4]\cdot 0.5\text{H}_2\text{O}$,¹⁰⁶ and $\text{KCs}_2[\text{Bi}(\text{SCN})_6]$.¹⁰⁷

II. X-ray Crystallography.

A. General Comments. Crystallographic and data-collection parameters for the fifteen structures described in this chapter are listed in Table 3.1. All crystal structures were of good-to-excellent quality (e.g., $R_1 < 0.007$, $wR_2 < 0.200$, B–F esd's ≤ 0.003 Å). Distances and angles involving atoms and B_{12} centroids (\odot) are listed in Tables 3.2 and 3.3.

The high symmetry, pseudo-spherical shape, and chemical hardness of the $\text{B}_{12}\text{F}_{12}^{2-}$ anion might have led one to expect that $\text{M}_2\text{B}_{12}\text{F}_{12}$ salts would exhibit either of the close-packed-like structures common for ionic M_2X compounds, the CCP-based anti-fluorite structure and the HCP-based Cs_2S structure (see Chapter 1). This expectation would be reinforced by the knowledge that $\text{M}_2\text{B}_{12}\text{H}_{12}$ ($\text{M}^+ = \text{Li}^+ - \text{Cs}^+$) and $\text{Ag}_2\text{B}_{12}\text{Cl}_{12}$ all exhibit the anti-fluorite structure or slightly-distorted variants of the anti-fluorite structure, and $\text{Cs}_2\text{B}_{12}\text{X}_{12}$ ($\text{X} = \text{Cl}, \text{Br}, \text{and I}$) all exhibit a slightly-distorted variant of the Cs_2S structure. However, only four of the fifteen salts described in this chapter exhibited expanded close-packed-like arrays of $\text{B}_{12}\text{F}_{12}^{2-}$ anions. This is undoubtedly due, at least in part, to the fact that $\text{B}_{12}\text{F}_{12}^{2-}$ is more weakly coordinating than $\text{B}_{12}\text{H}_{12}^{2-}$ and the other $\text{B}_{12}\text{X}_{12}^{2-}$ anions, and the salts described in this work invariably crystallize from solvents such as H_2O ,

CH₃CN, 30% aqueous H₂O₂, and anhydrous HF with coordinated solvent molecules, leading to a wider variety of anion packings than CCP or HCP.

The pair of salts K₂(H₂O)₂B₁₂F₁₂ and K₂(H₂O)₄B₁₂F₁₂ demonstrates that metal-ion salts of B₁₂F₁₂²⁻ can crystallize with varying numbers of solvent molecules coordinated to the metal ions. The irreversible conversion (in the absence of liquid H₂O) of K₂(H₂O)₄B₁₂F₁₂ to K₂(H₂O)₂B₁₂F₁₂ and the reversible interconversion of K₂(H₂O)₂B₁₂F₁₂ and K₂B₁₂F₁₂ will be discussed in Chapter 6. Another set of salts that differ only in the number of coordinated solvent molecules is Ag₂(CH₃CN)₄B₁₂F₁₂, Ag₂(CH₃CN)₅B₁₂F₁₂, and Ag₂(CH₃CN)₈B₁₂F₁₂, and these structures will be discussed in Chapter 4. A search of the literature revealed that multiple solvates are not known for monovalent metal-ion salts of either B₁₂H₁₂²⁻ or B₁₂Cl₁₂²⁻. (Note that both KF·2H₂O and KF·4H₂O are known.¹⁰⁸)

It is significant that none of the fifteen structures described in this chapter exhibit disorder of the anion, especially given the pseudo-spherical shape of B₁₂F₁₂²⁻. In fact, the only salt that exhibits cation-positional disorder is K₂(HF)₃B₁₂F₁₂ (this structure also exhibits disorder of the three HF molecules). Note that the cations in LiK(H₂O)₄B₁₂F₁₂ are ordered, as are the Li⁺ and K⁺ cations in LiK(BH₄)₂¹⁰⁹ and LiKSO₄.¹¹⁰

The structures of the B₁₂F₁₂²⁻ anions in all of the structures is invariably icosahedral, with only small deviations from uniform B–B and B–F distances. The structure of K₂(H₂O)₂B₁₂F₁₂ was the most precise structure determined (the standard errors on individual B–B and B–F bonds are 0.0009 and 0.0007 Å, respectively, in this structure). Plots showing the fifteen unique B–B bond distances and six unique B–F bond distances for the anion in this structure are shown in Figure 3.1 (the anion in this structure has crystallographic inversion symmetry).

B. Observed Stoichiometries. As mentioned above, the weakly-coordinating nature of the B₁₂F₁₂²⁻ anion is responsible for the formation of crystalline solvates when its salts with NH₄⁺ or the monovalent metal ions Li⁺, Na⁺, K⁺, Rb⁺, Cs⁺, and Ag⁺ were isolated from H₂O, CH₃CN, 30% aqueous H₂O₂, and anhydrous HF. The only solvent-free

(ligand-free) salt that could be prepared as crystals suitable for SC-XRD is $K_2B_{12}F_{12}$, and that is because the transformation shown in Equation 2 is topotactic and occurs readily at 25 °C. None of the fourteen compounds that crystallized with coordinated solvent molecules contained additional lattice solvent molecules.

The M^+ :solvent stoichiometries for the fourteen solvent-containing compounds are $2Ag^+:4H_2O$, $2Li^+:4H_2O$, $2Na^+:4H_2O$, $(Li^+K^+):4H_2O$, $2K^+:4H_2O$, $2K^+:3HF$, $2K^+:2H_2O_2$, $2K^+:2CH_3CN$, $2K^+:2H_2O$, $2Rb^+:2H_2O$, $2NH_4^+:2H_2O$, $2Cs^+:1CH_3CN$, $2Cs^+:1H_2O$, and $2Cs^+:1HF$.

C. Observed Structures. 1. Structures Based on Close-Packed-Like Arrays of Anions. (a) $K_2B_{12}F_{12}$. The structure of this compound exhibits a slightly-distorted HCP array of $B_{12}F_{12}^{2-}$ anions, as shown in Figures 3.2 and 3.3, not unlike the HCP arrays of Si, Ge, and Mn atoms in the hexagonal polymorphs of K_2SiF_6 ,⁵¹ K_2GeF_6 ,⁵⁹ and K_2MnF_6 .⁵⁷ However, unlike those compounds, which have a Cs_2S -like structure, half of the K^+ ions in $K_2B_{12}F_{12}$ fill every O_h hole and half fill every D_{3h} trigonal hole within the close-packed layers, holes that are midway between two T_d holes. This type of hole filling is known as the Ni_2In structure and is exhibited by a variety of intermetallic compounds^{111,112} and, more recently, has been observed as the high-pressure (GPa) structure of several ionic compounds including BaF_2 , SrH_2 , and K_2S .¹¹³⁻¹¹⁵ The compound Cs_2Pt was the first example of a rigorous Ni_2In structure for an "ionic" compound at ambient conditions.¹¹⁶

The B_{12} centroids (\odot 's) in $K_2B_{12}F_{12}$ do not form a perfect HCP array, but, with one exception, the deviations are minor. The $\odot \cdots \odot$ distances within the rigorously planar close-packed-like layers are 8.207 and 8.236 Å, and the acute $\odot \cdots \odot \cdots \odot$ angles within these layers are $60.0 \pm 0.2^\circ$. The $\odot \cdots K1 \cdots \odot$ angles are within $\pm 2.7^\circ$ of the ideal angles of 60, 90, 120, and 180°, and the $\odot \cdots K2 \cdots \odot$ angles are within $\pm 7.6^\circ$ of the ideal angle of 90° (the *trans* angles are rigorously 180°). The exception is that the $\odot \cdots \odot$ distances between the layers, 7.204, 7.417, and 7.517 Å, are ca. 10% shorter than within the layers. This is undoubtedly due to the absence of cations in the T_d holes, which has allowed the

perpendicular distance between the layers to decrease. (Even highly-symmetric structures such as hexagonal ZnS (wurtzite) do not have rigorous HCP lattices with 12 equal S···S distances for each S²⁻ ion: the S···S distances between the close-packed layers are 1.2% longer than the S···S distances within the layers, in this case *because* half of the T_d holes are filled, and for this reason there are also two different Zn···S distances.¹¹⁷)

The (K1)F₁₀ and (K2)F₈ coordination spheres in K₂B₁₂F₁₂ resemble a bicapped square antiprism and an idealized cubic prism, respectively, as shown in Figure 3.4. Note that K1 is bonded to F1 atoms belonging to anions above and below the close-packed-like plane containing K1. These are not weak or secondary interactions: the two K1···F1 distances are 2.664(2) Å, which are only slightly longer than the shortest K1···F5 distances of 2.651(2) Å in the (K1)F₁₀ coordination sphere. In this sense it can be said that the K1 ions are in trigonal bipyramidal holes, not just trigonal holes, although the distance from K1 to the "apical" O's, 5.672 Å, is ca. 20% longer than the distances to the "equatorial" O's, 4.719 and 4.810 Å.

An unusual feature of the structure of K₂B₁₂F₁₂ is the disparity in the bond-valence sums¹¹⁸ for K1 and K2. The bond-valence sum for the ten K1···F contacts from 2.651(2) to 3.405(2) Å is 1.16 (the ideal value for K⁺ is 1.00;¹¹⁸ the next F atom to K1 is more than 4 Å away; if the two K1···F1 distances of 3.405(2) Å are excluded based on the 3% bond-valence definition discussed in Chapter 1, the bond-valence sum for K1 is 1.12). However, the bond-valence sum for the eight K2···F contacts from 2.615(2) to 3.324(2) is only 0.70, an exceptionally low value (the next closest F atom to K2 is 3.8 Å away). Compare, for example, the following K⁺ bond-valence sums, all of which are in the range 0.89–1.17: KF, 0.98;⁵⁴ KBF₄, 1.03;⁴⁵ KAsF₆, 0.92;⁴⁹ K₂BeF₄, 0.89 and 1.17;⁵⁰ K₂SiF₆, 1.03;⁵⁸ K₂GeF₆, 1.04 and 1.13;⁵⁹ and cubic K₂MnF₆, 1.01.⁵⁶

Note that the thermal ellipsoid for K2, shown in Fig. 4, is elongated and might be the result of a slight disorder of two K2 positions along the long axis of the ellipsoid. This would result in a different set of K2···F distances. If K2 is artificially moved 0.255 Å in

the direction of the long axis of its thermal ellipsoid (a reasonable movement given the size of the thermal ellipsoid), the eight new $K_2 \cdots F$ distances generate a bond-valence sum of 0.73 instead of 0.70. If it is moved 0.510 Å in this direction (an unreasonable movement), the bond-valence sum increases again to 0.75. A search of the literature suggests that a K^+ bond-valence sum ≤ 0.75 involving hard ligands in an isolable compound is unprecedented.

It is not possible, without additional structural evidence, to explain fully why the K^+ ions in $K_2B_{12}F_{12}$ are in the largest (O_h) and the smallest (D_{3h}) holes in an expanded HCP lattice of $B_{12}F_{12}^{2-}$ anions but not in the intermediate-size T_d holes, as they are in K_2BeF_4 ⁵⁰ or K_2MnF_6 ⁵⁷ (CS_2S -like structures: half of the K^+ ions are in T_d holes) or in $K_2B_{12}H_{12}$ ¹¹⁹ (antifluorite structure; all of the K^+ ions in T_d holes). However, the answer is probably related to the different sizes and shapes of the high-symmetry fluoroanions BeF_4^{2-} , MnF_6^{2-} , and $B_{12}F_{12}^{2-}$ or to the different sizes and polarizabilities of $B_{12}H_{12}^{2-}$ and $B_{12}F_{12}^{2-}$. The polarizabilities of $B_{12}H_{12}^{2-}$ and $B_{12}F_{12}^{2-}$ in a dielectric-continuum model for CH_3CN have been predicted to be 36.5 Å³ and 26.4 Å³, respectively (see Chapter 2). One-half of the $F \cdots F$ "diameter" of the $B_{12}F_{12}^{2-}$ anion in $K_2B_{12}F_{12}$ (i.e., the simplest measure of its radius, not including the van der Waals radius of an F atom) is 3.083(3) Å (the average of six distances). This can be compared with typical B–F, Be–F, Sb–F, Si–F, Ge–F, Mn–F, and Zr–F bond distances in BF_4^- , BeF_4^{2-} , SiF_6^{2-} , GeF_6^{2-} , SbF_6^- , MnF_6^{2-} , and ZrF_6^{2-} , which are 1.383(3),¹²⁰ 1.553(2),¹²¹ 1.678(1),¹²² 1.792,⁵⁹ 1.847(5),⁴² 2.006,⁵⁶ and 2.002(2) Å.¹²³ (The "radius" 3.083 Å can also be compared with one-half of the $Cl \cdots Cl$ diameter of the $B_{12}Cl_{12}^{2-}$ anion, ca. 3.5 Å.⁴⁰) The effective volume of $B_{12}F_{12}^{2-}$ can be estimated, using the procedure of Jenkins and Passmore,¹²⁴ from the formula unit volume of $K_2B_{12}F_{12}$, 332.0(2) Å³, by subtracting twice the volume of K^+ , 19.7 Å³ (2×9.86 Å³).¹²⁴ The result, 312 Å³, can be compared with the effective volumes of BF_4^- , PF_6^- , AsF_6^- , and TiF_6^{2-} estimated from their alkali metal and alkaline earth metal salts, which are (73 ± 9) , (109 ± 8) , (110 ± 9) , and (122 ± 8) Å³, respectively.¹²⁴ Using the

same procedure for $\text{K}_2\text{B}_{12}\text{H}_{12}$,¹¹⁹ the effective volume of $\text{B}_{12}\text{H}_{12}^{2-}$ is 279 \AA^3 , ca. 12% smaller than for $\text{B}_{12}\text{F}_{12}^{2-}$ using this procedure.

(b) $\text{Cs}_2(\text{H}_2\text{O})\text{B}_{12}\text{F}_{12}$ and $\text{Cs}_2(\text{HF})\text{B}_{12}\text{F}_{12}$. There were two previously-published structures that have a distorted version of the Ni_2In structure, $\text{Cs}_2(\text{H}_2\text{O})\text{B}_{12}\text{F}_{12}$ and $\text{Cs}_2(\text{H}_2\text{O})\text{B}_{12}\text{H}_5\text{F}_7$,³⁰ although this was not pointed out by the authors of reference³⁰. However, even though it was not recognized as such at the time, $\text{Cs}_2(\text{H}_2\text{O})\text{B}_{12}\text{F}_{12}$ was the first example of a Ni_2In -type structure for an ionic compound at $25 \text{ }^\circ\text{C}$ and 1 atm, although Cs_2Pt remains the first example of a *rigorous* Ni_2In structure for an ionic compound at ambient conditions. The $\text{B}_{12}\text{H}_5\text{F}_7^{2-}$ anion in $\text{Cs}_2(\text{H}_2\text{O})\text{B}_{12}\text{H}_5\text{F}_7$ was severely disordered, and this structure will not be discussed further. The standard errors for individual B–B bonds in the original report for $\text{Cs}_2(\text{H}_2\text{O})\text{B}_{12}\text{F}_{12}$ were $\pm 0.01 \text{ \AA}$.³⁰ For this reason, the structure of $\text{Cs}_2(\text{H}_2\text{O})\text{B}_{12}\text{F}_{12}$ was redetermined in this work (B–B = $1.779(3)$ – $1.808(3) \text{ \AA}$).

The Cs^+ coordination spheres and a drawing of the hole filling in $\text{Cs}_2(\text{H}_2\text{O})\text{B}_{12}\text{F}_{12}$ are shown in Figures 3.5 and 3.6 respectively. The \odot 's form an expanded-HCP-like lattice, although the $\odot \cdots \odot$ distances span a much wider range (7.166 – 10.162 \AA) than in $\text{K}_2\text{B}_{12}\text{F}_{12}$ (7.204 – 8.236 \AA) and are not rigorously coplanar within the close-packed-like planes. Half of the Cs^+ ions occupy the O_h holes (displaced from the centers due to the presence of the H_2O molecules, which bridge Cs_2 ions; this leads to two $\text{Cs}_2\text{--O}$ distances of $3.1375(17)$ and $3.3095(16) \text{ \AA}$), with $\text{Cs}_2 \cdots \odot$ distances of 5.162 , 5.603 , 5.652 , 5.786 , 5.931 , and 8.137 \AA , and half of the Cs^+ ions occupy D_{3h} -like holes, with $\text{Cs}_1 \cdots \odot$ distances of 5.029 , 5.150 , and 6.006 \AA (the \odot 's in each close-packed-like layer are coplanar to within 0.10 \AA with a mean deviation from the least-squares plane of \odot 's of 0.07 \AA ; Cs_1 is displaced only 0.08 \AA from the plane formed by its three closest \odot 's). The Cs_1F_{11} and $\text{Cs}_2\text{O}_2\text{F}_7$ coordination spheres are very irregular. The sums of bond valences for Cs_1 and Cs_2 are 1.07 and 0.94 .

The H atoms of the H₂O molecule are hydrogen bonded to anion F atoms. One H atom forms a hydrogen bond to a single F atom, with an (H)O⋯F distance of 2.997(2) Å and an O–H⋯F angle of 149(2)°. The other H atom forms a bifurcated hydrogen bonds with two F atoms, with (H)O⋯F distances of 2.953(2) and 3.103(2) Å and O–H⋯F angles of 117(2) and 155(3)°, respectively.

The structure of Cs₂(HF)B₁₂F₁₂ is very similar to that of Cs₂(H₂O)B₁₂F₁₂, as shown in Figure 3.7 (the X-ray data for this structure were collected by R. Friedemann, who initially solved the structure; however, the final structure solution was carried out by the author of this dissertation). The Cs1 ions are near the *D*_{3h} trigonal holes in the close-packed-like layers of ⊖'s, as in the structure of Cs₂(H₂O)B₁₂F₁₂, although in this structure the Cs1 ions are displaced 0.64 Å from the plane formed by its three closest ⊖'s (and the ⊖'s in each close-packed-like layer deviates from the least-squares plane by 0.20–0.30 Å, with a mean deviation of 0.24 Å).

In this structure, the F atom of the HF molecule is disordered over two positions in a 0.63/0.37 ratio, leading to the shorter Cs2⋯FH distance being either 3.053(9) Å (for the 0.67 position) or 2.981(15) Å (for the 0.37 position) and the longer Cs⋯FH distance being either 3.443(12) Å (for the 0.67 position) or 3.91(2) Å (the longer of these two distances cannot be considered significant because the Cs–F bond valence for this distance is only 0.014, whereas it is 0.049 for the 3.443 Å distance). The sum of bond valences for Cs1 is 0.94 (the coordination sphere (not shown) is CsF₁₁, as in Cs₂(H₂O)B₁₂F₁₂) and, ignoring the 0.37 F atom position, the sum of bond valences for Cs2 is 1.09 (the coordination sphere (not shown) is CsF₉). The HF molecule is hydrogen bonded to one of the F atoms of the B₁₂F₁₂²⁻ anion. The FH⋯F distance is 1.94 Å and the F–H⋯F angle is 157°.

(c) **Cs₂(CH₃CN)B₁₂F₁₂**. This structure exhibits a distorted CCP-like lattice of B₁₂F₁₂²⁻ anions with Cs⁺ cations in all of the *T*_d holes, although not in the centers of the *T*_d holes, as they would be in a true antiferroite-like structure, as shown in Figure 3.8. The

four Cs $\cdots\ominus$ distances are 5.125, 5.153, 5.356, and 5.447 Å and the six $\ominus\cdots\text{Cs}\cdots\ominus$ angles, instead of being 109.5°, are 96.4, 105.4, 106.2, 107.2, 116.9, and 121.9°. The close-packed-like layers of \ominus 's are not coplanar: the mean deviation from the least-squares plane of \ominus 's is 0.24 Å. The CH₃CN molecule symmetrically bridges two Cs⁺ cations, with two equivalent Cs–N distances of 3.2428(16) Å. The geometry around the N atom is almost trigonal planar: the Cs–N–Cs' angle is 104.68(7)° and the two equivalent C–N–Cs angles of 125.46(7)°, for a total of 355.6(1)°. The C \equiv N distance is 1.136(4) Å, which is a normal triple-bond distance for nitriles. The CsNF₁₀ coordination geometry, shown in Figure 3.9, resembles a meridionally tricapped square antiprism (the ten Cs \cdots F interactions range from 3.068(1) to 3.429(1) Å. The sum of bond valences for the Cs⁺ ion is 1.00 (the Cs–N bond valence is 0.146, larger than the 3.068 Å Cs–F value of 0.136).

A comparison of this structure to those of the stoichiometrically similar compounds Cs₂(H₂O)B₁₂F₁₂ and Cs₂(HF)B₁₂F₁₂ raises the following question: Why is the anion packing CCP-like in the CH₃CN structure but HCP-like in the H₂O and HF structures? The difference in ΔG_f° and ΔH_f° for CCP and HCP polymorphs of simple compounds is generally small. For example, the difference in ΔH_f° for sphalerite (CCP ZnS, the thermodynamically stable polymorph) and wurtzite (HCP ZnS) is only 14 kJ mol⁻¹. Nevertheless, there appears to be a sensible reason for the difference in close-packing geometry for these three cesium salts, and that reason is related to the sizes of the solvent molecules (the "sizes" of CH₃CN, HF, and H₂O, or the volumes they would be expected to have in solid-state structures, can be estimated from the molar volumes of their liquids at 20 °C, which are 52.2, 20.9, and 18.1 mL mol⁻¹, respectively,¹²⁵ so a CH₃CN molecule is about 2.5 times larger than the other two solvent molecules at 20 °C, which are about the same size; at -70 °C, the molar volumes of H₂O(s) and α -CH₃CN() are 19.5 mL mol⁻¹ and 39.9 mL mol⁻¹,¹²⁶ respectively, so at a temperature more relevant to the structures in this chapter, a CH₃CN molecule is twice the size of a H₂O molecule).

Figure 3.10 shows the structures of $\text{Cs}_2(\text{H}_2\text{O})\text{B}_{12}\text{F}_{12}$ and $\text{Cs}_2(\text{CH}_3\text{CN})\text{B}_{12}\text{F}_{12}$ in more detail than in previous figures. It can be seen that the H_2O molecule shares the O_h hole with Cs^+ in $\text{Cs}_2(\text{H}_2\text{O})\text{B}_{12}\text{F}_{12}$ (and so does the HF molecule in $\text{Cs}_2(\text{HF})\text{B}_{12}\text{F}_{12}$, which is very similar). Apparently there is not enough room in O_h holes in a close-packed lattice of $\text{B}_{12}\text{F}_{12}^{2-}$ anions for both a Cs^+ ion and a CH_3CN molecule, so in the structure of $\text{Cs}_2(\text{CH}_3\text{CN})\text{B}_{12}\text{F}_{12}$ the counterparts of the Cs^+ in the H_2O structure "move" from O_h to T_d holes (a sizeable movement), the counterparts of the Cs^+ ions in the H_2O structure move from D_{3h} holes to T_d holes (a much smaller movement), and the CH_3CN molecules fill all of the O_h holes. However, since all of the T_d holes will now be filled with Cs^+ ions (there is only one type of Cs^+ ion in $\text{Cs}_2(\text{CH}_3\text{CN})\text{B}_{12}\text{F}_{12}$), the lattice can no longer be HCP-like and must become CCP-like (see the discussion in Chapter 1 regarding the fact that there is no HCP analog of the antifluorite structure). In nearly every other way (e.g., $\text{Cs}\cdots\text{Cs}$, $\text{Cs}\cdots\text{O}$, and $\text{O}\cdots\text{O}$ distances, and the sums of bond valences for the Cs^+ ions), the three structures are very similar. The geometry of Cs^+ ions around each $\text{B}_{12}\text{F}_{12}^{2-}$ anion in the antifluorite-like structure of $\text{Cs}_2(\text{CH}_3\text{CN})\text{B}_{12}\text{F}_{12}$, is shown in Figure 3.11.

2. Structures Based on Cube-Like Arrays of Anions. (a) $\text{K}_2(\text{HF})_3\text{B}_{12}\text{F}_{12}$. This compound crystallized in the $Fm\bar{3}c$ space group, and the anion centroids are arranged in a rigorous cubic array, with a single $\text{O}\cdots\text{O}$ distance of 7.242 Å. The high symmetry of the unit cell requires a significant disorder of the K^+ ions and HF molecules. Each cube of anions contains six partial K^+ ions and twenty-one partial HF molecules (the H atoms were not located due to the severe disorder). The disorder was modeled successfully as follows. The two K^+ ions in each cube of anions are situated close to opposite faces of the cube and are bridged by the three μ - HF molecules, as shown in Figure 3.11. Each K^+ interacts with four F atoms from the four anions that make up the face of the cube closest to the K^+ ion, with four equal $\text{K}\cdots\text{F}$ distances of 2.710(1) Å, and with the three F atoms from the bridging HF molecules, with $\text{K}\cdots\text{F}$ distances of 2.62(1), 2.686(7), and 2.76(1) Å.

The K^+ ions are displaced 1.554 Å from the face of the cube of \ominus 's closest to it. This is shown in more detail in Figures 3.12 and 3.13.

Even though the H atoms were not located, it is virtually certain that they are not hydrogen bonded to one another. The $F\cdots F$ distances involving the HF molecules are ≥ 2.87 Å, whereas the (H) $F\cdots F$ (B) distances involving an HF molecule and a $B_{12}F_{12}^{2-}$ anion are 2.56(1) and 2.72(1) Å. The shorter of these distances is similar to the 2.51–2.53 Å distances observed in crystalline HF and in gas-phase HF oligomers.⁵⁴ The longer distance suggests that this HF molecule forms a bifurcated hydrogen bond with two anions, as shown in Figure 3.13.

The relative orientations of the anions in this structure are shown in Figure 3.14. The anions are rotated 90° relative to their nearest-neighbor anions. In this way, a planar F–B–B–F moiety of one anion dovetails with the perpendicular F–B–B–F moieties of its six nearest neighbor anions. The orientation allows for efficient packing of icosahedral $B_{12}F_{12}^{2-}$ anions in a lattice. The closest interanion $F\cdots F$ contact in $K_2(HF)_3B_{12}F_{12}$ is 3.064(1) Å, which is just slightly more than 2.94 Å, twice the van der Waals radius of a F atom.⁶¹ For comparison, the $F\cdots F$ contacts within the $B_{12}F_{12}^{2-}$ anion are 3.244(1)–3.288(1) Å.

(b) $K_2(H_2O_2)_{1.5}(H_2O)_{0.5}B_{12}F_{12}$. There is a compositional disorder in crystals of this compound: the proper formula is ca. $K_2(H_2O_2)_{1.52(1)}(H_2O)_{0.48(1)}B_{12}F_{12}$ (the disorder was best modeled with a $H_2O_2:H_2O$ mole ratio of 0.758(6):0.242(6)). It is not uncommon for H_2O_2 complexes of metal ions to crystallize from 30% aqueous H_2O_2 with some H_2O molecules replacing H_2O_2 molecules in the lattice.¹²⁷⁻¹²⁹ The discussion below will focus on the structural model with two H_2O_2 molecules per two K^+ ions. Four drawings of the structure are shown in Figures 3.15–3.18.

This structure is similar to the previous structure, except that the array of anions is tetragonal instead of cubic and the two K^+ ions are bridged by four O atoms from two $\mu\text{-}\eta^2\text{-}H_2O_2$ molecules instead of three F atoms from three $\mu\text{-}HF$ molecules. The $\ominus\cdots\ominus$

distances for each tetragonal array are 7.055 ($\times 8$) and 7.719 ($\times 4$) Å. The KO_4F_4 coordination sphere is a distorted square antiprism. The bond valence sum for K^+ is 1.31 (it is 1.14 for a K^+ ion if one H_2O molecule substitutes for one H_2O_2 molecule).

The $\text{K}_2(\text{H}_2\text{O}_2)_2^{2+}$ dication dimers occupy the interiors of the tetragonal arrays formed by the $\text{B}_{12}\text{F}_{12}^{2-}$ anions, resembling the CsCl structure of dication-dianion salts such as CaO.⁵⁴ The perpendicular distance from the nearest rectangular face formed by the \odot 's to each K^+ ion is 1.286 Å. The dication dimers are rotated 90° relative to one another in adjacent tetragonal arrays, minimizing repulsions between the cations in neighboring arrays: the $\text{K}^+\cdots\text{K}^+$ distance for the dimer is 4.483(1) Å, while the shortest $\text{K}^+\cdots\text{K}^+$ distance between adjacent arrays is 5.310(1) Å.

The shortest $\odot\cdots\odot$ distance in the structure is 7.055 Å, shorter than the 7.242 Å distances in cubic $\text{K}_2(\text{HF})_3\text{B}_{12}\text{F}_{12}$. The anions in this structure are also rotated 90° relative to their nearest-neighbor anions to minimize $\text{F}\cdots\text{F}$ repulsions. The interanion $\text{F}\cdots\text{F}$ distances for the 7.055 Å $\odot\cdots\odot$ distance are 2.975(1) and 2.985(1) Å, barely longer than the van der Waals distance of 2.94 Å.

(c) $\text{K}_2(\text{H}_2\text{O})_2\text{B}_{12}\text{F}_{12}$ and $\text{Rb}_2(\text{H}_2\text{O})_2\text{B}_{12}\text{F}_{12}$. These two structures, which are similar, are shown in Figures 3.19 and 3.20. Both have the anions arranged in tilted cube-like (i.e., arrays (hereinafter referred to as the anion rhomb or simply the rhomb)). The $\odot\cdots\odot$ distances within the $\text{K}_2(\text{H}_2\text{O})_2\text{B}_{12}\text{F}_{12}$ rhomb are 7.276 Å ($\times 8$) and 7.295 ($\times 4$) Å, which is only a 0.3% difference. The rhomb is tilted so that the acute $\odot\cdots\odot\cdots\odot$ angles are $78.7(1)^\circ$ and $81.3(1)^\circ$ instead of 90° . The $\odot\cdots\odot$ distances within the $\text{Rb}_2(\text{H}_2\text{O})_2\text{B}_{12}\text{F}_{12}$ rhomb are 7.166 Å ($\times 8$) and 7.851 ($\times 4$) Å, a 10% difference. This rhomb is tilted so that the acute $\odot\cdots\odot\cdots\odot$ angles are $77.0(1)^\circ$ and $88.4(1)^\circ$. The volumes of these two rhombs only differ by 27.3 Å³ (the rubidium compound, of course, has the larger rhomb).

Conceptually, the substitution of both H_2O_2 molecules in crystalline $\text{K}_2(\text{H}_2\text{O})_2\text{B}_{12}\text{F}_{12}$ with H_2O molecules to form crystalline $\text{K}_2(\text{H}_2\text{O})_2\text{B}_{12}\text{F}_{12}$ only changes the volumes of their respective rhombs by 32.6 Å³ but does result in a tilted rhomb in $\text{K}_2(\text{H}_2\text{O})_2\text{B}_{12}\text{F}_{12}$

instead of the tetragonal rhomb in $\text{K}_2(\text{H}_2\text{O})_{1.5}(\text{H}_2\text{O})_{0.5}\text{B}_{12}\text{F}_{12}$. Both $\text{K}_2(\text{H}_2\text{O})_2\text{B}_{12}\text{F}_{12}$ and $\text{Rb}_2(\text{H}_2\text{O})_2\text{B}_{12}\text{F}_{12}$ have similar $\text{M}_2(\mu\text{-H}_2\text{O})_2^{2+}$ dication dimers within each anion rhomb. The coordination sphere of the K^+ ions in $\text{K}_2(\text{H}_2\text{O})_2\text{B}_{12}\text{F}_{12}$ is KO_2F_6 , and the bond valence sum for K^+ is 1.00. The $\text{K}\cdots\text{K}$ distance within the dication dimer 4.2529(3) Å and the shortest $\text{K}\cdots\text{K}$ distance between different dimers is 5.0754(3) Å. The coordination sphere of the Rb^+ ions $\text{Rb}_2(\text{H}_2\text{O})_2\text{B}_{12}\text{F}_{12}$ is RbO_2F_8 , and the bond valence sum for Rb^+ is 1.03. The $\text{Rb}\cdots\text{Rb}$ distance within the dication dimer 4.797(1) Å and the shortest $\text{Rb}\cdots\text{Rb}$ distance between different dimers is 4.400(1) Å. All of the F atoms of the $\text{B}_{12}\text{F}_{12}^{2-}$ anions in both structures are either bonded to the metal ions or are hydrogen bonded to H atoms belonging to the water molecules (i.e., $\text{F}\cdots\text{H} \leq 2.2$ Å).

(d) $\text{K}_2(\text{H}_2\text{O})_4\text{B}_{12}\text{F}_{12}$. Drawings of this structures are shown in Figures 3.21–3.23. The anions also form rhombs in this structure, which contain $\text{K}_2(\text{H}_2\text{O})_4^{2+}$ dication dimers. The acute $\odot\cdots\odot\cdots\odot$ angles of the rhomb are 71.7, 75.0, and 75.3° and the $\odot\cdots\odot$ distances are 6.915, 8.399, and 8.598 Å. The KO_3F_5 coordination geometries in $\text{K}_2(\text{H}_2\text{O})_4\text{B}_{12}\text{F}_{12}$ are a bicapped trigonal prism for K1 and a distorted square antiprism for K2. The non-bridging water H_2O molecules of each dication dimer are hydrogen bonded to each other, connecting pairs of $\text{K}_2(\text{H}_2\text{O})_4^{2+}$ dimers via pairs of $\text{O}\text{--}\text{H}\cdots\text{O}$ hydrogen bonds. The resulting ribbons are oriented parallel to each other as shown in Figure 3.23.

Additional details about the structures of $\text{K}_2\text{B}_{12}\text{F}_{12}$, $\text{K}_2(\text{H}_2\text{O})_2\text{B}_{12}\text{F}_{12}$, and $\text{K}_2(\text{H}_2\text{O})_4\text{B}_{12}\text{F}_{12}$ will be discussed in the Chapter 6 with respect to the dehydration/-hydration reactions $\text{K}_2(\text{H}_2\text{O})_4\text{B}_{12}\text{F}_{12} \rightarrow \text{K}_2(\text{H}_2\text{O})_2\text{B}_{12}\text{F}_{12} \rightleftharpoons \text{K}_2\text{B}_{12}\text{F}_{12}$.

(e) $\text{Li}_2(\text{H}_2\text{O})_4\text{B}_{12}\text{F}_{12}$. This is the last structure based on a rhomb of eight anions, and it is different than the five structures discussed above in that the Li^+ ions do not share H_2O ligands. Drawings of the structure are shown in Figures 3.24 and 3.25. The $\odot\cdots\odot\cdots\odot$ angles of the rhomb are 90, 90, and 89.9° and the $\odot\cdots\odot$ distances are 6.767 and 7.287 ($\times 2$) Å. The 6.767 Å distance is the shortest such distance observed to date in any crystal structure containing the $\text{B}_{12}\text{F}_{12}^{2-}$ anion.

The Li^+ cation is coordinated to two water molecules and four F atoms, one from each of four anions, forming a distorted octahedral LiO_2F_4 coordination sphere, as shown in Figure 3.25 ($\text{Li}-\text{O} = 1.995(1) \text{ \AA} (\times 2)$; $\text{Li}\cdots\text{F} = 2.109(1) (\times 2)$ and $2.118(1) \text{ \AA} (\times 2)$). The combined bond valences for the two $\text{Li}-\text{O}$ bonds is 0.48. The combined bond valences for the four $\text{Li}\cdots\text{F}$ interactions is 0.52, for a total sum of bond valences of 1.00. The Li^+ cations are located on four of the six faces of the anion rhomb; four H_2O molecules, one from each $\text{Li}(\text{H}_2\text{O})_2^+$ moiety, are inside each rhomb, and these H_2O molecules are hydrogen bonded to one another.

The orientation of the anions is shown in Figure 3.24. They are rotated 74.3° relative to their nearest-neighbor anions to minimize FF repulsions. The closest interanion $\text{F}\cdots\text{F}$ contact in $\text{Li}_2(\text{H}_2\text{O})_4\text{B}_{12}\text{F}_{12}$ is $2.637(2) \text{ \AA}$, which, interestingly, is significantly less than the 2.94 \AA van der Waals sum.⁶¹ Recall that dovetailing of nearest-neighbor anions was also observed in the structures of $\text{K}_2(\text{H}_2\text{O})_{1.5}(\text{H}_2\text{O})_{0.5}\text{B}_{12}\text{F}_{12}$ and $\text{K}_2(\text{HF})_3\text{B}_{12}\text{F}_{12}$, although, as discussed above, the two nearest-neighbor $\text{F}-\text{B}-\text{B}-\text{F}$ planes in those structures are perpendicular (89.7° and exactly 90° , respectively).

3. Structures Based on Pseudo-Hexagonal Layers of Anions Offset Along One B_{12} Centroid \cdots Centroid Vector. (a) $\text{Ag}_2(\text{H}_2\text{O})_4\text{B}_{12}\text{F}_{12}$. This structure and the four others in this section have a significantly different anion packing arrangement than CCP-like, HCP-like, or an eight-anion rhomb. All of them have planar or nearly-planar hexagonal arrays of anions (i.e., of \ominus 's), but these planes are not offset in the usual way found in a CCP-like or HCP-like lattice. Instead, they are either almost in register or are offset by ca. $1/2$ of the $\ominus\cdots\ominus$ distance along the $\ominus\cdots\ominus$ vector, as shown in Figure 3.26 (in some cases they are also offset by a small amount in the direction perpendicular to the $\ominus\cdots\ominus$ vector in question within the planar array). Between the layers are infinite chains of metal ions bridged by pairs of H_2O molecules or, in one case, pairs of CH_3CN molecules, or infinite chains of NH_4^+ ions bridged by single H_2O molecules via $\text{N}-\text{H}\cdots\text{O}$

hydrogen bonds (the H atoms of the H₂O molecules in all of the H₂O structures are hydrogen bonded to F atoms of the anions).

If the hexagonal arrays were perfect hexagons and if the offset was exactly 1/2 of the $\odot \cdots \odot$ distance along that vector, the anion packing would be body-centered tetragonal, as shown in Figure 3.27 for the structure of Ag₂(H₂O)₄B₁₂F₁₂. The $\odot \cdots \odot$ distances in this structure are in the range 7.006–8.439 Å. The linear chains of {Ag1(μ-H₂O)₂Ag2(μ-H₂O)₂}_n²ⁿ⁺ polycations located between the close-packed-like layers of \odot 's give rise to AgO₄F₄ coordination spheres, with Ag–O distances from 2.371(4) to 2.524(4) Å and Ag \cdots F distances from 2.734(4) to 3.322(4) Å, as shown in Figure 3.28. The ranges of O–Ag1–O and O–Ag2–O angles are 84.2(2)–134.6(2)° and 82.7(2)–134.3(2)°, respectively.

(b) Na₂(H₂O)₄B₁₂F₁₂ and LiK(H₂O)₄B₁₂F₁₂. These two structures are very similar to the structure of Ag₂(H₂O)₄B₁₂F₁₂ and are remarkably similar to one another (see Figure 3.26). The formula unit volumes for the sodium and lithium-potassium salts only differ by 0.2 Å³ (394.3 vs. 394.5 Å³, respectively; the formula unit volume for the silver salt is 399.9 Å³). The ranges of $\odot \cdots \odot$ distances for the sodium and lithium-potassium salts are 6.888–8.798 and 7.032–8.971 Å, respectively.

There are four unique Na⁺ cations in Na₂(H₂O)₄B₁₂F₁₂, and the four NaO₄F₂ coordination spheres are shown in Figures 3.29 and 3.30. Unlike the Ag₂(H₂O)₄B₁₂F₁₂ structure, in which the Ag–O distances (2.358(7)–2.528(6) Å) are significantly shorter than Ag–F distances (2.733(4)–3.322(4) Å), the Na–O (2.368(9)–2.473(9) Å) and Na–F (2.313(8)–2.381(7) Å) distances are comparable. The bond valence sums are 1.14 (0.34 from Na1–F and 0.80 from Na1–O), 1.07 (0.32 from Na2–F and 0.75 from Na2–O), 1.07 (0.30 from Na3–F and 0.77 from Na3–O), and 1.01 (0.28 from Na4–F and 0.73 from Na4–O).

The holes in a body-centered tetragonal lattice are usually described as adjacent pairs of T_d holes.⁵⁴ However, in the structure LiK(H₂O)₄B₁₂F₁₂ the adjacent edge of the T_d hole

pair is elongated and the pair can be described as a distorted O_h hole, as shown in Figure 3.31. Each Li^+ and K^+ cation is close to four \ominus 's: the unique $\text{Li}\cdots\ominus$ distance is 5.843 Å and the unique $\text{K}\cdots\ominus$ distance is 5.399 Å. The tetrahedral LiO_4 and square-antiprismatic KO_4F_4 coordination spheres shown in Figure 3.32 (the unique O–Li–O angles are $108.5(3)^\circ$ and $110.0(3)^\circ$). The sums of bond valences for the Li^+ and K^+ cations are 1.09 and 1.27, respectively (the sum for the K^+ ion is unusually large). Surprisingly there is no cation disorder in the $\text{LiK}(\text{H}_2\text{O})_4\text{B}_{12}\text{F}_{12}$ structure: the Li^+ and K^+ cations alternate perfectly along the $\{\text{Li}(\mu\text{-H}_2\text{O})_2\text{K}(\mu\text{-H}_2\text{O})_2\}_n^{2n+}$ polycation infinite chains.

(c) **$\text{K}_2(\text{CH}_3\text{CN})_2\text{B}_{12}\text{F}_{12}$** . The anion packing in this structure is similar to the three structures described above (see Figure 3.26). However, the stoichiometry is different. There are only two CH_3CN molecules per formula unit instead of four H_2O molecules (in fact, the structure of $\text{K}_2(\text{H}_2\text{O})_4\text{B}_{12}\text{F}_{12}$, also described above, has an entirely different anion packing arrangement). Drawing of the structure of $\text{K}_2(\text{CH}_3\text{CN})_2\text{B}_{12}\text{F}_{12}$ are shown in Figures 3.33 and 3.34. The CH_3CN molecules bridge the K^+ ions unsymmetrically, with K–N distances of 2.863(1) and 3.058(1) Å and K–N–C angles of $139.5(\text{X})$ and $95.9(\text{X})^\circ$, respectively (recall that the CH_3CN ligand in $\text{Cs}_2(\text{CH}_3\text{CN})\text{B}_{12}\text{F}_{12}$ bridged two Cs^+ ions much more symmetrically, with Cs–N–C angles of 125.5 and 104.7°). The 95.9° K–N–C angle suggests that this K^+ –acetonitrile interaction is η^2 , albeit unsymmetric η^2 , and not η^1 . The 3.374(2) Å K–C distance is 10% longer than the 3.058(1) Å distance. Whether or not there is any covalent bonding between the K^+ ion and the π electrons of the $\text{C}\equiv\text{N}$ triple bond cannot be determined at that time (a theoretical study of this interaction might be revealing in this regard, and perhaps this will be performed in the future by another student/postdoc who works on this project).

The $\{\text{K}(\mu\text{-}\eta^1, \eta^2\text{-CH}_3\text{CN})\}_n^{n+}$ polycation infinite chains lie between the rigorously planar, pseudo-hexagonal \ominus layers. Each K^+ cation is surrounded by four anions, with $\text{K}\cdots\ominus$ distances of 4.949, 5.013, 5.607 and 5.661 Å. The KN_2F_6 coordination sphere is a square antiprism, and the sum of bond valences for the K^+ ion is 0.99.

(d) $[\text{NH}_4\cdot\text{H}_2\text{O}]_2\text{B}_{12}\text{F}_{12}$. The anion packing in this structure is similar to the anion packings in the previous four structures, all of which have four H_2O molecules per formula unit. However, this compound only has two H_2O molecules hydrogen bonded to the NH_4^+ cations, which form $\{\cdots(\text{H}_2)\text{O}\cdots\text{H}-\text{N}(\text{H}_2)-\text{H}\cdots\}_n^{n+}$ infinite chains, as shown in Figure 3.35. All but one of the eight H(N) atoms is hydrogen bonded to O or F atoms, and one of the two H(O) atoms on each H_2O molecule is hydrogen bonded to a F atom.

III. Thermal Stabilities of Monovalent Metal-Ion Salts of $\text{B}_{12}\text{F}_{12}^{2-}$.

The thermal stability of the alkali-metal salts of $\text{B}_{12}\text{F}_{12}^{2-}$ anion was studied using thermogravimetric analysis (TGA) with He as the carrier gas. Figure 3.36 shows TGA curves for $\text{Li}(1\text{-Me-CB}_{11}\text{F}_{11})$,³³ $\text{Li}_2(\text{H}_2\text{O})_4\text{B}_{12}\text{F}_{12}$, $\text{K}_2\text{B}_{12}\text{F}_{12}$, and $\text{Cs}_2(\text{H}_2\text{O})\text{B}_{12}\text{F}_{12}$. The data for the Cs^+ salt show that after the loss of the H_2O molecule at 30–60 °C, the anhydrous compound $\text{Cs}_2\text{B}_{12}\text{F}_{12}$ was stable up to 600 °C. It is also known that the $\text{B}_{12}\text{F}_{12}^{2-}$ anion is stable in anhydrous HF at 550 °C.³⁰ The compounds $\text{Cs}_2\text{B}_{12}\text{X}_{12}$ (X = Cl, Br, I) are also very stable at high temperature. The chloro compound did not undergo mass loss until ca. 600 °C and the bromo and iodo compounds did not undergo mass loss until ca. 800 °C.⁴⁰ As expected, $\text{K}_2\text{B}_{12}\text{F}_{12}$ and $\text{Li}_2\text{B}_{12}\text{F}_{12}$ underwent decomposition at lower temperatures than $\text{Cs}_2\text{B}_{12}\text{F}_{12}$, 550 and 450 °C, respectively, but are still very stable thermally. For comparison, alkali-metal salts of other superweak anions have much lower thermal stabilities. For example, LiPF_6 decomposes at 105 °C,¹³⁰ $\text{K}(\text{B}(3,5\text{-C}_6\text{H}_3(\text{CF}_3)_2)_4)$ at 350 °C,¹³¹ and $\text{Li}(1\text{-MeCB}_{11}\text{F}_{11})$ at 300 °C (this work).

Table 3.1. Crystallographic and Data-Collection Parameters for $M_2(L)_nB_{12}F_{12}$ salts (L = Solvent Molecules Ligated to M)

compound	$Li_2(H_2O)_4B_{12}F_{12}$	$Na_2(H_2O)_4B_{12}F_{12}$	$LiK(H_2O)_4B_{12}F_{12}$	$K_2B_{12}F_{12}$
empirical formula	$B_{12}F_{12}H_8Li_2O_4$	$B_{12}F_{12}H_8Na_2O_4$	$B_{12}F_{12}H_8LiKO_4$	$B_{12}F_{12}K_2$
formula weight	443.70	475.76	475.82	435.92
habit, color	cube, colorless	prism, colorless	plate, colorless	prism, colorless
crystal size	$0.09 \times 0.10 \times 0.15$	$0.12 \times 0.15 \times 0.24$	$0.12 \times 0.16 \times 0.32$	$0.01 \times 0.02 \times 0.04$
space group	<i>Ibam</i>	<i>P</i> $\bar{1}$	<i>P4</i> ₂ / <i>ncm</i>	<i>C2/c</i>
<i>a</i> (Å)	10.3005(11)	10.6491(10)	10.5921(5)	8.2072(8)
<i>b</i> (Å)	10.3100(13)	10.8501(10)	10.5921(5)	14.2818(17)
<i>c</i> (Å)	13.5337(13)	13.8432(11)	14.0638(9)	11.3441(9)
α (deg)	96.813(3)	96.813(3)	90	90
β (deg)	90	96.479(3)	90	92.832(5)
γ (deg)	90	91.347(4)	90	90
<i>V</i> (Å ³)	1437.3(3)	1577.0(2)	1577.85(11)	1328.1(2)
<i>Z</i>	4	4	4	4
<i>T</i> (K)	120(1)	120(1)	120(1)	120(2)
ρ_{calc} (g cm ⁻³)	2.050	2.004	2.003	2.180
<i>R</i> (<i>F</i>) (<i>I</i> > 2 σ (<i>I</i>)) ^a	0.0295	0.0666	0.0463	0.0493
<i>wR</i> (<i>F</i> ²) [all data] ^a	0.1488	0.2163	0.1694	0.1084
min., max. e ⁻ dens., (e Å ⁻³)	-0.63, 0.45	-0.44, 0.84	-0.44, 0.44	-0.36, 0.39

Table 3.1, continued

compound	$\text{K}_2(\text{H}_2\text{O})_2\text{B}_{12}\text{F}_{12}$	$\text{K}_2(\text{H}_2\text{O})_4\text{B}_{12}\text{F}_{12}$	$\text{K}_2(\text{H}_2\text{O}_2)_{1.5}(\text{H}_2\text{O})_{0.5}\text{B}_{12}\text{F}_{12}$	$\text{Rb}_2(\text{H}_2\text{O})\text{B}_{12}\text{F}_{12}$
empirical formula	$\text{B}_{12}\text{F}_{12}\text{H}_4\text{K}_2\text{O}_2$	$\text{B}_{12}\text{F}_{12}\text{H}_8\text{K}_2\text{O}_4$	$\text{B}_{12}\text{F}_{12}\text{H}_4\text{K}_2\text{O}_{3.5}$	$\text{B}_{12}\text{F}_{12}\text{H}_4\text{O}_2\text{Rb}_2$
formula weight	471.95	507.98	495.94	564.69
habit, color	prism, colorless	prism, colorless	prism, colorless	prism, colorless
crystal size, mm	$0.28 \times 0.55 \times 0.55$	$0.18 \times 0.28 \times 0.34$	$0.06 \times 0.07 \times 0.23$	$0.11 \times 0.22 \times 0.28$
space group	$P2_1/c$	$P\bar{1}$	$I\bar{4}c2$	$P2_1/c$
a (Å)	7.2955(2)	8.3988(3)	9.9768(4)	7.8511(3)
b (Å)	11.2522(3)	8.5982(4)	9.9768(4)	10.2749(4)
c (Å)	9.2260(2)	12.7454(5)	15.4378(8)	9.9917(4)
α (deg)	90	98.830(2)	90	90
β (deg)	103.730(1)	102.056(2)	90	108.775(1)
γ (deg)	90	104.958(2)	90	90
V (Å ³)	735.80(3)	848.39(6)	1536.63(8)	763.13(5)
Z	2	2	4	2
T (K)	110(2)	110(1)	120(2)	130(1)
ρ_{calc} (g cm ⁻³)	2.130	1.989	2.141	2.457
$R(F)$ ($I > 2\sigma(I)$) ^a	0.0198	0.0204	0.0154	0.0184
$wR(F^2)$ [all data] ^a	0.0579	0.0582	0.0409	0.0422
min., max. e ⁻ dens., (e Å ⁻³)	-0.45, 0.28	-0.41, 0.28	-0.23, 0.24	-0.57, 0.28

Table 3.1, continued.

compound	CS ₂ (H ₂ O)B ₁₂ F ₁₂	Ag ₂ (H ₂ O) ₄ B ₁₂ F ₁₂	[NH ₄ ·H ₂ O] ₂ B ₁₂ F ₁₂	K ₂ (CH ₃ CN) ₂ B ₁₂ F ₁₂
empirical formula	B ₁₂ C ₂ S ₂ F ₁₂ H ₂ O	Ag ₂ B ₁₂ F ₁₂ H ₈ O ₄	B ₁₂ F ₁₂ H ₁₂ N ₂ O ₂	H ₁₂ C ₈ B ₁₂ F ₁₂ K ₂ N ₄
formula weight	641.56	645.52	429.84	518.03
habit, color	prism, colorless	needle, colorless	prism, colorless	plate, colorless
crystal size, mm	0.16 × 0.19 × 0.42	0.05 × 0.06 × 0.16	0.04 × 0.13 × 0.21	0.13 × 0.19 × 0.39
space group	<i>P</i> 2 ₁ 2 ₁ 2 ₁	<i>P</i> 2 ₁ / <i>c</i>	<i>Pna</i> 2 ₁	<i>I</i> 4 ₁ / <i>a</i>
<i>a</i> (Å)	9.7475(4)	10.4428(7)	14.0969(5)	15.0184(3)
<i>b</i> (Å)	10.2579(4)	10.9458(5)	7.7225(3)	15.0184(3)
<i>c</i> (Å)	15.0549(5)	14.0126(7)	13.8729(5)	16.5603(8)
<i>α</i> (deg)	90	90	90	90
<i>β</i> (deg)	90	93.089(1)	90	90
<i>γ</i> (deg)	90	90	90	90
<i>V</i> (Å ³)	1505.3(1)	1599.38(2)	1510.25(10)	3735.22(14)
<i>Z</i>	4	4	4	8
<i>T</i> (K)	110(1)	120(1)	120(1)	110(1)
<i>ρ</i> _{calc} (g cm ⁻³)	2.831	2.681	1.890	1.842
<i>R</i> (<i>F</i>) (<i>I</i> > 2σ(<i>I</i>)) ^a	0.0123	0.0443	0.0359	0.0265
<i>wR</i> (<i>F</i> ²) [all data] ^a	0.0328	0.1411	0.0920	0.0770
min., max. E ⁻ dens. (e Å ⁻³)	-0.56, 0.95	-0.81, 0.87	-0.25, 0.33	-0.30, 0.33
^a <i>R</i> (<i>F</i>) = Σ <i>F</i> _o - <i>F</i> _c / Σ <i>F</i> _o ; <i>wR</i> (<i>F</i> ²) = (Σ[<i>w</i> (<i>F</i> _o ² - <i>F</i> _c ²) ²] / Σ[<i>w</i> (<i>F</i> _o ²) ²]) ^{1/2}				

Table 3.1, continued.

Compound	Cs ₂ (CH ₃ CN)B ₁₂ F ₁₂	K ₂ (HF) ₃ B ₁₂ F ₁₂	Cs ₂ (HF)B ₁₂ F ₁₂
empirical formula	H ₆ C ₄ B ₁₂ Cs ₂ F ₁₂ N ₂	B ₁₂ F ₁₅ H ₃ K ₂	B ₁₂ Cs ₂ F ₁₃ H
formula weight	664.59	495.93	643.55
habit, color	prism, colorless	prism, colorless	plate, colorless
crystal size, mm	0.18 × 0.25 × 0.25	0.10 × 0.10 × 0.20	0.03 × 0.10 × 0.30
space group	<i>Pnma</i>	<i>Fm</i> $\bar{3}$ <i>c</i>	<i>P2</i> ₁ / <i>c</i>
<i>a</i> (Å)	12.4011(6)	14.4841(17)	8.3463(8)
<i>b</i> (Å)	11.2152(6)	14.4841(17)	16.1160(17)
<i>c</i> (Å)	12.5163(6)	14.4841(17)	11.5031(9)
α (deg)	90	90	90
β (deg)	90	90	98.059(7)
γ (deg)	90	90	90
<i>V</i> (Å ³)	1740.78(15)	3038.6(11)	1532.0(3)
<i>Z</i>	4	8	4
<i>T</i> (K)	120(2)	133(1)	133(1)
ρ_{calc} (g cm ⁻³)	2.536	2.142	2.790
<i>R</i> (<i>F</i>) (<i>I</i> > 2 σ (<i>I</i>)) ^a	0.0200	0.0297	0.0204
<i>wR</i> (<i>F</i> ²) [all data] ^a	0.0538	0.0817	0.0495
min., max. E ⁻ dens. (e Å ⁻³)	-1.17, 0.41	-0.17, 0.23	-0.57, 0.75
^a <i>R</i> (<i>F</i>) = $\Sigma F_o - F_c / \Sigma F_o $; <i>wR</i> (<i>F</i> ²) = $(\Sigma[w(F_o^2 - F_c^2)^2] / \Sigma[w(F_o^2)^2])^{1/2}$			

Table 3.2. Selected Interatomic Distances (Å) and Angles (°) for $M_2(H_2O)_nB_{12}F_{12}$ and $K_2B_{12}F_{12}$

parameter	$Li_2(H_2O)_4B_{12}F_{12}$	$Na_2(H_2O)_4B_{12}F_{12}$	$LiK(H_2O)_4B_{12}F_{12}$	$K_2B_{12}F_{12}$
M–F(B)	2.109(1) × 2 2.118(1) × 2	2.313(8)–2.381(7)	2.633(2) × 4 (K)	2.664(2) × 2 (K1) 2.615(2)–3.324(2) (K2)
M–O	1.995(1) × 2	2.368(9)–2.473(9)	1.946(2) × 4 (Li) 2.857(2) × 4 (K)	–
(H)O···F	2.951(2)	2.855(1)–3.128(1)	2.906(3)–3.234(4)	–
O–H···F	142(3)	128(3)–167(3)	123(4)–145(4)	–
(H)O···O	2.778(2)–2.785(2)	–	–	–
O–H···O	156(3)–169(3)	–	–	–
Σ(M–F bond valences)	0.52	0.34(Na1), 0.32(Na2), 0.30(Na3), 0.28(Na4)	0.00 (Li) 0.71 (K)	1.16 (K1) 0.70 (K2)
Σ(M–O bond valences)	0.48	0.79(Na1), 0.75(Na2), 0.77(Na3), 0.73 (Na4)	1.09 (Li) 0.56 (K)	–
Σ(all M bond valences)	1.00	1.13(Na1), 1.07(Na2), 1.07(Na3), 1.01 (Na4)	1.09 (Li) 1.27 (K)	1.16 (K1) 0.70 (K2)
⊙···⊙	6.767, 7.287 × 2	6.888–8.775	7.032 × 2, 7.777 × 2, 8.971 × 4	7.204–8.236
M···M'	5.155(1)	3.558(6), 3.586(6), 3.598(6), 3.609(6)	3.516(1)	5.421(1)
B–F	1.376(2)–1.388(2)	1.37(1)–1.34(1)	1.375(4)–1.396(4)	1.378(3)–1.392(3)
B–B	1.787(2)–1.810(2)	1.77(2)–1.82(2)	1.784(5)–1.810(5)	1.767(4)–1.805(5)

Table 3.2, continued

parameter	$\text{K}_2(\text{H}_2\text{O})_2\text{B}_{12}\text{F}_{12}$	$\text{K}_2(\text{H}_2\text{O})_4\text{B}_{12}\text{F}_{12}$	$\text{K}_2(\text{H}_2\text{O})_{1.5}(\text{H}_2\text{O})_{0.5}\text{B}_{12}\text{F}_{12}$
M–F(B)	2.5984(4)–3.1593(5)	2.6501(6)–3.2843(6) (K1) 2.7069(8)–3.2843(7) (K2)	2.641(1) × 2, 2.694(1) × 2
M–O	2.7698(6), 2.7716(6)	2.6685(7), 2.8126(8), 2.8306(8) (K1) 2.7070(8), 2.7469(9), 2.7703(9) (K2)	2.708(3) × 2, 2.907(3) × 2
(H)O···F	2.9715(7)–2.9784(7)	2.874(1)–3.085(1)	2.782(2)
O–H···F	125(1)–165(1)	131(1)–174(1)	155(3)
(H)O···O	–	2.888(1); 2.874(1)	–
O–H···O	–	173.4(2); 174.0(2)	–
Σ(M–F bond valences)	0.65	0.55 (K1) ; 0.45 (K2)	0.65
Σ(M–O bond valences)	0.35	0.54 (K1) ; 0.58 (K2)	0.67
Σ(all M bond valences)	1.00	1.09 (K1) ; 1.03 (K2)	1.32
⊙···⊙	7.276 × 2, 7.295	6.915 × 2, 8.399 × 2, 8.598 × 2	7.055 × 4, 7.719 × 2
M···M'	4.2529(3)	4.1293(5)	4.483(2)
B–F	1.3791(7)–1.3875(7)	1.373(1)–1.389(1)	1.384(2)–1.385(2)
B–B	1.7774(9)–1.8059(8)	1.778(1)–1.797(1)	1.787(2)–1.800(2)

Table 3.2, continued

parameter	Rb ₂ (H ₂ O) ₂ B ₁₂ F ₁₂	Cs ₂ (H ₂ O) ₂ B ₁₂ F ₁₂	Ag ₂ (H ₂ O) ₂ B ₁₂ F ₁₂	[NH ₄ ·H ₂ O] ₂ B ₁₂ F ₁₂
M–F(B)	2.910(1)–3.237(1)	3.049(1)–3.387(1) (Cs1) 3.069(1)–3.470(1) (Cs2)	2.734(4) (Ag1) 2.742(4),2.751(4) (Ag2)	–
M–O	2.857(1)–2.915(1)	3.148(1), 3.304(2)	2.371(4)–2.524(4) (Ag1) 2.376(5)–2.511(5) (Ag2)	–
(H)O···F	2.857(2)–2.931(2)	2.097(1) × 2	2.702(6)–3.080(6)	2.870(2)–3.112(1)
O–H···F	133(2)–162(2)	2.767(2)–3.136(1)	123(1)–163(1)	135(2)–169(2)
(H)O···O	–	140(6)–175(2)	–	–
O–H···O	–	2.785(2)	–	–
Σ(M–F bond valences)	0.66	1.08 (Cs1) 0.71 (Cs2)	0.08 (Ag1) 0.16 (Ag2)	–
Σ(M–O bond valences)	0.37	0 0.23 (Cs2)	0.83 (Ag1) 0.89 (Ag2)	–
Σ(all M bond valences)	1.03	1.08 (Cs1) 0.94 (Cs2)	0.91 (Ag1) 1.05 (Ag2)	–
⊙···⊙	7.166 × 2, 7.851	7.166–10.162	7.003–10.949	7.275–9.205
M···M'	4.400(1)	4.928(1)	3.540(1)	–
B–F	1.380(2)–1.391(2)	1.378(2)–1.389(2)	1.364(8)–1.389(8)	1.376(2)–1.383(2)
B–B	1.776(2)–1.803(2)	1.779(3)–1.808(3)	1.780(9)–1.823(9)	1.773(2)–1.793(2)

Table 3.3. Selected Interatomic Distances (Å) and Angles (I) for $M_2(CH_3CN)_nB_{12}F_{12}$ and $M_2(HF)_nB_{12}F_{12}$ Salts

parameter	$K_2(CH_3CN)_2B_{12}F_{12}$	$Cs_2(CH_3CN)B_{12}F_{12}$	$K_2(HF)_3B_{12}F_{12}$	$Cs_2(HF)B_{12}F_{12}$
M–F(B)	2.638(1)–2.977(1)	3.067(1)–3.429(1)	2.709(1) × 4, 2.62(1), 2.686(7), 2.764(1)	3.105(2)–3.542(2) (Cs1) 2.980(7)–3.44(1) (Cs2)
M–N	2.863(1), 3.058(1)	3.243(2)	–	–
(H)F···F	–	–	2.56(1)–2.72(1)	2.67(1)
Σ(M–F bond valences)	0.65	0.86	1.03	0.93 (Cs1) 1.08 (Cs2)
Σ(M–N bond valences)	0.31	0.33	–	–
Σ(all M bond valences)	0.99	1.19	1.03	0.93 (Cs1) 1.08 (Cs2)
⊙···⊙	7.015–9.545	7.882–9.445	7.242 × 6	7.217–9.408
M···M'	4.840(1)	5.134(1)	4.134(2)	5.155(1)
B–F	1.373(1)–1.393(1)	1.374(3)–1.386(3)	1.387(2) × 12	1.371(4)–1.392(4)
B–B	1.785(1)–1.804(1)	1.784(3)–1.801(3)	1.794(2) × 12	1.772(5)–1.804(5)

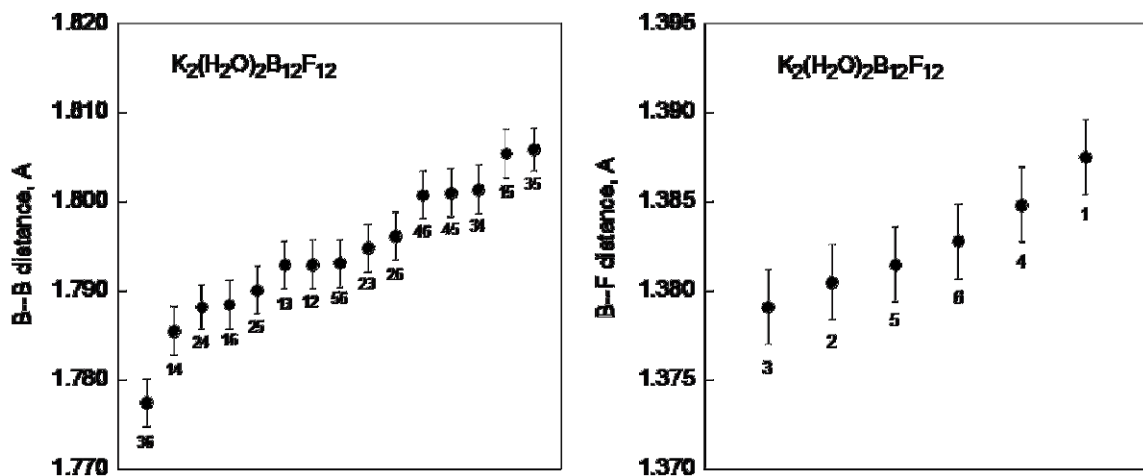


Figure 3.1. Plots of the unique B–B and B–F distances in the structure of $K_2(H_2O)_2B_{12}F_{12}$. The numbers refer to the individual B or F atoms. The error bars shown are $\pm 3\sigma$. The DFT-predicted B–B and B–F distances (PBE0 functional; calculated by Dr. Alexey A. Popov) for the isolated $B_{12}F_{12}^{2-}$ anion are 1.792 and 1.384 Å, respectively, in the gas phase, and 1.788 and 1.382 Å, respectively, in a dielectric continuum equivalent to an acetonitrile solution.

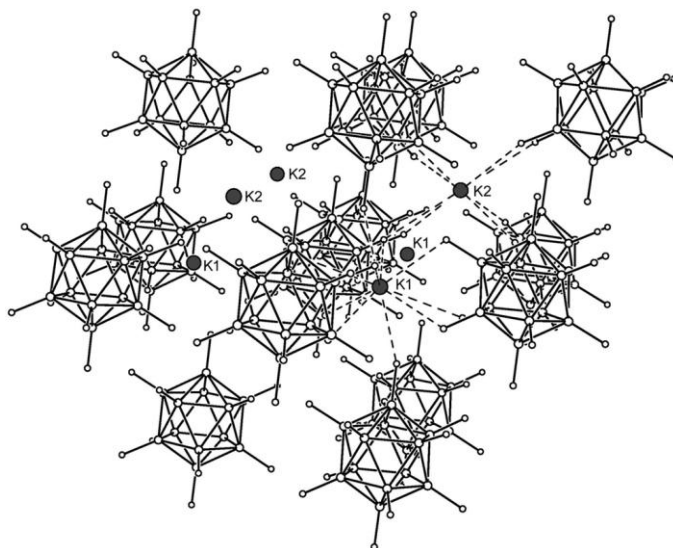


Figure 3.2. The structure of $K_2B_{12}F_{12}$. The K^+ ions are shown as gray spheres. For clarity, only those $K1^+$ ions in the D_{3h} holes (common to two T_d holes) in the middle layer of expanded close-packed $B_{12}F_{12}^{2-}$ anions (i.e., the expanded close-packed layer of their B_{12} centroids, \odot) are shown, and only those $K2^+$ ions in O_h holes between the top and middle layers of close-packed-like $B_{12}F_{12}^{2-}$ anions are shown. The $K1^+$ ions are rigorously coplanar with the \odot 's in the middle layer, and the $K2^+$ ions are equidistant from the top and middle planes of \odot 's.

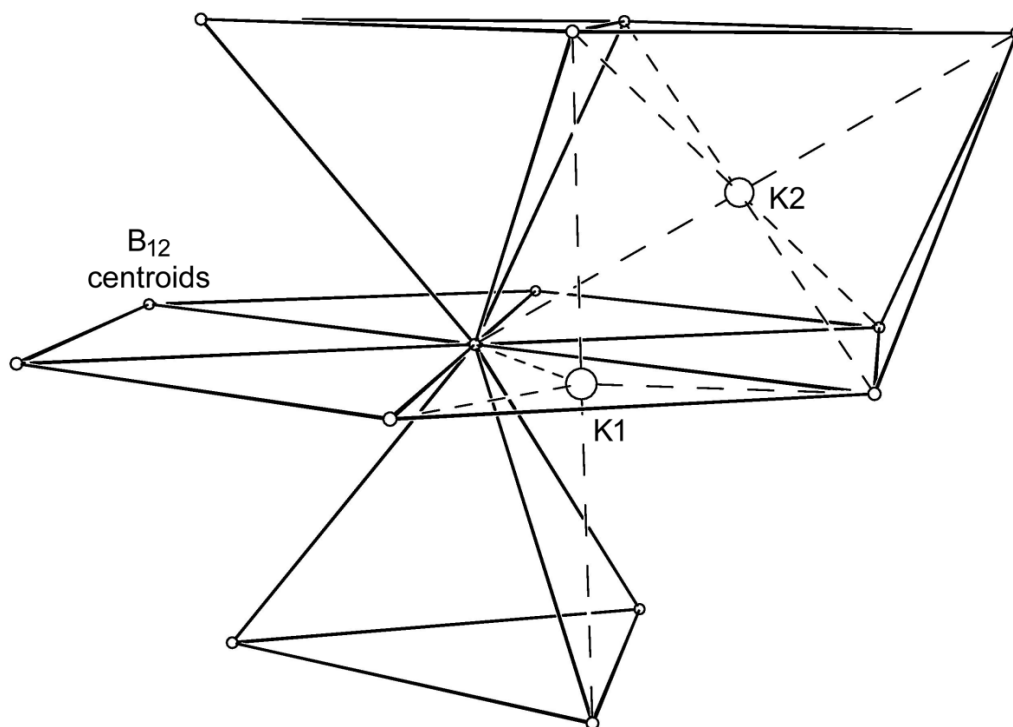


Figure 3.3. The expanded HCP-like geometry of O^{2-} 's (small spheres) and K^+ ions (large spheres) in the structure of $\text{K}_2\text{B}_{12}\text{F}_{12}$. For clarity, only two potassium cations are shown, the K1^+ cation in a D_{3h} hole in the middle layer of expanded close-packed $\text{B}_{12}\text{F}_{12}^{2-}$ anions (i.e., the expanded close-packed layer of their O^{2-} 's) and the K2^+ cation in an O_h holes between the top and middle planes of close-packed-like O^{2-} 's. The acute $\text{O}^{2-}\cdots\text{O}^{2-}\cdots\text{O}^{2-}$ angles within the close-packed-like planes are $60.0 \pm 0.2^\circ$. The $\text{O}^{2-}\cdots\text{O}^{2-}$ distances are 8.207 and 8.236 Å within the close-packed-like planes and are 7.204, 7.417, and 7.517 Å between the planes. The $\text{K1}\cdots\text{O}^{2-}$ distances are 4.719 and 4.810 Å within the middle plane and are 5.692 Å between two adjacent planes. The $\text{K2}\cdots\text{O}^{2-}$ distances are 5.445, 5.497, and 5.652 Å.

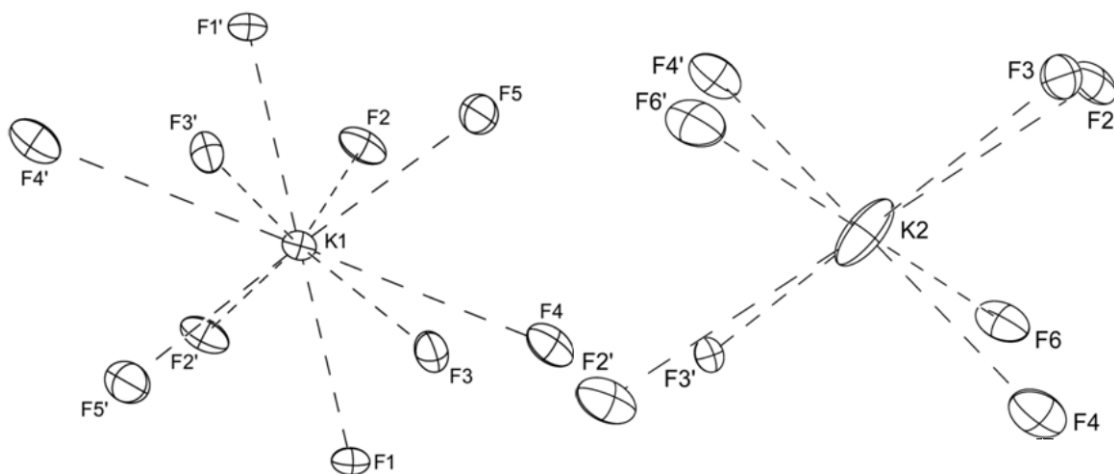


Figure 3.4. The K_1F_{10} (left) and K_2F_8 (right) coordination spheres in the structure of anhydrous $K_2B_{12}F_{12}$ (50% probability ellipsoids). The K_1F_{10} coordination sphere is a distorted bicapped square antiprism and the K_2F_8 coordination sphere is a distorted square antiprism. The two $K_1 \cdots F_1$ distances of $3.405(2)$ Å are non-bonding according to the 3% bond-valence definition discussed in Chapter 1. If they are not included, then the K_1F_8 coordination sphere is a distorted square antiprism and the sum of bond valences for K_1 is 1.12 instead of 1.16.

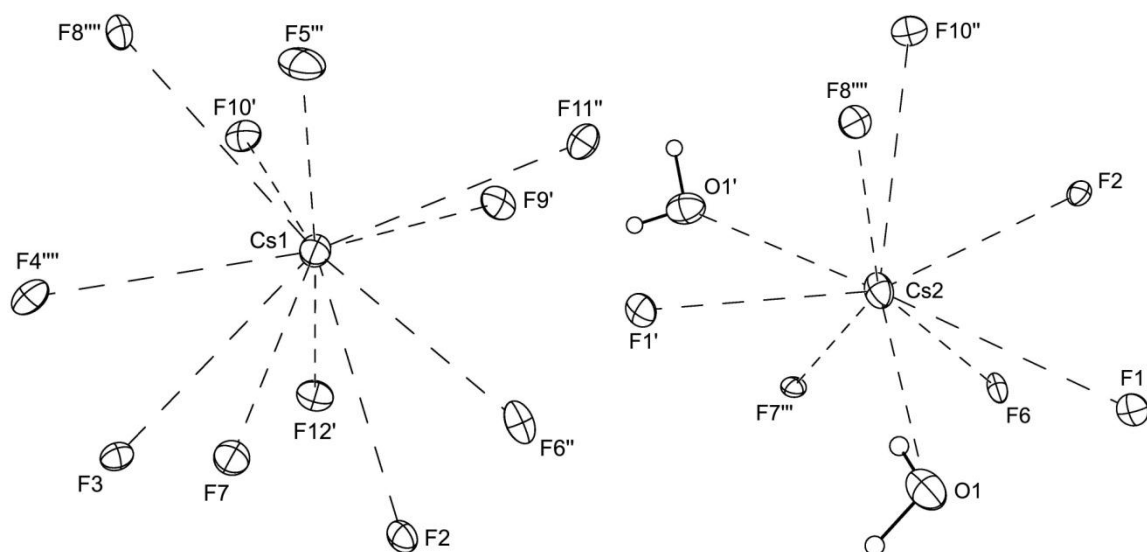


Figure 3.5. The Cs_1F_{11} (left) and $Cs_2O_2F_7$ (right) coordination spheres in the structure of $Cs_2(H_2O)B_{12}F_{12}$ (50% probability ellipsoids). The coordination spheres do not resemble any monocapped or polycapped regular polyhedron.

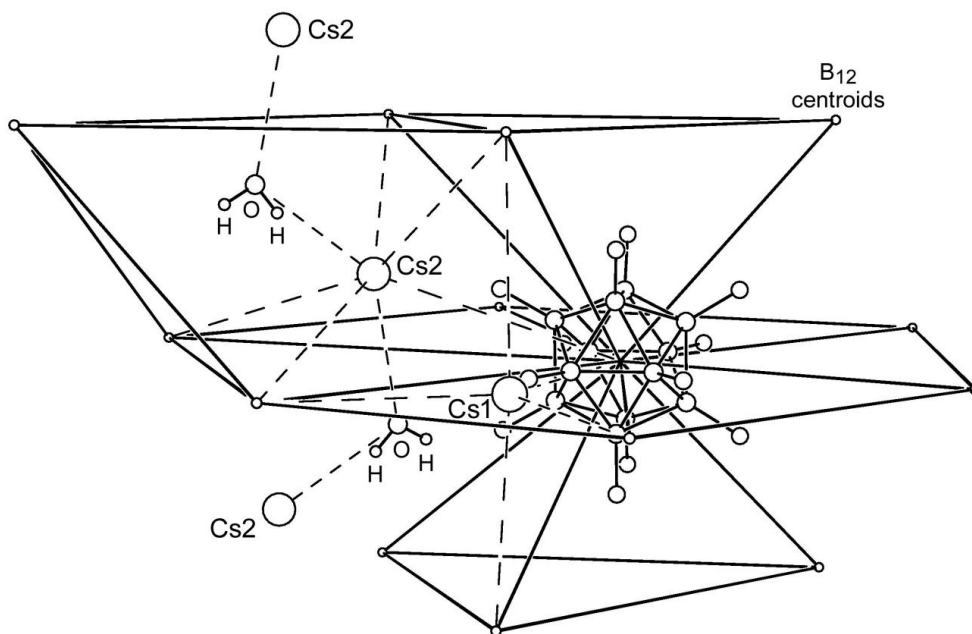


Figure 3.6. The packing of cations, anions, and H₂O molecules in the structure of Cs₂(H₂O)B₁₂F₁₂. The \ominus 's are shown as small spheres.

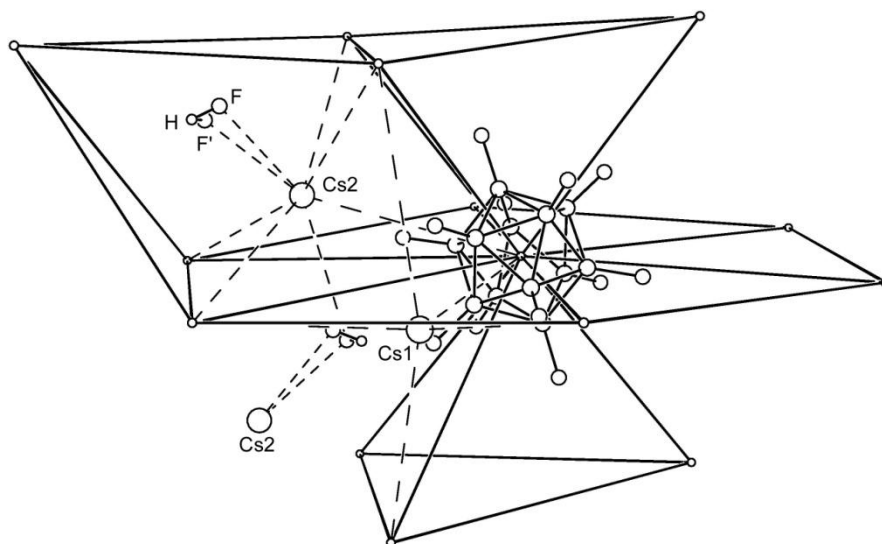


Figure 3.7. The packing of cations, anions, and HF molecules in the structure of Cs₂(HF)B₁₂F₁₂. The \ominus 's are shown as small spheres. The F atoms of the HF molecules are disordered between two positions.

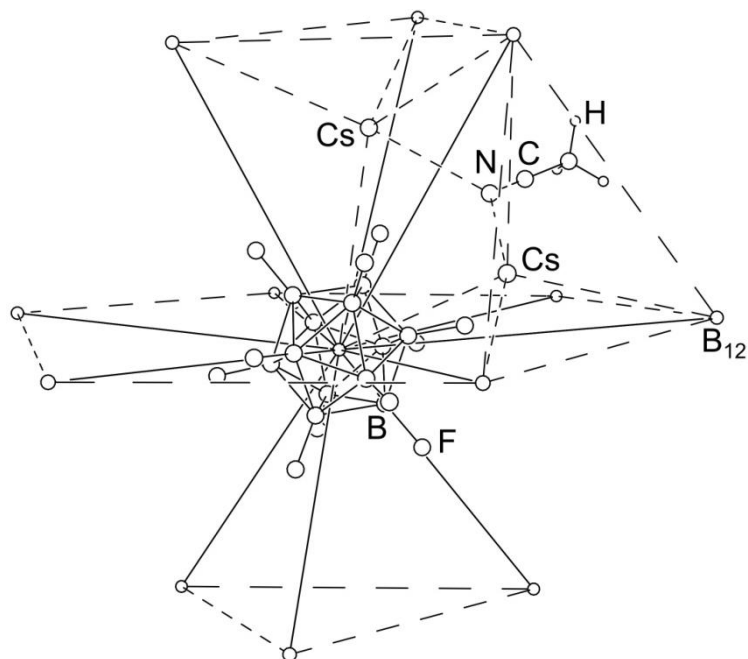


Figure 3.8. The packing of cations, anions, and CH_3CN molecules in the structure of $\text{Cs}_2(\text{CH}_3\text{CN})\text{B}_{12}\text{F}_{12}$. Only two Cs^+ cations and one CH_3CN molecule are shown for clarity. The \ominus 's, which are arranged in an expanded CCP-like array, are shown as small spheres.

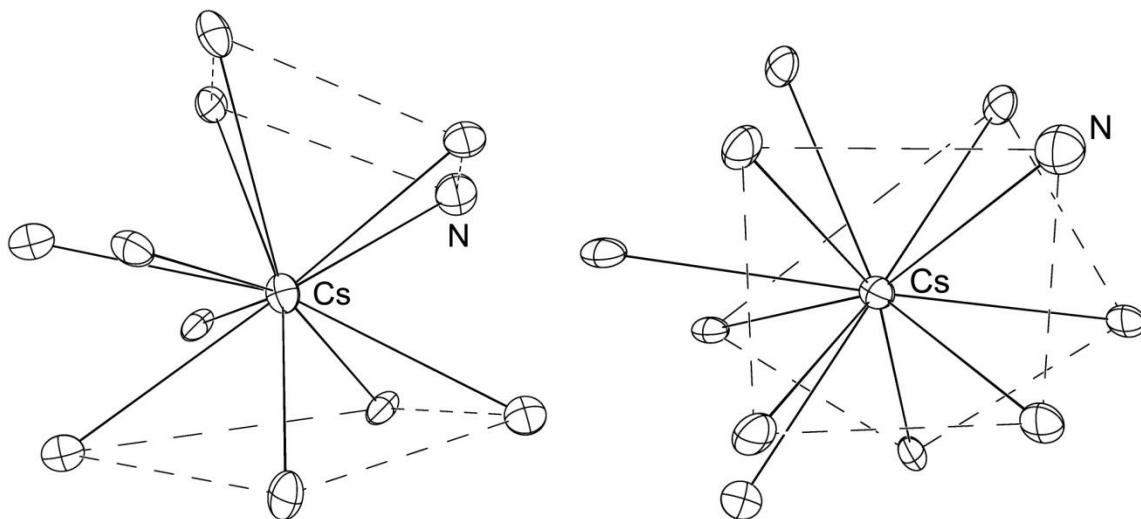


Figure 3.9. Two perpendicular views of the CsNF_{10} coordination sphere in the structure of $\text{Cs}_2(\text{CH}_3\text{CN})_2\text{B}_{12}\text{F}_{12}$ (50% probability ellipsoids). The unlabelled atoms are F atoms. The coordination sphere resembles a tricapped square antiprism. The sum of bond valences for the Cs^+ ion is 1.00.

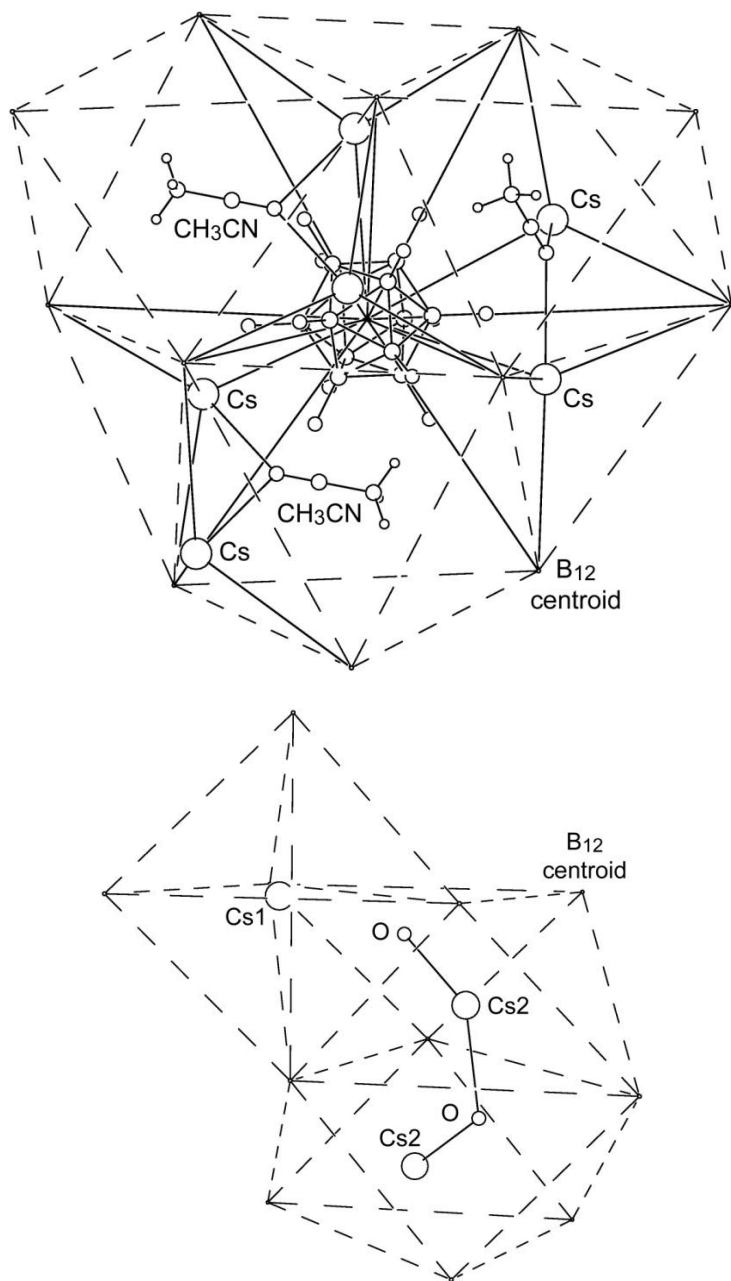


Figure 3.10. Comparison of the structures of $\text{Cs}_2(\text{CH}_3\text{CN})\text{B}_{12}\text{F}_{12}$ (top) and $\text{Cs}_2(\text{H}_2\text{O})\text{B}_{12}\text{F}_{12}$ (bottom; H atoms omitted for clarity). In the former structure, the Cs^+ ions occupy all of the T_d holes between the close-packed-like layers of F^- 's and the CH_3CN molecules occupy all of the O_h holes. In the latter structure, each Cs^{2+} ion and its closest H_2O molecule occupy all of the O_h holes and the Cs^{1+} ions occupy the D_{3h} holes between pairs of T_d holes in adjoining layers, effectively “filling” all of the T_d holes in the lattice. In that sense, all of the T_d and O_h holes are filled in both structures. The difference is that H_2O is small enough to occupy O_h holes already filled with Cs^{2+} ions, but CH_3CN is too big to occupy an O_h hole already occupied by a Cs^+ ion.

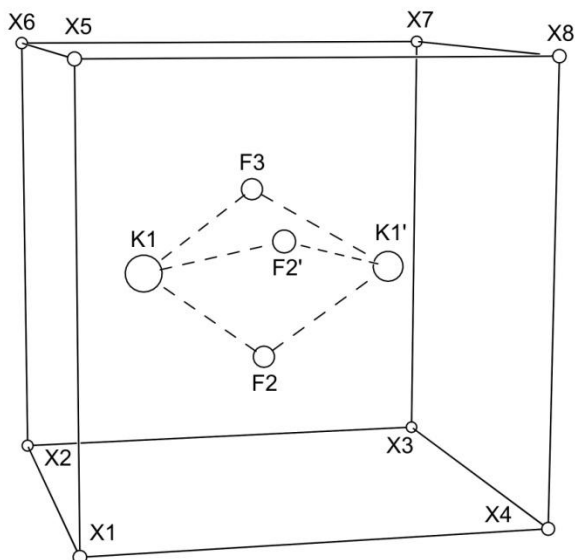


Figure 3.11. Packing of ion in the crystal structure of $\text{K}_2(\text{HF})_3\text{B}_{12}\text{F}_{12}$. The \ominus 's (X1–X8) form a rigorous cube with an edge length of 7.242 \AA . Two K^+ ions are located inside the cube and are bridged by three HF molecules. The isotropic nature of the unit cell is maintained because the K^+ ions and HF molecules are disordered (six partial K^+ ions and 21 partial HF molecules per cube). The K^+ ions are displaced 1.554 \AA from the closest face of the cube and the $\text{K}\cdots\text{K}$ distance is $4.134(2) \text{ \AA}$ ($4.134 \text{ \AA} + 2(1.554 \text{ \AA}) = 7.242 \text{ \AA}$).

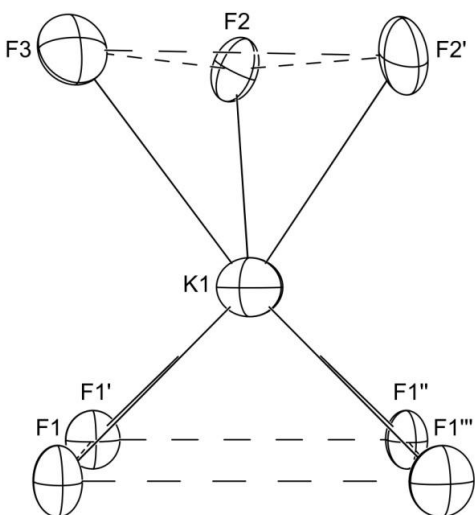


Figure 3.12. The KF_7 coordination sphere in the structure of $\text{K}_2(\text{HF})_3\text{B}_{12}\text{F}_{12}$ (50% probability ellipsoids). The F2 and F3 atoms belong to the three μ -HF molecules that bridge pairs of K^+ ions. The H atoms belonging to these HF molecules were not located.

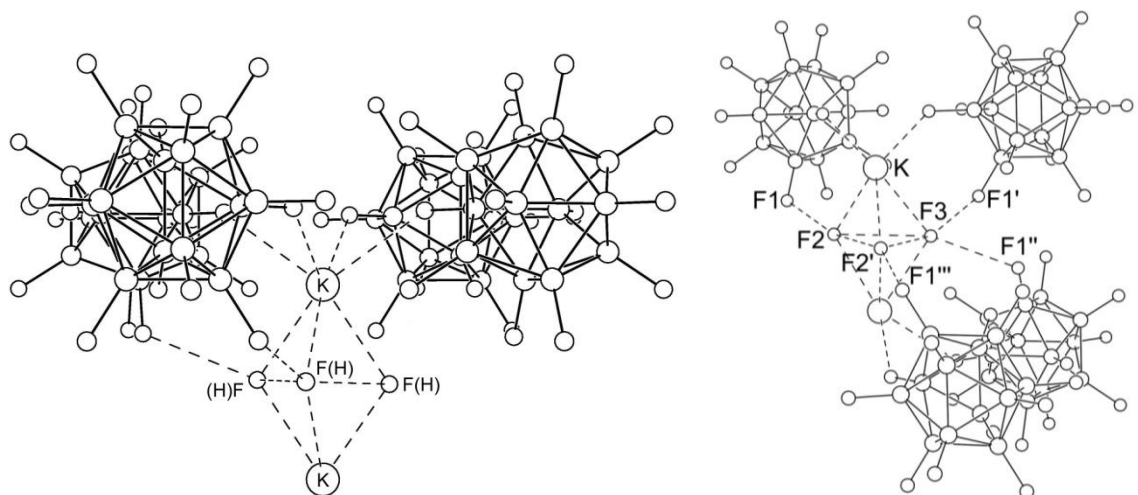


Figure 3.13. Two views of the $\text{K}_2(\mu\text{-HF})_3^{2+}$ cations and the F–H \cdots F–B hydrogen bonding in the structure of $\text{K}_2(\text{HF})_3\text{B}_{12}\text{F}_{12}$. The F \cdots F distances are 2.56(1) Å for the F2–H \cdots F1–B and the F2'–H \cdots F1'''–B hydrogen bonds, and 2.72(1) Å for the bifurcated F3–H \cdots F1'–B and F3–H \cdots F1''–B hydrogen bonds. The HF molecules are severely disordered due to the high crystallographic symmetry (space group $\text{Fm}\bar{3}\text{c}$). For this reason, the H atoms were not located in this structure.

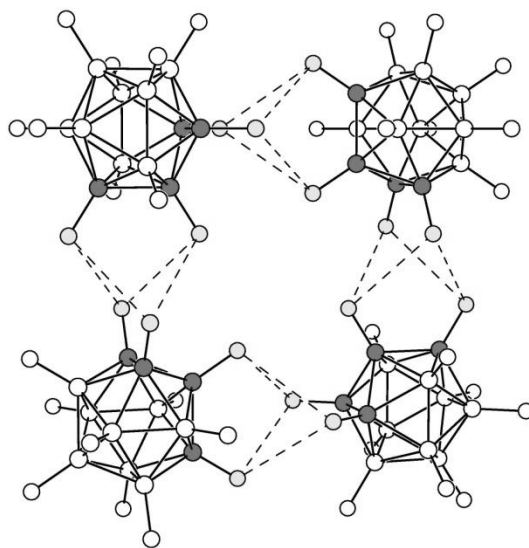


Figure 3.14. One face of the cube of $\text{B}_{12}\text{F}_{12}^{2-}$ anions in the structure of $\text{K}_2(\text{HF})_3\text{B}_{12}\text{F}_{12}$. The $\ominus\cdots\ominus$ distances are 7.242 Å. The anions are rotated 90° relative to their nearest neighbors to minimize F \cdots F repulsions between the anions. The mutually perpendicular FBBF moieties are highlighted. The interanion F \cdots F distances shown are 3.066(1) Å.

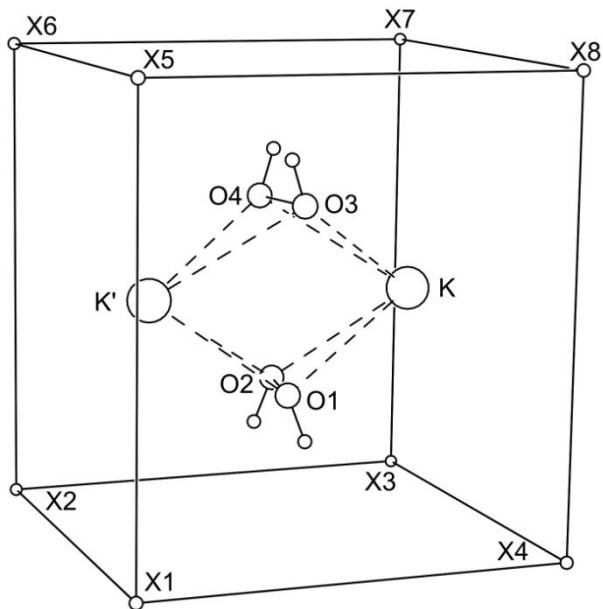


Figure 3.15. The packing of cations, anions, and H_2O_2 molecules in the structure of $\text{K}_2(\text{H}_2\text{O}_2)_{1.5}(\text{H}_2\text{O})_{0.5}\text{B}_{12}\text{F}_{12}$. The \ominus 's (X1–X8) form a tetragonal array with the following $\ominus \cdots \ominus$ distances: X1–X5, 7.719 Å; X1–X2 and X1–X4, 7.055 Å. Two K^+ ions are located inside the anion array and are bridged by two H_2O_2 molecules. Water molecules have been omitted for clarity.

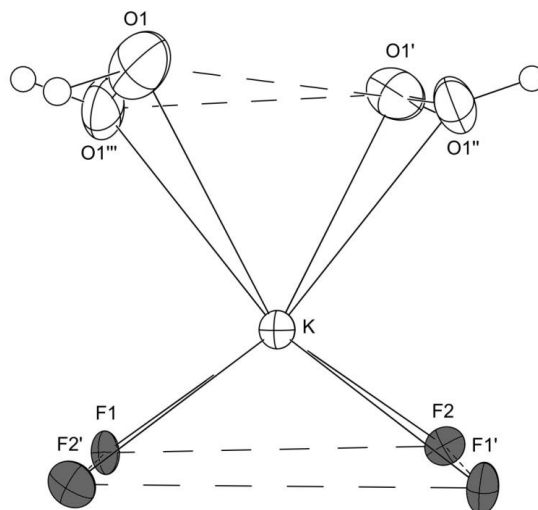


Figure 3.16. The KO_4F_4 coordination sphere in the structure of $\text{K}_2(\text{H}_2\text{O}_2)_{1.5}(\text{H}_2\text{O})_{0.5}\text{B}_{12}\text{F}_{12}$ (50% probability ellipsoids except for H atoms, which are shown as spheres of arbitrary size). The F atoms are shaded dark gray.

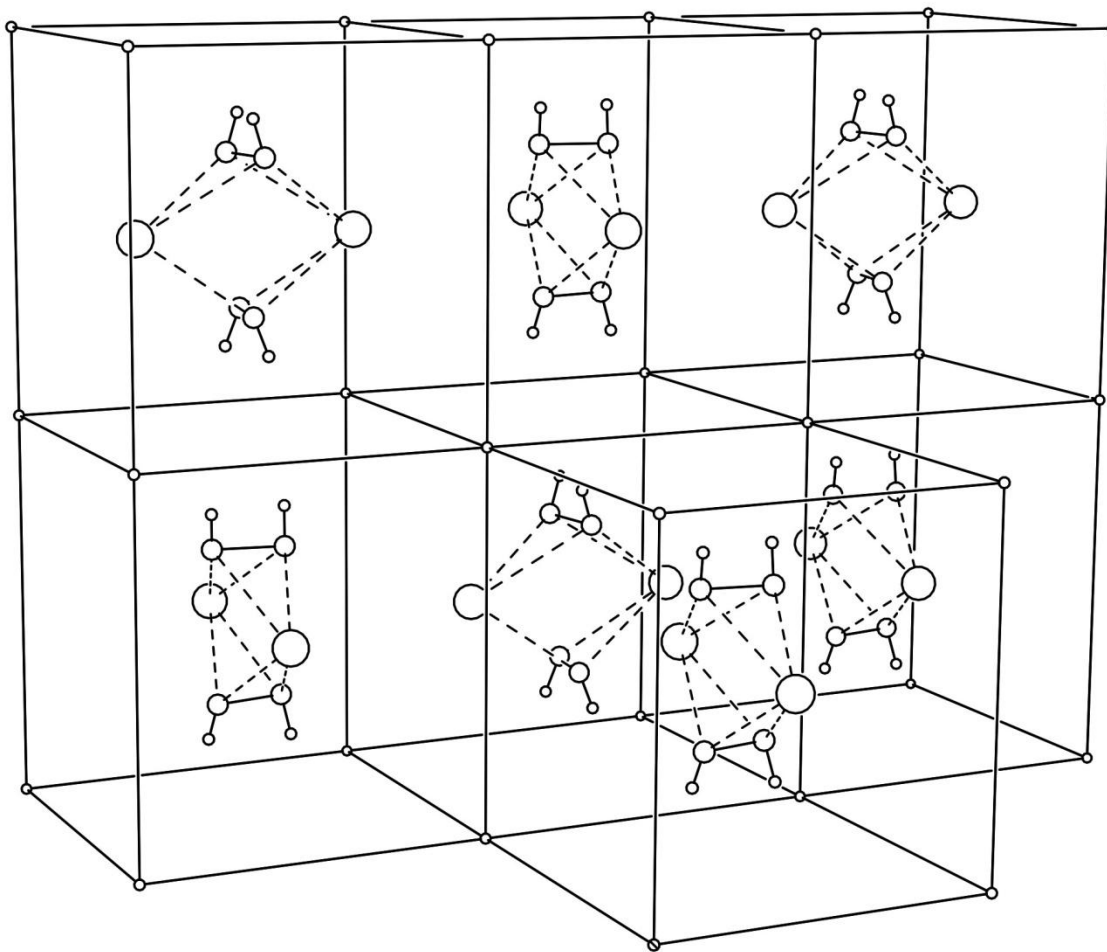


Figure 3.17. The packing and relative orientations of $\text{K}_2(\text{H}_2\text{O}_2)_2^{2+}$ dimers and \ominus 's (small spheres) in the structure of $\text{K}_2(\text{H}_2\text{O})_{1.5}(\text{H}_2\text{O})_{0.5}\text{B}_{12}\text{F}_{12}$.

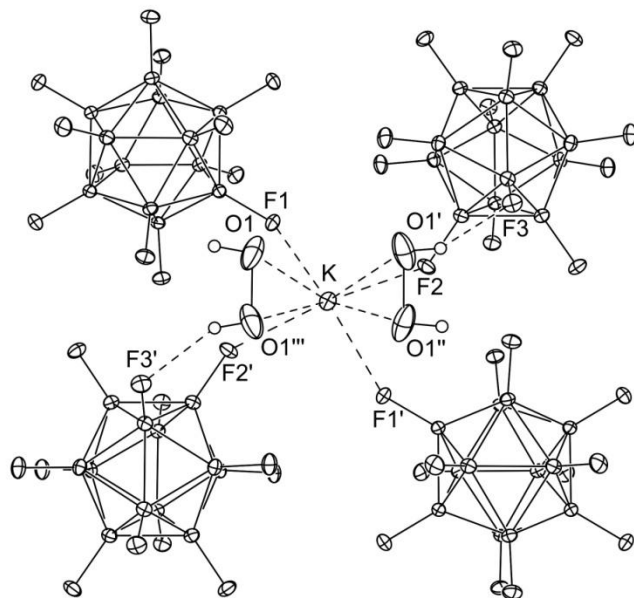


Figure 3.18. One face of the anion rhomb in the structure of $\text{K}_2(\text{H}_2\text{O})_{2.5}\text{B}_{12}\text{F}_{12}$ (50% probability ellipsoids except for H atoms, which are shown as spheres of arbitrary size). The four $\ominus \cdots \ominus$ distances in this view are 7.055 Å. As in the structure of $\text{K}_2(\text{HF})_3\text{B}_{12}\text{F}_{12}$, the anions are rotated 90° relative to their nearest neighbors to minimize $\text{F} \cdots \text{F}$ repulsions.

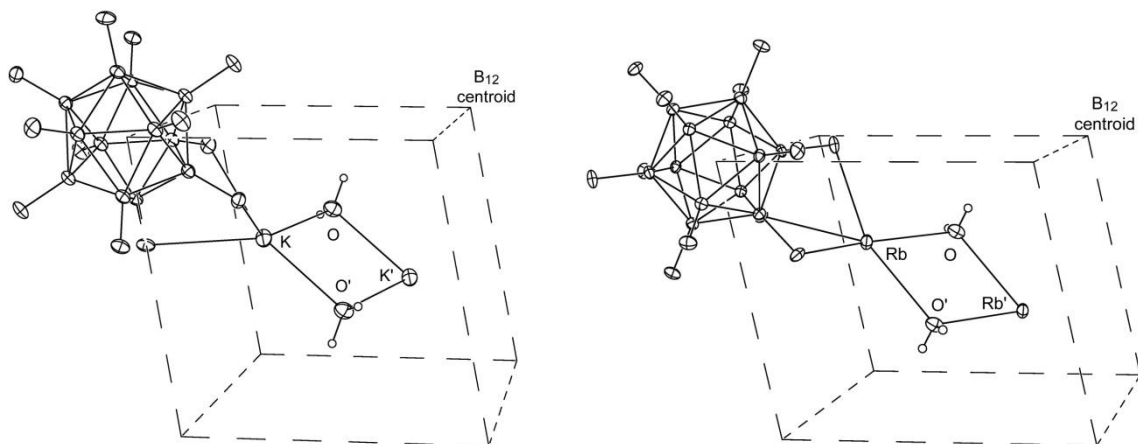


Figure 3.19. The packing of cations, anions, and H_2O molecules in the structures of $\text{K}_2(\text{H}_2\text{O})_2\text{B}_{12}\text{F}_{12}$ and $\text{Rb}_2(\text{H}_2\text{O})_2\text{B}_{12}\text{F}_{12}$ (50% probability ellipsoids except for H atoms, which are shown as spheres of fixed size; each vertex of the anion rhombs is a B_{12} centroid (\ominus)).

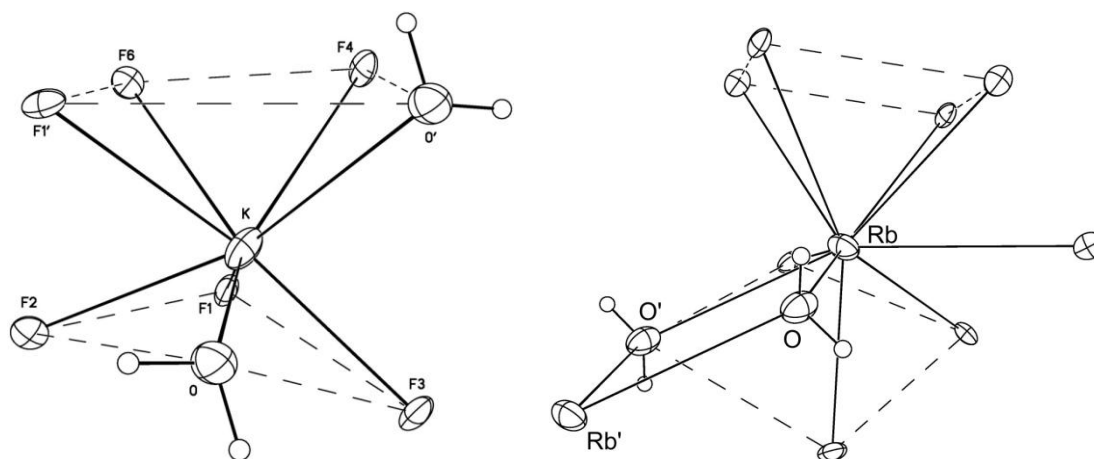


Figure 3.20. The KO_2F_6 and RbO_2F_8 coordination sphere in the structures of $\text{K}_2(\text{H}_2\text{O})_2\text{B}_{12}\text{F}_{12}$ and $\text{Rb}_2(\text{H}_2\text{O})_2\text{B}_{12}\text{F}_{12}$ (50% probability ellipsoids except for the H atoms, which are shown as spheres of arbitrary size). The KO_2F_6 coordination sphere is a distorted square antiprism and the RbO_2F_8 coordination sphere is a distorted bicapped square antiprism.

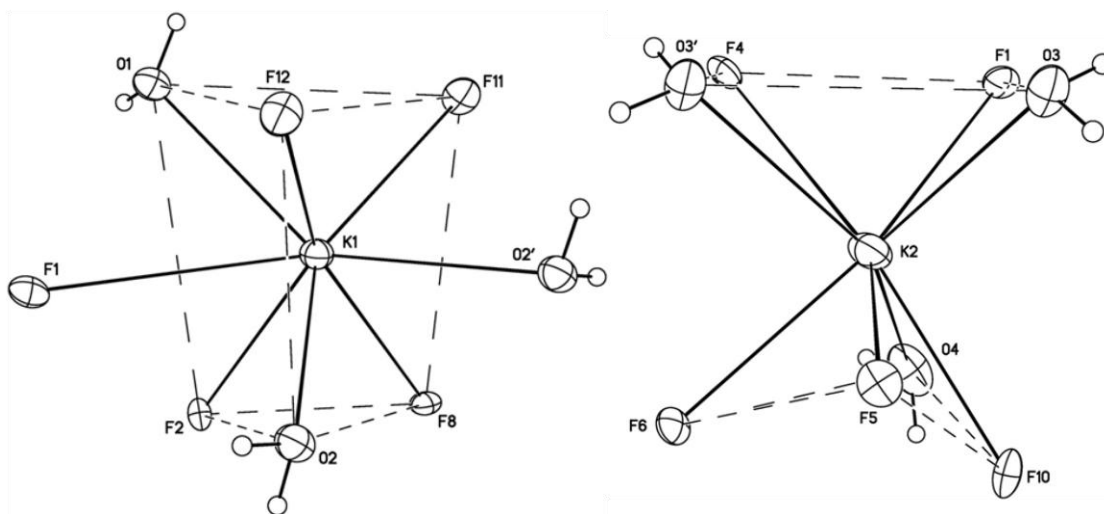


Figure 3.21. The $\text{K}_1\text{O}_3\text{F}_5$ (left) and $\text{K}_2\text{O}_3\text{F}_5$ (right) coordination spheres in the structure of $\text{K}_2(\text{H}_2\text{O})_4\text{B}_{12}\text{F}_{12}$ (50% probability ellipsoids except for H atoms, which are shown as spheres of arbitrary size). The $\text{K}_1\text{O}_3\text{F}_5$ coordination sphere is a bicapped trigonal prism and the $\text{K}_2\text{O}_3\text{F}_5$ coordination sphere is a highly-distorted square antiprism similar to the KO_2F_6 coordination sphere in the structure of $\text{K}_2(\text{H}_2\text{O})_2\text{B}_{12}\text{F}_{12}$.

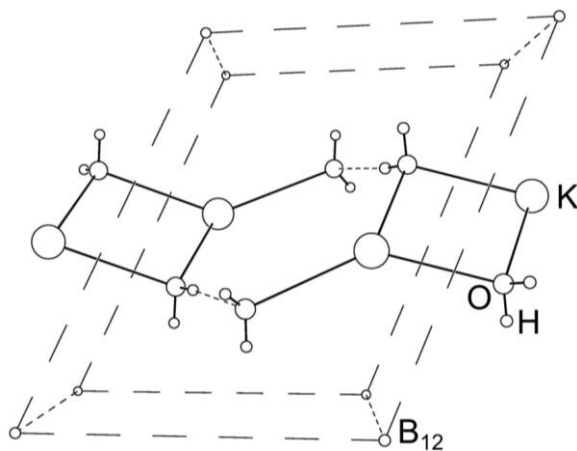


Figure 3.22. The packing of cations, anions, and H₂O molecules in the structure of K₂(H₂O)₄B₁₂F₁₂. The B₁₂ centroids are shown as small spheres at the corners of the anion rhomb.

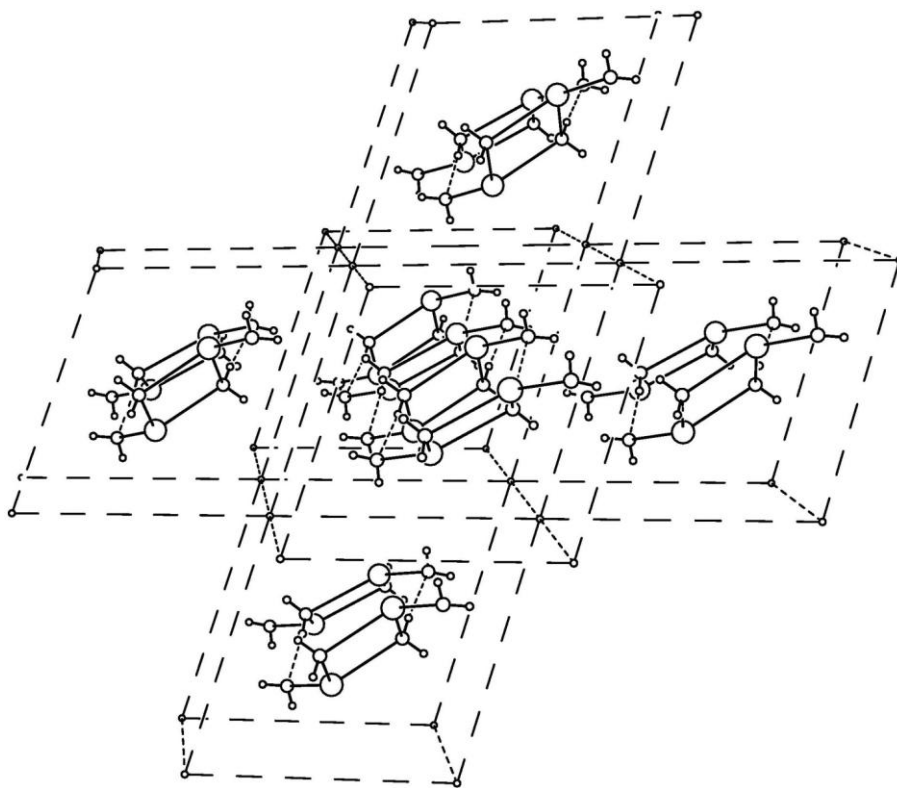


Figure 3.23. The packing of B₁₂ centroids (small circles) and K₂(H₂O)₄²⁺ cation dimers in the structure of K₂(H₂O)₄B₁₂F₁₂. The hydrogen-bonded ribbons of cation dimers continue along the short 6.915 Å centroid-centroid vectors. The two other ⊙⋯⊙ distances are 8.399 and 8.598 Å.

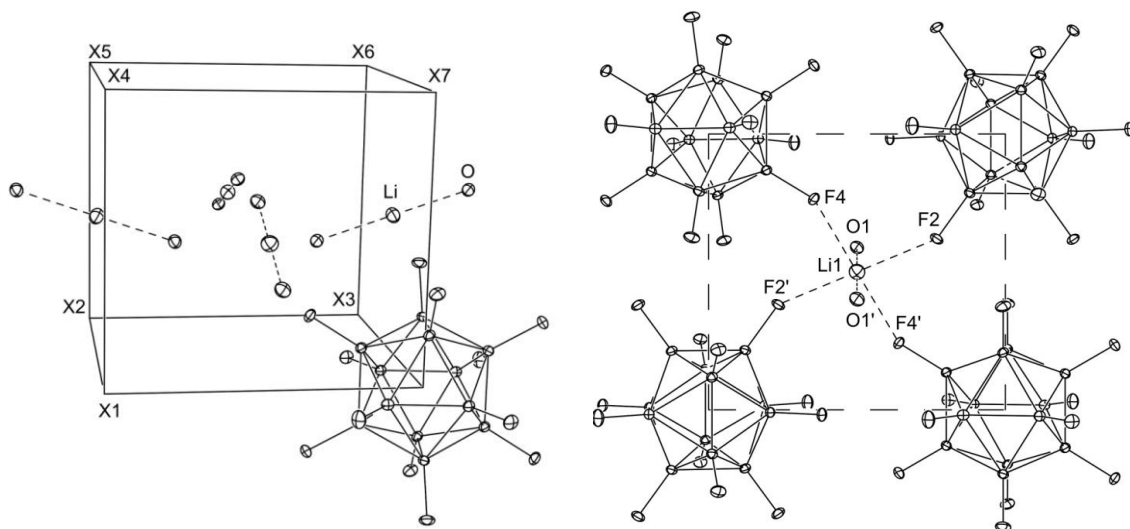


Figure 3.24. Left. The packing of cations, anions, and H₂O molecules in the structure of Li₂(H₂O)₄B₁₂F₁₂ (50% probability ellipsoids). The eight B₁₂ centroids at the corners of the anion rhomb are X1–X8. Hydrogen atoms have been omitted for clarity. Right. One face of the anion rhomb (50% probability ellipsoids; H atoms omitted for clarity). The Li⁺ ion and the four anion centroids are rigorously coplanar. Two of the four ⊖⋯⊖ distances shown are 6.767 Å and two are 7.287 Å. Note that the anions are rotated 74.3° relative to their nearest neighbors to minimize F⋯F repulsions.

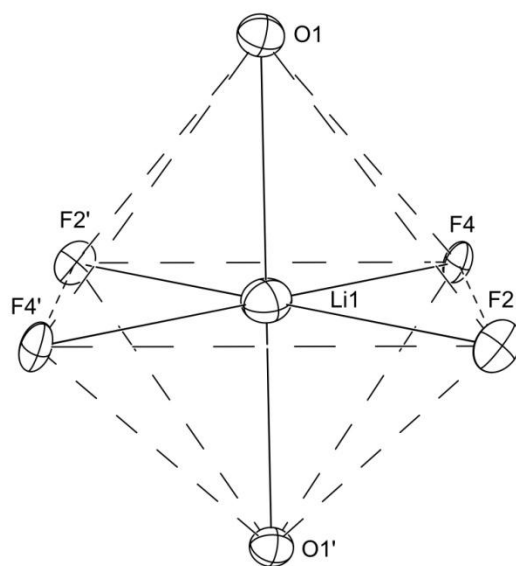


Figure 3.25. The octahedral LiO₂F₆ coordination sphere in the structure of Li₂(H₂O)₄B₁₂F₁₂ (50% probability ellipsoids; H atoms omitted for clarity).

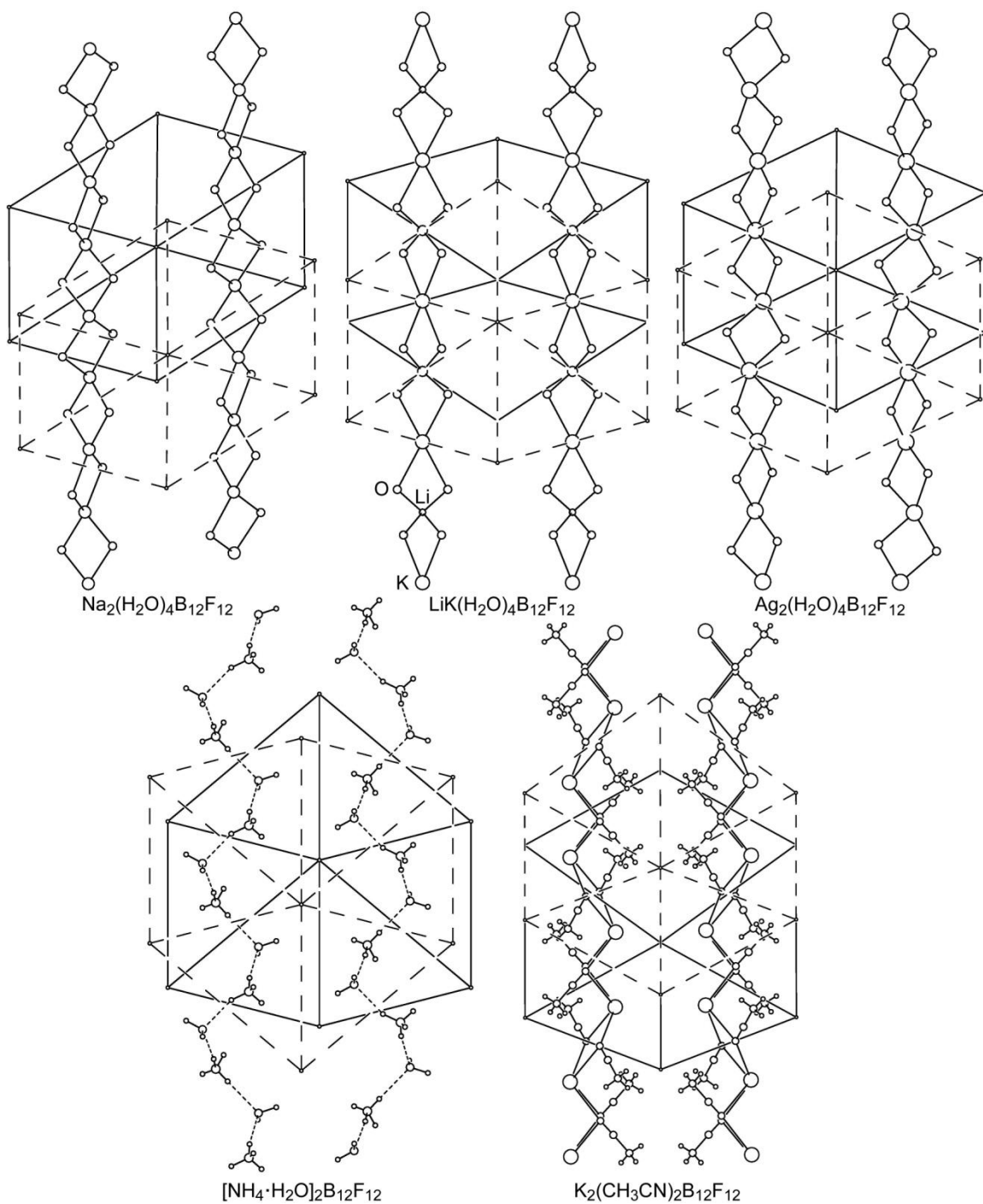


Figure 3.26. The packing of anion centroids (\odot 's; very small spheres), cations, and either H_2O or CH_3CN molecules in five structures containing the $\text{B}_{12}\text{F}_{12}^{2-}$ anion. Each structure is shown with the least-squares plane of the hexagonal arrays of \odot 's parallel to the plane of the page. One layer of \odot 's (solid lines) is above another one (dashed lines).

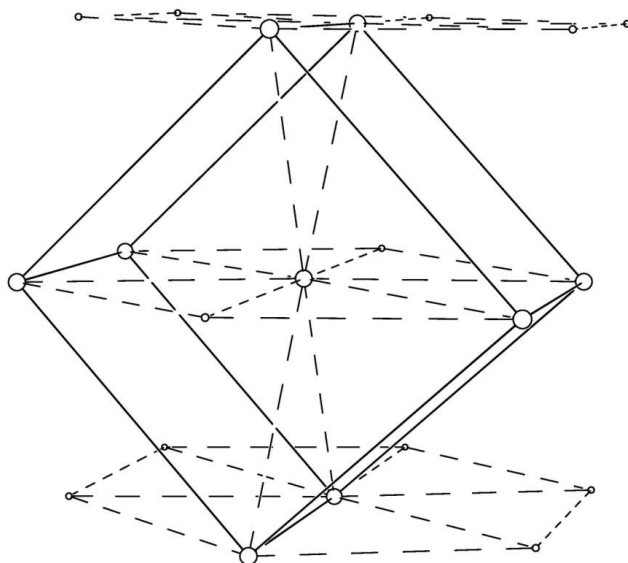


Figure 3.27. The idealized body-centered tetragonal packing of anion centroids (\ominus 's) in the structure of $\text{Ag}_2(\text{H}_2\text{O})_4\text{B}_{12}\text{F}_{12}$ (only the \ominus 's are shown).

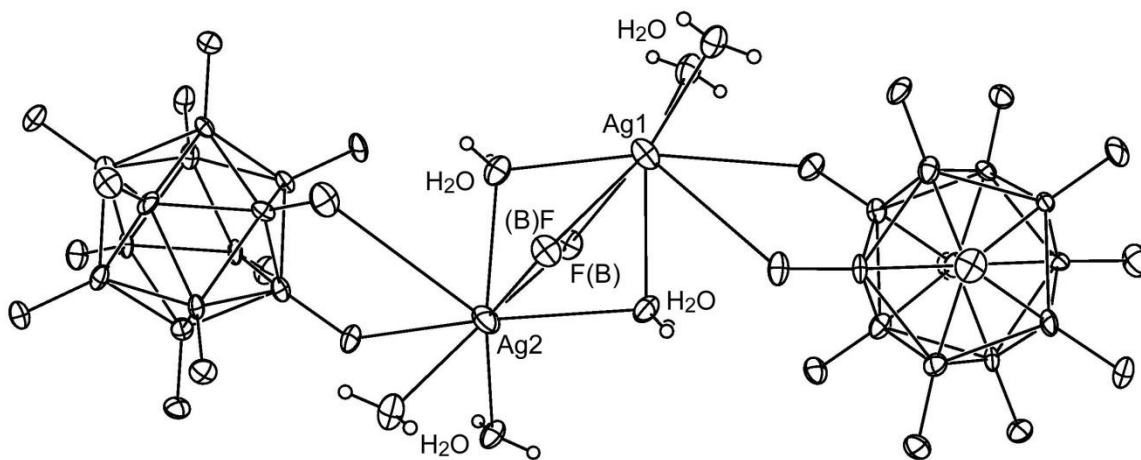


Figure 3.28. Part of one of the $\{\text{Ag}(\mu\text{-H}_2\text{O})_2\text{Ag}'(\mu\text{-H}_2\text{O})_2\}_n^{2n+}$ linear chains located between the close-packed-like layers of \ominus 's give rise to AgO_4F_4 coordination spheres in the structure of $\text{Ag}_2(\text{H}_2\text{O})_4\text{B}_{12}\text{F}_{12}$ (50% probability ellipsoids except for H atoms, which are shown as spheres of arbitrary size).

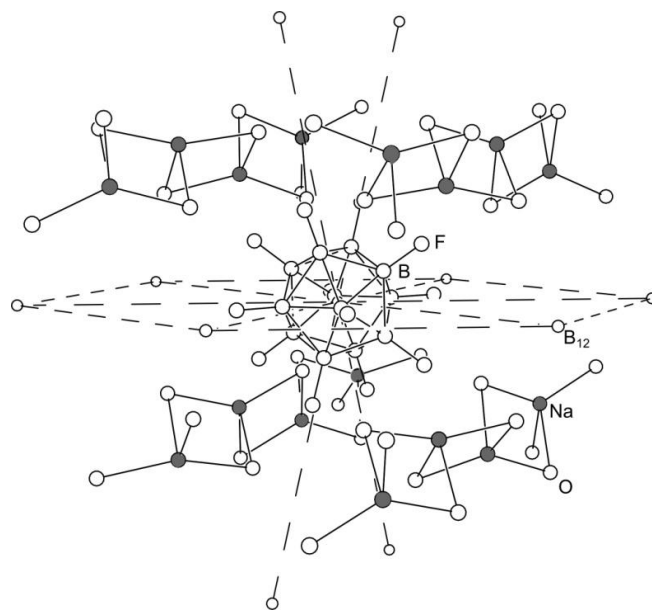


Figure 3.29. The packing of cations, anions, and H₂O molecules in the structure of Na₂(H₂O)₄B₁₂F₁₂ (H atoms have been omitted for clarity). The B₁₂ centroids are shown as small spheres and the Na⁺ cations are highlighted in gray. The contacts between Na⁺ ions and F(B) atoms are not shown (see Figure 3.30 for the NaO₄F₂ coordination spheres).

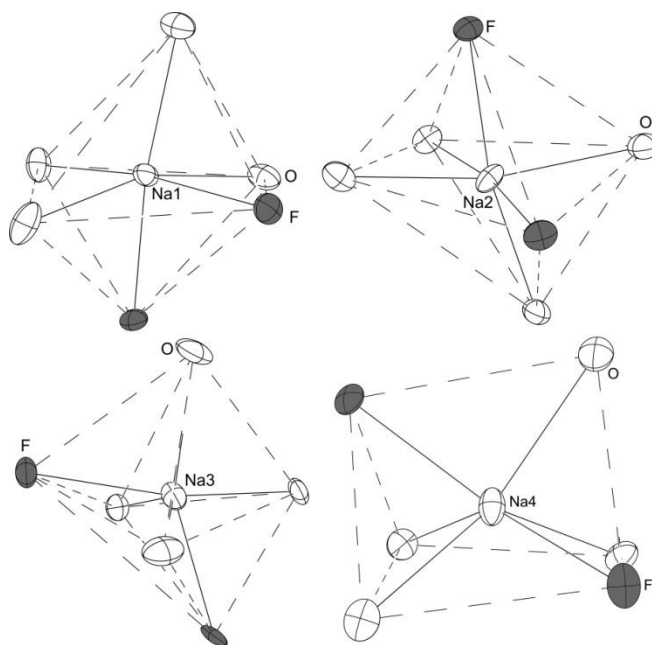


Figure 3.30. The NaO₄F₂ coordination spheres in the structure of Na₂(H₂O)₄B₁₂F₁₂ (50% probability ellipsoids; H atoms omitted for clarity). The F atoms are highlighted in gray.

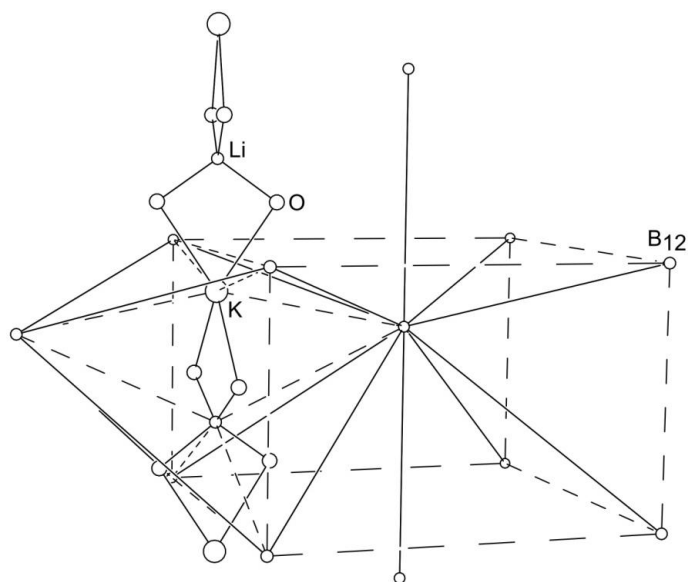


Figure 3.31. The packing of cations, anion centroids (\ominus 's), and H_2O molecules in the structure of $\text{LiK}(\text{H}_2\text{O})_4\text{B}_{12}\text{F}_{12}$ (H atoms omitted for clarity). The \ominus 's are shown as small spheres in the center and at the corners of the pseudo-body-centered tetragonal anion array. Only one of the $\{\text{Li}(\mu\text{-H}_2\text{O})_2\text{K}(\mu\text{-H}_2\text{O})_2\}_n^{2n+}$ infinite chains is shown.

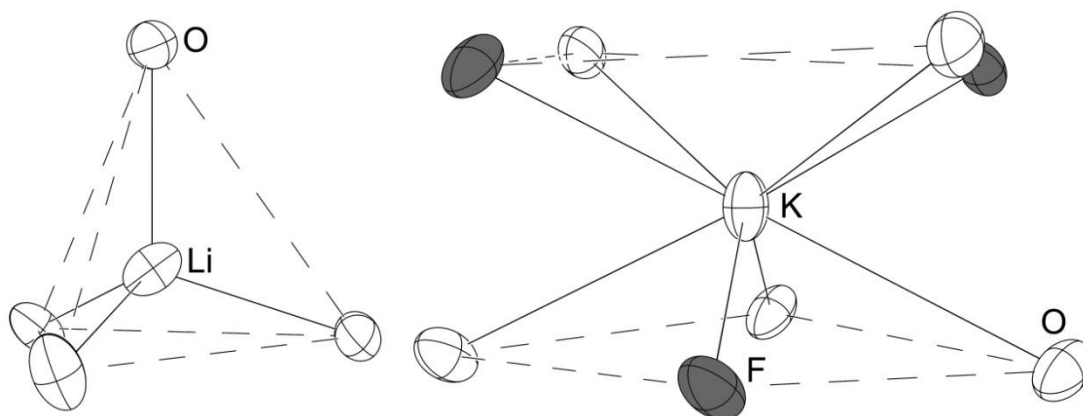


Figure 3.32. The tetrahedral LiO_4 (left) and square-antiprismatic KO_4F_4 (right) coordination spheres in the structure of $\text{LiK}(\text{H}_2\text{O})_4\text{B}_{12}\text{F}_{12}$ (50% probability ellipsoids; H atoms omitted for clarity). The F atoms are highlighted in gray.

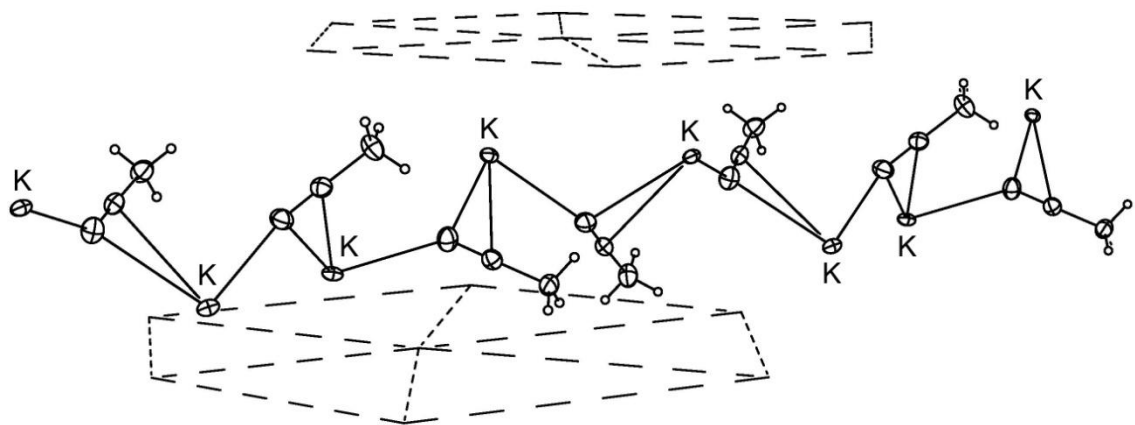


Figure 3.33. The packing of cations, anion centroids (\ominus 's), and CH_3CN molecules in the structure of $\text{K}_2(\text{CH}_3\text{CN})_4\text{B}_{12}\text{F}_{12}$ (50% probability ellipsoids except for H atoms, which are shown as spheres of arbitrary size). The distorted hexagonal layers of \ominus 's are readily seen. The CH_3CN molecules bridge two K^+ ions, forming $\{\text{K}(\mu\text{-}\eta^1, \eta^2\text{-CH}_3\text{CN})\}_n^{n+}$ polycation infinite chains. Only one of the infinite chain polycations is shown.

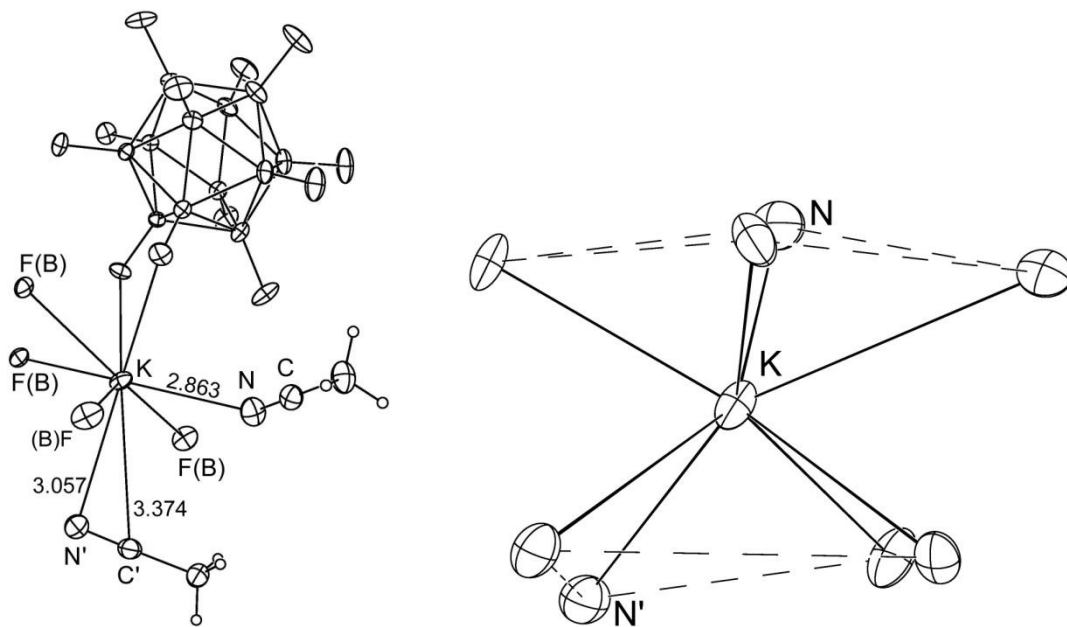


Figure 3.34. Two views of the square-antiprismatic KN_2F_6 coordination sphere in the structure of $\text{K}_2(\text{CH}_3\text{CN})_4\text{B}_{12}\text{F}_{12}$ (50% probability ellipsoids). The K–N and K–C distances (\AA) are shown in the drawing on the left. The weak K–C interaction has been omitted in the drawing on the right.

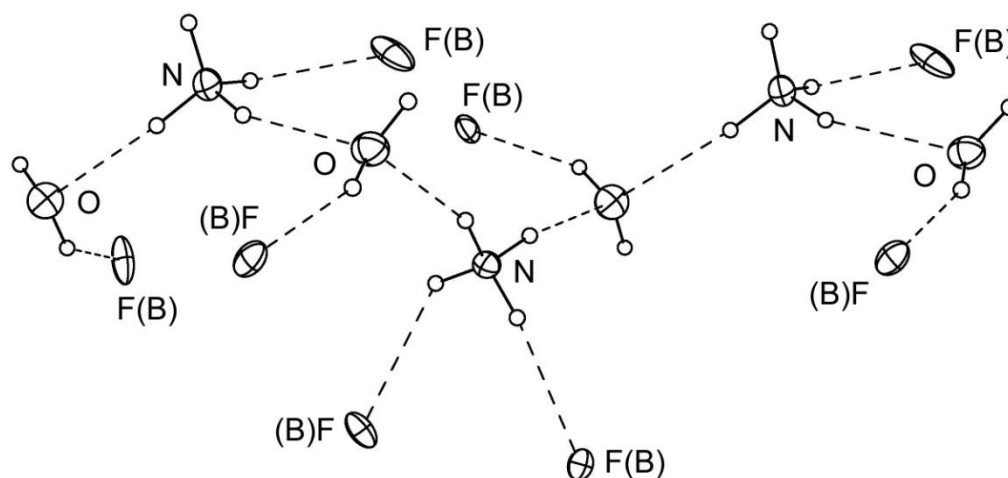


Figure 3.35. The $\{\cdots(\text{H}_2\text{O}\cdots\text{H}-\text{N}(\text{H}_2)-\text{H}\cdots)\}_n^{n+}$ polycationic infinite chain in the structure of $[\text{NH}_4\cdot\text{H}_2\text{O}]_2\text{B}_{12}\text{F}_{12}$ (50% probability ellipsoids except for H atoms, which are shown as spheres of arbitrary size).

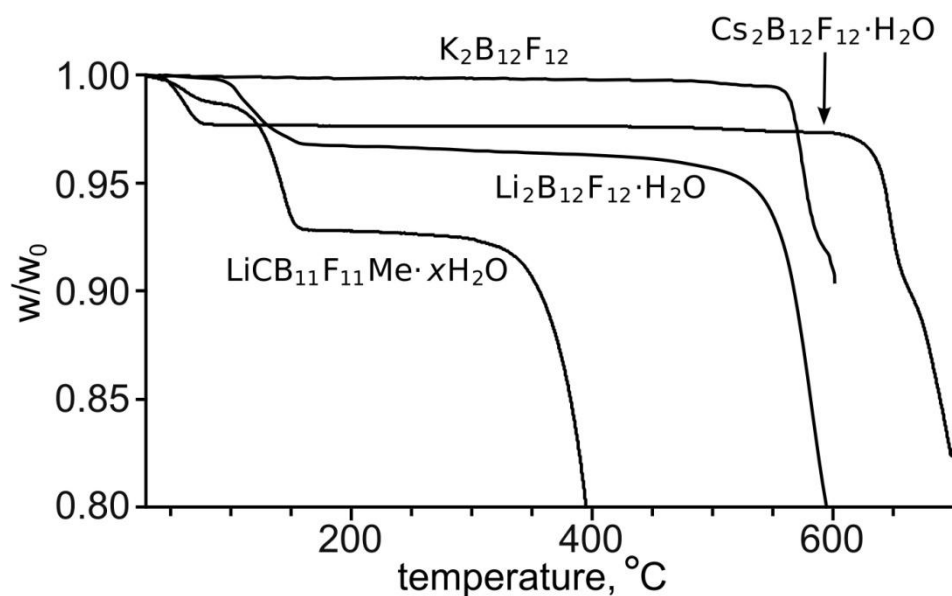


Figure 3.36. TGA traces (He carrier gas) showing the dehydration (except for $\text{K}_2\text{B}_{12}\text{F}_{12}$) and eventual decomposition of the four indicated samples. The $\text{K}_2\text{B}_{12}\text{F}_{12}$ sample had been dehydrated by exposure to the dry air in Fort Collins, CO, at 25 °C. See Chapter 6 for an in-depth discussion of the interesting hydration/dehydration behavior of $\text{K}_2\text{B}_{12}\text{F}_{12}$.

CHAPTER 4. SILVER(I) SALTS OF $B_{12}F_{12}^{2-}$ ANION

Introduction.

High thermal and chemical stability of the $B_{12}F_{12}^{2-}$ is exceptional among fluorinated superweak anions. Therefore, it is reasonable to suggest that the preparation of highly active solvent-free transition metal salts $M_xB_{12}F_{12}$ can be achieved by the simple thermal deligation of $M_x(L)_nB_{12}F_{12}$. The high reactivity of the metal cation towards coordination of small and weak ligands, such as carbon monoxide, is expected in the flexible lattice of the relatively large and highly symmetric icosahedral $B_{12}F_{12}^{2-}$. The weakly coordinated lattice of perfluorinated anions may expand and contract “on demand” allowing for reactivity of the cations towards small-molecule gases. Similarly to zeolites, “fluorolite” term may be used to describe these reactive compounds. In this chapter the preparation and reactivity of the first solvent-free transition metal salt of $B_{12}F_{12}^{2-}$ anion, $Ag_2B_{12}F_{12}$ and the crystal structures and unusual ionic packing of various $Ag_2(L)_nB_{12}F_{12}$ salts which were prepared from the desolvated compound, are reported. Formation of the nonclassical cationic carbonyl $[Ag(CO)]_2B_{12}F_{12}$ and crystallization of the Ag^+ salts containing weak ligands such as $[Ag(CH_2Cl_2)_2]_2B_{12}F_{12}$ and $[Ag(C_7H_8)_3]_2B_{12}F_{12}$ demonstrate superweak nature of $B_{12}F_{12}^{2-}$ anion.

Experimental

I. Reagents and Solvents.

Acetonitrile (Fisher Scientific) was dried as described in Chapter 1. The anhydrous salt $K_2B_{12}F_{12}$ was prepared as described in Chapter 1. Toluene (Fisher Scientific) and dichloromethane (Fisher Scientific) were dried by reflux over sodium metal and calcium

hydride, respectively, and were distilled under nitrogen atmosphere. Anhydrous AgNO_3 (Aldrich) was used as received.

II. Preparation and Crystallization of $\text{Ag}_2(\text{L})_n\text{B}_{12}\text{F}_{12}$ salts.

A. Preparation of $\text{Ag}_2(\text{CH}_3\text{CN})_4\text{B}_{12}\text{F}_{12}$. A solution of $\text{K}_2\text{B}_{12}\text{F}_{12}$ (200 mg; 0.459 mmol) in dry acetonitrile (10 mL) was added quickly to a solution of anhydrous AgNO_3 (156 mg; 0.918 mmol) in dry acetonitrile (10 mL) and vigorously stirred for 20 min. After removing the white precipitate of KNO_3 , the filtrate was evaporated to dryness under vacuum. The white solid was dissolved in dry dichloromethane (20 mL). Insoluble white residue was filtered and the filtrate was cooled to $-20\text{ }^\circ\text{C}$. Colorless crystals of $\text{Ag}_2(\text{CH}_3\text{CN})_4\text{B}_{12}\text{F}_{12}$ were formed and were characterized by TGA and single-crystal X-ray diffraction. When the dichloromethane filtrate was evaporated to dryness under vacuum, the $\text{Ag}_2(\text{CH}_3\text{CN})_4\text{B}_{12}\text{F}_{12}$ (310 mg; 0.422 mmol) was isolated as a white powder. The yield was 92% based on the amount of $\text{K}_2\text{B}_{12}\text{F}_{12}$.

B. Preparation of $\text{Ag}_2(\text{CH}_3\text{CN})_8\text{B}_{12}\text{F}_{12}$. A solution of $\text{K}_2\text{B}_{12}\text{F}_{12}$ (200 mg; 0.459 mmol) in dry acetonitrile (10 mL) was added quickly to a solution of anhydrous AgNO_3 (156 mg; 0.918 mmol) in dry acetonitrile (10 mL) and vigorously stirred for 20 min. After removing the white precipitate of KNO_3 , the filtrate was added to dry dichloromethane (20 mL) and cooled to $-20\text{ }^\circ\text{C}$. Colorless crystals of $\text{Ag}_2(\text{CH}_3\text{CN})_8\text{B}_{12}\text{F}_{12}$ were formed and were characterized by single-crystal X-ray diffraction.

C. Preparation of $\text{Ag}_2(\text{CH}_3\text{CN})_5\text{B}_{12}\text{F}_{12}$. A solution of $\text{K}_2\text{B}_{12}\text{F}_{12}$ (200 mg; 0.459 mmol) in dry acetonitrile (10 mL) was added quickly to a solution of anhydrous AgNO_3 (156 mg; 0.918 mmol) in dry acetonitrile (10 mL) and vigorously stirred for 20 min. After removing the white precipitate of KNO_3 , the filtrate was added to dry dichloromethane (20 mL) and was allowed to slowly evaporate. Colorless crystals of $\text{Ag}_2(\text{CH}_3\text{CN})_5\text{B}_{12}\text{F}_{12}$ were formed and were characterized by single-crystal X-ray diffraction.

D. Preparation of $\text{Ag}_2(\text{C}_7\text{H}_8)_6\text{B}_{12}\text{F}_{12}$. A solid $\text{Ag}_2(\text{CH}_3\text{CN})_4\text{B}_{12}\text{F}_{12}$ (100 mg, 0.136 mmol) was heated at 270 °C under vacuum for 2 h. The white-off solid was added to dry toluene (15 mL) and heated at 50 °C for 18 h. Colorless crystals of $\text{Ag}_2(\text{C}_7\text{H}_8)_6\text{B}_{12}\text{F}_{12}$ were formed and were characterized by single-crystal X-ray diffraction.

E. Preparation of $\text{Ag}_2(\text{CH}_2\text{Cl}_2)_4\text{B}_{12}\text{F}_{12}$. A solid $\text{Ag}_2(\text{CH}_3\text{CN})_4\text{B}_{12}\text{F}_{12}$ (100 mg, 0.136 mmol) was heated at 270 °C under vacuum for 2 h. The white-off solid was dissolved in dry dichloromethane (15 mL). Colorless crystals of $\text{Ag}_2(\text{CH}_2\text{Cl}_2)_4\text{B}_{12}\text{F}_{12}$ were formed by diffusion of hexane vapor to the dichloromethane solution and were characterized by single-crystal X-ray diffraction.

III. Single-Crystal X-ray Diffraction.

Unit cell parameters were obtained from least-squares fits to the angular coordinates of all reflections, and intensities were integrated from a series of frames (ω and φ rotation) covering more than a hemisphere of reciprocal space. Absorption and other corrections were applied using SADABS. The structures were solved using direct methods and refined (on F^2 , using all data) by a full-matrix, weighted least squares process. Standard Bruker control and integration software (APEX II) was employed, and Bruker SHELXTL software was used for structure solution, refinement, and molecular graphics.

The B_{12} centroid–centroid distances are listed without the corresponding esd.’s. The individual esd.’s of the individual B–B bonds are in the range 0.001–0.005 Å for the reported structures. The centroid position is derived from the positions of twelve boron atoms and therefore the esd.’s of the centroid coordinates are generally one order of magnitude smaller (i.e., 0.0001–0.0005 Å).

IV. Thermogravimetric Analysis (TGA).

Samples for TGA were analyzed using a TA Instruments TGA-2950 instrument (platinum sample pans; *ca.* 10 mg samples; 25–500 °C temperature range; heating rate 3 °C min^{-1}).

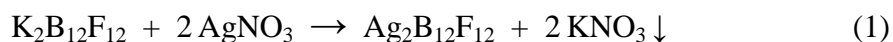
V. Infrared spectroscopy (FTIR).

Samples for infrared spectroscopy were Nujol mulls between either KBr windows or sapphire windows under high pressures of CO using a high-pressure cell of local design. Spectra were recorded on a Nicolet FTIR spectrometer at 1 cm^{-1} resolution.

Results and Discussion

I. Synthesis and Thermal Stability of $\text{Ag}_2(\text{L})_n\text{B}_{12}\text{F}_{12}$

Silver(I) salts of superweak anions are important reagents in the armamentarium of coordination chemists. The metathesis reaction that produced $\text{Ag}_2\text{B}_{12}\text{F}_{12}$ is shown in Eqn. 1 (the solvent was a- CH_3CN):



The reaction mixture was filtered to remove insoluble KNO_3 and an equal volume of 1,2-dichloromethane was added. This solution was cooled to $-20\text{ }^\circ\text{C}$, resulting in diffraction-quality crystals of $\text{Ag}_2(\text{CH}_3\text{CN})_8\text{B}_{12}\text{F}_{12}$. When the solution was slowly evaporated on air the colorless crystals of $\text{Ag}_2(\text{CH}_3\text{CN})_5\text{B}_{12}\text{F}_{12}$ were formed. When the filtered reaction mixture was evaporated to dryness quickly at room temperature, a white powder was isolated. The dissolution of the powder in anhydrous dichloromethane with subsequent cooling to $-20\text{ }^\circ\text{C}$ led to formation of colorless crystals of $\text{Ag}_2(\text{CH}_3\text{CN})_4\text{B}_{12}\text{F}_{12}$. The thermal stability of tetrakisacetonitrile salt was studied using thermogravimetry (Figure 4.1). Before heating, the IR spectrum of the white powder exhibited two $\nu(\text{CN})$ bands at 2325 and 2298 cm^{-1} . After a sample was heated to $270\text{ }^\circ\text{C}$ under vacuum, no bands were observed in the $\nu(\text{CN})$ region. According to the % mass loss between room temperature and $300\text{ }^\circ\text{C}$ ($\Delta\%m = 22\%$), the white powder is formulated as $\text{Ag}_2(\text{CH}_3\text{CN})_4\text{B}_{12}\text{F}_{12}$ and the heat-treated product (an off-white powder) as $\text{Ag}_2\text{B}_{12}\text{F}_{12}$. To demonstrate the integrity of the heat-treated product, it was re-dissolved in

temperature with formation of proposed $2\text{AgF} + \text{B}_8$ mixture (% $m = 44.6\%$ vs. 44.9% % $m(\text{theor.})$).

II. X-ray crystallography

The five crystal structures reported in this chapter are of good quality ($R_1 < 0.05$, $wR_2 < 0.10$, B–F esd's ≤ 0.003 Å). Relevant X-ray crystallographic parameters are listed in Table 4.1. The selected distances and angles are listed in Tables 4.2 and 4.3. Two of the four independent acetonitrile molecules in the structure of $\text{Ag}_2(\text{CH}_3\text{CN})_8\text{B}_{12}\text{F}_{12}$ were treated as positionally disordered with site occupancy ratios of 60:40.

A. Structure of $\text{Ag}_2(\text{CH}_3\text{CN})_8\text{B}_{12}\text{F}_{12}$. The B_{12} centroids form a distorted cube around two discrete, symmetry-related, pseudo-tetrahedral $\text{Ag}(\text{CH}_3\text{CN})_4^+$ cations, which exhibit a minor disorder in the positions of two of the CH_3CN ligands. The four Ag–N distances range from 2.225(3) to 2.442(6) Å (the C–N distances range from 1.132(9) to 1.141(9) Å) and the N–Ag–N angles range from $95.0(2)^\circ$ to $117.7(2)^\circ$ and average 109.2° . Discrete pseudotetrahedral $\text{Ag}(\text{CH}_3\text{CN})_4^+$ cations were previously observed with BF_4^- ,¹³³ ClO_4^- ,¹³⁴ $\text{Co}(\text{C}_2\text{B}_9\text{H}_{11})_2^-$,^{135,136} and other anions.¹³⁷ The closest $\text{Ag}\cdots\text{F}$ contact is 3.351(2) Å, longer than the ca. 3.2 Å sum of van der Waals radii for Ag and F atoms.⁶¹

The cation-anion packing is shown in Figure 4.3. The $\odot\cdots\odot$ distances are 9.17 Å ($\times 8$) and 10.19 Å ($\times 4$) and the $\odot\cdots\odot\cdots\odot$ angles are 78.9° , 88.8° , 91.2° , and 101.1° . The structure of $\text{Ag}_2(\text{CH}_3\text{CN})_8\text{B}_{12}\text{F}_{12}$ is very unusual with a pseudo-cubic array of anions surrounding *two* monocations. It is only the second example of a pseudo-cubic array of dianions with both monocations located inside the cube. The $\text{Ag}\cdots\text{Ag}$ distance inside the cube, at 4.084(1) Å, is much shorter than the shortest $\text{Ag}\cdots\odot$ distance, which is 6.345(4) Å. The other examples of this motif are the structures discussed in Chapter 3 ($\text{K}_2(\text{H}_2\text{O})_2\text{B}_{12}\text{F}_{12}$, $\text{K}_2(\text{H}_2\text{O})_4\text{B}_{12}\text{F}_{12}$, $\text{Rb}_2(\text{H}_2\text{O})_2\text{B}_{12}\text{F}_{12}$, $\text{K}_2(\text{HF})_3\text{B}_{12}\text{F}_{12}$, and $\text{K}_2(\text{H}_2\text{O})_{1.5}(\text{H}_2\text{O})_{0.5}\text{B}_{12}\text{F}_{12}$) and the structure of $[\text{Li}(\text{SO}_2)_4]_2\text{B}_{12}\text{Cl}_{12}$.¹³⁸

B. Structure of $\text{Ag}_2(\text{CH}_3\text{CN})_5\text{B}_{12}\text{F}_{12}$. The Ag^+ ions in the structure of $\text{Ag}_2(\text{CH}_3\text{CN})_5\text{B}_{12}\text{F}_{12}$ are coordinated to two terminal and one bridging acetonitrile molecules. The Ag^+ ion is co-planar with three nitrogen atoms (Ag–N distances are 2.139(1), 2.160(1), and 2.453(1) Å; N–Ag–N angles are 89.25(4), 110.84(4), and 158.73(5)°) and is also close to two fluorine atoms above and below the plane (Ag–F distances are 2.920(1) and 3.041(1) Å). The bond valence sum contributions from Ag–N and Ag–F contacts are 1.09 and 0.08, respectively. Therefore, the coordination sphere of Ag^+ ion can be considered as trigonal planar. There is one crystal structure reported in literature with isolated planar $[\text{Ag}(\text{CH}_3\text{CN})_3]^+$ fragment: $[\text{Ag}(\text{CH}_3\text{CN})_3][\text{V}_4(\text{C}_6\text{H}_5\text{PO}_3)_4]\text{F}$ (Ag–N distances 2.201(6), 2.218(6), and 2.226(6) Å, N–Ag–N angles 113.5(2), 116.2(2), and 129.6(2)°).¹³⁹

The $\text{B}_{12}\text{F}_{12}^{2-}$ anions form complex hexagon-like channels with $\odot\cdots\odot$ distances in the range 8.689–9.444 Å (4.4). The discrete $\text{Ag}_2(\text{CH}_3\text{CN})_5^{2+}$ cations are located inside this channels. The intracationic Ag \cdots Ag distances are 3.548(1) Å, the intercationic distances are 4.091(1) Å.

C. Structure of $\text{Ag}_2(\text{CH}_3\text{CN})_4\text{B}_{12}\text{F}_{12}$. The $\text{Ag}_2(\text{CH}_3\text{CN})_4\text{B}_{12}\text{F}_{12}$ crystal structure is formed by a distorted body-centered tetragonal array of $\text{B}_{12}\text{F}_{12}^{2-}$ anions with *pairs* of $\text{Ag}(\text{CH}_3\text{CN})_2^+$ cations occupying distorted tetrahedral holes (Figure 4.5). The $\odot\cdots\odot$ distances are in the range 8.895 Å–10.375 Å. The $\text{Ag}^+\cdots\text{Ag}^+$ distance within a pair of $\text{Ag}(\text{CH}_3\text{CN})_2^+$ cations is 3.1313(3) Å (Figure 4.6). The $\text{Ag}^+\cdots\text{Ag}^+$ interaction is essentially unsupported with only weak Ag \cdots F \cdots Ag bridging (Ag \cdots F distance is 2.797(1) Å) and it is longer than in the most crystal structures with proposed $\text{Ag}^+\cdots\text{Ag}^+$ bonding. For example, the shortest reported unsupported $\text{Ag}^+\cdots\text{Ag}^+$ distance is 2.820(6) Å which is shorter than in metallic silver¹⁴⁰. The $\text{Ag}(\text{CH}_3\text{CN})_2^+$ cation is essentially linear with N–Ag–N angle 172.44(7)° and Ag–N distance 2.101(2) Å. There are two other known crystal structures containing isolated $\text{Ag}(\text{CH}_3\text{CN})_2^+$ cation: $[\text{Ag}(\text{CH}_3\text{CN})_2]\text{BAr}_4^{\text{F}}$ (Ag–N distance 2.066(4) × 2 Å, N–Ag–N angle 180°, Ag–F distance 3.131(2) Å)¹⁴¹ and

[Ag(CH₃CN)₂][Co(C₂B₉H₁₁)₂] (Ag–N distances 2.144(4) and 2.155(5) Å, N–Ag–N angle 167.3(2)°, Ag–H 2.35(1)–2.56(1) Å).¹³⁵

The structure features the occupation of tetrahedral holes by *pairs* of discrete Ag(CH₃CN)₂⁺ cations. This type of packing is unprecedented for ionic lattices. Each Ag⁺ ion is close to two anions with Ag⁺⋯⊖ distance 5.029 Å. The Ag⁺⋯Ag⁺ centroid is located in the geometrical center of the octahedral hole and is equidistant from the four closest ⊖'s at 5.924 Å.

D. Structure of Ag₂(C₆H₅CH₃)₆B₁₂F₁₂. The Ag⁺ ion is η¹-coordinated to three toluene rings, as shown in Figure 4.7. The corresponding Ag–C distances and Ag–C–C angles are 2.428(3), 2.407(3), 2.513(3) Å and 92.9(2), 81.6(2), 91.3(2)°, respectively. The sum of C–Ag–C angles is 351.8(1)°. The midpoints of two of the C–C bonds coordinated to Ag⁺ and the C15 carbon atom form a nearly equilateral triangle with sides of 4.083, 4.176, and 4.449 Å and angles of 56.4, 58.4, and 65.2°. The Ag⁺ is displaced only 0.029 Å from the plane of this triangle. The closest Ag⁺⋯F contact is 2.989(2) Å which can be considered as non-bonding. The Ag⁺ thermal ellipsoid is elongated perpendicularly to the coordination plane suggesting a low-barrier equilibrium between η¹ and η² coordination modes.

The B₁₂F₁₂²⁻ anions in the crystal structure form slightly distorted close-packed layers with ⊖⋯⊖ distances 11.163 (× 2) Å and 11.381 (× 4) Å. Each layer is shifted 2.852 Å from idealized AAA layer stacking; the shortest ⊖⋯⊖ distance between the layers is 11.017 Å, as shown in Figure 4.8. Each Ag⁺ ion is close to two ⊖'s, with Ag⁺⋯⊖ distances of 5.787 and 6.998 Å.

E. Structure of Ag₂(CH₂Cl₂)₄B₁₂F₁₂. The crystal structure is formed by a distorted body-centered tetragonal array of B₁₂F₁₂²⁻ anions with ⊖⋯⊖ distances 8.956 Å×4 and 9.842 Å×4 (4.9). The *pairs* of Ag(CH₂Cl₂)₂⁺ cations are located in pairs of *adjacent* distorted tetrahedral holes of anions. The distortion of these tetrahedral holes in the structure leads to formation of the compressed octahedral hole from two tetrahedral

holes. Therefore, the *pairs* of the cations can be considered as occupying *one* octahedral hole. This is the unique example of the packing of such a type. Each cation is close to two anions with Ag \cdots O distances 4.766 and 5.234 Å. The Ag \cdots Ag distance within the octahedral hole is 6.327(1) Å.

The Ag⁺ coordination sphere consists of four Ag–Cl contacts (2.6586(4), 2.6912(4), 2.8340(4), and 2.8837(4) Å) and three Ag \cdots F contacts (2.6336(7), 2.6387(7), and 2.6794(7) Å). The contributions of the Ag–Cl and Ag \cdots F interactions to the bond valence sum for Ag⁺ are 0.66 and 0.30, respectively, with the total of 0.96. The angle between two nearly planar (maximum deviations from planarity are 0.003 Å and 0.262 Å) four-membered (–Ag–Cl–C–Cl–) rings is 35.9°.

There are several crystal structures of the silver salts of weakly coordinating anions ([Pd(OTeF₅)₄]²⁻,^{142,143} SbF₆⁻,¹⁴⁴ [Al(OCH(CF₃)₂)]⁻,¹⁴⁵ [Ti(OTeF₅)₆]⁻,¹⁴⁶ [Al(OC(CF₃)₃)₄]⁻,¹⁴⁷ [(F₃C)₃CO)₃AlFAl(OC(CF₃)₃)₃]⁻,¹⁴⁸ and [Al(OC(CF₃)₂(CH₃))₄]⁻¹⁴⁵) with dichloromethane molecules coordinated to Ag⁺. The range of Ag–Cl coordination distances in these structures varies from 2.613(2) to 2.882(3) Å. In some cases, both (Ag(CH₂Cl₂)₂[SbF₆])¹⁴⁴ or two out of three (Ag(CH₂Cl₂)₃[Ti(OTeF₅)₆])¹⁴⁶ dichloromethane molecules are coordinated to silver cation only through one chlorine atom.

III. Confirming the Superweak Nature of B₁₂F₁₂²⁻

One test of the coordinating ability of weakly-basic anions Y⁻ is whether salts such as AgY or Ag₂Y absorb CO at 1 atm or less to form Ag(CO)⁺ or Ag(CO)₂⁺ carbonyl species in the solid state.¹⁴⁹ Examples of Y⁻ anions that do allow silver(I) carbonyl cations to form are OTeF₅⁻, B(OTeF₅)₄⁻, Zn(OTeF₅)₄²⁻, Nb(OTeF₅)₆⁻, Ti(OTeF₅)₆²⁻,¹⁴⁹ and B(CF₃)₄⁻.¹⁵⁰ Note that a 2- charge does not preclude the formation of Ag(CO)_n⁺ cations. Silver(I) carbonyls are also formed in some silver(I)-exchanged zeolites,^{151,152} and some unusual silver(I) carbonyls with fluorinated pyrazolylborate ligands have also been isolated.¹⁵³ Significantly, AgClO₄ and AgSbF₆ do *not* absorb CO at 1 atm in the solid

state.¹⁴⁹ Therefore, despite the 2- charge, $B_{12}F_{12}^{2-}$ is more-weakly-coordinating than either ClO_4^- or SbF_6^- .

The solvent-free (and extremely hygroscopic) salt $Ag_2B_{12}F_{12}$ was treated with 500 Torr CO for several minutes. The gas was removed under vacuum, and an IR spectrum of a Nujol mull of the resulting compound was recorded. A single strong $\nu(CO)$ band was observed at 2198 cm^{-1} , with a weak $\nu(^{13}CO)$ band at 2152 cm^{-1} , as shown in Figure 4.10. This is assigned to $Ag(CO)^+$ moieties in $[Ag(CO)]_2B_{12}F_{12}$ based on similarities to $Ag(CO)Nb(OTeF_5)_6$ ($\nu(CO) = 2208\text{ cm}^{-1}$)¹⁴⁹ and $[Ag(CO)^+]ZSM-5$ ($\nu(CO) = 2192\text{ cm}^{-1}$)¹⁵⁴ both of which, like $[Ag(CO)]_2B_{12}F_{12}$, are stable under vacuum for extended periods of time at room temperature.

The solvent-free salt $Ag_2B_{12}F_{12}$ was also treated with 68 atm CO in a high-pressure IR cell of local design.⁶⁶ In this cell, a thick Nujol mull of the compound is sandwiched between two sapphire windows held 0.1 mm apart. High-pressure CO gas can slowly (hours) diffuse through the Nujol and react with the compound. In this way, a transmission IR spectrum of a metal carbonyl compound with $\nu(CO)$ bands near 2143 cm^{-1} (the value for CO gas) can be recorded while the sample is in equilibrium with high-pressure CO but without the IR beam passing through the CO gas. Spectra recorded at 4, 22, and 108 h are shown in Figure 4.10. At short times (e.g., 4 h) only the 2198 cm^{-1} band of $[Ag(CO)]_2B_{12}F_{12}$ was observed. At longer times it was replaced by a similar intensity band at 2190 cm^{-1} , which is assigned to $\nu_{\text{asym}}(CO)$ for $Ag(CO)_2^+$ moieties in $[Ag(CO)_2]_2B_{12}F_{12}$ (cf. $\nu_{\text{asym}}(CO) = 2198\text{ cm}^{-1}$ for $Ag(CO)_2Nb(OTeF_5)_6$ ¹⁴⁹ and $\nu_{\text{asym}}(CO) = 2186\text{ cm}^{-1}$ for $[Ag(CO)_2^+]ZSM-5$ ¹⁵⁴). It is not known at this time whether a pressure of CO gas lower than 68 atm would be sufficient to form the dicarbonyl salt $[Ag(CO)_2]_2B_{12}F_{12}$.

Metal carbonyl species with $\nu(CO)$ values above 2143 cm^{-1} are generally referred to as nonclassical metal carbonyls.¹⁵⁵ A common characteristic of these species is relatively little or negligible π backbonding from the metal ion to the CO ligand(s), resulting in M-

CO bonds that are essentially σ bonds, with CO acting as a Lewis base and the metal ion as a Lewis acid. Since CO is an extremely weak base,¹⁵⁶ superweak anions must be used as counterions to avoid displacing CO from the coordination sphere of the metal ion. The experimental results showed that $\text{Ag}(\text{CO})^+$ and $\text{Ag}(\text{CO})_2^+$ species can be formed in the salt $\text{Ag}_2\text{B}_{12}\text{F}_{12}$, therefore, it is proper to include the $\text{B}_{12}\text{F}_{12}^{2-}$ anion in the growing panoply of modern superweak anions.

Interestingly, the silver salt of another halogenated dodecaborate anion, $\text{Ag}_2\text{B}_{12}\text{Cl}_{12}$ does not form cationic silver carbonyls when exposed to 24 atm of CO in the high-pressure IR cell (Figure 4.11). Also, the solvent-free $\text{Ag}_2\text{B}_{12}\text{Cl}_{12}$ has a limited solubility in water and can be crystallized from aqueous solution.^{39,157} The crystal structure of $\text{Ag}_2\text{B}_{12}\text{Cl}_{12}$ contains the silver cation coordinated to six chlorine atoms with the bond valence sum 0.80.³⁹ In contrast, the solvent-free $\text{Ag}_2\text{B}_{12}\text{F}_{12}$ is extremely moisture-sensitive when briefly exposed to air. These facts suggest that Ag–Cl interactions are much stronger than Ag–F interactions in these salts, and the silver cation is coordinatively saturated in $\text{Ag}_2\text{B}_{12}\text{Cl}_{12}$. This is similar to the situation with AgF and AgCl. The silver fluoride is an ionic compound soluble in water while silver chloride is more covalent and exhibits strong silver–halogen interactions. Therefore, even though $\text{B}_{12}\text{Cl}_{12}^{2-}$ anion is generally accepted as a weakly coordinating,^{158,159} the cation–anion interactions in $\text{Ag}_2\text{B}_{12}\text{Cl}_{12}$ are strong enough to prevent nonclassical carbonyl formation.

Table 4.1. Crystallographic and Data-Collection Parameters of Ag₂(L)_{*n*}B₁₂F₁₂ salts

compound	Ag ₂ (CH ₃ CN) ₄ B ₁₂ F ₁₂	Ag ₂ (CH ₃ CN) ₅ B ₁₂ F ₁₂	Ag ₂ (CH ₃ CN) ₈ B ₁₂ F ₁₂
empirical formula	C ₈ H ₁₂ B ₁₂ F ₁₂ Ag ₂ N ₄	C ₁₀ H ₁₅ Ag ₂ B ₁₂ F ₁₂ N ₅	C ₁₆ H ₂₄ Ag ₂ B ₁₂ F ₁₂ N ₄
formula weight	737.68	778.73	901.90
habit, color	prism, colorless	prism, colorless	plate, colorless
crystal size, mm	0.07 × 0.07 × 0.30	0.17 × 0.20 × 0.37	0.13 × 0.18 × 0.20
space group	Cccm	C2/c	P2 ₁ /c
<i>a</i> (Å)	11.4426(7)	10.2588(5)	10.1859(5)
<i>b</i> (Å)	13.6213(7)	27.6109(13)	11.6479(7)
<i>c</i> (Å)	15.6534(8)	9.0019(4)	14.1573(7)
<i>α</i> (deg)	90	90	90
<i>β</i> (deg)	90	92.487(2)	91.609(3)
<i>γ</i> (deg)	90	104.958(2)	90
<i>V</i> (Å ³)	2439.8(2)	2547.4(2)	1679.02(15)
<i>Z</i>	4	4	2
<i>T</i> (K)	120(1)	120(1)	120(1)
<i>ρ</i> _{calc} (g cm ⁻³)	2.008	2.030	1.784
<i>R</i> (<i>F</i>) (<i>I</i> > 2σ(<i>I</i>)) ^a	0.0264	0.0249	0.0465
<i>wR</i> (<i>F</i> ²) [all data] ^a	0.0766	0.0662	0.1041
min., max. e ⁻ dens. (e Å ⁻³)	-1.06, 1.07	-0.66, 0.47	-1.06, 0.76

^a $R(F) = \Sigma||F_o| - |F_c|| / \Sigma|F_o|$; $wR(F^2) = (\Sigma[w(F_o^2 - F_c^2)^2] / \Sigma[w(F_o^2)^2])^{1/2}$

Table 4.1, continued.

compound	Ag ₂ (CH ₂ Cl ₂) ₄ B ₁₂ F ₁₂	Ag ₂ (C ₇ H ₈) ₃ B ₁₂ F ₁₂
empirical formula	C ₄ H ₈ Ag ₂ B ₁₂ Cl ₈ F ₁₂	C ₄₂ H ₄₈ Ag ₂ B ₁₂ F ₁₂
formula weight	913.16	1126.26
habit, color	needle, colorless	prism, colorless
crystal size, mm	0.10 × 0.12 × 0.32	0.09 × 0.09 × 0.20
space group	<i>P</i> 2 ₁ / <i>n</i>	<i>P</i> 2 ₁ / <i>c</i>
<i>a</i> (Å)	10.6082(4)	11.0173(6)
<i>b</i> (Å)	10.3304(4)	11.1634(6)
<i>c</i> (Å)	11.6143(5)	19.8355(9)
<i>α</i> (deg)	90	90
<i>β</i> (deg)	97.762(2)	105.492(2)
<i>γ</i> (deg)	90	90
<i>V</i> (Å ³)	1261.11(9)	2350.9(2)
<i>Z</i>	2	2
<i>T</i> (K)	120(1)	120(1)
ρ_{calc} (g cm ⁻³)	2.405	1.591
<i>R</i> (<i>F</i>) (<i>I</i> > 2σ(<i>I</i>)) ^a	0.0171	0.0414
<i>wR</i> (<i>F</i> ²) [all data] ^a	0.0441	0.1044
min., max. e ⁻ dens. (e Å ⁻³)	-0.85, 0.61	-2.01, 2.87

^a $R(F) = \Sigma||F_o| - |F_c|| / \Sigma|F_o|$; $wR(F^2) = (\Sigma[w(F_o^2 - F_c^2)^2] / \Sigma[w(F_o^2)^2])^{1/2}$

Table 4.2. Selected Interatomic Distances (Å) and Angles (deg) for $\text{Ag}_2(\text{CH}_3\text{CN})_n\text{B}_{12}\text{F}_{12}$

parameter	$\text{Ag}_2(\text{CH}_3\text{CN})_8\text{B}_{12}\text{F}_{12}$	$\text{Ag}_2(\text{CH}_3\text{CN})_5\text{B}_{12}\text{F}_{12}$	$\text{Ag}_2(\text{CH}_3\text{CN})_4\text{B}_{12}\text{F}_{12}$
M–F(B)	–	2.920(1), 3.041(1)	$2.797(1) \times 2$
M–N	2.225(3)–2.442(6)	2.139(1), 2.160(1), 2.453(1)	$2.101(2) \times 2$
N–M–N	95.0(2)–117.7(2)	89.25(4), 110.84(4), 158.73(5)	172.44(7)
$\Sigma(\text{Ag–F bond valences})$	0	0.09	0.14
$\Sigma(\text{Ag–O bond valences})$	1.08	1.09	1.01
$\Sigma(\text{all Ag bond valences})$	1.08	1.18	1.15
$\odot \cdots \odot$	9.172×2 , 10.193	8.689–9.444	8.895–10.375
$\text{Ag} \cdots \text{Ag}'$	4.084(1)	3.548(1), 4.091(1)	3.1313(3)
B–F	1.381(4)–1.388(4)	1.381(1)–1.386(1)	1.380(3)–1.387(3)
B–B	1.787(5)–1.800(5)	1.786(2)–1.800(2)	1.787(3)–1.792(3)

Table 4.3. Selected Interatomic Distances (Å) and Angles (deg) for $\text{Ag}_2(\text{L})_n\text{B}_{12}\text{F}_{12}$

parameter	$\text{Ag}_2(\text{C}_7\text{H}_8)_8\text{B}_{12}\text{F}_{12}$	$\text{Ag}_2(\text{CH}_2\text{Cl}_2)_2\text{B}_{12}\text{F}_{12}$
M–F(B)	2.989(2)	2.6336(7), 2.6387(7), 2.6794(7)
M–X	2.407(3)–2.653(3)	2.6586(4), 2.6912(4), 2.8340(4), 2.8837(4)
$\Sigma(\text{Ag–F bond valences})$	0.04	0.66
$\Sigma(\text{Ag–X bond valences})$	–	0.30
$\Sigma(\text{all Ag bond valences})$	–	0.96
$\odot \cdots \odot$	11.163×2 , 11.381×4 , 11.017×2	8.956×4 , 9.842×4
$\text{Ag} \cdots \text{Ag}'$	8.057(2)	6.327(1)
B–F	1.377(4)–1.387(4)	1.379(1)–1.383(1)
B–B	1.783(5)–1.801(5)	1.785(2)–1.803(2)

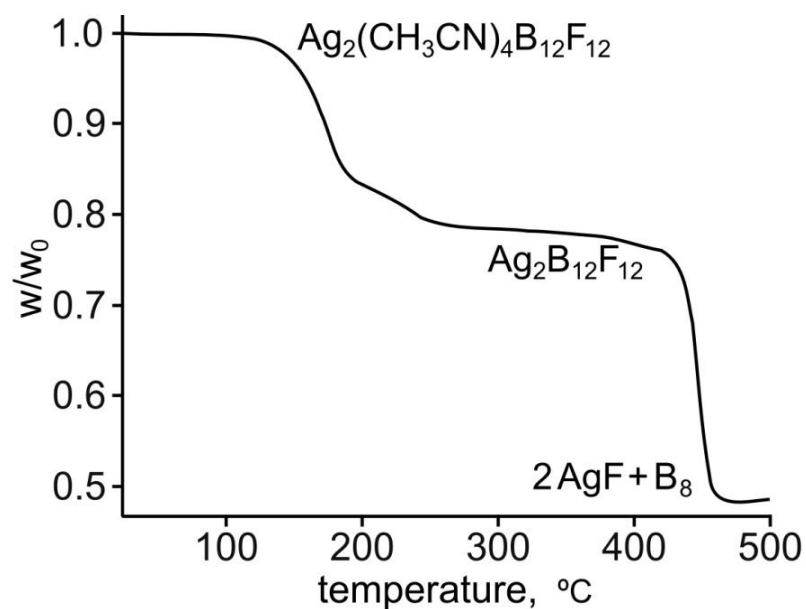


Figure 4.1. The thermogravimetric curve for $\text{Ag}_2(\text{CH}_3\text{CN})_4\text{B}_{12}\text{F}_{12}$. The heating rate was $3\text{ }^\circ\text{C min}^{-1}$.

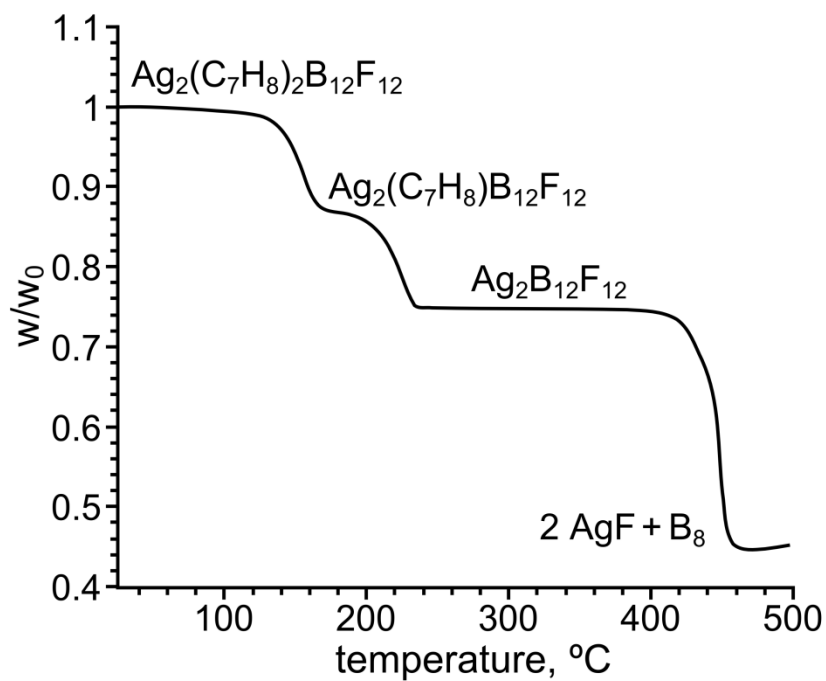


Figure 4.2. The thermogravimetric curve for $\text{Ag}_2(\text{C}_7\text{H}_8)_6\text{B}_{12}\text{F}_{12}$. The heating rate was $3\text{ }^\circ\text{C min}^{-1}$.

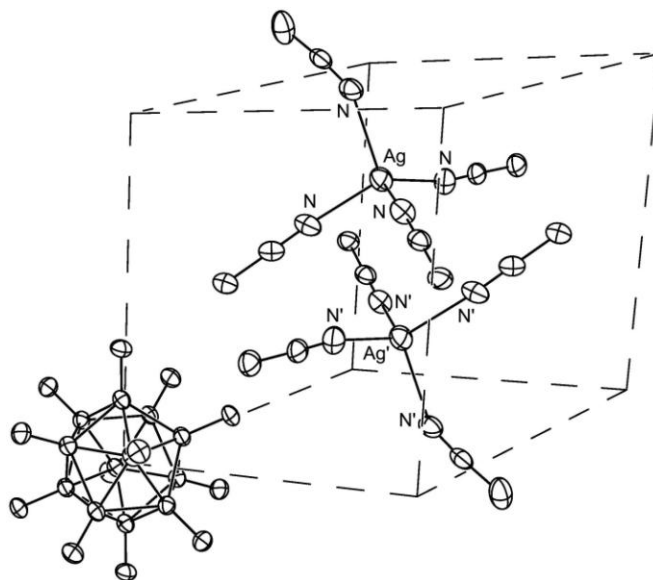


Figure 4.3. The packing of cations, anions, and acetonitrile molecules in the structure of $\text{Ag}_2(\text{CH}_3\text{CN})_8\text{B}_{12}\text{F}_{12}$ (50% probability ellipsoids). The $\odot \cdots \odot$ distances in the distorted cube are 9.172 \AA ($\times 8$) and 10.191 \AA ($\times 4$). The $\text{Ag}^+ \cdots \text{Ag}^+$ distance inside the cube is $4.084(1) \text{ \AA}$. Hydrogen atoms have been omitted for clarity.

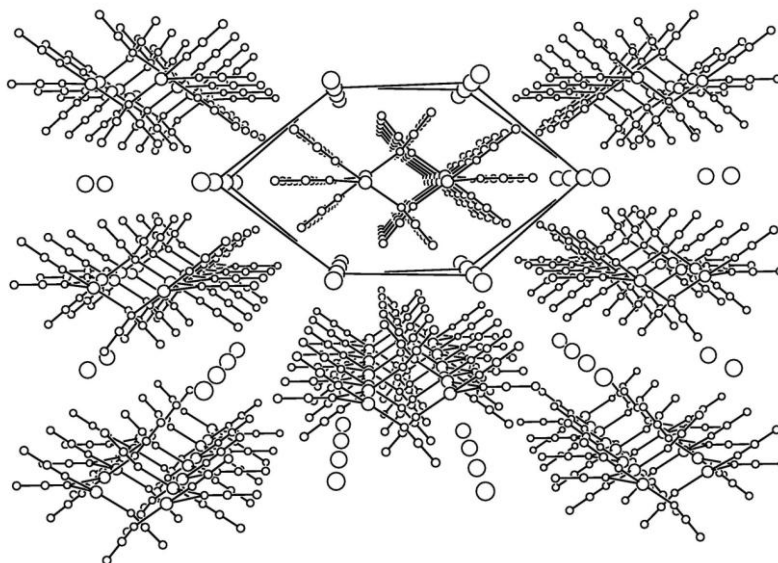


Figure 4.4. The packing of cations, anions, and acetonitrile molecules in the structure of $\text{Ag}_2(\text{CH}_3\text{CN})_5\text{B}_{12}\text{F}_{12}$. The B_{12} centroid are shown as large circles. Hydrogen atoms have been omitted for clarity.

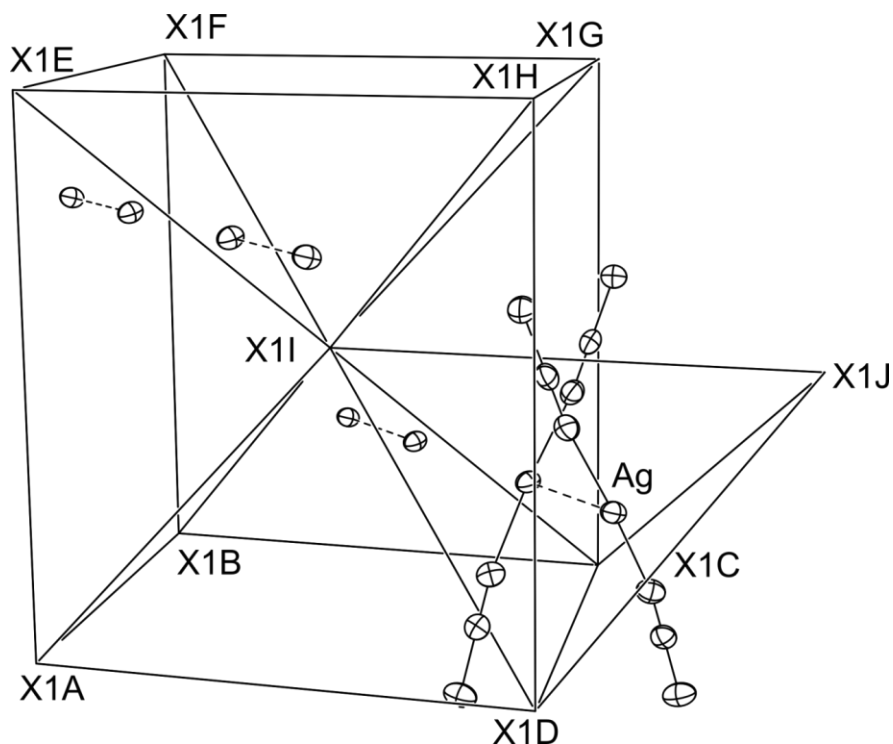


Figure 4.5. The packing of cations, anions, and acetonitrile molecules in the structure of $\text{Ag}_2(\text{CH}_3\text{CN})_4\text{B}_{12}\text{F}_{12}$ (50% probability ellipsoids). Hydrogen atoms have been omitted for clarity. The anions form a distorted tetragonal body-centered lattice. The independent $\ominus \cdots \ominus$ distances are 10.375 Å (X1A–X1B, X1A–X1D), 11.443 Å (X1A–X1E), 8.895 Å (X1A–X1I), and 9.695 Å (X1D–X1I). The Ag...Ag distance 3.1313(3) Å. The $[\text{Ag} \cdots \text{Ag}]^{2+}$ cation is located in a distorted tetrahedral hole; the Ag...Ag centroid is equidistant (5.924 Å) from X1D, X1C, X1J, and X1I.

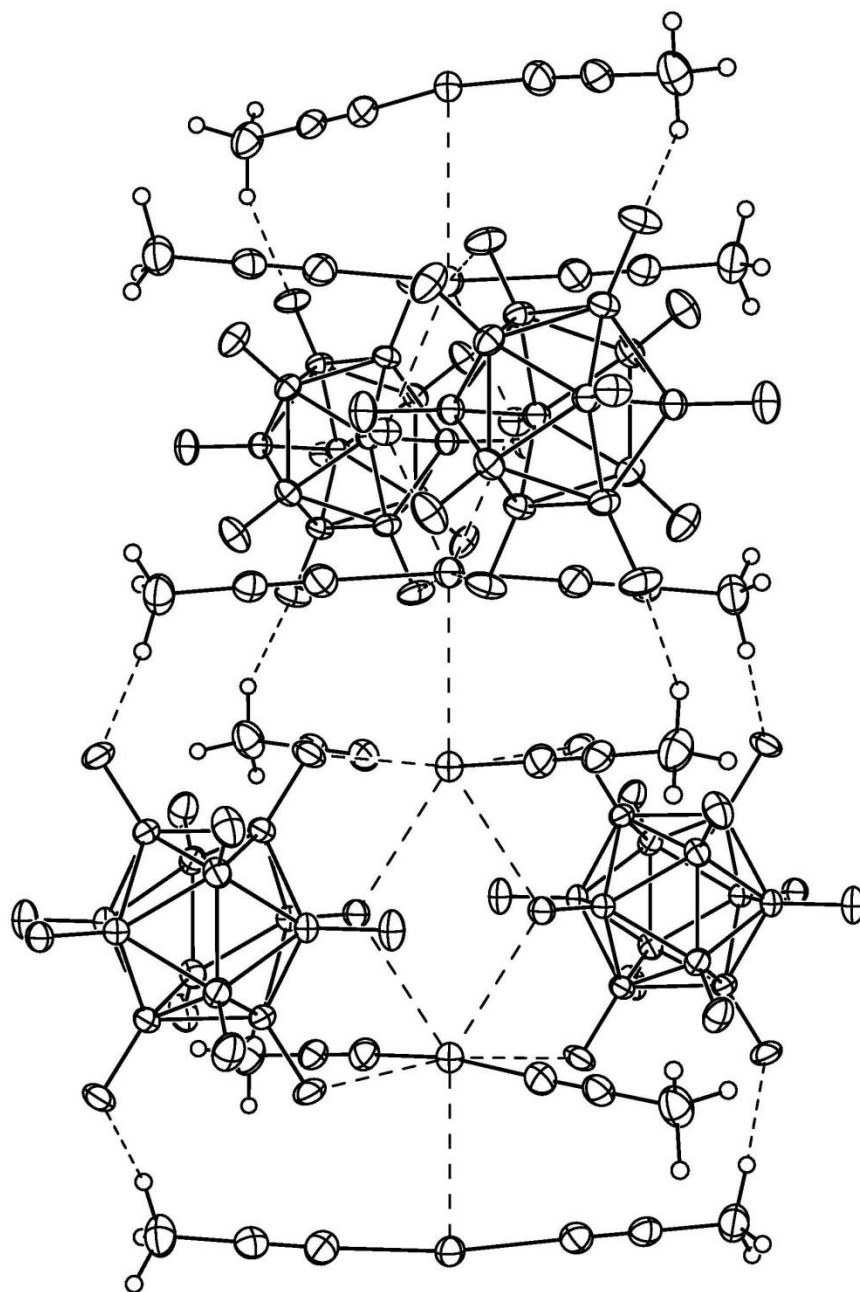


Figure 4.6. The crystal structure of $\text{Ag}_2(\text{CH}_3\text{CN})_4\text{B}_{12}\text{F}_{12}$ (50% probability ellipsoids). The Ag–N distance is $2.101(2) \times 2$ Å, the Ag \cdots F contacts are $2.797(1) \times 2$ Å and $2.992(1) \times 2$ Å. The $[\text{Ag}(\text{CH}_3\text{CN})_4]_2^+$ cations are aligned along Ag \cdots Ag vectors. The N–Ag–N angle is $172.44(7)^\circ$.

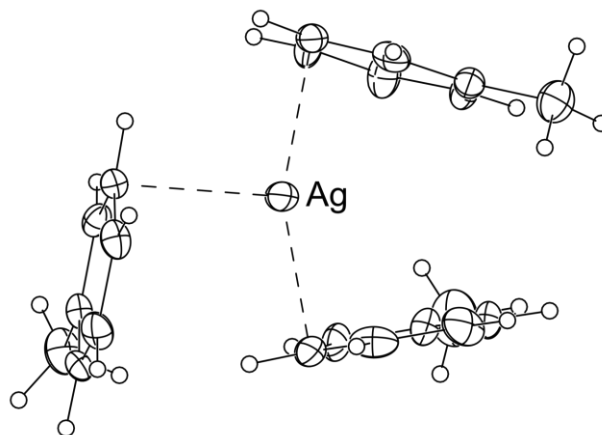


Figure 4.7. The coordination of silver cation in the structure of $[\text{Ag}(\text{C}_7\text{H}_8)_3]_2[\text{B}_{12}\text{F}_{12}]$. The Ag–C distances and Ag–C(C) angles are 2.428(3), 2.407(3), 2.513(3) Å, 92.9(2), 81.6(2), and 91.3(2)°, respectively.

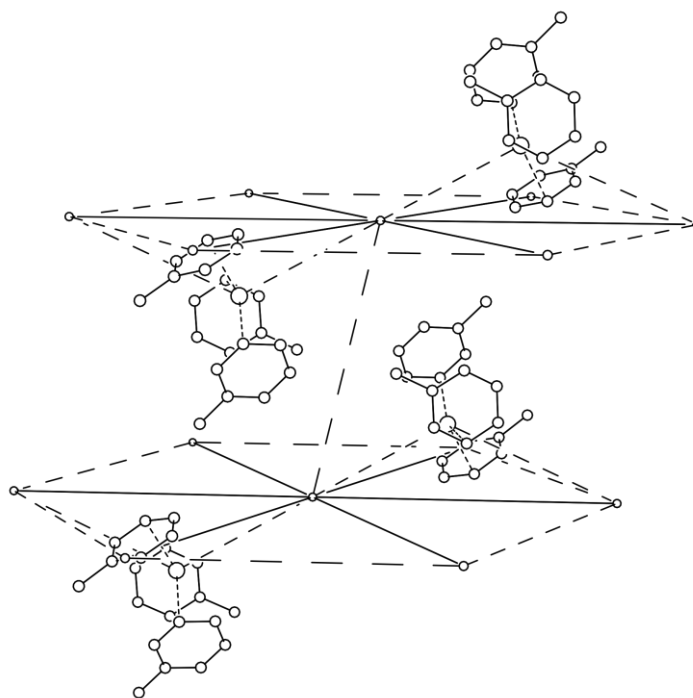


Figure 4.8. The packing of cations, anions, and toluene molecules in the structure of $[\text{Ag}(\text{C}_7\text{H}_8)_3]_2[\text{B}_{12}\text{F}_{12}]$. The B_{12} centroids are shown as small circles. The $\ominus \cdots \ominus$ distances in the distorted close-packed layers are $11.163 \text{ \AA} \times 2$ and $11.381 \text{ \AA} \times 4$. The closest interlayer $\ominus \cdots \ominus$ distance is 11.017 \AA . Hydrogen atoms have been omitted for clarity.

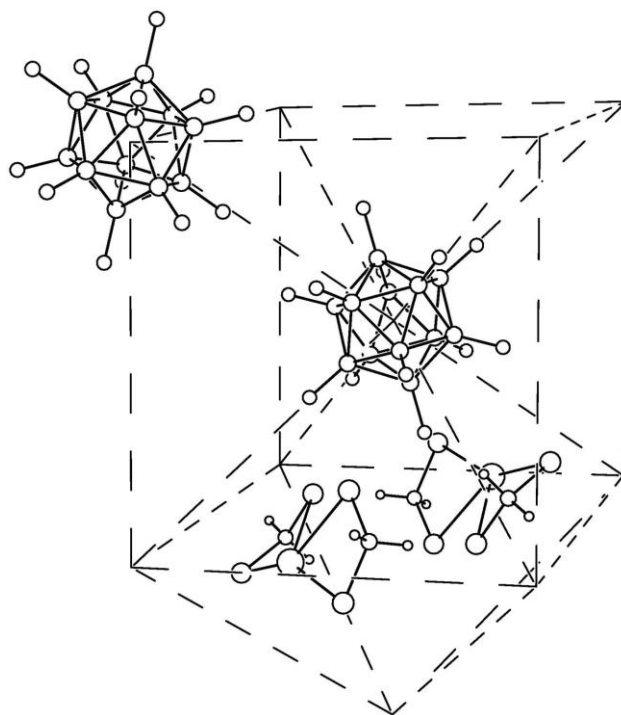


Figure 4.9. The packing of cations, anions, and dichloromethane molecules in the structure of $[\text{Ag}(\text{CH}_2\text{Cl}_2)_3]_2[\text{B}_{12}\text{F}_{12}]$. The B_{12} centroids are shown as small circles. The $\ominus \cdots \ominus$ distances $8.956 \text{ \AA} \times 4$ and $9.842 \text{ \AA} \times 4$. The $\text{Ag}-\text{Ag}$ distance within the octahedral hole is $6.327(1) \text{ \AA}$.

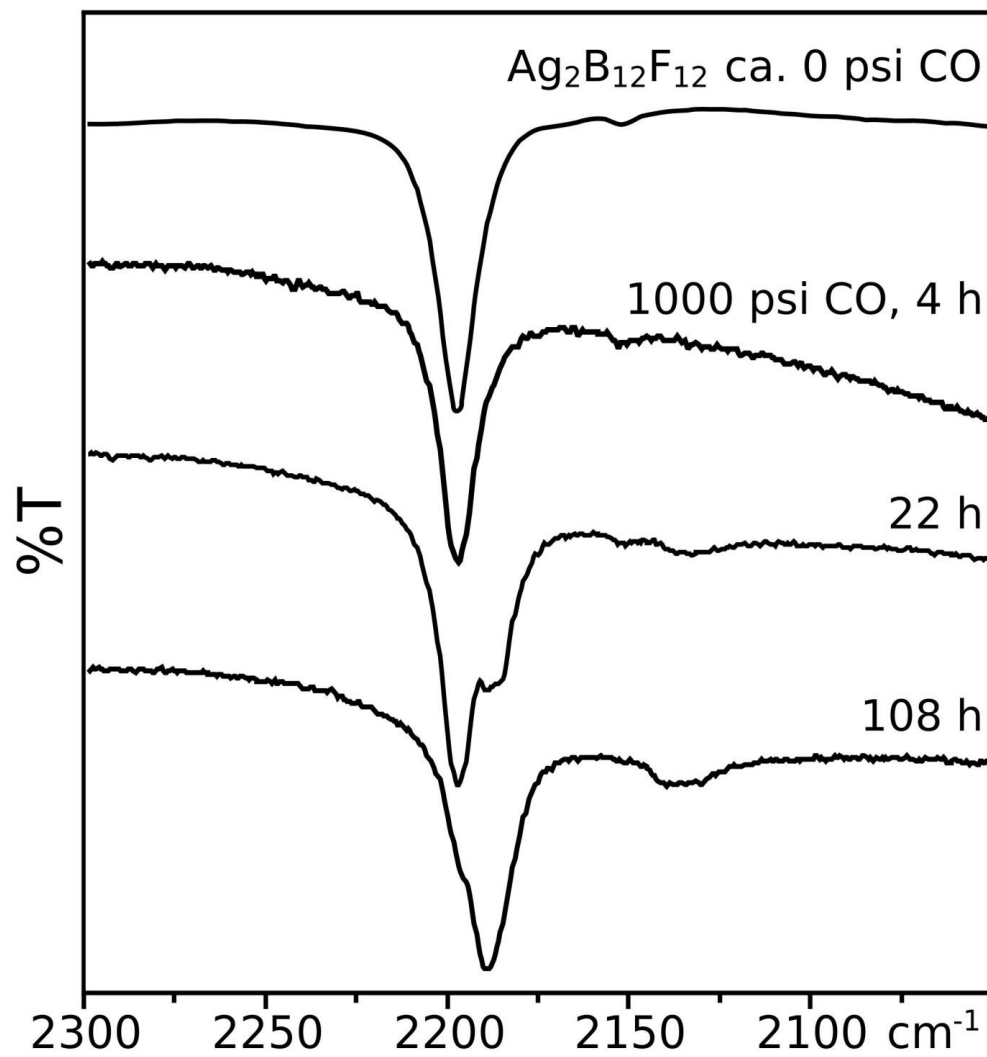


Figure 4.10. FTIR spectra of $\text{Ag}_2\text{B}_{12}\text{F}_{12}$ exposed to 1 atm CO and then evacuated for several minutes (top spectrum) and under 68 atm (1000 psi) CO over time.

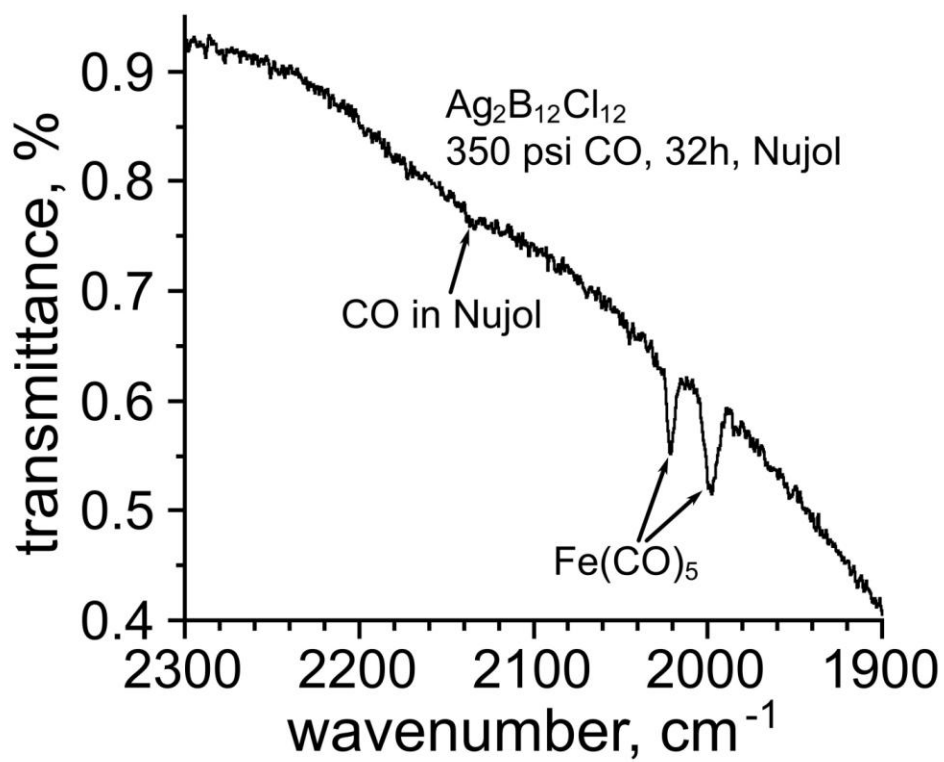


Figure 4.11. FTIR spectrum of $\text{Ag}_2\text{B}_{12}\text{Cl}_{12}$ exposed to 24 atm (350 psi) of CO for 32 h.

CHAPTER 5. DIVALENT METAL-ION SALTS OF $B_{12}F_{12}^{2-}$

Introduction

The successful removal of the coordinated solvent molecules from $Ag_2(L)_nB_{12}F_{12}$ salts (as well as from $K_2(H_2O)_{2,4}B_{12}F_{12}$) and the formation of the reactive solvent-free compound $Ag_2B_{12}F_{12}$ prompted the preparation and characterization of divalent metal-ion salts of $B_{12}F_{12}^{2-}$ with coordinated H_2O and CH_3CN molecules. The primary goal was to prepare and characterize by SC-XRD a number of compounds with a variety of M^{2+} ions to see if as wide a variety of structure types as were found for the M^+ salts discussed in Chapters 3 and 4 would be found for these compounds. A secondary goal was to begin to study their thermal desolvation/-decomposition by TGA. The following crystalline salts were chosen for SC-XRD characterization: $Mg(H_2O)_6B_{12}F_{12}$; $Ca(H_2O)_7B_{12}F_{12}$; $Ba(H_2O)_5B_{12}F_{12}$; $Ni(H_2O)_6B_{12}F_{12}$; $Co(H_2O)_6B_{12}F_{12}$; $Zn(H_2O)_2(CH_3CN)_4 \cdot H_2O$; $Ni(CH_3CN)_6B_{12}F_{12}$; $Co(CH_3CN)_6B_{12}F_{12}$; and $Pd(CH_3CN)_6B_{12}F_{12} \cdot 2CH_3CN$. Only $Ni(H_2O)_6B_{12}F_{12}$, $Co(H_2O)_6B_{12}F_{12}$, $Ni(CH_3CN)_6B_{12}F_{12}$, $Zn(H_2O)_2(CH_3CN)_4 \cdot H_2O$, and $Pd(CH_3CN)_6B_{12}F_{12} \cdot 2CH_3CN$ were studied by TGA in this work.

Experimental Section

I. Reagents and Solvents.

Acetonitrile (Fisher Scientific) was dried as described in Chapter 2. Distilled water was passed through a Barnstead Nanopure deionizer. The deionized distilled water had a resistivity of at least $18 M\Omega$ and will be referred to as dd- H_2O . Samples of $NiCl_2 \cdot 6H_2O$ (Aldrich), $CoCl_2 \cdot 6H_2O$ (Aldrich), and $ZnCl_2 \cdot 6H_2O$ (Aldrich) were dried by refluxing

each one with a large excess of SOCl_2 (Fisher Scientific) followed by drying under vacuum. The resulting anhydrous compounds NiCl_2 , CoCl_2 , and ZnCl_2 were stored in a purified-dinitrogen-filled glovebox. Anhydrous PdCl_2 (Alfa Aesar) was used as received. The compounds $\text{K}_2\text{B}_{12}\text{F}_{12}$ and $\text{Ag}_2(\text{CH}_3\text{CN})_4\text{B}_{12}\text{F}_{12}$ were prepared as described in Chapters 2 and 4, respectively. Single crystals of $\text{Mg}(\text{H}_2\text{O})_6\text{B}_{12}\text{F}_{12}$, $\text{Ca}(\text{H}_2\text{O})_7\text{B}_{12}\text{F}_{12}$, and $\text{Ba}(\text{H}_2\text{O})_5\text{B}_{12}\text{F}_{12}$ were prepared by either Mr. Matic Lozinšek or Mr. Travis C. Folsom, co-workers in the Strauss research group; only their X-ray structures, which were determined by the author, are reported in this dissertation.

II. Preparation and Crystallization of Divalent Metal-Ion Salts of $\text{B}_{12}\text{F}_{12}^{2-}$.

A. $\text{Ni}(\text{H}_2\text{O})_6\text{B}_{12}\text{F}_{12}$. A solution of $\text{Ag}_2(\text{CH}_3\text{CN})_4\text{B}_{12}\text{F}_{12}$ (200 mg; 0.271 mmol) in dry acetonitrile (5 mL) was added quickly to a solution of anhydrous NiCl_2 (35.1 mg; 0.271 mmol) in ddH₂O (5 mL) and vigorously stirred for 10 min. After removing the white precipitate of AgCl , the filtrate was allowed to slowly evaporate. Pale green crystals of $\text{Ni}(\text{H}_2\text{O})_6\text{B}_{12}\text{F}_{12}$ were formed and were characterized by TGA and SC-XRD.

B. $\text{Ni}(\text{CH}_3\text{CN})_6\text{B}_{12}\text{F}_{12}$. A solution of $\text{Ag}_2(\text{CH}_3\text{CN})_4\text{B}_{12}\text{F}_{12}$ (200 mg; 0.271 mmol) in dry acetonitrile (5 mL) was added quickly to a solution of anhydrous NiCl_2 (35.1 mg; 0.271 mmol) in dry acetonitrile (5 mL) and vigorously stirred for 60 min. After removing the white precipitate of AgCl , the filtrate was allowed to slowly evaporate. Pale green crystals of $\text{Ni}(\text{CH}_3\text{CN})_6\text{B}_{12}\text{F}_{12}$ were formed and were characterized by TGA and SC-XRD. Alternatively, $\text{Ni}(\text{CH}_3\text{CN})_6\text{B}_{12}\text{F}_{12}$ was prepared by repeated dissolution of $\text{Ni}(\text{H}_2\text{O})_6\text{B}_{12}\text{F}_{12}$ in anhydrous acetonitrile with following removal of the solvent under vacuum and recrystallization.

C. $\text{Co}(\text{H}_2\text{O})_6\text{B}_{12}\text{F}_{12}$. A solution of $\text{Ag}_2(\text{CH}_3\text{CN})_4\text{B}_{12}\text{F}_{12}$ (200 mg; 0.271 mmol) in dry acetonitrile (5 mL) was added quickly to a solution of anhydrous CoCl_2 (35.2 mg, 0.271 mmol) in ddH₂O (5 mL) and vigorously stirred for 10 min. After removing the white precipitate of AgCl , the filtrate was allowed to slowly evaporate. Pale pink crystals of $\text{Co}(\text{H}_2\text{O})_6\text{B}_{12}\text{F}_{12}$ were formed and were characterized by TGA and SC-XRD.

D. $\text{Co}(\text{CH}_3\text{CN})_6\text{B}_{12}\text{F}_{12}$. A solution of $\text{Ag}_2(\text{CH}_3\text{CN})_4\text{B}_{12}\text{F}_{12}$ (200 mg; 0.271 mmol) in dry acetonitrile (5 mL) was added quickly to a solution of anhydrous CoCl_2 (35.2 mg, 0.271 mmol) in dry acetonitrile (5 mL) and vigorously stirred for 10 min. After removing the white precipitate of AgCl , the filtrate was allowed to slowly evaporate. Pale pink crystals of $\text{Co}(\text{CH}_3\text{CN})_6\text{B}_{12}\text{F}_{12}$ were formed and were characterized by TGA and SC-XRD.

E. $\text{Pd}(\text{CH}_3\text{CN})_6\text{B}_{12}\text{F}_{12}\cdot 2\text{CH}_3\text{CN}$. A solution of $\text{Ag}_2(\text{CH}_3\text{CN})_4\text{B}_{12}\text{F}_{12}$ (225 mg; 0.339 mmol) in dry acetonitrile (10 mL) was added quickly to a solid of anhydrous PdCl_2 (35.2 mg, 0.271 mmol) and vigorously stirred for 24 h at 50 °C. The white precipitate of AgCl was removed. The pale yellow crystals of $\text{Pd}(\text{CH}_3\text{CN})_6\text{B}_{12}\text{F}_{12}\cdot 2\text{CH}_3\text{CN}$ were grown by slow diffusion of hexane vapor into the CH_3CN solution and were characterized by TGA and SC-XRD.

F. $\text{Zn}(\text{H}_2\text{O})_2(\text{CH}_3\text{CN})_4\text{B}_{12}\text{F}_{12}\cdot \text{H}_2\text{O}$. A solution of $\text{Ag}_2(\text{CH}_3\text{CN})_4\text{B}_{12}\text{F}_{12}$ (200 mg, 0.271 mmol) in dry acetonitrile (5 mL) was added quickly to a solution of anhydrous ZnCl_2 (19 mg, 0.139 mmol) in dd- H_2O (5 mL) and vigorously stirred for 10 min. After removing the white precipitate of AgCl , the filtrate was allowed to slowly evaporate. Colorless crystals of $\text{Zn}(\text{H}_2\text{O})_2(\text{CH}_3\text{CN})_4\text{B}_{12}\text{F}_{12}\cdot \text{H}_2\text{O}$ were formed and were characterized by TGA and SC-XRD.

III. Characterization.

A. Single-Crystal X-ray Diffraction. Unit cell parameters were obtained from least-squares fits to the angular coordinates of all reflections, and intensities were integrated from a series of frames (ω and ϕ rotation) covering more than a hemisphere of reciprocal space. Absorption and other corrections were applied using SADABS. The structures were solved using direct methods and refined (on F^2 , using all data) by a full-matrix, weighted least squares process. Standard Bruker control and integration software (APEX II) was employed, and Bruker SHELXTL software was used for structure solution, refinement, and molecular graphics. The diffraction data for the single crystal of

Zn(H₂O)₂(CH₃CN)₄B₁₂F₁₂·H₂O were collected at Advances Light Source, Lawrence National Lab, Berkeley ($\lambda = 0.41328 \text{ \AA}$).

The B₁₂ centroid–centroid ($\odot \cdots \odot$) distances are listed without the corresponding esd's. The individual esd's of the individual B–B bonds are in the range 0.001–0.005 \AA for the reported structures. The \odot position is derived from the positions of twelve boron atoms; therefore the esd's of the \odot coordinates are generally one order of magnitude smaller (i.e., 0.0001–0.0005 \AA).

B. Thermogravimetric Analysis. Samples for TGA were analyzed using a TA Instruments TGA-2950 instrument (platinum sample pans; ca. 10 mg sample size; 25–650 °C temperature range; heating rate 3 °C min⁻¹, He carrier gas).

Results and Discussion

I. Synthesis and Crystallization.

The divalent metal salts of B₁₂F₁₂²⁻ anion were prepared in metathesis reactions of metal chlorides and Ag₂(CH₃CN)₄B₁₂F₁₂, as shown in Equation 1. All reagents were used in stoichiometric amounts (i.e., a 1:1 mole ratio). Despite the fact that aqueous solutions of MCl₂ were used in the reactions, waters of hydration in the metal-chloride starting materials were removed to obtain materials with precisely known molar masses.



The silver salt Ag₂(CH₃CN)₄B₁₂F₁₂ was used as a solution in acetonitrile. The hydrated salts M(H₂O)_nB₁₂F₁₂ (with the exception of Zn(H₂O)₂(CH₃CN)₄B₁₂F₁₂·H₂O) were obtained when aqueous solutions of MCl₂ were used despite the presence of CH₃CN in the solvent mixture. For the homoleptic acetonitrile complexes, the metathesis reactions were performed using a-CH₃CN.

II. X-ray Crystallography.

A. General Comments. Crystallographic and data-collection parameters for the nine structures described in this chapter are listed in Table 5.1. All crystal structures were of good quality ($R_1 < 0.007$, $wR_2 < 0.200$, B–F esd's ≤ 0.003 Å). The selected distances and angles for the structures described in this Chapter are listed in Table 5.2.

B. Observed Structures. 1. CsCl-Type Structures. (a) $\text{Co}(\text{H}_2\text{O})_6\text{B}_{12}\text{F}_{12}$, $\text{Ni}(\text{H}_2\text{O})_6\text{B}_{12}\text{F}_{12}$, $\text{Mg}(\text{H}_2\text{O})_6\text{B}_{12}\text{F}_{12}$. These three compounds are isomorphous and all exhibit a CsCl-type structure, with eight \odot 's forming rhombs with equal sides (7.532, 7.510, and 7.536 Å for the cobalt, nickel, and magnesium structures, respectively), and with $\odot\cdots\odot\cdots\odot$ angles of $90 \pm 2^\circ$, as shown in Figure 5.1. The idealized octahedral $\text{M}(\text{H}_2\text{O})_6^{2+}$ cations are located in the centers of the rhombs and have S_6 symmetry, which requires two unique M–O distances (2.066(1) and 2.091(1) Å for the cobalt structure, 2.030(1) and 2.053(1) Å for the nickel structure, and 2.035(2) and 2.062(2) Å for the magnesium structure. These distances are consistent with the accepted six-coordinate radii of these divalent metal ions, 0.75 Å for Co^{2+} , 0.69 Å for Ni^{2+} , and 0.72 Å for Mg^{2+} .⁵⁴ There are no $\text{M}\cdots\text{F}$ contacts shorter than the sum of van der Waals radii. The H atoms of the H_2O molecules form typical O–H \cdots F hydrogen bonds with the anions.

(b) $\text{Ca}(\text{H}_2\text{O})_7\text{B}_{12}\text{F}_{12}$. This compound, which is also shown in Figure 5.1, is similar to the three described above except that the rhomb is much less symmetric and the Ca^{2+} ion, which is the center of the rhomb, has seven H_2O ligands instead of six. The six $\odot\cdots\odot$ distances range from 7.467 to 8.392 Å and the four acute $\odot\cdots\odot\cdots\odot$ angles range from 82.1 to 83.5°. The seven Ca–O distances range from 2.347(1) to 2.489(1) Å. As in the previous structures, the H atoms of the H_2O molecules form O–H \cdots F hydrogen bonds with the anions.

(c) $\text{Ba}(\text{H}_2\text{O})_5\text{B}_{12}\text{F}_{12}$. This barium structure is different for the four structures described above because the Ba^{2+} ion displaced ca. 60% of the distance from the center of the distorted cube towards one face of the cube, as shown in Figure 5.2. This allows the Ba^{2+} to make six $\text{Ba}\cdots\text{F}$ contacts with the four anions comprising that face of the cube. It

is possible that under a different set of crystallization conditions, the Ba^{2+} ion would have more than five coordinated H_2O molecules and the $\text{Ba}(\text{H}_2\text{O})_n^{2+}$ cation would be centered in a distorted cubic array. Note that the $\odot\cdots\odot\cdots\odot$ angles in the barium structure are all 90° . The five Ba–O distances range from 2.712(2) to 2.866(2) Å and six Ba \cdots F distances range from 2.794(1) to 3.268(1) Å.

2. NiAs-Type Structures. (a) $\text{Co}(\text{CH}_3\text{CN})_6\text{B}_{12}\text{F}_{12}$, $\text{Ni}(\text{CH}_3\text{CN})_6\text{B}_{12}\text{F}_{12}$, and $\text{Zn}(\text{CH}_3\text{CN})_4(\text{H}_2\text{O})_2\text{B}_{12}\text{F}_{12}\cdot\text{H}_2\text{O}$. These three structures are formed by a distorted hexagonal close-packed lattice of anions and cations in octahedral holes (Figures 5.4–5.6). In the structure of $\text{Co}(\text{CH}_3\text{CN})_6\text{B}_{12}\text{F}_{12}$ the $\odot\cdots\odot$ distances are in the range from 8.980 Å to 11.008 Å. The distorted octahedral (six Co–N distances are in the range from 2.095(5) to 2.128(5) Å) $[\text{Co}(\text{CH}_3\text{CN})_6]^{2+}$ cation occupy the distorted octahedral holes in the lattice of the anions (Co \cdots B₁₂ centroid distances are 6.555–7.793 Å).

The $\odot\cdots\odot$ distances in the $\text{Ni}(\text{CH}_3\text{CN})_6\text{B}_{12}\text{F}_{12}$ structure are 8.953–11.026 Å. The Ni \cdots B₁₂ centroid distances in the distorted octahedral holes are 6.795–7.705 Å. Six Ni–N distances are in the range from 2.043(2) to 2.101(3) Å.

The $\odot\cdots\odot$ distances in the $\text{Zn}(\text{H}_2\text{O})_2(\text{CH}_3\text{CN})_4\text{B}_{12}\text{F}_{12}\cdot 2\text{H}_2\text{O}$ structure are 8.569 Å–11.791 Å. The Zn $\cdots\odot$ distances are 6.543–7.542 Å. The cation is octahedral with water molecules in *trans* positions. The Zn–O distances are 2.097(1) Å \times 2 and Zn–N distances are 2.080(1) Å \times 2 and 2.168(2) Å \times 2. The uncoordinated water molecules are located in the D_{3h} holes of the $\text{B}_{12}\text{F}_{12}^{2-}$ lattice and are hydrogen bonded to water molecules of the cation and fluorine atoms of the anions.

3. $\text{Pd}(\text{CH}_3\text{CN})_4\text{B}_{12}\text{F}_{12}\cdot 2\text{CH}_3\text{CN}$. The structure of this compound is formed by slightly distorted rigorously-planar close-packed-like array of $\text{B}_{12}\text{F}_{12}^{2-}$ anions, as shown in Figure 5.7. The anionic layers are stacked in the distorted AAA sequence and shifted 0.854 Å from the idealized positions along the $\odot\cdots\odot$ vector within the layer. The \odot 's form trigonal prismatic holes. The $\text{Pd}(\text{CH}_3\text{CN})_4^{2+}$ cations and uncoordinated CH_3CN molecules occupy faces of these holes. The Pd^{2+} is co-planar with four \odot 's. The PdN_4

coordination geometry is square-planar (the Pd–N distances are 1.960(2) ($\times 2$) Å and 1.964(2) ($\times 2$) Å). The shortest Pd \cdots F contact is 3.745(2) Å and is not considered to be a bonding interaction.

III. Thermogravimetric Analysis.

The stabilities of the hexacoordinate complexes of the nickel(II) were studied by thermal analysis with a heating rate of 3 °C/min. In the case of Ni(H₂O)₆B₁₂F₁₂, four out of the six H₂O molecules were removed upon heating up to 300 °C, as shown in Figure 5.8. The loss of water molecules occurred in two stages: three water molecules were removed during the heating up to 260 °C and the removal of the fourth molecule was complete at 300 °C. The yellow compound formulated as Ni(H₂O)₂B₁₂F₁₂ was stable up to 370 °C after which temperature the decomposition associated with large weight loss occurred. In case of Ni(CH₃CN)₆B₁₂F₁₂, the loss of four acetonitrile molecules occurred in three successive stages: at 140 °C the first molecule was removed, at 220 °C two more solvent molecules were lost, and at 280 °C the removal of the fourth molecule was complete, as shown in Figure 5.9. The resulting Ni(CH₃CN)₂B₁₂F₁₂ compound was stable up to 380 °C after which temperature the decomposition occurred. The integrity of Ni(H₂O)₂B₁₂F₁₂ and Ni(CH₃CN)₂B₁₂F₁₂ samples was confirmed by re-dissolution in CD₃CN (samples completely dissolved) and ¹⁹F{¹¹B} NMR. It is important to note, however, that the thermal stability of Ni(CH₃CN)₆B₁₂F₁₂ is much higher than corresponding salts of other superweak anions. For example, the thermal decomposition of Ni(CH₃CN)₆[B(C₆H₃(CF₃)₂)₄]₂ occurs at 150 °C when the loss of the solvent is accompanied with the fluoride abstraction from the anion. At this temperature, the Ni(CH₃CN)₅B₁₂F₁₂ compound is stable. The thermal stability of Co(H₂O)₆B₁₂F₁₂ compound is similar to that of Ni(H₂O)₆B₁₂F₁₂. The loss of three water molecules is complete at 240 °C and the fourth molecule is removed at 260 °C, as shown in Figure 5.10. The Co(H₂O)₂B₁₂F₁₂ compound is stable up to 340 °C; above this temperature the

weight loss corresponding to two water molecules occurs followed by rapid decomposition. It is unclear at the moment if the last two water molecules can be removed without anion decomposition. The prolonged heating of the sample at 380 °C led to the formation of a solid that was insoluble in CD₃CN, presumably due to decomposition.

The TGA trace for a sample of Pd(CH₃CN)₄B₁₂F₁₂·2CH₃CN is shown in Figure 5.11. The loss of the uncoordinated acetonitrile molecules started at room temperature and finished at 50 °C. The weight loss corresponding to four acetonitrile molecules started at 170 °C and ended at 310 °C, followed by slower weight loss presumably due to decomposition. The TGA data suggested that the compound can be thermally desolvated. To test this hypothesis, a sample of the Pd(CH₃CN)₄B₁₂F₁₂·2CH₃CN was heated under vacuum at 200 °C for 3 h. The black product that formed was insoluble in acetonitrile, indicating that the sample had decomposed. Therefore, it was concluded that solvent loss and decomposition of the compound occurred simultaneously.

The weight loss of the Zn(H₂O)₂(CH₃CN)₄B₁₂F₁₂·H₂O upon heating was found to be consistent with the initial composition Zn(H₂O)₂(CH₃CN)₄B₁₂F₁₂ and the loss of one acetonitrile molecule at 60 °C, the loss of the second acetonitrile molecule at 180 °C, and the loss of one water molecule at 330 °C, as shown in Figure 5.12. The significant weight loss indicating the decomposition occurs at 400 °C.

There is one potential problem associated with the deligation of the salts salt of a superweak anion with M²⁺ cation. The coordinative unsaturation of the M²⁺ in the solvent-free salts may be too great and the electrophilic cation may abstract the F atoms, in the form of F⁻ ions, from the WCA (even from the highly stable B₁₂F₁₂²⁻ anion) at high temperatures. This may be further exaggerated by the higher temperatures required for successive ligand removal compared to the M₂(L)_nB₁₂F₁₂ salts for the exactly same reason – the M²⁺ transition metal cation is generally smaller (compare ionic radii of Ni²⁺ (0.69 Å, CN 6), Co²⁺ (0.75 Å, CN 6 high spin), and Pd²⁺ (0.64 Å, CN 4) to Ag⁺ (1.0 Å,

CN 4)) and possesses higher positive charge and, therefore, binds stronger to a few remaining ligands. This high reactivity of the “naked” M^{2+} may prevent the successful desolvation of the WCA containing salts and lead to decomposition. It is significant that there is no report in the literature of the complete desolvation/deligation of divalent transition metal salts of the superweak anions BF_4^- , AsF_6^- , SbF_6^- , $Sb_2F_{11}^-$, PF_6^- , and $B(3,5-C_6H_3(CF_3)_2)_4^-$. A summary of literature reports pertaining to the decomposition temperatures and decomposition products transition metals salts of these anions is presented in Table 5.3.

Table 5.1. Crystallographic and Data-Collection Parameters of $M(L)_nB_{12}F_{12}$ Salts

compound	Ni(H ₂ O) ₆ B ₁₂ F ₁₂	Co(H ₂ O) ₆ B ₁₂ F ₁₂	Ni(CH ₃ CN) ₆ B ₁₂ F ₁₂	Co(CH ₃ CN) ₆ B ₁₂ F ₁₂
empirical formula	B ₁₂ F ₁₂ H ₁₂ NiO ₆	B ₁₂ CoF ₁₂ H ₁₂ O ₆	C ₁₂ H ₁₈ B ₁₂ F ₁₂ N ₆ Ni	C ₁₂ H ₁₈ B ₁₂ CoF ₁₂ N ₆
formula weight	524.51	524.75	662.73	662.97
habit, color	prism, green	prism, pink	plate, blue	prism, pink
crystal size, mm	0.22 × 0.40 × 0.63	0.25 × 0.25 × 0.59	0.04 × 0.08 × 0.32	0.12 × 0.20 × 0.39
space group	$R\bar{3}$	$R\bar{3}$	$P2_1/c$	$Pca2_1$
<i>a</i> (Å)	10.4301(5)	10.4562(3)	9.0933(4)	17.8277(5)
<i>b</i> (Å)	10.4301(5)	10.4562(3)	18.7372(9)	9.1481(3)
<i>c</i> (Å)	26.9302(5)	27.0213(15)	16.3912(8)	16.5633(4)
<i>α</i> (deg)	90	90	90	90
<i>β</i> (deg)	90	90	94.549(2)	90
<i>γ</i> (deg)	120	120	90	90
<i>V</i> (Å ³)	2537.3(2)	2558.5(1)	2784.0(2)	2701.3(1)
<i>Z</i>	6	6	4	4
<i>T</i> (K)	120(1)	120(1)	120(1)	120(2)
ρ_{calc} (g cm ⁻³)	2.060	2.043	1.581	1.630
$R(F)$ ($I > 2\sigma(I)$) ^a	0.0209	0.0186	0.0368	0.0706
$wR(F^2)$ [all data] ^a	0.0560	0.0527	0.0949	0.2003
min., max. e ⁻ dens., (e Å ⁻³)	-0.32, 0.63	-0.28, 0.51	-0.38, 0.51	-0.80, 1.52

Table 5.1, continued

compound	Pd(CH ₃ CN) ₄ B ₁₂ F ₁₂ ·2CH ₃ CN	Zn(H ₂ O) ₂ (CH ₃ CN) ₄ B ₁₂ F ₁₂ ·H ₂ O	Mg(H ₂ O) ₆ B ₁₂ F ₁₂
empirical formula	C ₁₆ H ₂₄ B ₁₂ F ₁₂ N ₈ Pd	C ₈ H ₁₈ B ₁₂ F ₁₂ N ₄ O ₃ Zn	B ₁₂ F ₁₂ H ₁₂ MgO ₆
formula weight	710.44	641.37	490.13
habit, color	prism, yellow	plate, colorless	cube, colorless
crystal size, mm	0.09 × 0.13 × 0.21	0.02 × 0.03 × 0.07	0.19 × 0.25 × 0.32
space group	<i>P</i> 2 ₁ / <i>c</i>	<i>P</i> 2 ₁ / <i>m</i>	<i>R</i> $\bar{3}$
<i>a</i> (Å)	10.4485(3)	8.5693(3)	10.5017(7)
<i>b</i> (Å)	16.1838(4)	16.3691(6)	10.5017(7)
<i>c</i> (Å)	8.3846(3)	9.4859(4)	26.8548(19)
α (deg)	90	90	90
β (deg)	100.494(1)	105.329(1)	90
γ (deg)	90	90	120
<i>V</i> (Å ³)	1394.09(7)	1283.27(8)	2564.9(2)
<i>Z</i>	2	2	6
<i>T</i> (K)	120(2)	95(1)	130(1)
ρ_{calc} (g cm ⁻³)	1.692	1.660	1.904
<i>R</i> (<i>F</i>) (<i>I</i> > 2 σ (<i>I</i>)) ^a	0.0315	0.0286	0.0315
<i>wR</i> (<i>F</i> ²) [all data] ^a	0.0855	0.1063	0.1208
min., max. e ⁻ dens., (e Å ⁻³)	-0.49, 1.06	-0.37, 0.91	-0.51, 0.37

Table 5.1, continued

compound	Ca(H ₂ O) ₇ B ₁₂ F ₁₂	Ba(H ₂ O) ₅ B ₁₂ F ₁₂
empirical formula	B ₁₂ CaF ₁₂ H ₁₄ O ₇	B ₁₂ BaF ₁₂ H ₁₀ O ₅
formula weight	523.91	585.13
habit, color	prism, colorless	prism, colorless
crystal size, mm	0.14 × 0.34 × 0.36	0.11 × 0.28 × 0.29
space group	<i>P</i> 2 ₁ / <i>c</i>	<i>P</i> 2 ₁ / <i>c</i>
<i>a</i> (Å)	8.3922(11)	7.7197(2)
<i>b</i> (Å)	11.2270(13)	13.8865(4)
<i>c</i> (Å)	19.812(3)	15.0598(5)
<i>α</i> (deg)	90	90
<i>β</i> (deg)	90.101(4)	90
<i>γ</i> (deg)	90	90
<i>V</i> (Å ³)	1866.7(4)	1614.41(8)
<i>Z</i>	4	4
<i>T</i> (K)	130(1)	130(1)
ρ_{calc} (g cm ⁻³)	1.864	2.407
<i>R</i> (<i>F</i>) (<i>I</i> > 2σ(<i>I</i>)) ^a	0.0283	0.0189
<i>wR</i> (<i>F</i> ²) [all data] ^a	0.0772	0.0414
min., max. e ⁻ dens., (e Å ⁻³)	-0.28, 0.30	-0.52, 0.43

Table 5.2. Selected interatomic distances (Å) and angles (deg)

parameter	Ni(H ₂ O)B ₁₂ F ₁₂	Co(H ₂ O) ₆ B ₁₂ F ₁₂	Mg(H ₂ O) ₆ B ₁₂ F ₁₂	Ca(H ₂ O) ₇ B ₁₂ F ₁₂	Ba(H ₂ O) ₅ B ₁₂ F ₁₂
M–F(B)	–	–	–	–	2.794(1)–3.268(1)
M–O	2.030(1) × 3 2.053(1) × 3	2.066(1) × 3, 2.091(1) × 3	2.035(2) × 3, 2.062(2) × 3	2.347(1)–2.489(1)	2.712(2)–2.866(2)
(H)O···F	2.732(1)–2.910(1)	2.740(1)–3.009(1)	2.724(2)–3.006(2)	2.839(1)–3.095(1)	2.807(2)–3.035(2)
O–H···F	161(2)–173(2)	153(2)–172(2)	123(3)–169(3)	121(2)–178(2)	132(2)–163(3)
(H)O···O	–	–	–	–	2.938(2), 3.074(2)
O–H···O	–	–	–	–	154(2), 164(2)
Σ(M–F bond valences)	0	0	0	0	0.60
Σ(M–O bond valences)	2.11	2.11	2.30	2.23	1.29
Σ(all M bond valences)	2.11	2.11	2.30	2.23	1.89
⊙···⊙	7.510 × 6	7.532 × 6	7.536 × 6	7.590 × 2, 7.623 × 2, 8.392 × 2	6.943 × 2, 7.530 × 2, 7.720 × 2
⊙···⊙···⊙	87.9, 90, 92.1	87.9 × 2, 92.1	88.3 × 3	82.1, 82.3, 83.5	90 × 3
B–F	1.380(1)–1.383(1)	1.379(1)–1.384(1)	1.383(3)–1.389(3)	1.373(2)–1.389(2)	1.374(3)–1.390(3)
B–B	1.791(1)–1.800(1)	1.791(1)–1.801(1)	1.785(4)–1.800(4)	1.783(2)–1.798(2)	1.773(3)–1.812(3)

Table 5.2, continued

parameter	Ni(CH ₃ CN) ₆ B ₁₂ F ₁₂	Co(CH ₃ CN) ₆ B ₁₂ F ₁₂	Zn(H ₂ O) ₂ (CH ₃ CN) ₄ B ₁₂ F ₁₂ ·2H ₂ O	Pd(CH ₃ CN) ₄ B ₁₂ F ₁₂ ·2CH ₃ CN
M–F(B)	–	–	–	–
M–N	2.043(2)–2.101(3)	2.095(5)–2.127(5)	2.080(1) × 2 2.168(2) × 2	1.960(2) Å × 2, 1.964(2) Å × 2
M–O	–	–	2.097(1) × 2	–
(H)O···F	–	–	2.767(2)–3.136(1)	–
O–H···F	–	–	140(6)–175(2)	–
(H)O···O	–	–	2.785(2)	–
O–H···O	–	–	168(2)	–
Σ(M–N bond valences)	2.11	1.70	1.35	2.67
Σ(M–O bond valences)	–	–	0.69	–
Σ(all M bond valences)	2.23	1.70	2.04	2.67
⊙···⊙	8.953–11.222	8.980–11.008	8.569–11.791	8.385–10.412
⊙···⊙···⊙	66.7–86.6	53.3–78.5	82.1, 82.3, 83.5	54.8–85.2
B–F	1.373(1)–1.389(1)	1.370(1)–1.403(1)	1.374(3)–1.391(3)	1.378(3)–1.386(3)
B–B	1.778(1)–1.797(1)	1.723(1)–1.824(1)	1.778(3)–1.798(3)	1.784(4)–1.796(4)

Table 5.3. Decomposition Temperatures and Products of the Transition metal Salts of Weakly Coordinated Anions Reported in Literature

Formula	T _{dec} , °C	Products	Reference
Fe(CO) ₆ (BF ₄) ₂	90	FeF ₂ + BF ₃ + CO	160
Ru(CO) ₆ (BF ₄) ₂	195	Unknown + CO + BF ₃	160
Os(CO) ₆ (BF ₄) ₂	300	Unknown + CO + BF ₃	160
Fe(CO) ₆ (AsF ₆) ₂	25	Unknown	160
Fe(CO) ₆ (SbF ₆) ₂	180	Fe(SbF ₆) ₂ + CO	161
	350	FeF ₂ + unknown	
Ru(CO) ₆ (SbF ₆) ₂	280	unknown	161
Os(CO) ₆ (SbF ₆) ₂	350	unknown	
Pd(CO) ₄ (Sb ₂ F ₁₁) ₂	140	unknown	162
Pt(CO) ₄ (Sb ₂ F ₁₁) ₂	200	Pt + SbF ₅ + COF ₂ + CO	162
Cd(H ₂ O) ₆ (BF ₄) ₂	51	Cd(H ₂ O) ₄ (BF ₄) ₂ + H ₂ O	163
	152	CdF ₂ + BF ₃ + HF + H ₂ O	
NH ₄ BF ₄	~270	NH ₃ + BF ₃ + HF	164
LiPF ₆ + H ₂ O(traces)	55–75	LiF + POF ₃ + HF	130
LiPF ₆	190–220	LiF + PF ₅	165
Zn(H ₂ O) ₆ (BF ₄) ₂	140	Zn(H ₂ O) ₄ (BF ₄) ₂ + H ₂ O	166
	220	ZnF ₂ + BF ₃ + H ₂ O	
Ag[B(C ₆ H ₃ (CF ₃) ₂) ₄]	120	AgF + unknown	131
[Ni(CH ₃ CN) ₆][B(C ₆ H ₃ (CF ₃) ₂) ₄] ₂	~150	NiF ₂ + unknown	131
[Co(CH ₃ CN) ₆][B(C ₆ H ₃ (CF ₃) ₂) ₄] ₂	~145	unknown	131
[Fe(CH ₃ CN) ₆][B(C ₆ H ₃ (CF ₃) ₂) ₄] ₂	~145	unknown	131
[Mn(CH ₃ CN) ₆][B(C ₆ H ₃ (CF ₃) ₂) ₄] ₂	~140	Unknown	131
[Cr(CH ₃ CN) ₆][B(C ₆ H ₃ (CF ₃) ₂) ₄] ₂	~130	Unknown	131
[V(CH ₃ CN) ₆][B(C ₆ H ₃ (CF ₃) ₂) ₄] ₂	~145	unknown	131

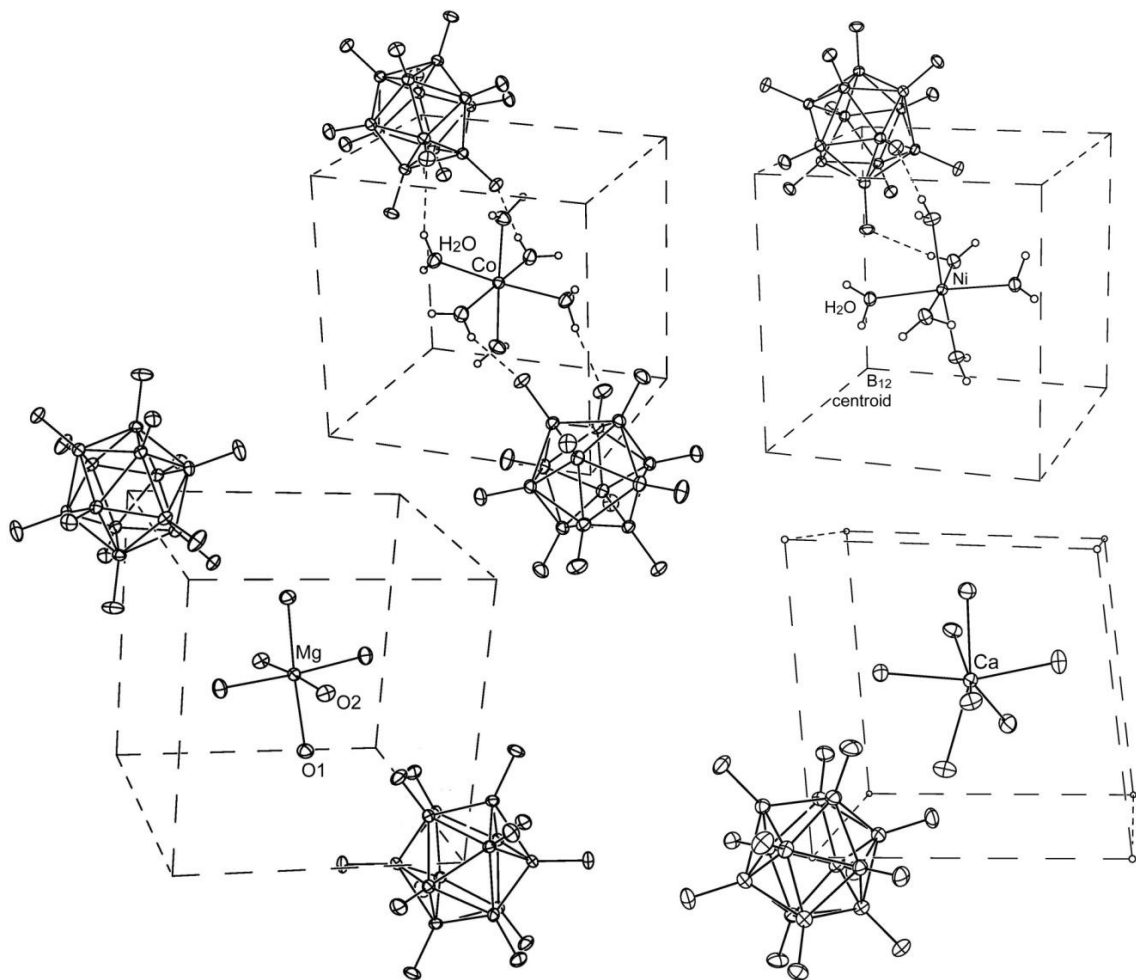


Figure 5.1. The packing of cations, anions, and H₂O molecules in the structures of Co(H₂O)₆B₁₂F₁₂, Ni(H₂O)₆B₁₂F₁₂, Mg(H₂O)₆B₁₂F₁₂, and Ca(H₂O)₇B₁₂F₁₂ (50% probability ellipsoids except for H atoms, which are shown in the cobalt and nickel structures as spheres of arbitrary size). The eight ⊙'s that form the idealized cubic rhombs are connected with dashed lines.

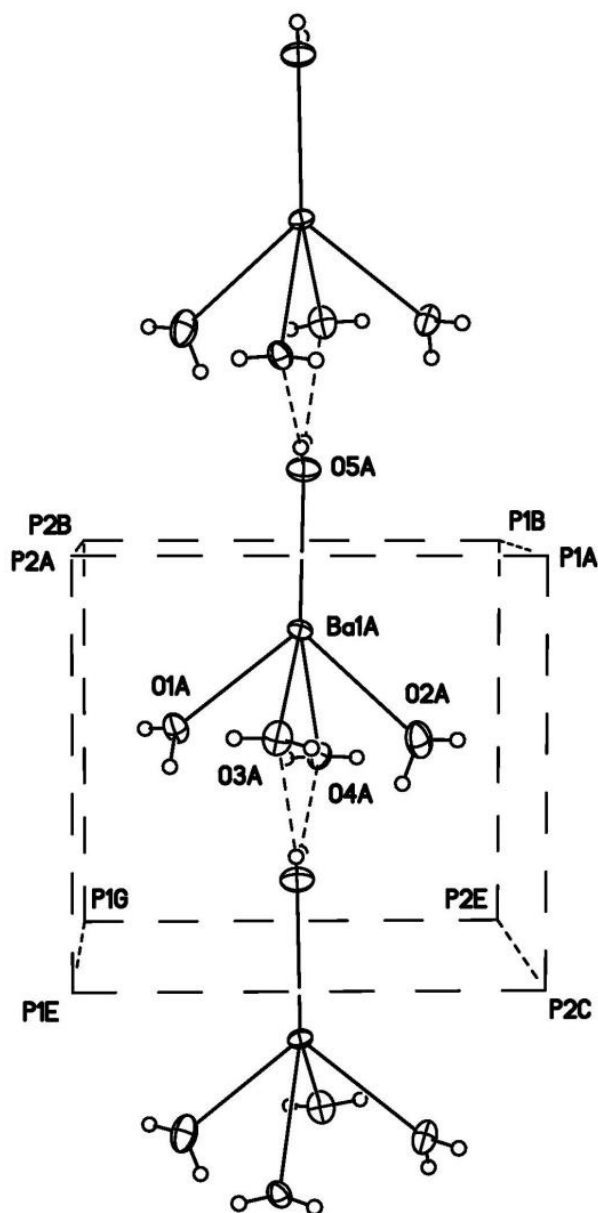


Figure 5.2. The pseudo-cubic array of anion centroids and the disposition of the $\text{Ba}(\text{H}_2\text{O})_5^{2+}$ cation (50% probability ellipsoids except for H atoms, which are shown as spheres of arbitrary size). The $\odot \cdots \odot$ distances are 6.943, 7.530, and 7.720 Å and the $\odot \cdots \odot \cdots \odot$ angles are rigorously 90° . The Ba^{2+} ion is displaced 2.058 Å from the center of the \odot array towards one face of the cube (the vertical dimension of the idealized cube in this orientation is 6.943 Å). The distances between the Ba^{2+} ion and the \odot 's labeled P1A, P2A, P1B, and P2B are 5.773, 5.780, 5.376, and 5.384 Å, respectively. The plane formed by the four H_2O molecules in the middle of the cube is tilted 9.9° from the top plane of the cube.

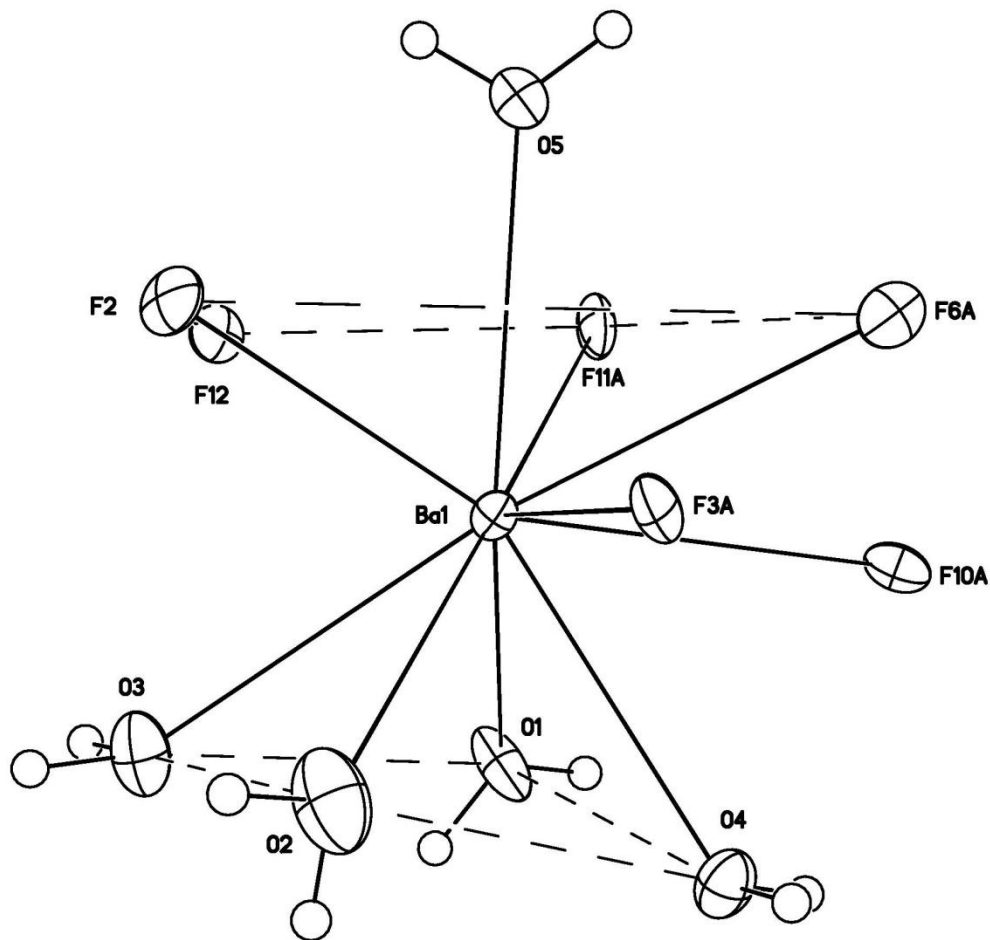


Figure 5.3. The BaO₅F₆ coordination sphere in the structure of Ba(H₂O)₅B₁₂F₁₂ (50% probability ellipsoids except for H atoms, which are shown as spheres of arbitrary size). The coordination geometry is based on a distorted cubic array of O and F atoms with O5, F3A, and F10A capping three faces of the idealized cube.

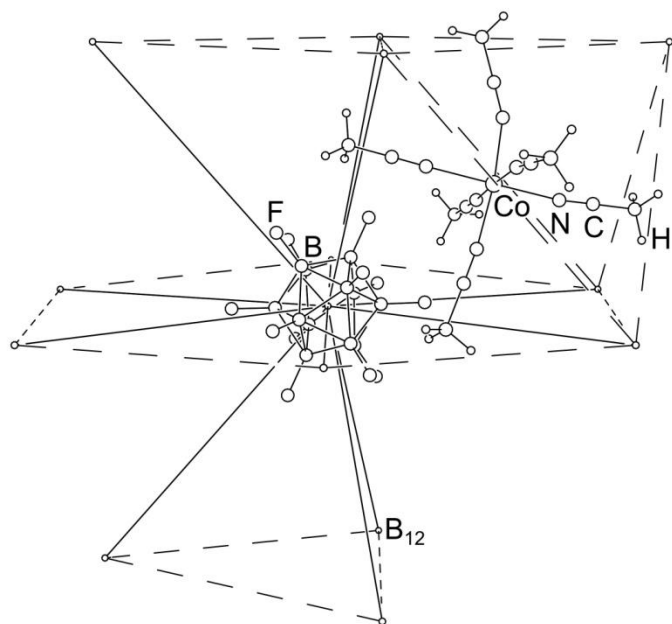


Figure 5.4. The packing of cations, anions, and CH_3CN molecules in the structure of $\text{Co}(\text{CH}_3\text{CN})_6\text{B}_{12}\text{F}_{12}$. The \ominus 's, which form a distorted HCP array, are shown as small circles.

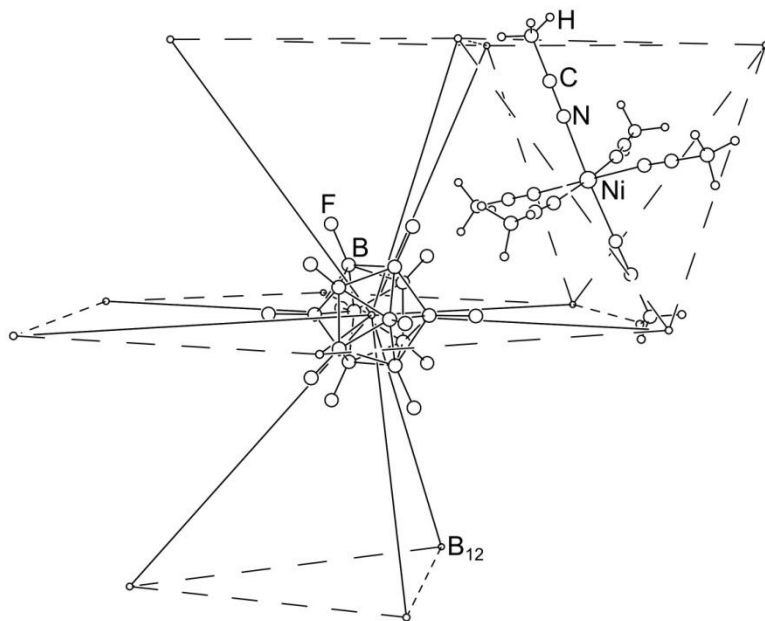


Figure 5.5. The packing of cations, anions, and CH_3CN molecules in the structure of $\text{Ni}(\text{CH}_3\text{CN})_6\text{B}_{12}\text{F}_{12}$. The \ominus 's, which form a distorted HCP array, are shown as small circles.

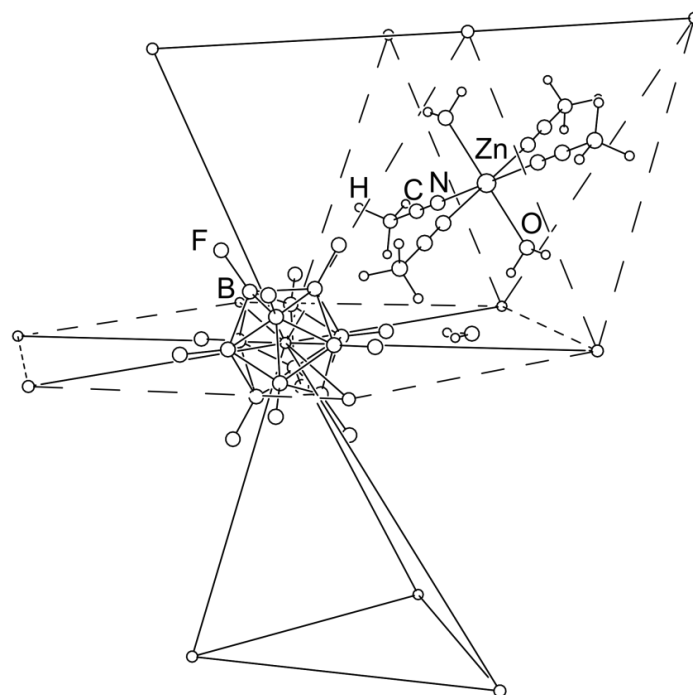


Figure 5.6. The packing of cations, anions, and H₂O and CH₃CN molecules in the structure of Zn(H₂O)₂(CH₃CN)₄B₁₂F₁₂·H₂O. The B₁₂ centroids are shown as small circles.

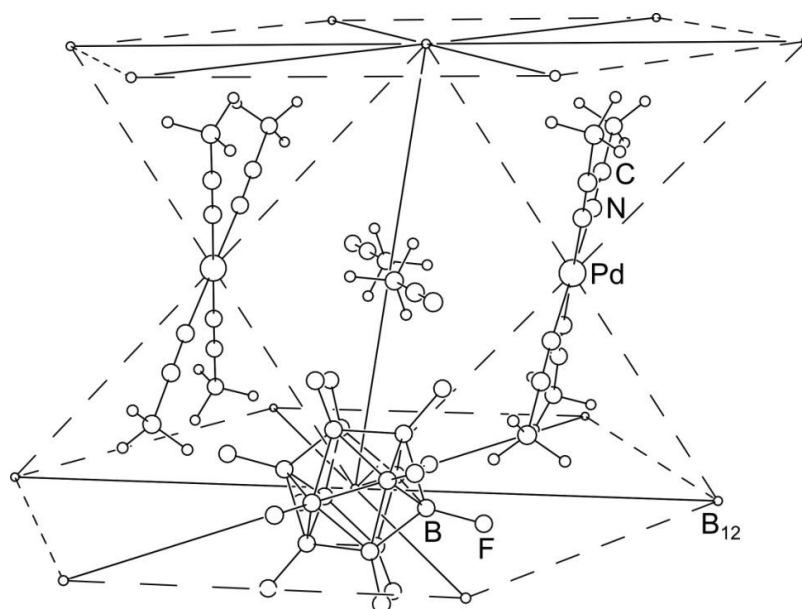


Figure 5.7. The packing of cations, anions, and CH₃CN molecules in the structure of Pd(CH₃CN)₄B₁₂F₁₂·2CH₃CN. The B₁₂ centroid, which form pseudo-hexagonal planar arrays, are shown as small circles.

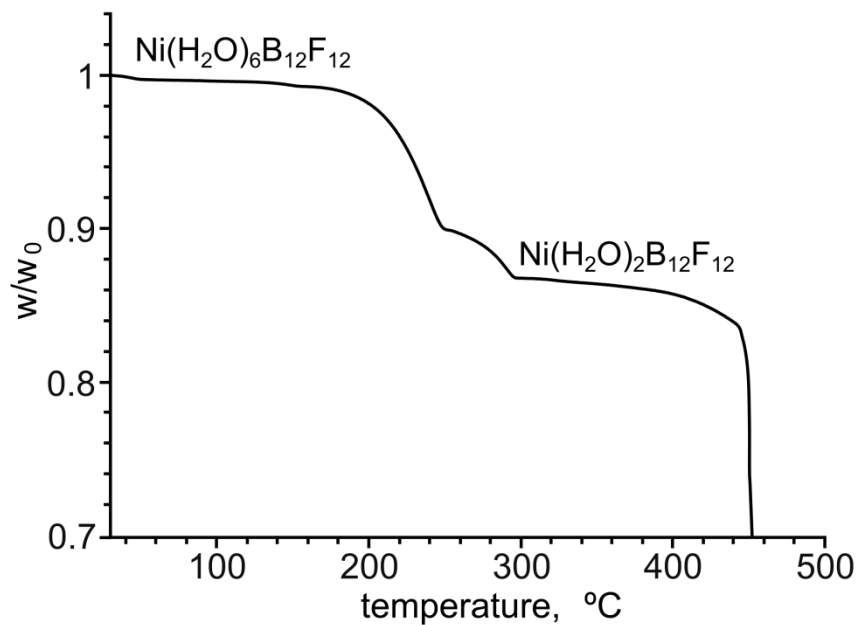


Figure 5.8. The thermogravimetry curve for a sample of $\text{Ni}(\text{H}_2\text{O})_6\text{B}_{12}\text{F}_{12}$. The heating rate was $3\text{ }^\circ\text{C}/\text{min}$.

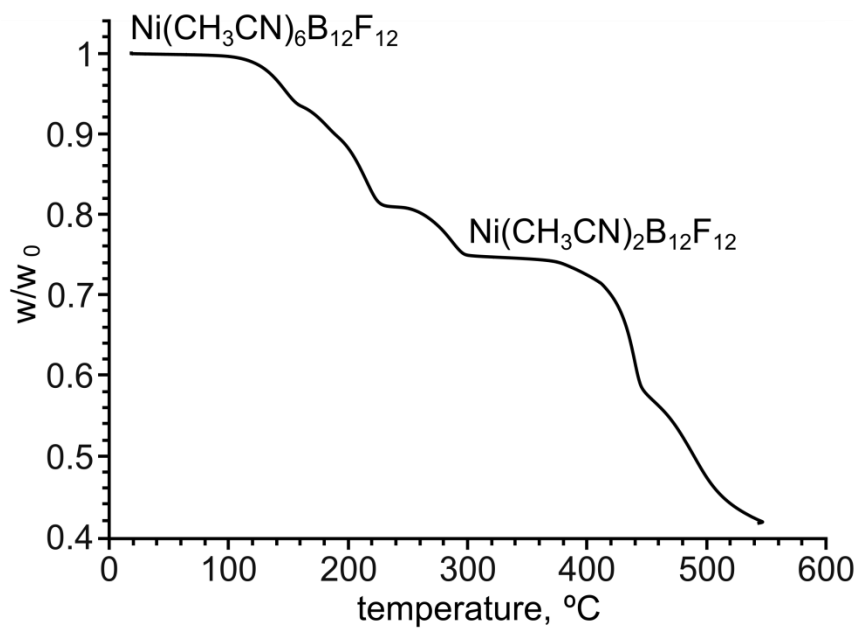


Figure 5.9. The thermogravimetry curve for a sample of $\text{Ni}(\text{CH}_3\text{CN})_6\text{B}_{12}\text{F}_{12}$. The heating rate was $3\text{ }^\circ\text{C}/\text{min}$.

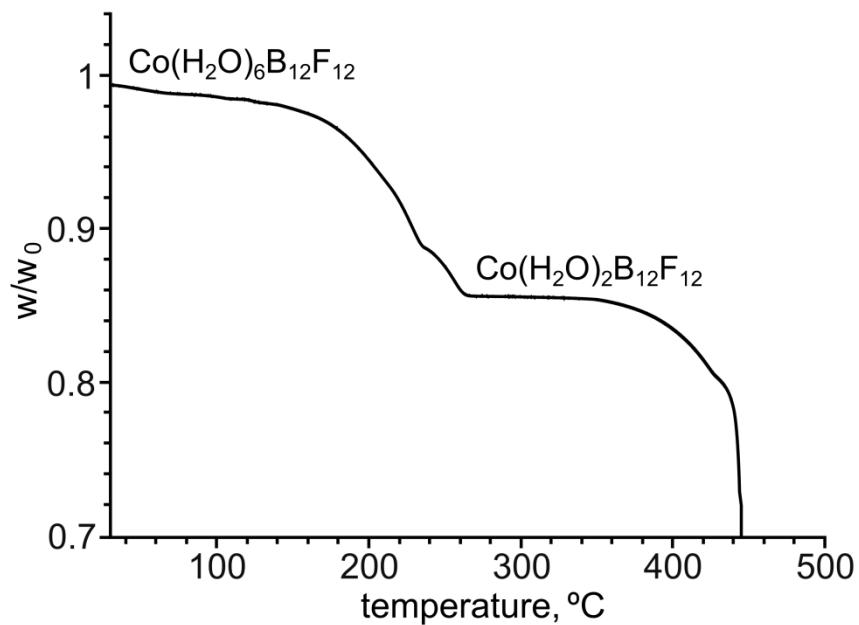


Figure 5.10. The thermogravimetry curve for a sample of $\text{Co}(\text{H}_2\text{O})_6\text{B}_{12}\text{F}_{12}$. The heating rate was $3\text{ }^\circ\text{C}/\text{min}$.

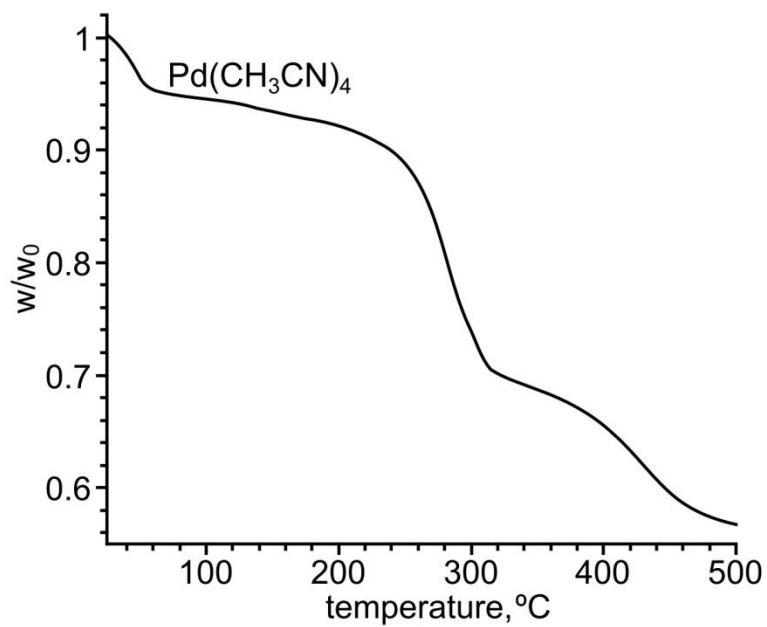


Figure 5.11. The thermogravimetry curve for a sample of $\text{Pd}(\text{CH}_3\text{CN})_4\text{B}_{12}\text{F}_{12} \cdot 2\text{CH}_3\text{CN}$. The heating rate was $3\text{ }^\circ\text{C}/\text{min}$.

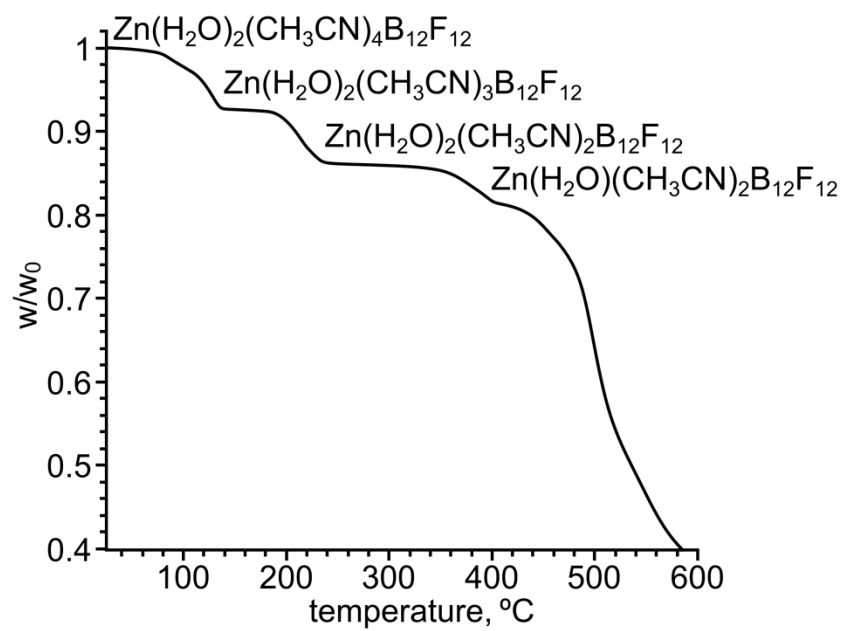


Figure 5.12. The thermogravimetry curve for a sample of $\text{Zn}(\text{H}_2\text{O})_2(\text{CH}_3\text{CN})_4\text{B}_{12}\text{F}_{12}$. The heating rate was 3 °C/min.

CHAPTER 6. REVERSIBLE HYDRATION/DEHYDRATION AND LATENT POROSITY OF $K_2B_{12}F_{12}$

Introduction

The rapid and reversible absorption/desorption of small molecules by rigid⁷⁻¹¹ or flexible (breathable)¹²⁻¹⁵ microporous solids is an historically important¹⁶⁻¹⁸ as well as a current area of fundamental and applied research. In addition to technological applications, rapid and reversible absorption reactions involving crystalline materials can serve as model systems for studying the mechanisms of solid-state reactions, whether or not those reactions involve single-crystal-to-single-crystal transformations.^{7-10,19-27} The difficulties of combining the frequently-incompatible features of thermal stability, porosity, reversible dynamic motion, and crystallinity in solids has been discussed recently.²⁷

The new concept in the creation of microporosity, combining the large, highly-symmetric, rigid, and robust superweak^{2,4,5,167} anion $B_{12}F_{12}^{2-}$ ^{28,30} with metal ions that have few or no ancillary ligands was investigated. This has the potential to create real or virtual (i.e., latent) coordinative unsaturation^{3,168} at a metal center in a crystalline material, enabling small molecules L to displace some or all of the weak, non-directional $M \cdots F(B)$ bonds, and in so doing create their own micropores as needed. In principle, the high symmetry and superweak nature of the $B_{12}F_{12}^{2-}$ anion might render lattice-expanding equilibria such as $M_x B_{12}F_{12} + nxL \rightleftharpoons [ML_n]_x B_{12}F_{12}$ rapid enough, even at mild temperatures, to be useful in a variety of applications for which microporous materials are typically used, including catalysis, separations, absorbents, membranes, and sensors.^{15-18,169-173}

Experimental

I. Reagents and Solvents.

The anhydrous salt $K_2B_{12}F_{12}$ was prepared as described in Chapter 2. Distilled water was passed through a Barnstead Nanopure deionizer; the double deionized water (dd- H_2O) had a resistivity of at least 18 M Ω . Samples of the water isotopomers D_2O (99.9% D) and $H_2^{18}O$ (97% ^{18}O) were obtained from Cambridge Isotope Laboratories, Inc, and used as received. Copper(II) sulfate pentahydrate (Fisher) was used as received. Single crystals of $K_2B_{12}F_{12}$, $K_2(H_2O)_2B_{12}F_{12}$ and $K_2(H_2O)_4B_{12}F_{12}$ were grown as described in Chapter 3.

II. Thermogravimetric Analysis (TGA) and Differential Scanning Calorimetry (DSC).

Samples for isothermal thermogravimetric analysis (TGA; platinum sample pans; *ca.* 10 mg samples; 25.0(5) or 35.0(5) °C) and differential scanning calorimetry (DSC; aluminum sample pans, *ca.* 10 mg samples; 25.0(5) °C) were analyzed using TA Instruments Series-2950 instrumentation. Dry helium or helium bubbled through H_2O or D_2O at 23(1) °C (TGA) or dry nitrogen or nitrogen bubbled through H_2O or D_2O at 23(1) °C (DSC) with flow rates that varied from 60 to 100 mL min^{-1} depending on the experiment, were used to maintain a constant-composition atmosphere above the samples ($P(H_2O) = 21(1)$ Torr at 23(1) °C). However, when dry the carrier gas was switched to wet carrier gas (or vice versa), there was a delay of several minutes before the composition of the atmosphere in the sample chamber became constant (as monitored by the mass spectrum of the carrier gas exiting the sample chamber).

III. Powder X-ray Diffraction (PXRD).

X-ray powder diffraction patterns were recorded using Scintag X2 X-ray diffractometer (Cu K_α radiation) at 25(1) °C with a step size of 0.02 deg and a scan rate of 1.67 deg min^{-1} .

IV. Infrared Spectroscopy (FTIR) and Raman Spectroscopy (RS).

FTIR spectra were recorded with a Nicolet Magna-760 FTIR spectrometer operating at 2 cm^{-1} resolution using a special IR cell of local design.⁶⁶ The "D₂O sample" was not allowed to undergo complete isotopomer exchange, so the sample was $\text{K}_2(\text{H}_2\text{O})_x(\text{HDO})_y(\text{D}_2\text{O})_z\text{B}_{12}\text{F}_{12}$, where $x + y + z = 2$. Raman spectra were recorded with a Nicolet Magna-760 FTIR spectrometer at 1 cm^{-1} resolution.

V. Scanning Electron Microscopy (SEM).

Scanning electron microscopy was performed by Dr. Patrick McCurdy on a finely ground sample of anhydrous $\text{K}_2\text{B}_{12}\text{F}_{12}$ using a JSM-6500F field emission system (operating voltage = 15 kV). A 5 nm layer of gold was sputtered onto the surface of the sample to make it conductive.

VI. DFT Calculations.

All DFT calculations were performed by Dr. Alexey Popov (Leibniz Institute for Solid State and Materials Research, Dresden, Germany) using the ORCA code.⁶⁷ The B2-PLYP-D functional¹⁷⁴⁻¹⁷⁷ and def2-QZVPP basis set⁷⁰ augmented with diffuse functions from aug-cc-pVTZ basis set¹⁷⁸ for oxygen and hydrogen atoms was employed for all calculations. The B2-PLYP-D double hybrid density functional includes a semi-empirical mixture of DFT and MP2 correlation energies^{176,177} as well as semi-empirical correction to account for dispersion forces.¹⁷⁶ Symmetry restrictions were not used in the course of optimization.

Results and Discussion

I. The Comparison of Ionic Lattices in $\text{K}_2(\text{H}_2\text{O})_n\text{B}_{12}\text{F}_{12}$ ($n = 0, 2, 4$)

The array of $\text{B}_{12}\text{F}_{12}^{2-}$ anions in the simple salt $\text{K}_2\text{B}_{12}\text{F}_{12}$ is approximately hexagonal close-packed, with K^+ ions in all of the O_h holes and in all of the D_{3h} trigonal holes that lie between pairs of T_d holes (i.e., the Ni_2In structure, as discussed in Chapter 3). The 12 nearest-neighbor $\odot \cdots \odot$ distances were found to be 8.207 and 8.236 Å within the pseudo-

close-packed layers and 7.204, 7.471, and 7.517 Å between the layers. The arrays of anions in the two hydrates are best described as distorted variations of the CsCl structure with two K⁺ ions occupying the anion rhomb (i.e., parallelepiped) voids between the B₁₂F₁₂²⁻ anions, as shown in Figure 6.1, which also shows a similar view of the K₂B₁₂F₁₂ lattice for comparison. The anion rhomb in K₂(H₂O)₂B₁₂F₁₂ is the closest to being a cube: the ⊙⋯⊙ distances only vary by 0.3% (7.276 and 7.295 Å), but the cubes are tilted so that the acute ⊙⋯⊙⋯⊙ angles are 78.7° and 81.3° instead of 90° (for comparison, the corresponding angles are 71.7°, 75.0°, and 75.3° in K₂(H₂O)₄B₁₂F₁₂ and 54.3°, 56.4°, and 60.1° in nearly-close-packed K₂B₁₂F₁₂). These and other results discussed below are listed in Table 3.2.

The drawings in Figure 6.1 show that the dehydration/rehydration reactions $\text{K}_2(\text{H}_2\text{O})_4\text{B}_{12}\text{F}_{12} \rightarrow \text{K}_2(\text{H}_2\text{O})_2\text{B}_{12}\text{F}_{12} \rightleftharpoons \text{K}_2\text{B}_{12}\text{F}_{12}$ can occur with relatively minor structural rearrangements involving the distances and angles between the large weakly-coordinating B₁₂F₁₂²⁻ anions and between the K⁺ cations. The average ⊙⋯⊙ distances for the rhombs shown in Figure 6.1 are 7.987, 7.282, and 7.971 Å, for K₂B₁₂F₁₂, K₂(H₂O)₂B₁₂F₁₂, and K₂(H₂O)₄B₁₂F₁₂, respectively, and the formula unit volumes are 332.0(2), 367.90(3), and 424.20(6) Å³, respectively. Note, however, that the average of the 12 ⊙⋯⊙ distances for each B₁₂ centroid in nearly-close-packed K₂B₁₂F₁₂ is 7.812 Å, so the ⊙'s in this compound are, on average, closer together than the rhomb in Figure 6.1 depicts. Note also that the ⊙'s are significantly closer together, on average, in K₂(H₂O)₂B₁₂F₁₂ than in nearly-close-packed K₂B₁₂F₁₂ is (7.282 vs. 7.812 Å, respectively) even though the formula unit volume for the dihydrate is 10.8% larger than for the anhydrous salt K₂B₁₂F₁₂.

The K1⋯K2 distances shown in the rhomb in Figure 6.1 for K₂B₁₂F₁₂ are 5.543(1) Å, just longer than the K1⋯K2 distance in K₂(H₂O)₄B₁₂F₁₂, which is 5.2470(4) Å. (There are also 5.421(1) Å K1⋯K2 distances in K₂B₁₂F₁₂.) The K⋯K' distance in K₂(H₂O)₂B₁₂F₁₂ is 4.2529(3) Å and the K1⋯K1 and K2⋯K2 distances in

$\text{K}_2(\text{H}_2\text{O})_4\text{B}_{12}\text{F}_{12}$ are 4.3188(4) and 4.1293(5) Å, respectively, ca 30% shorter than 5.5 Å. (As points of reference, the $\text{K}\cdots\text{K}$ distances in KF^{179} and K_2O^{180} are 3.795(2) and 3.218 Å, respectively). Therefore, as $\text{K}_2\text{B}_{12}\text{F}_{12}$ is transformed into $\text{K}_2(\text{H}_2\text{O})_2\text{B}_{12}\text{F}_{12}$ in the presence of water vapor (see below), the weakly-coordinating anions shift their positions in the lattice and pairs of K^+ ions move from ca. 5.5 Å apart to ca. 4.2 Å apart. In both cases, the pairs of K^+ ions share pairs of $\text{B}_{12}\text{F}_{12}^{2-}$ anions, as shown in Figures 6.2, 6.3, and 6.4. The direct comparison in Figure 6.4 shows that relatively small motions of pairs of bridging anions are involved in the solid-state transformation $\text{K}_2\text{B}_{12}\text{F}_{12(s)} + 2\text{H}_2\text{O}(g) \rightleftharpoons \text{K}_2(\text{H}_2\text{O})_2\text{B}_{12}\text{F}_{12(s)}$.

II. The $\text{K}_2(\text{H}_2\text{O})_2^{2+}$ and $\text{K}_2(\text{H}_2\text{O})_4^{2+}$ Dimers.

Table 6.1 lists relevant DFT and experimental results. The DFT methodology was validated by comparing results for the gas-phase monocations $\text{K}(\text{H}_2\text{O})^+$ and $\text{K}(\text{H}_2\text{O})_2^+$ with recent counterpoise-corrected DFT results¹⁸¹ and with the classic experimental work of Kebarle and coworkers.^{182,183} The DFT calculations show that the $\text{K}_2(\text{H}_2\text{O})_n^{2+}$ dimers are thermodynamically stabilized by the lattice of anions: the ΔE values for the gas-phase dimerization of two $\text{K}(\text{H}_2\text{O})^+$ or $\text{K}(\text{H}_2\text{O})_2^+$ monocations into $[\text{K}(\mu\text{-H}_2\text{O})_2\text{K}]^{2+}$ or $[(\text{H}_2\text{O})\text{K}(\mu\text{-H}_2\text{O})_2\text{K}(\text{H}_2\text{O})]^{2+}$ dications are predicted to be +232 and +205 kJ mol⁻¹, respectively. The calculations also predict that ΔE for the gas-phase reaction $2\text{K}^+ + 2\text{H}_2\text{O} \rightarrow [\text{K}(\mu\text{-H}_2\text{O})_2\text{K}]^{2+}$ is +81.0 kJ mol, whereas the enthalpy change for the reversible solid-state reaction $\text{K}_2\text{B}_{12}\text{F}_{12} + 2\text{H}_2\text{O} \rightarrow \text{K}_2(\text{H}_2\text{O})_2\text{B}_{12}\text{F}_{12}$, which was measured by DSC, was found to be -110(2) kJ mol⁻¹. For comparison, the enthalpy of deposition of 2 mol $\text{H}_2\text{O}(s)$ from 2 mol $\text{H}_2\text{O}(g)$ is -99(1) kJ.¹⁸⁴

There are significant differences in the structures of the $[\text{K}(\mu\text{-H}_2\text{O})_2\text{K}]^{2+}$ and $[(\text{H}_2\text{O})\text{K}(\mu\text{-H}_2\text{O})_2\text{K}(\text{H}_2\text{O})]^{2+}$ dications in $\text{K}_2(\text{H}_2\text{O})_2\text{B}_{12}\text{F}_{12}$, and $\text{K}_2(\text{H}_2\text{O})_4\text{B}_{12}\text{F}_{12}$ and their predicted gas-phase structures, as shown in Figure 6.5. As stated above, the $\text{K}\cdots\text{K}$ distances in the two hydrates range from 4.1293(5) to 4.3188(4) Å, whereas in the gas phase the predicted $\text{K}\cdots\text{K}$ distances are 4.886 Å for $\text{K}_2(\text{H}_2\text{O})_2^{2+}$ and 4.835 Å for

$\text{K}_2(\text{H}_2\text{O})_4^{2+}$, ca. 0.7 Å (ca. 17%) longer. This can be understood in the following way. In the gas phase, the effective positive charge on each K^+ ion is higher, and hence the repulsion between the two cations is greater, than in the crystalline compounds. This can be quantified to a first approximation by comparing the sums of K–O bond valences for the gas phase cations, 0.19 for $\text{K}_2(\text{H}_2\text{O})_2^{2+}$ and 0.45 for $\text{K}_2(\text{H}_2\text{O})_4^{2+}$, with the sums of K–O and $\text{K}\cdots\text{F}$ bond valences for the compounds, 1.00 for $\text{K}_2(\text{H}_2\text{O})_2\text{B}_{12}\text{F}_{12}$ and 1.03/1.09 for $\text{K}_2(\text{H}_2\text{O})_4\text{B}_{12}\text{F}_{12}$. In fact, the sum of K–O bond valences for $\text{K}_2(\text{H}_2\text{O})_2\text{B}_{12}\text{F}_{12}$, 0.35, is nearly twice as large as for the gas-phase dication $\text{K}_2(\text{H}_2\text{O})_2^{2+}$ because, with so much more positive-charge "neutralization" in the compound, the two K^+ ions experience much less repulsion, have a much shorter $\text{K}\cdots\text{K}$ distance, and, as a consequence, have much shorter K–O distances.

The stabilization of dimeric dications by a host lattice of weakly-coordinating anions was recently observed by Knapp and co-workers in $\text{Li}_2(\text{SO}_2)_8\text{B}_{12}\text{Cl}_{12}$ (a drawing of this structure is shown in Figure 6.6).¹³⁸ In that case, the gas-phase dimerization of two tetrahedral $\text{Li}(\text{SO}_2)_4^+$ monocations into the observed $[(\text{SO}_2)_3\text{Li}(\mu\text{-SO}_2\text{-}1\kappa\text{O}:2\kappa\text{O}')_2\text{Li}(\text{SO}_2)_3]^{2+}$ dication was predicted to be endothermic by 142 kJ mol^{-1} . This is smaller than the predicted dimerization endothermicities for $[\text{K}_2(\text{H}_2\text{O})_2]^{2+}$ (232 kJ mol^{-1}) and $[\text{K}_2(\text{H}_2\text{O})_4]^{2+}$ (205 kJ mol^{-1}), probably for two reasons. The first reason is that the predicted $\text{Li}\cdots\text{Li}$ distance in the gas-phase dimer, at 5.626 Å, is ca. 0.7 Å longer than the predicted ca. 4.9 Å $\text{K}\cdots\text{K}$ distances (this is due to the fact that the bridging ligands in $\text{Li}_2(\text{SO}_2)_8^{2+}$ are $\mu\text{-SO}_2\text{-}1\kappa\text{O}:2\kappa\text{O}'$ ligands). In fact, the predicted $\text{Li}\cdots\text{Li}$ distance in the gas-phase dimer is only 6% longer than the $\text{Li}\cdots\text{Li}$ distance in crystalline $\text{Li}_2(\text{SO}_2)_8\text{B}_{12}\text{Cl}_{12}$. The second reason is that the sums of Li–O bond valences are quite similar, 0.92 for gas-phase $\text{Li}_2(\text{SO}_2)_8^{2+}$ and 1.02 for $\text{Li}_2(\text{SO}_2)_8\text{B}_{12}\text{Cl}_{12}$. (The coordination spheres are LiO_5 in both the gas-phase dimer and in the solid-state, whereas they are KO_2 and KO_2F_6 (or KO_3 and KO_3F_5) for the potassium systems.) For comparison, the $\text{Li}\cdots\text{Li}$ distances in LiF ,¹⁸⁵ Li_2O ,¹⁸⁶ and Li_2CrF_6 ¹⁸⁷ are 2.8475, 2.3070(5), and 2.92(2) Å, respectively.

There are 56 structures in the Cambridge Structural Database alone with $\text{K}_2(\text{H}_2\text{O})_2$ moieties. One of them, $\text{K}_2(\text{H}_2\text{O})_2(\text{trans-SnMe}_2\text{F}_4)$,¹⁸⁸ is particularly relevant to the structure of $\text{K}_2(\text{H}_2\text{O})_2\text{B}_{12}\text{F}_{12}$ because the K^+ ions in each structure are bridged only by the two H_2O molecules and because the only contacts between the cations and anions are $\text{K}\cdots\text{F}$ contacts. The distances and angles in the K_2O_2 core are similar to those in $\text{K}_2(\text{H}_2\text{O})_2\text{B}_{12}\text{F}_{12}$, as shown in Figure 6.7. Even the sum of K-O bond valences are the same for the two compounds, 0.35. Therefore, the water molecules are bound about as strongly in $\text{K}_2(\text{H}_2\text{O})_2(\text{SnMe}_2\text{F}_4)$ as they are in $\text{K}_2(\text{H}_2\text{O})_2\text{B}_{12}\text{F}_{12}$. Furthermore, the $\text{F}\cdots\text{H}(\text{O})$ hydrogen bonds are also similar (1.92/1.98 Å, and 161/165°, in $\text{K}_2(\text{H}_2\text{O})_2(\text{SnMe}_2\text{F}_4)$, and 2.12(1)/2.17(1) Å, and 154(1)/165(1)°, in $\text{K}_2(\text{H}_2\text{O})_2\text{B}_{12}\text{F}_{12}$). The biggest difference is that the coordination spheres are KO_2F_3 in $\text{K}_2(\text{H}_2\text{O})_2(\text{SnMe}_2\text{F}_4)$, with three relatively short $\text{K}\cdots\text{F}$ distances of 2.60(1), 2.60(1), and 2.62(2) and K-O distances of 2.74(1) and 2.83(1) Å, and KO_2F_6 in $\text{K}_2(\text{H}_2\text{O})_2\text{B}_{12}\text{F}_{12}$, with six K-F distances from 2.5984(4) to 3.1593(5) Å and K-O distances of 2.7698(6) and 2.7716(6) Å. The sum of K-O and $\text{K}\cdots\text{F}$ bond valences are 0.91 for $\text{K}_2(\text{H}_2\text{O})_2(\text{SnMe}_2\text{F}_4)$ and, as discussed above, 1.00 for $\text{K}_2(\text{H}_2\text{O})_2\text{B}_{12}\text{F}_{12}$. Perhaps because of the slight difference in bond-valence sums, the waters of hydration in $\text{K}_2(\text{H}_2\text{O})_2(\text{SnMe}_2\text{F}_4)$ are not lost at room temperature, only above 50 °C, with a maximum rate of loss at 75 °C.¹⁸⁸ (However, the structure of $\text{K}_2(\text{H}_2\text{O})_2(\text{SnMe}_2\text{F}_4)$ was determined at 293 K, so the bond-valence sum for K^+ would probably be somewhat higher than 0.91 at 110 K.) It is not known if the dehydration of $\text{K}_2(\text{H}_2\text{O})_2(\text{SnMe}_2\text{F}_4)$ is reversible and, if so, if the rehydrated product is crystalline. Other relevant compounds with similar $\text{K}_2(\text{H}_2\text{O})_2^{2+}$ cores are $\text{K}_2(\text{H}_2\text{O})_2(\text{Pt}_2(\mu\text{-OH})_2\text{F}_4(\text{CF}_3)_4)$ (refcode: ISITIN),¹⁸⁹ $\text{K}_2(\text{H}_2\text{O})\text{SnCl}_4$,¹⁹⁰ $\text{K}_2(\text{H}_2\text{O})\text{HgCl}_4$,¹⁹¹ and $\text{KF}\cdot 4\text{H}_2\text{O}$.¹⁹²

The FTIR spectrum of $\text{K}_2(\text{H}_2\text{O})_2\text{B}_{12}\text{F}_{12}$ under ca. 21 Torr $\text{H}_2\text{O}(\text{g})$ exhibited two relatively sharp $\nu(\text{OH})$ bands at 3638 and 3576 cm^{-1} , as shown in Figure 6.8. These and relevant frequencies for related compounds are listed in Table 6.2,¹⁹³⁻¹⁹⁹ and the $\text{K}_2(\text{H}_2\text{O})_2^{2+}$ moieties in $\text{K}_2(\text{H}_2\text{O})\text{SnCl}_4$ ¹⁹⁰ and $\text{K}_2(\text{H}_2\text{O})\text{HgCl}_4$ ¹⁹¹ are shown in Figure 6.9.

The coordination of H₂O to a metal ion lowers $\nu(\text{OH})$ values, as seen for the gas-phase $[\text{Ar-K-OH}_2]^+$ cation.¹⁹⁴ In addition, (O)H \cdots X hydrogen bonding further lowers $\nu(\text{OH})$ values and tends to broaden the bands in $\text{K}_2(\text{H}_2\text{O})_2\text{B}_{12}\text{F}_{12}$, $\text{K}_2(\text{H}_2\text{O})\text{SnCl}_4$,¹⁹⁵ $\text{K}_2(\text{H}_2\text{O})\text{HgCl}_4$,¹⁹⁶ and $\text{K}_2(\text{H}_2\text{O})_2(\text{SnMe}_2\text{F}_4)$ ¹⁸⁸ (X = F, Cl). However, the $\nu(\text{OH})$ bands in $\text{K}_2(\text{H}_2\text{O})_2\text{B}_{12}\text{F}_{12}$ are at higher energy and are more narrow than the bands in the other three compounds with $\text{K}_2(\text{H}_2\text{O})_2^{2+}$ moieties, despite the fact that the K–O distances are similar in all four compounds. These results suggest that the (O)H \cdots F hydrogen bonds in $\text{K}_2(\text{H}_2\text{O})_2\text{B}_{12}\text{F}_{12}$ are significantly weaker than the (O)H \cdots Cl hydrogen bonds in $\text{K}_2(\text{H}_2\text{O})\text{SnCl}_4$ and $\text{K}_2(\text{H}_2\text{O})\text{HgCl}_4$ or the (O)H \cdots F hydrogen bonds in $\text{K}_2(\text{H}_2\text{O})_2(\text{SnMe}_2\text{F}_4)$.

The IR spectrum for a sample of $\text{K}_2(\text{H}_2\text{O})_2\text{B}_{12}\text{F}_{12}$ partially exchanged with HDO and D₂O ligands is also shown in Figure 6.8 (as is the IR spectrum of $\text{K}_2(\text{H}_2^{18}\text{O})_2\text{B}_{12}\text{F}_{12}$). The bands assigned to HDO, which are as sharp as the bands assigned to H₂O and D₂O ligands, indicate that the two O–H bonds for each H₂O molecule are, effectively, in the same environment, even though they are not symmetry related (the (O)H1 \cdots F4 and (O)H2 \cdots F5 distances and O–H1 \cdots F4 and O–H2 \cdots F5 angles are, respectively, 2.17(1) Å, 2.12(1) Å, 154(1)°, and 165(1)°). Furthermore, the Raman spectrum of $\text{K}_2(\text{H}_2\text{O})_2\text{B}_{12}\text{F}_{12}$, shown in Figure 6.10, exhibited the same two $\nu(\text{OH})$ bands as the IR spectrum (to within $\pm 2 \text{ cm}^{-1}$), indicating that the vibrational coupling between the H₂O molecules in the centrosymmetric $\text{K}_2(\text{H}_2\text{O})_2^{2+}$ cores is very weak. Finally, the A_{1g} and H_g $\nu(\text{BB})$ Raman bands for the $\text{B}_{12}\text{F}_{12}^{2-}$ anion in $\text{K}_2(\text{H}_2\text{O})_2\text{B}_{12}\text{F}_{12}$ are at 432 and 392 cm^{-1} , respectively, and these are the same values measured for a sample of the anhydrous compound $\text{K}_2\text{B}_{12}\text{F}_{12}$.

III. Dehydration/Rehydration Reactions

A. General Comments. It is well-known that rates of solid-state reactions can depend on many factors, including the surface area and/or the surface-area-to-volume ratio of the solid particles, the partial pressures of reactive gases as they are absorbed or evolved by the solid (water vapor in our case), and on the temperature and/or the rate of

temperature change of the sample.²⁰⁰⁻²⁰⁴ For an isothermal TGA experiment, the temperature of the sample can be particularly difficult to control precisely for rapid reactions that are strongly exothermic or endothermic, which is true for the hydration and dehydration reactions studied in this work.

The mechanisms by which hydrates as simple as monohydrates are known to, or are believed to, undergo dehydration are varied, and one particular mechanism can rarely be assigned unambiguously because different mechanism functions usually fit the kinetic data equally well.^{26,205-207} In fact, it may also be rare that a fixed mechanism operates throughout the entire dehydration, even for a monohydrate.²⁰⁵ Dehydrations that transform one phase to another can be monovariant or, as in the case of $\text{CaC}_2\text{O}_4 \cdot \text{H}_2\text{O}$, bivariant.^{206,208} With polyhydrates, of course, dehydration can occur in discrete steps or stages,^{27,209} and there are examples of two-stage dehydrations that appeared to be one-step processes by TGA.²¹⁰

All of these complications notwithstanding, an initial kinetic study of the $\text{K}_2(\text{H}_2\text{O})_{0,2,4}\text{B}_{12}\text{F}_{12}(\text{s})/\text{H}_2\text{O}(\text{g})$ system was carried out. For this reason, the temperature of the samples, the partial pressures of water in the TGA sample chamber during hydration/dehydration, and the sample particle sizes were known only approximately in the experiments described below. Nevertheless, some important hypotheses about the kinetics and mechanism of this equilibrium that are supported by observations can now be clearly stated, and experiments to test these hypotheses in the future can be designed.

B. Rapid and Irreversible Dehydration of $\text{K}_2(\text{H}_2\text{O})_4\text{B}_{12}\text{F}_{12}$. Figure 6.11 shows a 25.0(5) °C TGA trace for a sample consisting of "wet" crystals of $\text{K}_2(\text{H}_2\text{O})_4\text{B}_{12}\text{F}_{12}$ grown at 0 °C having a thin layer of mother liquor surrounding each crystal to avoid premature dehydration (in addition, the crystals were crushed with a spatula to decrease the size of the sample particles). The carrier gas was dry He. The ratios (molar mass $\text{K}_2(\text{H}_2\text{O})_4\text{B}_{12}\text{F}_{12}$)/(molar mass $\text{K}_2(\text{H}_2\text{O})_2\text{B}_{12}\text{F}_{12}$) and (molar mass $\text{K}_2\text{B}_{12}\text{F}_{12}$)/(molar mass $\text{K}_2(\text{H}_2\text{O})_2\text{B}_{12}\text{F}_{12}$) are 1.076 and 0.924, respectively. The trace is divided into six regions

labeled **a–f**. Region **a** is the rapid evaporation of mother-liquor water. Region **b** is the almost-equally-rapid dehydration of $\text{K}_2(\text{H}_2\text{O})_4\text{B}_{12}\text{F}_{12}$ to $\text{K}_2(\text{H}_2\text{O})_2\text{B}_{12}\text{F}_{12}$, which for this sample occurred in ca. 10 min. Region **c** is the slower but still rapid dehydration of $\text{K}_2(\text{H}_2\text{O})_2\text{B}_{12}\text{F}_{12}$ to $\text{K}_2\text{B}_{12}\text{F}_{12}$, which occurred in ca. 55 min. The sample showed no further mass loss for several hours at 25.0(5) °C (region **d**), after which time the carrier gas was switched to He bubbled through H_2O at 23(1) °C (at this temperature, $P(\text{H}_2\text{O}) = 21(1)$ Torr; note that the sample temperature remained 25.0(5) °C). Region **e** is the very rapid rehydration of $\text{K}_2\text{B}_{12}\text{F}_{12}$ to $\text{K}_2(\text{H}_2\text{O})_2\text{B}_{12}\text{F}_{12}$, which occurred in only 12 min for this sample. Significantly, region **f** shows that $\text{K}_2(\text{H}_2\text{O})_2\text{B}_{12}\text{F}_{12}$ does not absorb any more water at 25.0(5) °C in the presence of 21(1) Torr $\text{H}_2\text{O}(\text{g})$, even after many hours or days (the longer times are not shown in this particular figure).

Other experiments showed that $\text{K}_2(\text{H}_2\text{O})_2\text{B}_{12}\text{F}_{12}$ does not absorb more water even when exposed to 72 Torr of $\text{H}_2\text{O}(\text{g})$ at a sample temperature of 45(1) °C. (Furthermore, $\text{K}_2(\text{H}_2\text{O})_2\text{B}_{12}\text{F}_{12}$ is not deliquescent under these conditions.) The formation of the $\text{K}_2(\text{H}_2\text{O})_4\text{B}_{12}\text{F}_{12}$ appears to require the presence of liquid water. In this regard, the $\text{K}_2(\text{H}_2\text{O})_{0,2,4}\text{B}_{12}\text{F}_{12}$ system resembles the $\text{K}(\text{H}_2\text{O})_{0,2,4}\text{F}$ system (i.e., $\text{KF}\cdot(\text{H}_2\text{O})_{0,2,4}$).¹⁰⁸ The KF dihydrate crystallizes from aqueous solutions in the temperature range 19–41 °C, the tetrahydrate crystallizes at lower temperatures, and anhydrous KF crystallizes at temperatures above 41.4 °C.²¹¹ As it will be discussed below, crystalline $\text{K}_2\text{B}_{12}\text{F}_{12}$ does not absorb water vapor to any extent above 52 °C.

C. Rapid, Reconstructive, and Reversible Dehydration of $\text{K}_2(\text{H}_2\text{O})_2\text{B}_{12}\text{F}_{12}$. The observation that single crystals of $\text{K}_2(\text{H}_2\text{O})_2\text{B}_{12}\text{F}_{12}$ were grown by the evaporation of water from a saturated aqueous solution at 25(1) °C and that single-crystals of $\text{K}_2\text{B}_{12}\text{F}_{12}$ were grown by very slow evaporation of water, to dryness, of a saturated aqueous solution at 25(1) °C strongly suggests that the transformation $\text{K}_2(\text{H}_2\text{O})_2\text{B}_{12}\text{F}_{12}(\text{cryst}) \rightarrow \text{K}_2\text{B}_{12}\text{F}_{12}(\text{cryst}) + 2 \text{H}_2\text{O}(\text{g})$ can be a single-crystal-to-single-crystal transformation when it is carried out very slowly. This is sensible given the relationship between the unit cells of

the two compounds, which is shown in Figure 6.12. Nevertheless, visual inspection of macroscopic crystals of $\text{K}_2(\text{H}_2\text{O})_2\text{B}_{12}\text{F}_{12}$ showed that they became cloudy upon exposure to dry air (the size of the crystals used to collect the X-ray diffraction data was $0.55 \times 0.55 \times 0.28$ mm for $\text{K}_2(\text{H}_2\text{O})_2\text{B}_{12}\text{F}_{12}$ and only $0.04 \times 0.02 \times 0.01$ mm for $\text{K}_2\text{B}_{12}\text{F}_{12}$). Some of the smaller cloudy single crystals were mounted on the single-crystal diffractometer and, although they were still prisms of nearly the same dimensions, gave diffraction patterns that were essentially powder rings. In addition, powder X-ray diffraction patterns of (i) $\text{K}_2(\text{H}_2\text{O})_2\text{B}_{12}\text{F}_{12}$ that had been formed by rehydration of crystalline $\text{K}_2\text{B}_{12}\text{F}_{12}$ in a stream of He or N_2 containing (nominally) 21(1) Torr of water vapor and (ii) $\text{K}_2\text{B}_{12}\text{F}_{12}$ that had been formed by dehydration of crystalline $\text{K}_2(\text{H}_2\text{O})_2\text{B}_{12}\text{F}_{12}$ in a stream of dry He or N_2 indicated that both products were crystalline, as shown in Figure 6.13 (the 25(1) °C experimental PXRD patterns are also compared with simulated patterns using the coordinates and symcodes for the corresponding single-crystal X-ray structures at 110(2) K). These data also indicate that the crystalline product of solid-gas hydration of crystalline $\text{K}_2\text{B}_{12}\text{F}_{12}$ at 25(1) °C is identical with that obtained by slow evaporation of an aqueous solution of the salt at 25(1) °C.

DSC experiments revealed that the dehydration of crystalline $\text{K}_2(\text{H}_2\text{O})_2\text{B}_{12}\text{F}_{12}$ in a stream of dry N_2 was endothermic, with $\Delta H_{298} = 110(2)$ kJ mol⁻¹ (the initial temperature was 25.0(5) °C). This is only ca. 10% higher than an experimental ΔH value for $2 \text{H}_2\text{O}(s) \rightarrow 2 \text{H}_2\text{O}(g)$, which is 98.8 ± 1.6 kJ mol⁻¹.¹⁸⁴ Since the sample temperature in our experiments decreased to some extent during dehydration and increased during rehydration, the rates of these processes were not determined under strict isothermal conditions (a thermocouple close to the sample registered temperature changes of ± 0.1 °C during the hydrations and dehydrations, and the sample temperature may have varied by more than that). Two cycles of approximately-constant-temperature ($T_{\text{initial}} = 25.0(5)$ °C) hydration of $\text{K}_2\text{B}_{12}\text{F}_{12}$ and dehydration of $\text{K}_2(\text{H}_2\text{O})_2\text{B}_{12}\text{F}_{12}$ that were monitored by TGA-MS are shown in Figure 6.14. During the hydration cycles, the He carrier gas was

bubbled through water at 23(1) °C before entering the instrument. (Since the vapor pressure of water is 21(1) torr at 23(1) °C,²¹² the nominal partial pressure of water in the TGA or DSC sample chamber was assumed to be 21(1) torr.) To induce dehydration, the carrier gas was switched back to dry He. Since $K_2B_{12}F_{12}$ is known to be stable up to 550 °C,²⁹ the MS instrumentation was not being used to detect decomposition gases but only to monitor how quickly water vapor entered or left the sample chamber when the 23(1) °C water bubbler was included or excluded, respectively, from the carrier gas tubing (i.e., other than water vapor and small amounts of atmospheric gases, no other gases were observed).

The following observations and interpretations can be made about the black TGA trace in Figure 6.14 (and other results from similar experiments with samples that varied in size from 5 to 15 mg; note that the entire black trace in Figure 6.14 corresponds to 25.0(5) °C). First, there was almost no delay (< 1 min) in the appearance of an MS ion-current indicative of significant amounts of water vapor in the sample chamber after the carrier gas was switched from dry helium to helium that had been bubbled through water at 23(1) °C (compare the black and red portions of the traces for region **d** in Figure 6.14; the small apparent tick marks on the black trace indicate an apparent mass change when the carrier gas was changed, presumably due to a small temporary pressure change in the system; there is also an artificial apparent temporary decrease in mass due to the introduction into the carrier gas of the small amount of higher-density air in the water-filled bubbler). Second, there was a variable delay of ca. 2–10 minutes before a mass decrease was observed after the carrier gas was switched back to dry He (presumably due to relatively slow flushing of $H_2O(g)$ from the sample chamber; as discussed below, dehydration only occurred when $P(H_2O) \leq 7$ torr). Third, a small amount of water adhered to the surface of the $K_2(H_2O)_2B_{12}F_{12}$ crystallites when the sample was exposed to helium containing 21(1) Torr $H_2O(g)$. The amount of adsorbed water was ca. 0.014–0.030 equiv. H_2O per K^+ , depending on the surface area of the sample. This would constitute,

approximately, a monolayer of H₂O molecules on the surface of the crystallites if they were cubes with ca. 1 μm edges, a reasonable assumption based on the SEM images shown in Figure 6.15, and this amount of water disappeared rapidly when the sample was exposed to dry He (regions **b**, **b'**, and **f**). Fourth, as discussed above, K₂(H₂O)₂B₁₂F₁₂ was not converted to K₂(H₂O)₄B₁₂F₁₂ in the presence of 21(1) Torr H₂O(g), even after many hours or (not shown) days. Fifth, K₂B₁₂F₁₂ was rapidly hydrated to K₂(H₂O)₂B₁₂F₁₂ in the presence of 21(1) Torr H₂O(g) when $T_{\text{initial}} = 25(1) \text{ }^{\circ}\text{C}$, in 18 min for the hydration that began at 20 min (region **a**) and in 12 min for the hydration that began at 218 min (region **d**). Sixth, K₂(H₂O)₂B₁₂F₁₂ was rapidly dehydrated to K₂B₁₂F₁₂ in an atmosphere of dry He when $T_{\text{initial}} = 25.0(5) \text{ }^{\circ}\text{C}$, in 75 min for the dehydration that began at 75 min (region **c**) and in ca. 100 min for the dehydration that began at 218 min (region **g**; these times are for >98% dehydration).

A simple, albeit crude, kinetic figure of merit for the hydrations and dehydrations is the maximum positive or negative slopes of the TGA trace in the regions corresponding to hydration or dehydration, respectively. For example, the maximum positive slope in hydration region **d** is 1.1% min⁻¹. Note that the units of the slopes refer to the % change in mass for the complete *de*hydration process, which is 9.24%. Therefore, a maximum positive slope of 1.1% min⁻¹ corresponds to an instantaneous rate of 12% of the complete hydration reaction per minute. The maximum negative slopes in dehydration regions **c** and **g** are -0.22 and -0.19% min⁻¹, respectively, the absolute values of which are ca. 5 times smaller than the hydration maximum slope of 1.1% min⁻¹.

The TGA-MS experiments showed that the rates of mass decrease and mass increase for the solid-state equilibrium $\text{K}_2(\text{H}_2\text{O})_2\text{B}_{12}\text{F}_{12}(\text{s}) \rightleftharpoons \text{K}_2\text{B}_{12}\text{F}_{12}(\text{s}) + 2 \text{H}_2\text{O}(\text{g})$ varied as a function of (i) sample temperature at constant $P(\text{H}_2\text{O})$ and (ii) carrier-gas flow rate. Each of these will now be briefly discussed. A particular sample of K₂B₁₂F₁₂ had an average hydration maximum slope of 2.4% min⁻¹ and an average dehydration maximum negative slope of -0.48% min⁻¹ at 25.0(5) °C (three complete cycles). When the

temperature was changed to a constant 35.0(5) °C and $P(\text{H}_2\text{O})$ was still 21(1) Torr, the hydration maximum slope was only 0.17% min^{-1} , more than 10 times smaller than at the lower temperature, and the dehydration maximum negative slope in the presence of dry He was $-0.96\% \text{ min}^{-1}$, twice as large as at the lower temperature. This is a sensible result because, at some elevated temperature, anhydrous $\text{K}_2\text{B}_{12}\text{F}_{12}$ should not absorb water even with $P(\text{H}_2\text{O}) = 21(1)$ Torr. In a subsequent non-isothermal TGA experiment, this temperature was determined to be 52 °C.

Figure 6.16 shows the portion of region **d** in Figure 6.14 from 220 to 240 min, which represents ca. 90% of the total hydration process. It also shows that this portion of the curve could not be modeled with a single exponential function or with a sum of two exponential functions, both of which have been shown to model water sorption for microporous materials.²¹³ It is possible that this could be because $P(\text{H}_2\text{O})$ was not constant throughout this portion of the curve and/or because the reaction rates were limited by the rate at which water vapor was delivered to the sample. To address this possibility, a series of hydrations and dehydrations of a given sample were carried out in which the carrier-gas flow rate was either 30, 60, 88, or 100 mL min^{-1} . The results, shown in Figure 6.17, clearly indicate that both the hydration and dehydration reactions were indeed limited by the rate at which $\text{H}_2\text{O}(g)$ was delivered to or swept away from the microcrystal surfaces in these experiments. Therefore, the chemically-relevant processes of (i) absorption of H_2O to $\text{K}_2\text{B}_{12}\text{F}_{12}$ unit cells at the surface of the microcrystalline sample, (ii) desorption of H_2O from $\text{K}_2(\text{H}_2\text{O})_2\text{B}_{12}\text{F}_{12}$ unit cells at the surface of the microcrystalline sample, and (iii) the diffusion of H_2O across the constantly moving $\text{K}_2(\text{H}_2\text{O})_2\text{B}_{12}\text{F}_{12}(s)/\text{K}_2\text{B}_{12}\text{F}_{12}(s)$ phase boundary *must be faster* than the fastest "hydration" and "dehydration" rates that were measured in these experiments. Note that the fastest hydration of a sample of $\text{K}_2\text{B}_{12}\text{F}_{12}$ was complete in ca. 4 min and the fastest dehydration was complete in ca. 18 min, both at the maximum carrier-gas flow rate possible with the TGA instrument used in this work.

In order to lower $P(\text{H}_2\text{O})$ in the TGA carrier gas, He was bubbled through various saturated aqueous salt solutions at 23(1) °C. These experiments revealed that $\text{K}_2(\text{H}_2\text{O})_2\text{B}_{12}\text{F}_{12}$ is not stable at 25.0(5) °C when $P(\text{H}_2\text{O}) \leq 7$ torr (this is reported to be the vapor pressure of a saturated aqueous solution of MgCl_2 at ca. 23 °C;²¹⁴ it was verified that it is 6(1) torr at 23(1) °C by tensimetry). Separate tensimetric titrations of solid $\text{K}_2\text{B}_{12}\text{F}_{12}$ with water vapor showed that the equilibrium value of $P(\text{H}_2\text{O})$ above a mixture of $\text{K}_2\text{B}_{12}\text{F}_{12}(s)$ and $\text{K}_2(\text{H}_2\text{O})_2\text{B}_{12}\text{F}_{12}(s)$ is 6.1(3) torr at 25(1) °C.

In a future kinetic study, lower temperatures and/or more sophisticated instrumentation will be needed to study the $\text{K}_2(\text{H}_2\text{O})_{0,2}\text{B}_{12}\text{F}_{12}(s)$ system (and to study similar $[\text{ML}_n]_x\text{B}_{12}\text{F}_{12}$ solvates that are described in Chapter 3). At this point in time, it can be only concluded that the equilibrium $\text{K}_2(\text{H}_2\text{O})_2\text{B}_{12}\text{F}_{12}(s) \rightleftharpoons \text{K}_2\text{B}_{12}\text{F}_{12}(s) + 2 \text{H}_2\text{O}(g)$ involves, in principle, at least three elementary processes that are too fast to measure by straightforward isothermal TGA techniques at 25.0(5) °C. What sets $\text{K}_2(\text{H}_2\text{O})_2\text{B}_{12}\text{F}_{12}$ apart from other hydrates of potassium, and perhaps from most other hydrated metal ions in the solid state at 25 °C, is that this *crystalline* dihydrate is dehydrated extremely rapidly to the *crystalline* anhydrous salt and is even more rapidly rehydrated back to the *crystalline* dihydrate. The rapidity with which these solid-state transformations occur is especially noteworthy because $\text{K}_2\text{B}_{12}\text{F}_{12}$ is not a microporous solid (as discussed above, it has a close-packed structure³⁷). To put this into perspective, the dihydrate $\text{K}_2(\text{H}_2\text{O})_2(\text{SnMe}_2\text{F}_4)$, which has nearly the same $\text{K}_2(\text{H}_2\text{O})_2^{2+}$ core as $\text{K}_2(\text{H}_2\text{O})_2\text{B}_{12}\text{F}_{12}$ (see Figure 6.7), undergoes dehydration between 75 and 100 °C,¹⁸⁸ the monohydrate $\text{K}(\text{H}_2\text{O})\text{MnPO}_4$, in which the H_2O ligand bridges the K^+ and Mn^{2+} ions,²¹⁵ undergoes dehydration between 120 and 180 °C,²⁶ the monohydrate $\text{K}_2(\text{H}_2\text{O})\text{AlF}_5$, in which the H_2O ligand bridges two K^+ ions with K–O distances of 2.818(3) and 2.821(3) Å, undergoes dehydration between 80 and 100 °C (and the anhydrous compound requires several days to rehydrate),²¹⁶ the monohydrate $\text{K}(\text{H}_2\text{O})\text{Zn}_{2.5}\text{V}_2\text{O}_7(\text{OH})_2$, with very long K–O distances of 3.44(2) and 3.64(4) Å, undergoes dehydration between 100 and 210 °C,²¹⁷ and a fully-

dehydrated synthetic potassium gallosilicate natrolite, which *is* microporous, required between one and two weeks to undergo rehydration at 25 °C.⁸

D. Solid-State Diffusion of H₂O in Fully-Hydrated K₂(H₂O)₂B₁₂F₁₂. Figure 6.18 shows the isothermal TGA trace for an experiment in which the carrier gas for a sample of fully-hydrated K₂(H₂O)₂B₁₂F₁₂ at 25.0(5) °C (relative mass 1.000) was switched from He containing 21(1) torr H₂O(g) to He containing 18(1) torr D₂O(g), whereupon the sample mass increased by 0.83% (theo. 0.84% for the composition change K₂(H₂O)₂B₁₂F₁₂ → K₂(D₂O)₂B₁₂F₁₂), and then was switched back to He containing 21(1) torr H₂O(g), whereupon the relative sample mass returned to 1.000. Since there was a lag time between switching the carrier gas from being bubbled through liquid H₂O at 23(1) °C to being bubbled through liquid D₂O at 23(1) °C (or vice versa) and the attainment of a constant-composition atmosphere in the sample chamber, only the latter one-half to two-thirds of the relevant portions of the mass (*m*) vs. time (*t*) TGA trace was attempted to fit to the single exponential equation $m \propto e^{-kt}$. Both fits resulted in the same value of the time constant, k 5.0(1)·10⁻⁴ s⁻¹.

A different sample, presumably with a different average particle size, resulted in exponential fits with a different value of k , 1.9·10⁻³ s⁻¹, which was also the same whether H₂O replaced D₂O in the solid sample or vice versa, as shown in Figure 6.19, and the isotopomer exchange was complete in less than 1 h at 25.0(5) °C. Furthermore, k was 1.9·10⁻³ s⁻¹ whether $P(\text{H}_2\text{O})$ was 21(1) torr or 16(1) torr, as also shown in Figure 6.19. These results strongly suggest that the measured rate *is* the rate of H₂O diffusion within fully hydrated K₂(H₂O)₂B₁₂F₁₂, although the "fully-hydrated" compound may contain a small percentage of water-vacancy defects.

Calculation of a diffusion coefficient was not attempted for the waters of hydration in K₂(H₂O)₂B₁₂F₁₂ in order to compare it to literature values for other compounds because a particular model for diffusion would have to be assumed and the sample would have to have a known, uniform particle size and particle morphology. However, it may be

possible to measure the diffusion coefficient by solid-state NMR techniques in future work. At the present time, the following qualitative comparisons can be made. The mineral lawsonite, $\text{CaAl}_2\text{Si}_2\text{O}_7(\text{OH})_2\cdot\text{H}_2\text{O}$, was reported to undergo $\text{H}_2\text{O}/\text{D}_2\text{O}$ and OH/OD exchange in the presence of 24 torr $\text{D}_2\text{O}(\text{g})$ at 382 °C in ca. 150 h,⁷ the four lattice H_2O molecules in a 4.6 mg single crystal of $\text{UO}_2(\text{NO}_3)(\text{H}_2\text{O})_2\cdot 4 \text{H}_2\text{O}$ were reported to undergo $\text{H}_2\text{O}/\text{D}_2\text{O}$ exchange in ca. 36 min at 25 °C (but the two coordinated H_2O ligands did not undergo exchange to any extent under these conditions),²¹⁸ and the exchange of all 12 H_2O molecules in microcrystalline β -cyclodextrin dodecahydrate with either $\text{D}_2\text{O}(\text{g})$ or $\text{H}_2^{18}\text{O}(\text{g})$ at 25 °C was 90+% complete after ca. 1 h or longer depending on particle size.^{19,219} To provide an additional example, the initial rate of exchange of $\text{D}_2\text{O}(\text{g})$ with microcrystalline $\text{CuSO}_4\cdot 5 \text{H}_2\text{O}$ was measured, and found that only 0.15 equiv D_2O had exchanged with the five waters of hydration after two hours at 25.0(5) °C.

E. The Concept of Latent Porosity. The facile dehydration and rehydration, and $\text{H}_2\text{O}/\text{D}_2\text{O}$ or $\text{H}_2\text{O}/\text{H}_2^{18}\text{O}$ exchange, of $\text{K}_2(\text{H}_2\text{O})_2\text{B}_{12}\text{F}_{12}$ at 25 °C suggests that microporosity is not a requirement for rapid diffusion of reactive gases in solids. The close-packed structure of crystalline $\text{K}_2\text{B}_{12}\text{F}_{12}$ shows that it has no empty spaces, let alone channels, the size of H_2O molecules²²⁰ (this was determined using the program PLATON²²¹). The lattice can increase in volume by 10.8%, accommodating two H_2O molecules, in 4 min or less at 25 °C. This is an example of "virtual" or "latent" porosity, the rapid creation of space to accommodate reactive gases on demand. This concept is related to, but distinct from, recent work on solids that are already microporous but that require flexible lattices to open existing pores so that they are accessible to gas molecules, as in the recent elegant study by Shimizu and co-workers.²⁷ In that work, involving Ba^{2+} cations and organosulfonate anions, the dehydrated phase is stable at 550 °C (like $\text{K}_2\text{B}_{12}\text{F}_{12}$) and the facile opening and closing of pore spaces is believed to be a function of "the diffuse ionic nature of the intermolecular interactions and the adaptable coordination preferences of both metal and ligand components."²⁷ Compounds containing

metal ions from throughout the periodic table and the large, highly-symmetric, robust, and superweak fluoroanion $B_{12}F_{12}^{2-}$ may provide a new class of reactive solids with latent porosity.

Table 6.1. Calculated and Experimental Values for Potassium-Water Complexation

species of reaction	K–O distance(s) (Å) or ΔH (kJ mol ⁻¹)		
	DFT, this work ^a	DFT, ref (¹⁸¹) ^b	exp. values ^c
K(H ₂ O) ⁺	2.617	2.654	
K(H ₂ O) ₂ ⁺	2.654	2.688	
K ₂ (H ₂ O) ₂ ²⁺	2.999 ^d		
K ₂ (H ₂ O) ₄ ²⁺	2.997(b), 2.629(t) ^e		
K ⁺ + H ₂ O → K(H ₂ O) ⁺	-76.3	-72.8	-75.0 ^f
K(H ₂ O) ⁺ + H ₂ O → K(H ₂ O) ₂ ⁺	-68.1	-61.5	-67.4 ^f
2 K(H ₂ O) ⁺ → K ₂ (H ₂ O) ₂ ²⁺	+231.5		
K ₂ (H ₂ O) ₂ ²⁺ + 2 H ₂ O → K ₂ (H ₂ O) ₄ ²⁺	-162.4		
2 K(H ₂ O) ₂ ⁺ → K ₂ (H ₂ O) ₄ ²⁺	+205.3		
K ₂ B ₁₂ F ₁₂ (s) + 2 H ₂ O(g) → K ₂ (H ₂ O) ₂ B ₁₂ F ₁₂ (s)			-110(1) ^g
2 H ₂ O(g) → 2 H ₂ O(s)			-99(1) ^h

All reactions are in the gas phase unless otherwise noted. ^a B2PLYP-D/(aug)-def2-QZVPP. ^b B3LYP/6-31++G** with counterpoise corrected geometry optimizations. ^c High-pressure mass spectrometry; refs ^{182,183}. ^d K...K = 4.886 Å. ^e K...K = 4.835 Å. ^f This work. ^g Ref. ¹⁸⁴.

Table 6.2. IR Stretching Frequencies for Water Vapor and Water Coordinated to Potassium Cations^a

compound	K–O distance(s), Å	$\nu(\text{OH})$ and/or $\nu(\text{OD})$, cm^{-1}	refs. ^b
$\text{H}_2\text{O}(g)$	—	3756, 3657	197
$\text{H}_2^{18}\text{O}(g)$	—	3742, 3650	198
$\text{HDO}(g)$	—	3723, 2739	199
$\text{D}_2\text{O}(g)$	—	2789, 2666	193
$[\text{Ar}-\text{K}-\text{OH}_2]^+(g)$		3710, 3636 ^c	194
$\text{K}_2(\text{H}_2\text{O})_2\text{B}_{12}\text{F}_{12}(s)$	2.7698(6), 2.7716(6)	3638 sharp, 3576 sharp	tw
$\text{K}_2(\text{H}_2^{18}\text{O})_2\text{B}_{12}\text{F}_{12}(s)$		3624 sharp, 3569 sharp	tw
$\text{K}_2(\text{HDO})_2\text{B}_{12}\text{F}_{12}(s)$		3604 sharp, 2653 sharp	tw
$\text{K}_2(\text{D}_2\text{O})_2\text{B}_{12}\text{F}_{12}(s)$		2700 sharp, 2616 sharp	tw
$\text{K}_2(\text{H}_2\text{O})\text{SnCl}_4(s)$	2.650×2	3538 broad, 3439 broad	190, 195
$\text{K}_2(\text{H}_2\text{O})\text{HgCl}_4(s)$	$2.855(8) \times 2$	3505 broad, 3404 broad	191, 196
$\text{K}_2(\text{H}_2\text{O})_2(\text{SnF}_4(\text{CH}_3)_2)(s)$	2.74(1), 2.83(1)	3425 broad ^e	188

^a All stretching frequencies are from IR spectra at room temperature unless otherwise noted; tw = this work; O = ^{16}O ; sharp is defined here as $\Delta\nu_{1/2} \leq 30 \text{ cm}^{-1}$; broad is defined here as $\Delta\nu_{1/2} \geq 50 \text{ cm}^{-1}$. ^b The first reference is for the K–O distance(s) (if any); the second reference is for the stretching frequencies; a single reference is for both. ^c Temperature = 130 K. ^d DFT predicted $\nu(\text{OH})$ values; the structure used for the calculation was frozen at the X-ray coordinates. ^e Only one very broad band was observed.

Table 6.3. Results of the fits (red curves) in Figure 6.17 ($m \propto e^{-kt}$)

region	type of reaction	carrier gas flow rate, mL min ⁻¹	10 ³ k, s ⁻¹
a	dehydration	60	7.47(3)
c	dehydration	60	8.31(4)
i	dehydration	88	9.83(6)
e	dehydration	100 ^a	17.5(2) ^a
g	dehydration	100	12.0(1)
d	hydration	30	26(1)
b	hydration	60	62.5(1)
h	hydration	88	61(1)
f	hydration	100	82(1)
j	hydration	100	75(1)

^a Part of the dehydration that includes region **e** was carried out with a flow rate of 30 mL min⁻¹.

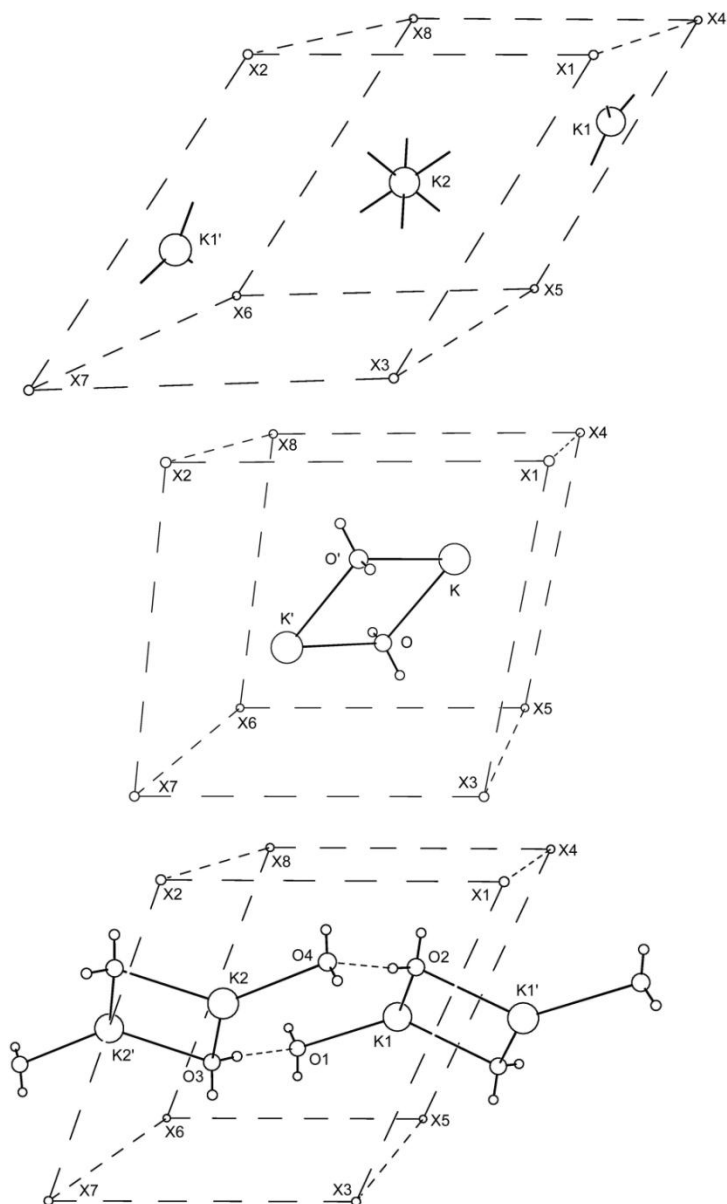


Figure 6.1. The B_{12} centroids (\odot 's, X_n) and $K_2(H_2O)_n^{2+}$ dimers in $K_2B_{12}F_{12}$ (top), $K_2(H_2O)_2B_{12}F_{12}$ (middle) and $K_2(H_2O)_4B_{12}F_{12}$ (bottom). The $X1\cdots X2$, $X1\cdots X3$, and $X1\cdots X4$ distances (\AA) are 7.517, 8.236, and 8.207 in $K_2B_{12}F_{12}$, 7.276, 7.295, and 7.276 in $K_2(H_2O)_2B_{12}F_{12}$, and 6.915, 8.598, and 8.399 in $K_2(H_2O)_4B_{12}F_{12}$. Note that the $X1\cdots X8$ and $X3\cdots X6$ distances in $K_2B_{12}F_{12}$ are 7.204 \AA (the \odot 's are approximately hexagonal close-packed in this structure). The small vectors radiating from the K^+ ions in $K_2B_{12}F_{12}$ point at the closest set of \odot 's (K1 and K1' are in trigonal holes in the close-packed layers and K2 is in an O_h hole).

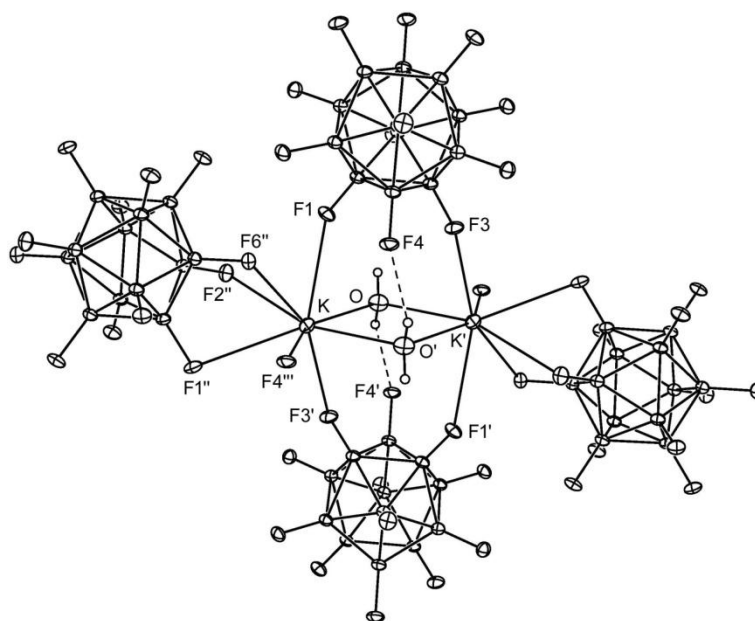


Figure 6.2. The structure of $\text{K}_2(\text{H}_2\text{O})_2\text{B}_{12}\text{F}_{12}$ (50% probability ellipsoids except for H atoms). For clarity, only four of the eight $\text{B}_{12}\text{F}_{12}^{2-}$ anions that form a pseudo-cubic array around the $\text{K}_2(\text{H}_2\text{O})_2^{2+}$ dimer are shown. Selected interatomic distances (\AA) and angles (deg): K–O, 2.7698(6); K–O', 2.7716(6); K \cdots F1, 2.8251(4); K \cdots F1'', 3.0368(4); K \cdots F2'', 2.7790(4); K \cdots F3', 2.5984(4); K \cdots F4''', 3.1593(4); K \cdots F6'', 2.7423(4); F4 \cdots H1', 2.17(1); F4 \cdots H1'–O', 154(1); K \cdots K', 4.2529(3) (not shown: F5'''' \cdots H2, 2.12(1), F5'''' \cdots H2–O, 165(1)).

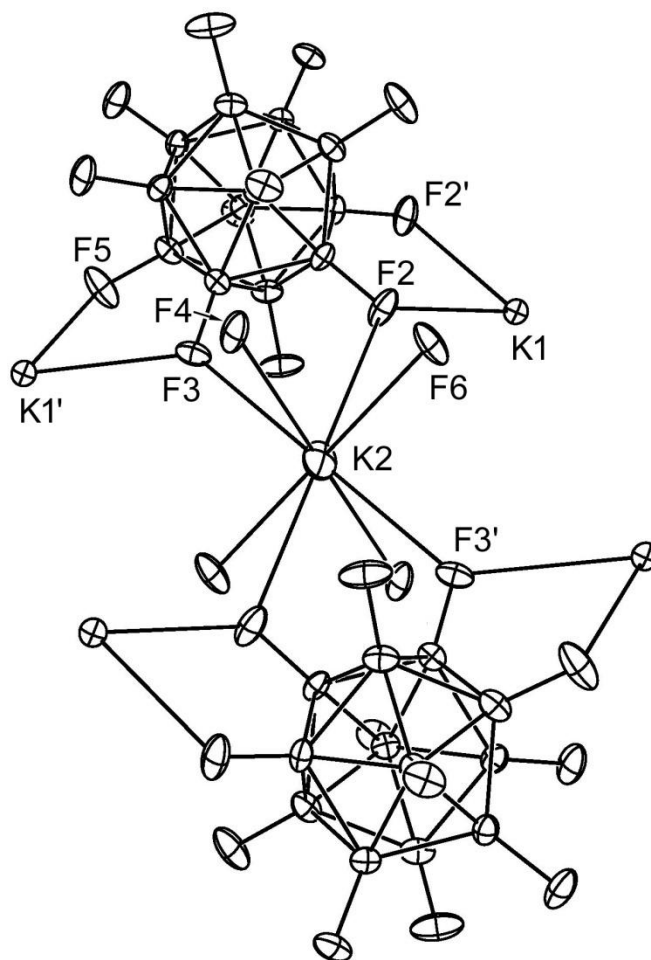


Figure 6.3. Part of the structure of $K_2B_{12}F_{12}$ (50% probability ellipsoids), showing the bridges formed between the K1 and K2 cations by the $B_{12}F_{12}^{2-}$ anions. The K2 cation is located on an inversion center and the K1 and K2 cations are rigorously coplanar. Selected interatomic distances (Å): K1 \cdots F2 and K1 \cdots F2', 2.734(2); K1' \cdots F3, 2.880(2); K1' \cdots F5, 2.612(2); K2 \cdots F2, 3.324(2); K2 \cdots F3, 3.147(2); K2 \cdots F4, 2.819(2); K2 \cdots F6, 2.615(2); K1 \cdots K2, 5.543(1); K1' \cdots K2, 5.421(1).

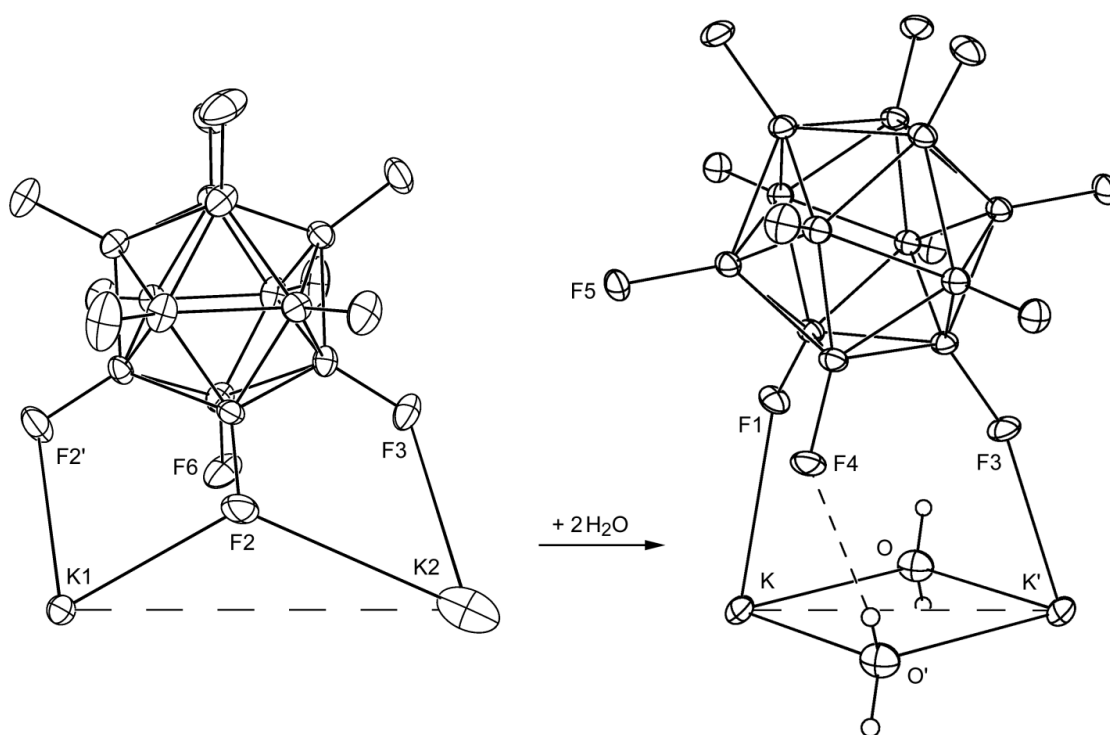


Figure 6.4. Parts of the structures of $\text{K}_2\text{B}_{12}\text{F}_{12}$ (left) and $\text{K}_2(\text{H}_2\text{O})_2\text{B}_{12}\text{F}_{12}$ (right; 50% probability ellipsoids). The separation of the K^+ ions in each of the two drawings is to scale ($\text{K1}\cdots\text{K2} = 5.421(1) \text{ \AA}$, $\text{K}\cdots\text{K}' = 4.2529(3) \text{ \AA}$). A minor rotation of pairs of $\text{B}_{12}\text{F}_{12}^{2-}$ anions (the one shown in each drawing and its symmetry-related partner) is involved in the solid-state equilibrium $\text{K}_2\text{B}_{12}\text{F}_{12}(\text{s}) + 2\text{H}_2\text{O}(\text{g}) \rightleftharpoons \text{K}_2(\text{H}_2\text{O})_2\text{B}_{12}\text{F}_{12}(\text{s})$ (F2, F2', F3, and F6 on the left become F4, F5, F3, and F1 on the right).

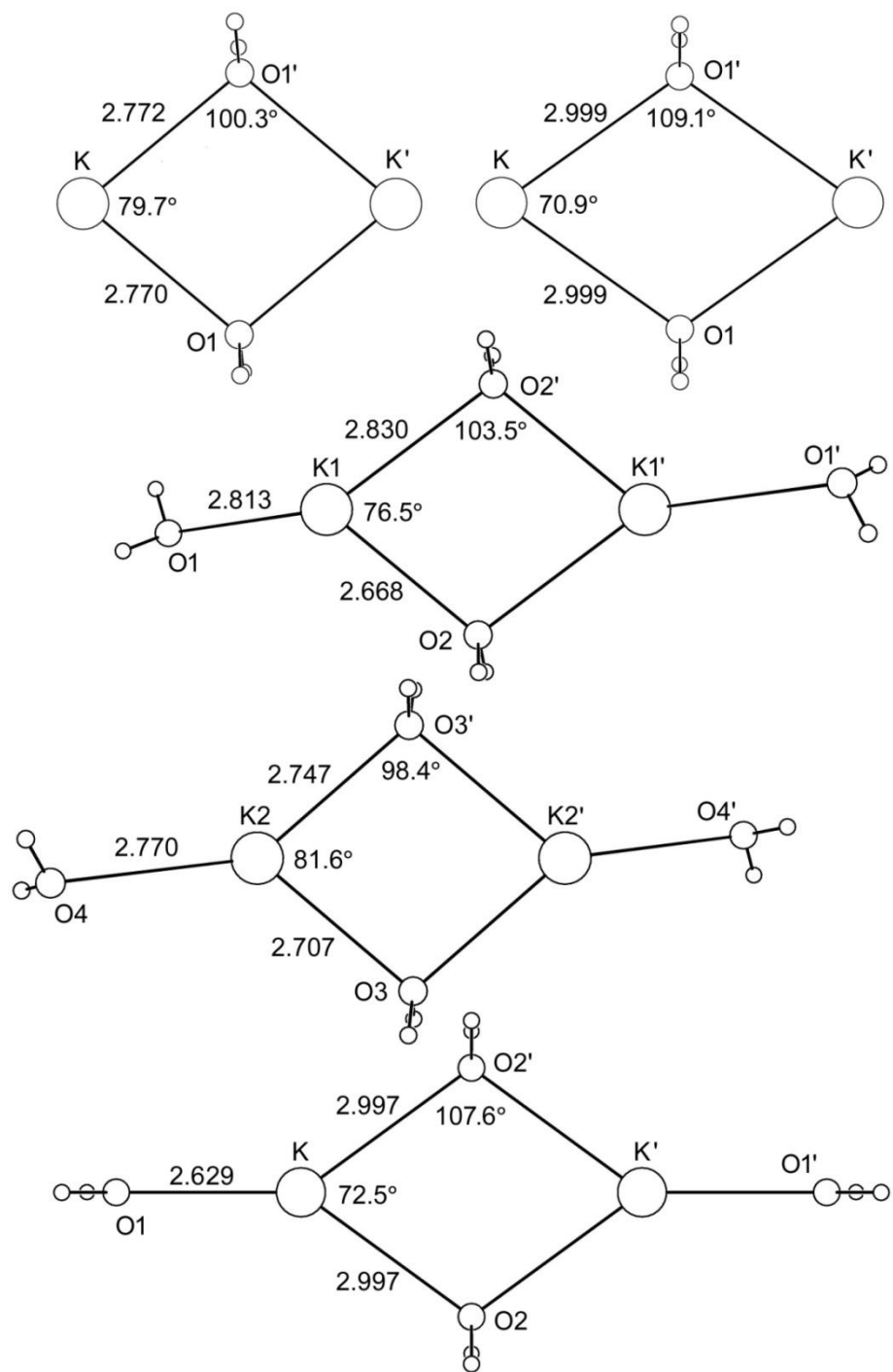


Figure 6.5. DFT-predicted (top right; bottom) and X-ray structures of $K_2(H_2O)_n^{2+}$ dimers.

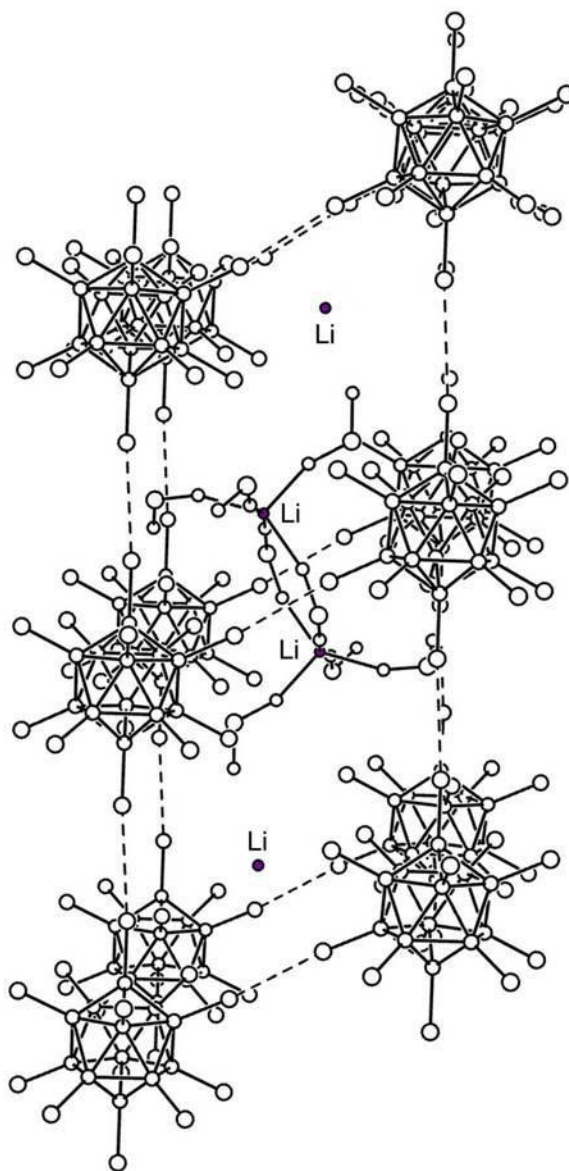


Figure 6.6. The structure of $\text{Li}_2(\text{SO}_2)_8\text{B}_{12}\text{Cl}_{12}$ (redrawn from the coordinates published in ref. ¹³⁸). For clarity, two of the four Li^+ cations are shown without their complement of SO_2 ligands (there is only one type of Li^+ cation in this structure). Several $\text{Cl}\cdots\text{Cl}$ interactions of 3.334 and 3.354 Å between $\text{B}_{12}\text{Cl}_{12}^{2-}$ anions are shown with dotted lines (twice the van der Waals radius of a Cl atom is 3.50 Å). There are no such interactions shorter than 3.50 Å in the direction perpendicular to the plane of the page.

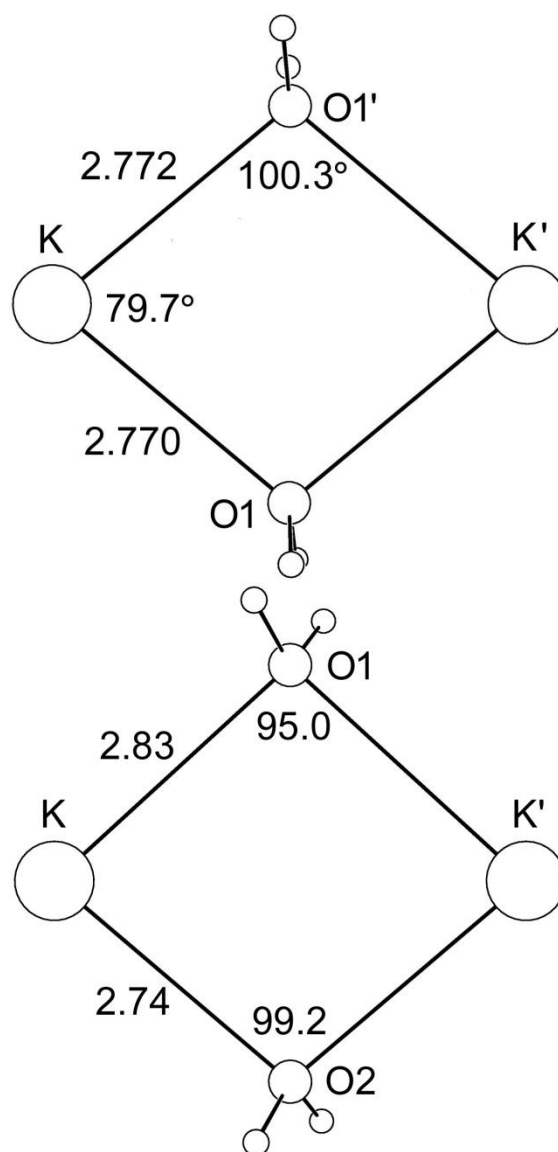


Figure 6.7. Comparison of the $\text{K}_2(\text{H}_2\text{O})_2^{2+}$ dications in $\text{K}_2(\text{H}_2\text{O})_2\text{B}_{12}\text{F}_{12}$ (left) and $\text{K}_2(\text{H}_2\text{O})_2(\text{trans-SnF}_4(\text{CH}_3)_2)$. The $\text{K}\cdots\text{K}'$ distances are 4.2529(3) Å in $\text{K}_2(\text{H}_2\text{O})_2\text{B}_{12}\text{F}_{12}$ and 3.939(1) Å in $\text{K}_2(\text{H}_2\text{O})_2(\text{trans-SnF}_4(\text{CH}_3)_2)$.

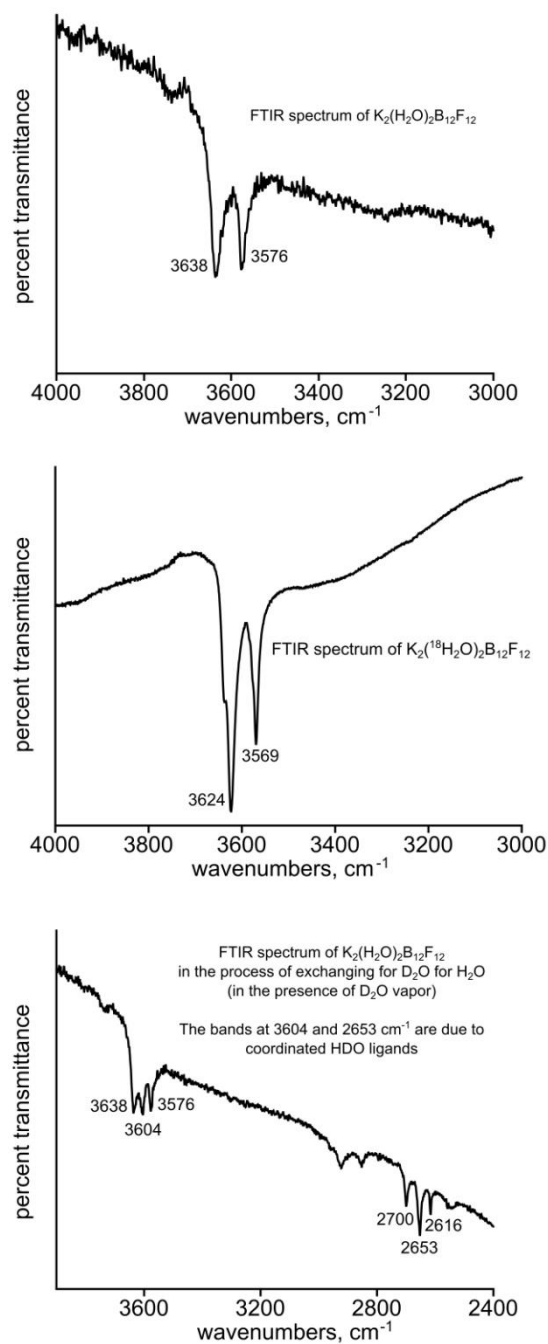


Figure 6.8. FTIR spectra of $K_2(H_2O)_2B_{12}F_{12}$, $K_2(H_2^{18}O)_2B_{12}F_{12}$, $K_2(D_2O)_2B_{12}F_{12}$, $K_2(HDO)_2B_{12}F_{12}$. The weak bands near 2900 cm^{-1} in the lower spectrum are due to a small amount of Superglue that was used to attach the sapphire window to the metal window mount (see ref. 66)

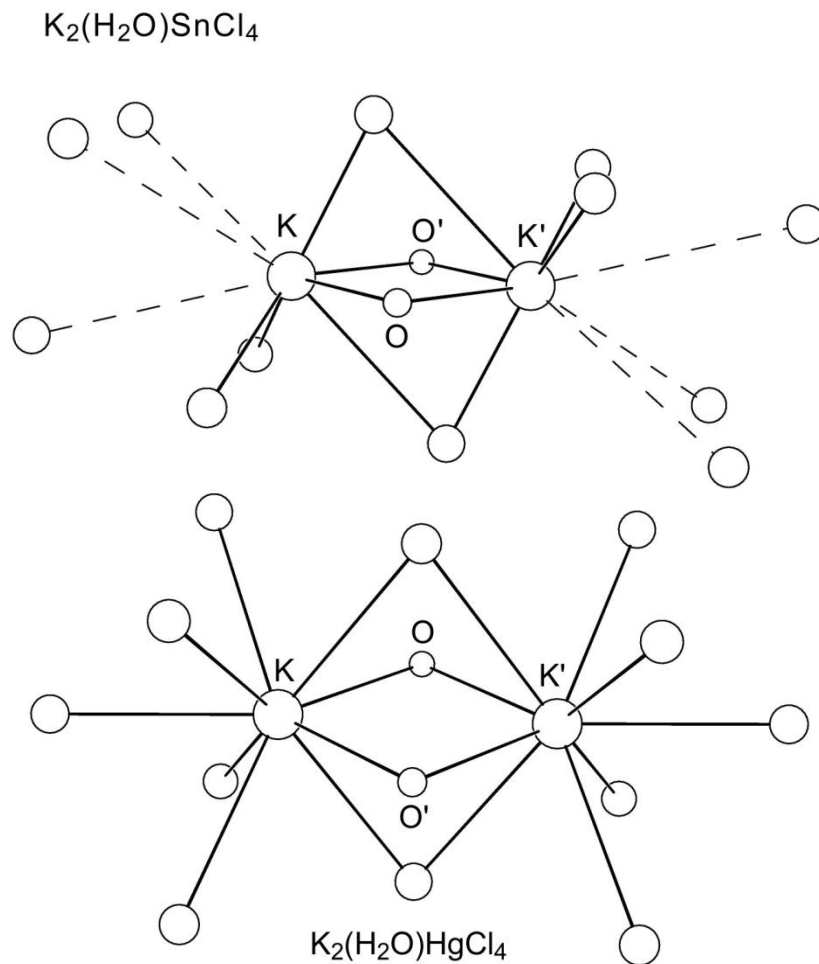


Figure 6.9. The $\text{K}_2(\text{H}_2\text{O})_2^{2+}$ moieties and their closest (unlabeled) Cl atoms in $\text{K}_2(\text{H}_2\text{O})\text{SnCl}_4$ (top) and $\text{K}_2(\text{H}_2\text{O})\text{HgCl}_4$ (bottom). Only one of the two types of K^+ ions are shown for each structure, and hydrogen atoms are not shown because their positions were not determined. The $\text{K}\cdots\text{K}'$ distances are 3.473 Å in $\text{K}_2(\text{H}_2\text{O})\text{SnCl}_4$ and 3.948(3) Å in $\text{K}_2(\text{H}_2\text{O})\text{HgCl}_4$. The $\text{K}-\text{Cl}$ distances are 2.642–3.996 Å in $\text{K}_2(\text{H}_2\text{O})\text{SnCl}_4$ and 3.248(5)–3.368(5) Å in $\text{K}_2(\text{H}_2\text{O})\text{HgCl}_4$. Standard errors are not available for the structure of the tin compound.

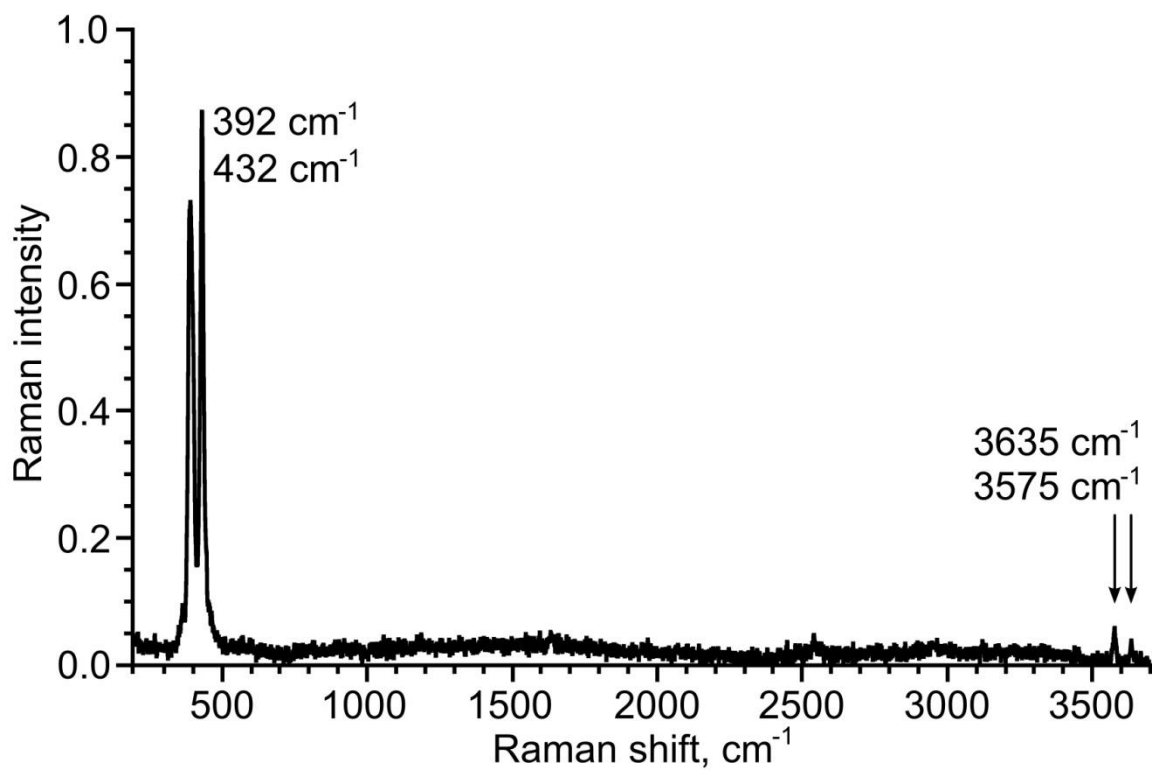


Figure 6.10. Raman spectrum of $\text{K}_2(\text{H}_2\text{O})_2\text{B}_{12}\text{F}_{12}$.

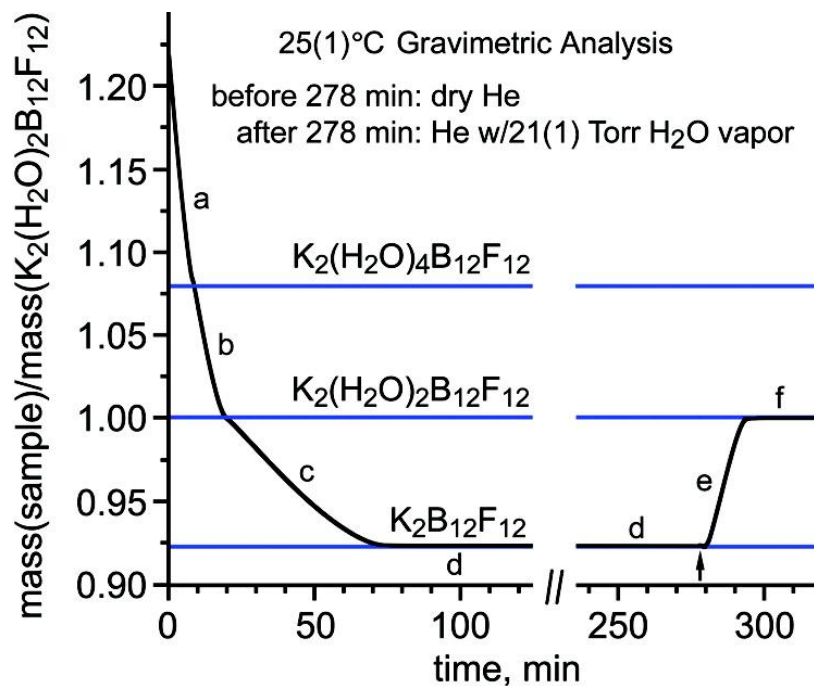


Figure 6.11. Constant-temperature gravimetric analysis of crushed wet crystals of $\text{K}_2(\text{H}_2\text{O})_4\text{B}_{12}\text{F}_{12}$ at 25.0(5) °C with dry helium as the carrier gas (60 mL min⁻¹) until 278 min and helium containing 21(1) Torr H₂O(g) after 278 min. The horizontal lines represent the relative molar masses of the three compounds (1.076 = 507.979 g mol⁻¹; 1.000 = 471.949 g mol⁻¹; and 0.9237 = 435.918 g mol⁻¹).

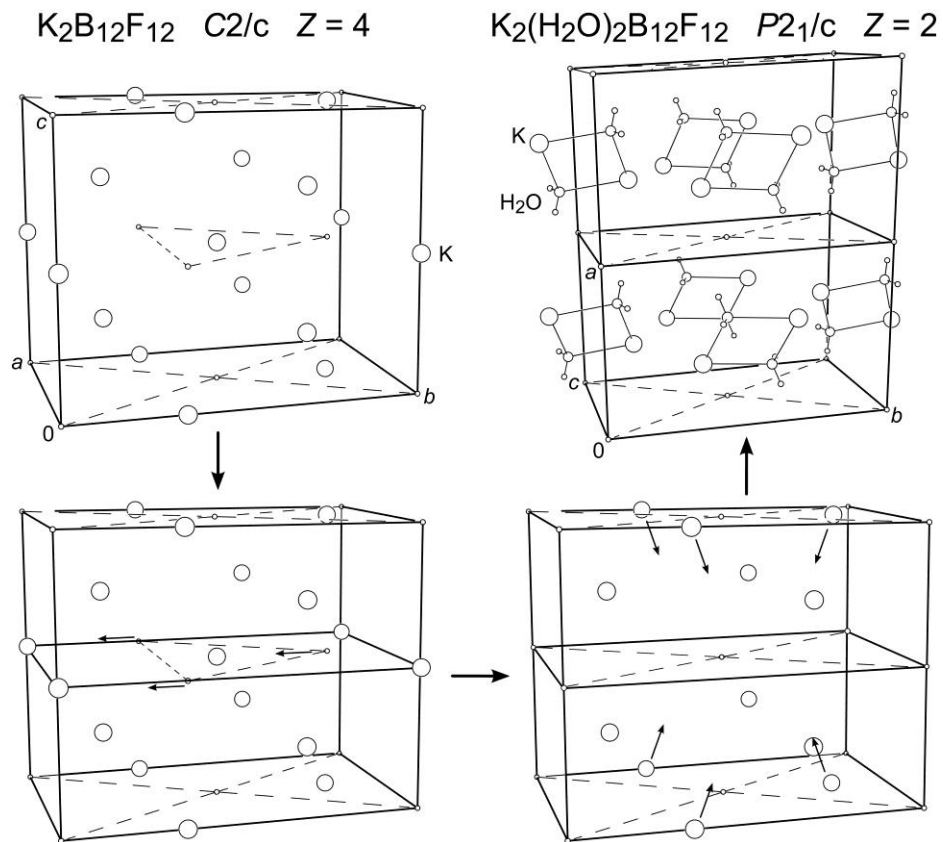


Figure 6.12. Relationship between the unit cell of $\text{K}_2\text{B}_{12}\text{F}_{12}$ (top left; monoclinic, $Z = 4$) and two unit cells of $\text{K}_2(\text{H}_2\text{O})_2\text{B}_{12}\text{F}_{12}$ (top right; monoclinic, $Z = 2$), and the idealized transformation of the former into the latter by the addition of water (note that no elementary-step mechanistic detail is implied). The small circles represent the B_{12} centroids. For $\text{K}_2\text{B}_{12}\text{F}_{12}$, $a = 8.207$, $b = 14.282$, and $c = 11.344$ Å; for $\text{K}_2(\text{H}_2\text{O})_2\text{B}_{12}\text{F}_{12}$, $2a = 14.591$, $b = 11.252$, and $c = 9.226$ Å. The 10.8% increase in unit cell volume for the reaction $\text{K}_2\text{B}_{12}\text{F}_{12(s)} + 2\text{H}_2\text{O}(g) \rightarrow \text{K}_2(\text{H}_2\text{O})_2\text{B}_{12}\text{F}_{12(s)}$ (i.e., 17.9 Å³ per H_2O molecule) is largely due to an increase in the "c" axis length of ca. 1.0 Å.

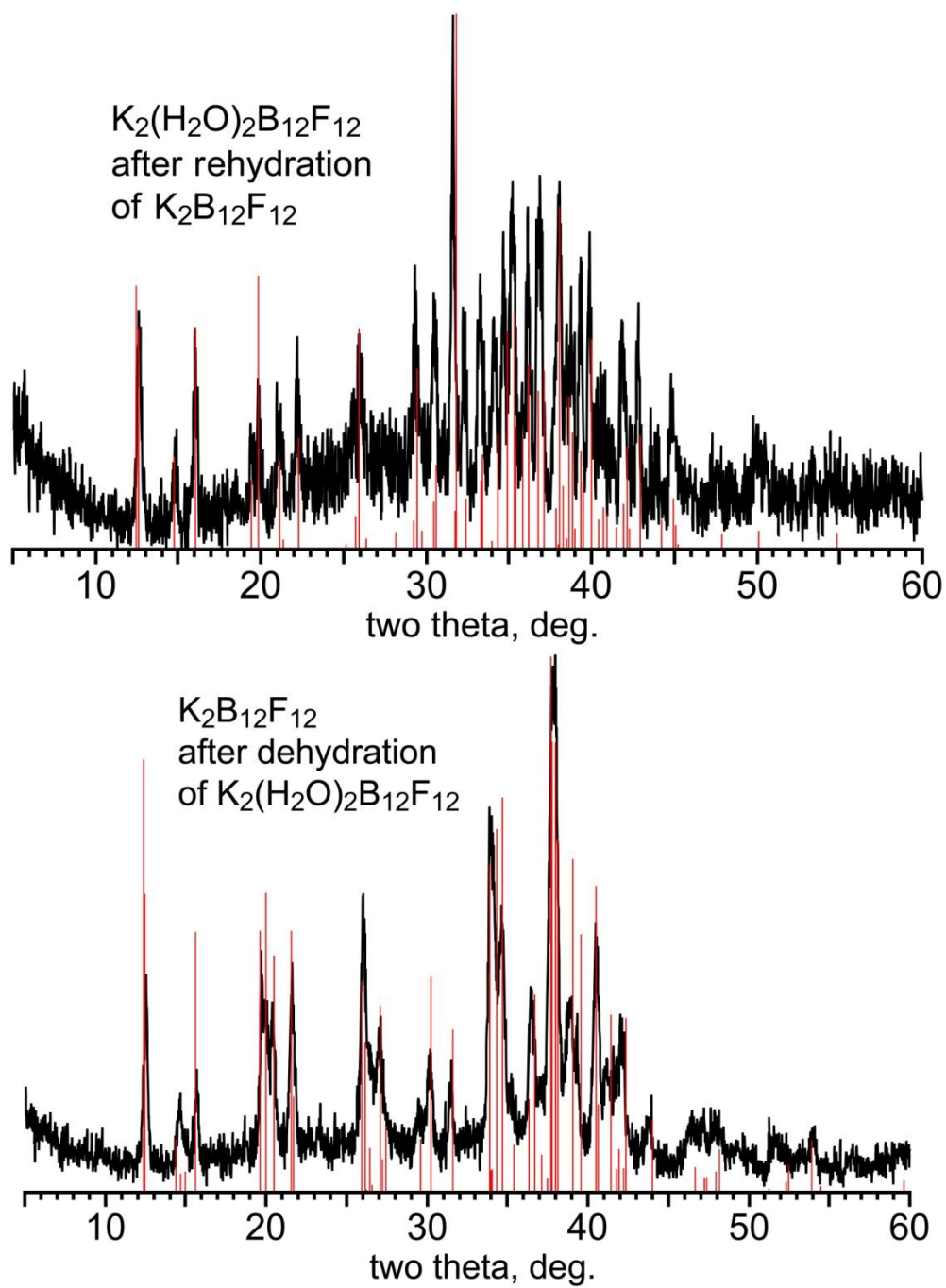


Figure 6.13. PXRD patterns for (top) $\text{K}_2(\text{H}_2\text{O})_2\text{B}_{12}\text{F}_{12}$ that had been formed by rehydration of crystalline $\text{K}_2\text{B}_{12}\text{F}_{12}$ and (bottom) $\text{K}_2\text{B}_{12}\text{F}_{12}$ that had been formed by dehydration of crystalline $\text{K}_2(\text{H}_2\text{O})_2\text{B}_{12}\text{F}_{12}$.

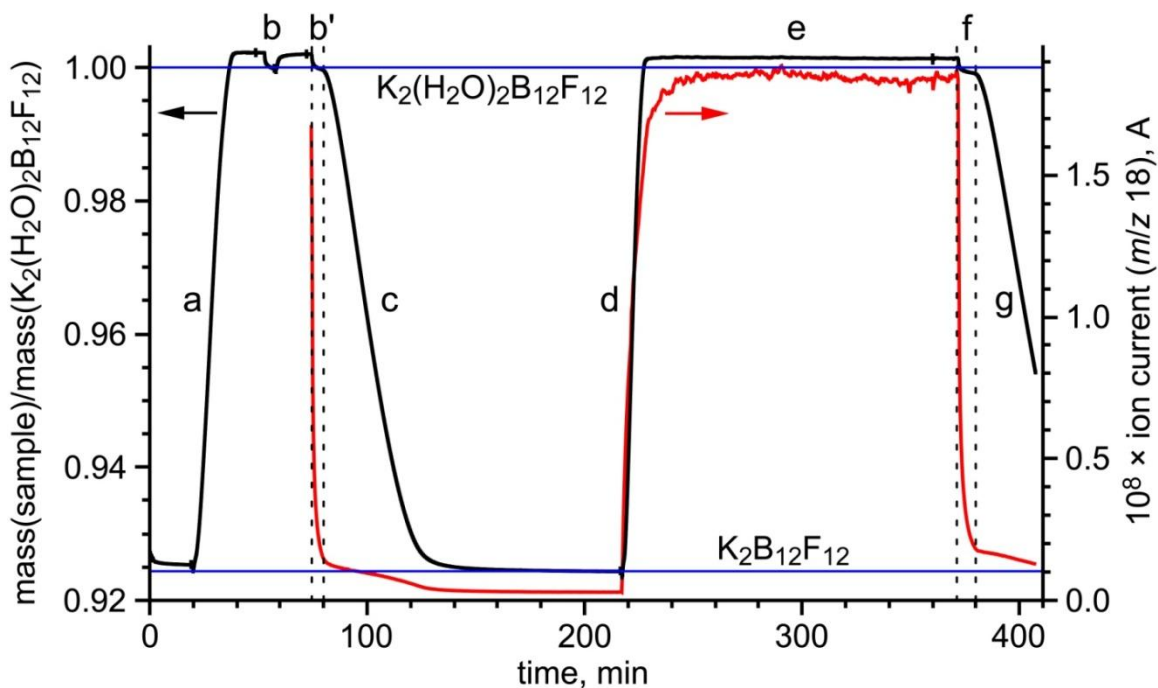


Figure 6.14. TGA-MS trace for two cycles of hydration/dehydration of $\text{K}_2\text{B}_{12}\text{F}_{12}$ at $25.0(5)^\circ\text{C}$. The black trace shows the relative mass of the sample; the red trace shows the mass-spectrometer response to $\text{H}_2\text{O}(g)$. The carrier gas was dry helium during dehydration and helium containing 21(1) Torr $\text{H}_2\text{O}(g)$ during hydration/rehydration (60 mL min^{-1}). The horizontal lines represent the relative molar masses of $\text{K}_2(\text{H}_2\text{O})_2\text{B}_{12}\text{F}_{12}$ ($1.000 = 471.949\text{ g mol}^{-1}$) and $\text{K}_2\text{B}_{12}\text{F}_{12}$ ($0.9237 = 435.918\text{ g mol}^{-1}$).

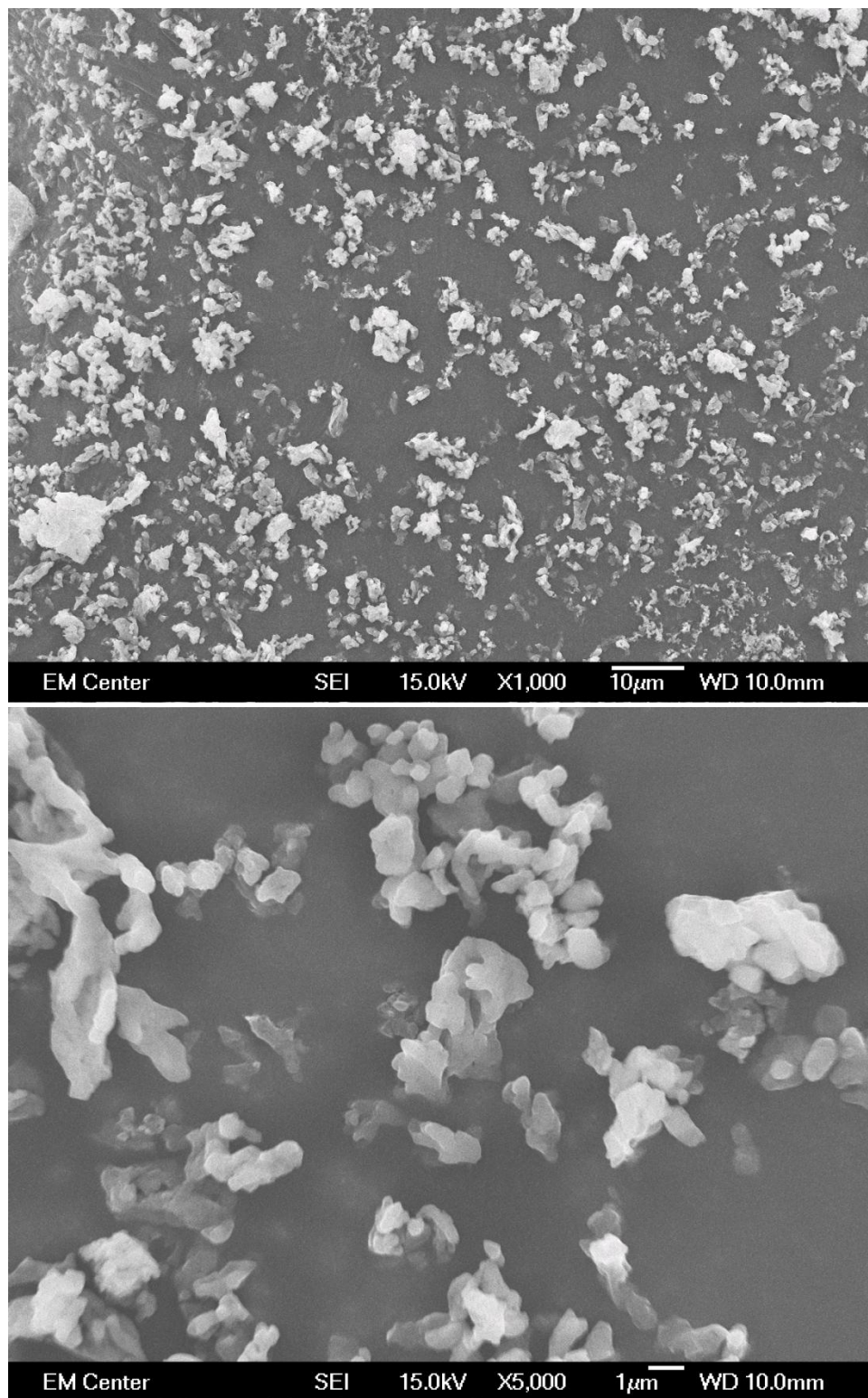


Figure 6.15. SEM images of a finely-ground sample of anhydrous $K_2B_{12}F_{12}$.

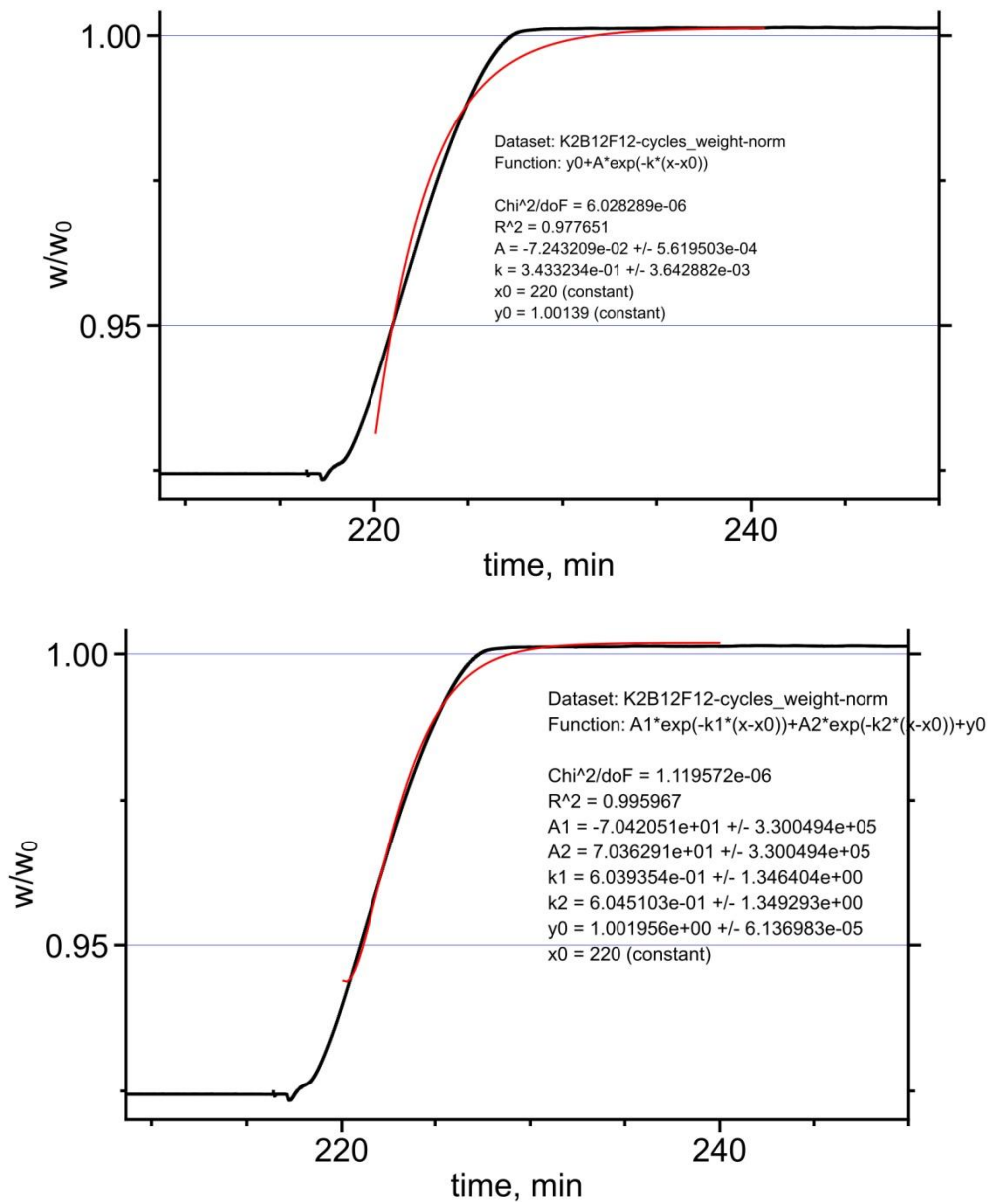


Figure 6.16. Attempts to fit hydration relative mass vs. time curve to either one exponential function or to a sum of two exponential functions. These data are from region **d** in Figure 6.14.

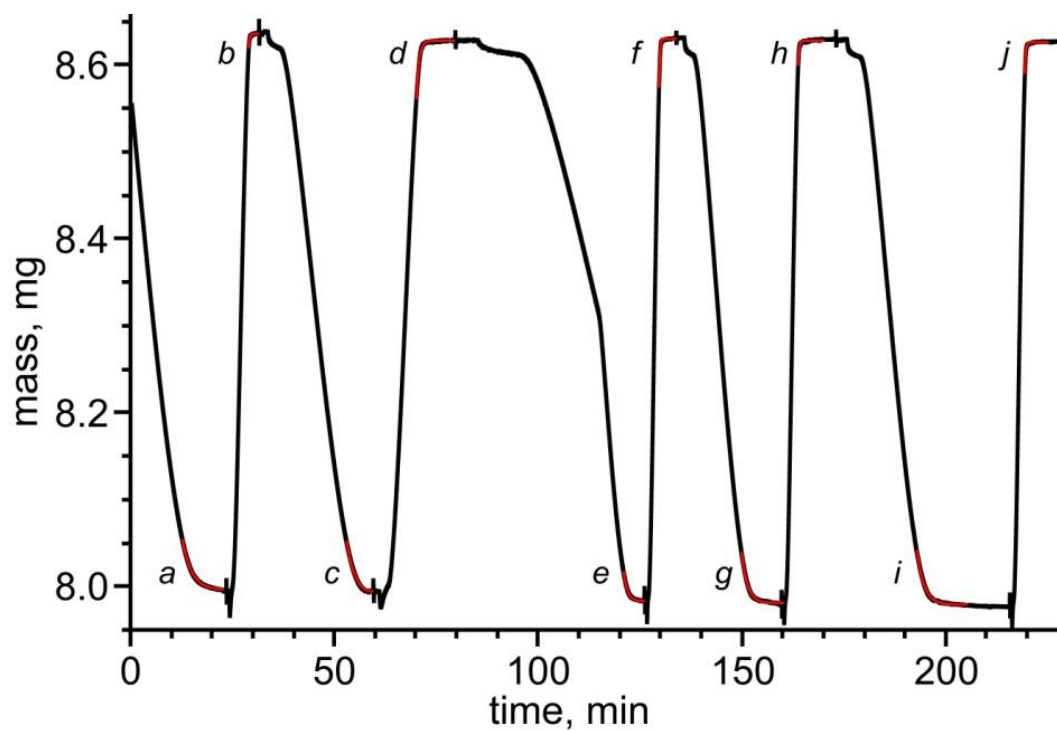


Figure 6.17. The effect of carrier-gas flow rate on the rates of hydration and dehydration. The red curves are fits to the latter 10–15% of individual hydration and dehydration regions of the mass (m) vs. time (t) TGA curve using the simple exponential function $m \propto e^{-kt}$. The results are shown in Table 6.3.

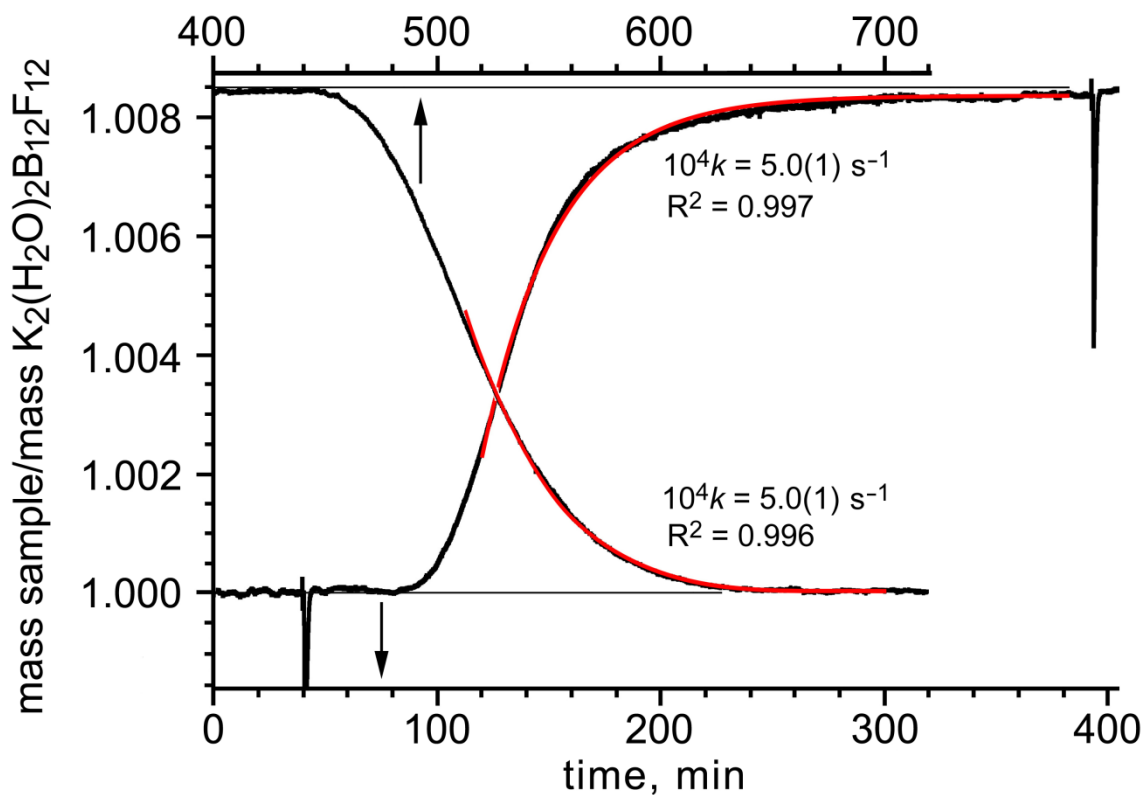


Figure 6.18. Gravimetric analysis for the consecutive transformations $K_2(H_2O)_2B_{12}F_{12}(s) + xS \text{ D}_2O(g) \rightarrow K_2(D_2O)_2B_{12}F_{12}(s) + 2 \text{ H}_2O(g)$ and $K_2(D_2O)_2B_{12}F_{12}(s) + xS \text{ H}_2O \rightarrow K_2(H_2O)_2B_{12}F_{12}(s) + 2 \text{ D}_2O(g)$. The red curves are single-exponential fits to the mass (m) vs. time (t) data sets covered by the red curves (i.e., the latter portion of the exchange reactions; $m \propto e^{-kt}$). The helium carrier gas was bubbled through either liquid H_2O or D_2O at 23(1) C (the flow rate was 60 mL min^{-1}).

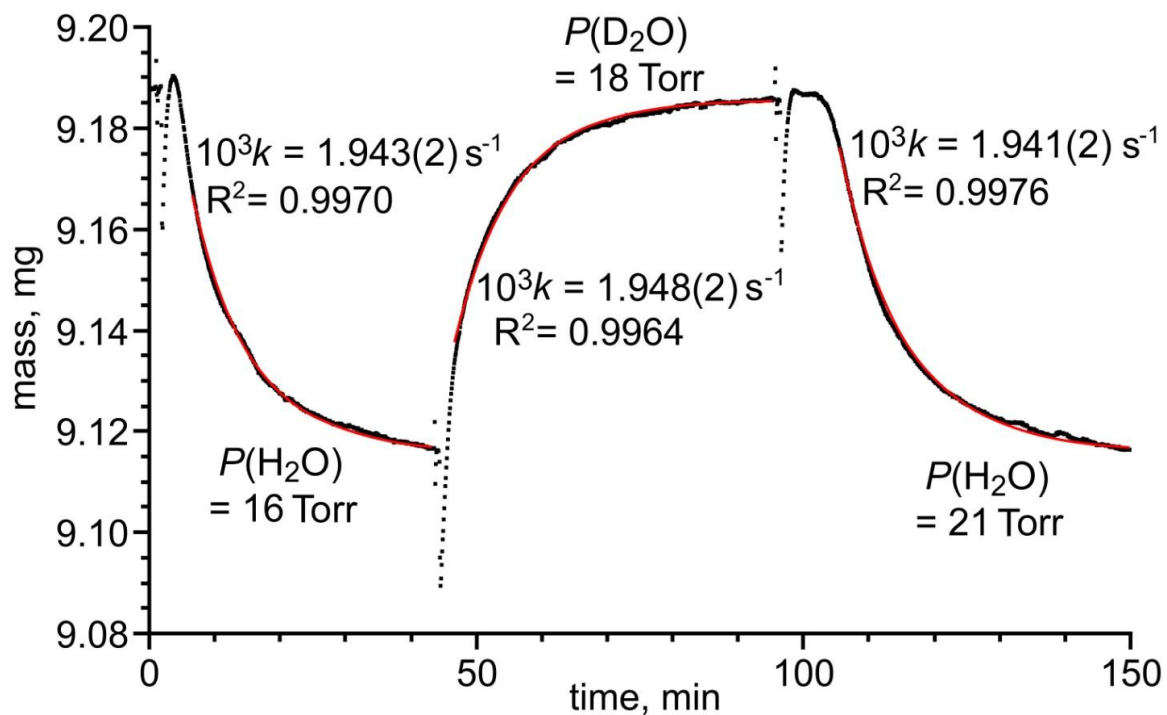


Figure 6.19. Isotopomer exchange of $\text{H}_2\text{O}(g)$ and $\text{K}_2(\text{D}_2\text{O})_2\text{B}_{12}\text{F}_{12}(s)$ and vice versa. The carrier gas for the leftmost portion of the mass (m) vs. time (t) isothermal ($25.0(5)^\circ\text{C}$) TGA trace was helium bubbled through a saturated aqueous solution of NaNO_3 at $23(1)^\circ\text{C}$ ($P(\text{H}_2\text{O}) = 16(1)$ Torr). The carrier gas for the central portion was helium bubbled through D_2O at $23(1)^\circ\text{C}$ ($P(\text{H}_2\text{O}) = 18(1)$ Torr). The carrier gas for the rightmost portion was helium bubbled through H_2O at $23(1)^\circ\text{C}$ ($P(\text{H}_2\text{O}) = 21(1)$ Torr). In all three cases the flow rate was 60 mL min^{-1} . The time constants, k , shown are from the portions of the TGA trace that were fit to the exponential function $m \propto e^{-kt}$ (the fits are shown in red).

CHAPTER 7. FUTURE WORK

The new fluorination method can be applied to other boron clusters, such as $\text{NH}_3\text{B}_{12}\text{H}_{11}^-$, $\text{CHB}_{11}\text{H}_{11}^-$, and $\text{B}_{10}\text{H}_{10}^{2-}$. The preliminary results showed that these anions can be fluorinated by fluorine gas in acetonitrile with excess of KF present. It would be especially interesting to achieve the perfluorination of $\text{B}_{10}\text{H}_{10}^{2-}$ since this anion is known to be unstable in anhydrous HF and other acidic media. The fluorination in acetonitrile in the presence of an excess of the base (KF) may be a solution. However, the optimization of reaction conditions is required since the yields are lower and reaction times are longer than those in case of $\text{B}_{12}\text{H}_{12}^{2-}$ fluorination.

Other transition metal salts of $\text{B}_{12}\text{F}_{12}^{2-}$ can be prepared and attempted to be desolvated under vacuum upon heating. Larger and catalytically active cations such as Pt^{2+} can be good candidates. Thermal removal of other, weaker ligands such as CH_3NO_2 can be studied.

The hydration (solvation) of other salts of $\text{B}_{12}\text{F}_{12}^{2-}$ can be studied using TGA and DSC. The kinetics of hydration/dehydration of these salts can be slower than that of $\text{K}_2\text{B}_{12}\text{F}_{12}$ and, therefore, not mass-transport limited (i.e., not be dependent on the flow rate of the carrier gas) so that the kinetic parameters can be measured accurately using TGA. Preliminary results show that $\text{Rb}_2(\text{H}_2\text{O})_2\text{B}_{12}\text{F}_{12}$, $\text{Cs}_2(\text{H}_2\text{O})\text{B}_{12}\text{F}_{12}$, and $\text{Ca}(\text{H}_2\text{O})_4\text{B}_{12}\text{F}_{12}$ undergo rapid hydration/dehydration in presence of water vapor. Furthermore, solvation by other small-molecules in gas phase can be studied. Preliminary results show that $\text{K}_2\text{B}_{12}\text{F}_{12}$ is rapidly solvated by $\text{CH}_3\text{CN}(\text{g})$. It was also found that rapid (on order of 10 min) transformation $\text{K}_2(\text{H}_2\text{O})_2\text{B}_{12}\text{F}_{12} \rightarrow \text{K}_2(\text{CH}_3\text{CN})_2\text{B}_{12}\text{F}_{12}$ occurs in the presence of acetonitrile vapor. The fast reverse transformation occurs in presence of water vapor. Solid-state NMR studies can provide information on behavior of ions and water

molecules in solid samples of hydrates such as $M_2(H_2O)_nB_{12}F_{12}$. The $K_2B_{12}F_{12}/K_2(H_2O)_2B_{12}F_{12}$ system is especially interesting in this regard, because every nucleus is NMR active and dynamics of the ionic lattice can be studied in great detail.

REFERENCES

- (1) Beck, W.; Sünkel, K. H. *Chem. Rev.* **1988**, *88*, 1405-1421.
- (2) Strauss, S. H. *Chem. Rev.* **1993**, *93*, 927-942.
- (3) Strauss, S. H. *Chemtracts: Inorganic Chemistry* **1994**, *6*, 1-13.
- (4) Krossing, I.; Raabe, I. *Angew. Chem.* **2004**, 2066-2090.
- (5) Lupinetti, A. J.; Strauss, S. H. *Chemtracts* **1998**, *11*, 565-595.
- (6) Reed, C. A. *Accounts Chem. Res.* **1998**, *31*, 133-139.
- (7) Marion, S.; Meyer, H.-W.; Carpenter, M.; Norby, T. *Am. Mineral.* **2001**, *86*, 1166-1169.
- (8) Lee, Y.; Kim, S. J.; Bull, I.; Celestian, A. J.; Parise, J. B.; Kao, C.-C.; Vogt, T. *J. Am. Chem. Soc.* **2007**, *129*, 13744-13748.
- (9) Xu, M.; Harris, K. D. M.; Thomas, J. M. *J. Am. Chem. Soc.* **2008**, *130*, 5880-5882.
- (10) O'Hare, B.; Grutzeck, M. W.; Kim, S. H.; Asay, D. B.; Benesi, A. J. *J. Mag. Reson.* **2008**, *195*, 85-102.
- (11) Wang, H.-W.; Bish, D. L. *Eur. J. Mineral.* **2010**, *22*, 271-284.
- (12) Bureekaew, S.; Shimomura, S.; Kitagawa, S. *Sci. Technol. Adv. Mater.* **2008**, *9*, 014108 (014112 pp).
- (13) Colodrero, R. M. P.; Cabeza, A.; Olivera-Pastor, P.; Infantes-Molina, A.; Barouda, E.; Demadis, K. D.; Aranda, M. A. G. *Chem. Eur. J.* **2009**, *15*, 6612-6619.

- (14) Férey, G.; Serre, C. *Chem. Soc. Rev.* **2009**, *38*, 1380-1399.
- (15) Li, J.-R.; Kuppler, R. J.; Zhou, H.-C. *Chem. Soc. Rev.* **2009**, *38*, 1477-1504.
- (16) Sherman, J. D. *Proc. Natl. Acad. Sci. USA* **1999**, *96*, 3471-3478.
- (17) Auerbach, S. M.; Carrado, K. A.; Dutta, P. K. *Handbook of Zeolite Science and Technology*; Marcel Dekker: New York, 2003.
- (18) Xu, R.; Pang, W.; Yu, J.; Huo, Q.; Chen, J. *Chemistry of Zeolites and Related Porous Materials: Synthesis and Structure*; Wiley-VCH: Weinheim, 2007.
- (19) Steiner, T.; Moreira da Silva, A. M.; Teixeira-Dias, J. J. C.; Müller, J.; Saenger, W. *Angew. Chem. Int. Ed.* **1995**, *34*, 1452-1453.
- (20) Kawasaki, T.; Jiang, L.; Iyoda, T.; Aradki, T.; Hashimoto, K.; Fuhishima, A. *J. Phys. Chem. B* **1998**, *102*, 1989-1993.
- (21) Thallapally, P. K.; Lloyd, G. O.; Atwood, J. L.; Barbour, L. J. *Angew. Chem.* **2005**, *117*, 3916-3919.
- (22) Bowers, G. M.; Bish, D. L.; Kirkpatrick, R. J. *J. Phys. Chem. C* **2008**, *112*, 6430-6438.
- (23) Pfeiffer, H.; Lima, E.; Lara, V.; Velente, J. S. *Langmuir* **2009**, *26*, 4074-4079.
- (24) Volkringer, C.; Loiseau, T.; Guillou, N.; Férey, G.; Haouas, M.; Taulelle, F.; Audebrand, N.; Margiolaki, I.; Popov, D.; Burghammer, M.; Riekel, C. *Cryst. Growth Design* **2009**, *9*, 2927-2936.
- (25) Mobin, S. M.; Srivastava, A. K.; Mathur, P.; Lahiri, G. K. *Inorg. Chem.* **2009**, *48*, 4652-4654.
- (26) Noisong, P.; Danvirutai, C. *Ind. Eng. Chem. Res.* **2010**, *49*, 3146-3151.
- (27) Chandler, B. D.; Enright, G. D.; Udachin, K. A.; Pawsey, S.; Ripmeester, J. A.; Cramb, D. T.; Shimizu, G. K. H. *Nature Mater.* **2008**, *7*, 229-235.
- (28) Ivanov, S. V.; Miller, S. M.; Anderson, O. P.; Solntsev, K. A.; Strauss, S. H. *J. Am. Chem. Soc.* **2003**, *125*, 4694-4695.

- (29)Peryshkov, D. V.; Popov, A. A.; Strauss, S. H. *J. Am. Chem. Soc.* **2009**, *131*, 18393-18403.
- (30)Solntsev, K. A.; Mebel, A. M.; Votnova, N. A.; Kuznetsov, N. T.; Charkin, O. P. *Koord. Khim.* **1992**, *18*, 340-364.
- (31)Peryshkov, D. V.; Popov, A. A.; Strauss, S. H. *J. Amer. Chem. Soc.* **2010**, *132*, 13902-13913.
- (32)Muller, P. *Pure Appl. Chem.* **1994**, *66*, 1077-1184.
- (33)Ivanov, S. V.; Rockwell, J. J.; Polyakov, O. G.; Gaudinski, C. M.; Anderson, O. P.; Solntsev, K. A.; Strauss, S. H. *J. Am. Chem. Soc.* **1998**, *120*, 4224-4225.
- (34)Ivanov, S. V.; Davis, J. A.; Miller, S. M.; Anderson, O. P.; Strauss, S. H. *Inorg. Chem.* **2003**, *42*, 4489-4491.
- (35)Peryshkov, D. V.; Goresnik, E.; Mazej, Z.; Strauss, S. H. *J. Fluorine Chem.* **2010**, *131*, 1225-1228.
- (36)Ivanov, S. V., unpublished results, Colorado State University, 1999.
- (37)Her, J.-H.; Yousufuddin, M.; Zhou, W.; Jalisatgi, S. S.; Kulleck, J. G.; Zan, J. A.; Hwang, S.-J.; Bowman, J., R. C.; Udovic, T. J. *Inorg. Chem.* **2008**, *47*, 9657-9759.
- (38)Tiritiris, I.; Schleid, T.; Muller, K.; Preetz, W. *Z. Anorg. Allg. Chem.* **2000**, *626*, 323-325.
- (39)Tiritiris, I.; Schleid, T. *Z. Anorg. Allg. Chem.* **2003**, *629*, 581-583.
- (40)Tiritiris, I.; Schleid, T. *Z. Anorg. Allg. Chem.* **2004**, *630*, 1555-1563.
- (41)Peymann, T.; Knobler, C. B.; Khan, S. I.; Hawthorne, M. F. *Inorg. Chem.* **2001**, *40*, 1291-1294.
- (42)Matsumoto, K.; Hagiwara, R.; Mazej, Z.; Goresnik, E.; Žemva, B. *J. Phys. Chem. B* **2006**, *110*, 2138-2141.
- (43)Brunton, G. *Acta Crystallogr.* **1968**, *B25*, 1703.

- (44) Strømme, K. E. *Acta Chem. Scand. A* **1974**, 28, 546-550.
- (45) Brunton, G. *Acta Crystallogr.* **1969**, B25, 2161-2162.
- (46) Goresnik, E.; Mazej, Z. *Solid State Sci.* **2005**, 7, 1225-1229.
- (47) Clark, M. J. R.; Lynton, H. *Can. J. Chem.* **1969**, 47, 2579-2586.
- (48) Kemmitt, R. D. W.; Russell, D. R.; Sharp, D. W. A. *J. Chem. Soc.* **1963**, 4408-4414.
- (49) Gafner, G.; Kruger, G. J. *Acta Cryst.* **1974**, B30, 250-251.
- (50) Onodera, A.; Sawada, T.; Kawamura, Y.; Takama, T.; Fujita, M.; Yamashita, H. *J. Korean Phys. Soc.* **1998**, 32, S73-S76.
- (51) Gramaccioli, C. M.; Campostrini, I. *Canadian Mineralogist* **2007**, 45, 1275-1280.
- (52) Bukovec, P.; Hoppe, R. *J. Fluorine Chem.* **1983**, 23, 579-587.
- (53) Hoard, J. L.; Vincent, W. B. *J. Am. Chem. Soc.* **1939**, 61, 2849-2852.
- (54) Wells, A. F. *Structural Inorganic Chemistry*; Oxford University Press: Oxford, 1984.
- (55) Holbrook, J. B.; Sabry-Grant, R.; Smith, B. C.; Tandel, T. V. *J. Chem. Ed.* **1990**, 67, 304-307.
- (56) Hoppe, R.; Hofmann, B. *Z. Anorg. Allg. Chem.* **1977**, 436, 65-74.
- (57) Bode, H.; Wendt, W. *Z. Anorg. Allg. Chem.* **1952**, 269, 165-172.
- (58) Hester, J. R.; Maslen, E. N.; Spadaccini, N.; Ishizawa, N.; Satow, Y. *Acta Crystallogr.* **1993**, B49, 967-973.
- (59) Bode, H.; Brockmann, R. *Z. Anorg. Allg. Chem.* **1952**, 269, 173-178.
- (60) Brown, I. D.; Altermatt, D. *Acta Cryst.* **1985**, B41, 244-247.

- (61) Bondi, A. *J. Phys. Chem.* **1964**, *68*, 441-451.
- (62) Brese, N. E.; O'Keeffe, M. *Acta Cryst.* **1991**, *B47*, 192-197.
- (63) Strauss, S. H.; Ivanov, S. V.; Colorado State University: USA, 2002.
- (64) Casteel, W. J., Jr.; Ivanov, S. V.; Air Products and Chemicals, Inc.: USA, 2004.
- (65) Walter, M.; Ramaley, L. *Anal. Chem.* **1973**, *45*, 165-166.
- (66) Rack, J. J.; Polyakov, O. G.; Gaudinski, C. M.; Hammel, J. W.; Kasperbauer, P.; Hochheimer, H. D.; Strauss, S. H. *Appl. Spectr.* **1998**, *52*, 1035-1038.
- (67) Neese, F.; Institute for Physical and Theoretical Chemistry: Bonn, 2000.
- (68) Perdew, J. P.; Burke, K.; Ernzerhof, M. *Phys. Rev. Lett.* **1996**, *77*, 3865-3868.
- (69) Adamo, C.; Barone, V. *J. Chem. Phys.* **1999**, *110*, 6158-6170.
- (70) Weigend, F.; Ahlrichs, R. *Phys. Chem. Chem. Phys.* **2005**, *7*, 3297-3305.
- (71) Sinnecker, S.; Rajendran, A.; Klamt, A.; Diedenhofen, M.; Neese, F. *J. Phys. Chem.* **2006**, *110*, 2235-2245.
- (72) Ivanov, S. V.; Lupinetti, A. J.; Solntsev, K. A.; Strauss, S. H. *J. Fluorine Chem.* **1998**, *89*, 65-72.
- (73) Sivaev, I. B.; Bregadze, V. I.; Sjöberg, S. *Collect. Czech. Chem. Commun.* **2002**, *67*, 679-727.
- (74) Shore, S. G.; Hamilton, E. J. M.; Bridges, A. N.; Bausch, J.; Krause-Bauer, J. A.; Dou, D.; Liu, J.; Liu, S.; Du, B.; Hall, H.; Meyers, E. A.; Vermillion, K. E. *Inorg. Chem.* **2003**, *42*, 1175-1186.
- (75) Mebel, A. M.; Charkin, O. P.; Solntsev, K. A.; Kuznetsov, N. T. *Zh. Neorg. Khim.* **1989**, *34*, 1444-1448.
- (76) Hop, C. E. C. A.; Saulys, D. A.; Gaines, D. F. *Inorg. Chem.* **1995**, *34*, 1977-1978.

- (77) Hop, C. E. C. A.; Saulys, D. A.; Bridges, A. N.; Gaines, D. F.; Bakhtiar, R. *Main Group Metal Chem.* **1996**, *19*, 743-751.
- (78) Rewick, R. T.; Tolberg, W. E.; Hill, M. E. *J. Chem. Eng. Data* **1970**, *15*, 527-530.
- (79) Gambaretto, G. P.; Conte, L.; Napoli, M.; Legnaro, E.; Carlini, F. M. *J. Fluorine Chem.* **1993**, *60*, 19-25.
- (80) Cacace, F.; Giacomello, P.; Wolf, A. P. *J. Am. Chem. Soc.* **1980**, *102*, 3511-3515.
- (81) Grakauskas, V.; Baum, K. *J. Org. Chem.* **1969**, *34*, 2840-2845.
- (82) Jähnisch, K.; Baerns, M.; Hessel, V.; Ehrfeld, W.; Haverkamp, V.; Löwe, H.; Wille, C.; Guber, A. *J. Fluorine Chem.* **2000**, *105*, 117-128.
- (83) Chambers, R. D.; Kenwright, A. M.; Parsons, M.; Sandford, G.; Moilliet, J. S. *J. Chem. Soc., Perkin Trans. 1* **2002**, 2190-2197.
- (84) Appleman, E. H.; Dunkelberg, O.; Kol, M. *J. Fluorine Chem.* **1992**, *56*, 199-213.
- (85) Rozen, S. *Eur. J. Org. Chem.* **2005**, 2433-2447.
- (86) Jungwirth, P.; Tobias, D. *J. Chem. Rev.* **2006**, *106*, 1259-1281.
- (87) Gopalakrishnan, S.; Lui, D.; Allen, H. C.; Kuo, M.; Shultz, M. J. *J. Chem. Rev.* **2006**, *106*, 1155-1175.
- (88) Chang, T.-M.; Dang, L. X. *J. Chem. Rev.* **2006**, *106*, 1305-1322.
- (89) Cheng, J.; Hoffmann, M. R.; Colussi, A. J. *J. Phys. Chem. B* **2008**, *112*, 7157-7161.
- (90) Picalek, J.; Minofar, B.; Kolafa, J.; Jungwirth, P. *Phys. Chem. Chem. Phys.* **2008**, *10*, 5765-5775.
- (91) Parfenyuk, V. I. *Colloid J.* **2004**, *66*, 520-524.
- (92) Cwiklik, L.; Andersson, G.; Dang, L. X.; Jungwirth, P. *ChemPhysChem* **2007**, *8*, 1457-1463.

- (93)Jungwirth, P.; Winter, B. *Annu. Rev. Phys. Chem.* **2008**, *59*, 343-366.
- (94)Marcus, Y. *Thermochim. Acta* **1986**, *104*, 389-394.
- (95)Sremaniak, L. S.; Perera, L.; Berkowitz, M. L. *Chem. Phys. Lett.* **1994**, *219*, 377-382.
- (96)Stockmayer, W. H.; Rice, D. W.; Stephenson, C. C. *J. Am. Chem. Soc.* **1955**, *77*, 1980-1983.
- (97)Werner, H.-J.; Meyer, W. *Mol. Phys.* **1976**, *31*, 855-872.
- (98)Solntsev, K. A.; Ivanov, S. V.; Sakharov, S. G.; Katser, S. B.; Chernayavskii, A. S.; Votina, N. A.; Klyuchishche, E. A.; Kuznetsov, N. T. *Russ. J. Coord. Chem.* **1997**, *23*, 369-376.
- (99)Dupon, R.; Papke, B. L.; Ratner, M. A.; Whitmore, D. H.; Shriver, D. F. *J. Am. Chem. Soc.* **1982**, *104*, 6247-6251.
- (100)Knoth, W. H.; Miller, H. C.; England, D. C.; Parshall, G. W.; Muetterties, E. L. *J. Am. Chem. Soc.* **1962**, *84*, 1056-1057.
- (101)Knoth, W. H.; Miller, H. C.; Sauer, J. C.; Balthis, J. H.; Chia, Y. T.; Muetterties, E. L. *Inorg. Chem.* **1964**, *3*, 159-167.
- (102)Sheldrick, G. M.; Bruker AXS: Madison, WI, 2003.
- (103)Sheldrick, G. M.; Bruker AXS: Madison, WI, 2006.
- (104)Sheldrick, G. M.; Bruker AXS: Madison, WI, 2001.
- (105)Khaliullin, R. S.; Khisamov, B. A. *High Energy Chem.* **1996**, *30*, 394-396.
- (106)Khramenko, S. P.; Baidina, I. A.; Kuratieva, N. V.; Gromilov, S. A. *J. Struct. Chem.* **2009**, *50*, 166-169.
- (107)Sieron, L.; Bukowska-Strzyzewska, M.; Cyganski, A.; Turek, A. *Polyhedron* **1996**, *15*, 3923-3931.

- (108)Preisinger, A.; Zottl, M.; Mereiter, K.; Mikenda, W.; Steinböck, S.; Dufek, P.; Schwarz, K.; Blaha, P. *Inorg. Chem.* **1994**, *33*, 4774-4780.
- (109)Nickels, E. A.; Jones, M. O.; David, W. I. F.; Johnson, S. R.; Lowton, R. L.; Sommariva, M.; Edwards, P. P. *Angew. Chem. Int. Ed.* **2008**, *47*, 2817-2819.
- (110)Schulz, H.; Zucker, U.; Frech, R. *Acta Cryst.* **1985**, *B41*, 21-26.
- (111)Raynor, G. V. In *Progress in Metal Physics*; Chalmers, B., Ed.; Pergamon Press Ltd.: London, 1950; Vol. 2.
- (112)Szytula, A.; Leciejewicz, J. *Handbook of Crystal Structures and Magnetic Properties of Rare Earth Intermetallics*; CRC Press: Boca Raton, FL, 1994.
- (113)Dorfman, S. M.; Jiang, F.; Mao, Z.; Kubo, A.; Meng, Y.; Prakapenka, V. B.; Duffy, T. S. *Phys. Rev. B* **2010**, *81*, 174131-174131-174121-174113.
- (114)Smith, J. S.; Desgreniers, S.; Klug, D. D.; Tse, J. S. *Solid State Commun.* **2009**, *149*, 830-834.
- (115)Vegas, A.; Grzechnik, A.; Hanfland, M.; Mühle, C.; Jansen, M. *Solid State Sci.* **2002**, *4*, 1077-1081.
- (116)Karpov, A.; Nuss, J.; Wedig, U.; Jansen, M. *Angew. Chem. Int. Ed.* **2003**, *42*, 4818-4821.
- (117)Aminoff, G. Z. *Kristallogr. Kristallgeom. Kristallphys. Kristallchem.* **1923**, *58*, 203-219.
- (118)Brown, I. D. *Chem. Rev.* **2009**, *109*, 6858-6919, and references therein.
- (119)Wunderlich, J. A.; Lipscomb, W. H. *J. Am. Chem. Soc.* **1960**, *82*, 4427-4428.
- (120)Sharma, R. P.; Bala, R.; Sharma, R.; Venugopalan, P.; Salas, J. M.; Quiros, M. J. *Fluorine Chem.* **2005**, *126*, 1543-1548.
- (121)Seiler, P. *Acta Crystallogr.* **1993**, *B49*, 223-225.
- (122)Rissom, C.; Schmidt, H.; Voigt, W. *Cryst. Res. Technol.* **2008**, *43*, 74-82.

- (123) Meng, W.; Kraus, F. *Eur. J. Inorg. Chem.* **2008**, 3068-3074.
- (124) Jenkins, H. D. B.; Roobottom, H. K.; Passmore, J.; Glasser, L. *Inorg. Chem.* **1999**, *38*, 3609-3620.
- (125) *CRC Handbook of Chemistry and Physics, 91st Edition, Internet Version 2011*; Lide, D. R., Ed.; Chemical Rubber Company, 2011.
- (126) Enjalbert, R.; Galy, J. *Acta Cryst.* **2002**, *B58*, 1005-1010.
- (127) Churakov, A. V.; Prikhodchenko, P. V.; Howard, J. A. K. *Cryst. Eng. Comm.* **2005**, *7*, 664-669.
- (128) Churakov, A. V.; Howard, J. A. K. *Acta Cryst.* **2007**, *E63*, o4483.
- (129) Laus, G.; Kahlenberg, V.; Wurst, K.; Lorting, T.; Schottenberger, H. *Cryst. Eng. Comm.* **2008**, *10*, 1638-1644.
- (130) Teng, X. G.; Li, F. Q.; Ma, P. H.; Ren, Q. D.; Li, S. Y. *Thermochim. Acta* **2005**, *436*, 30-34.
- (131) Buschmann, W. E.; Miller, J. S. *Chem. Eur. J.* **1998**, *4*, 1731-1737.
- (132) Meshri, D. T. *Kirk-Othmer Encyclopedia of Chemical Technology* **1994**, doi 10.1002/0471238961.1909122213051908.a1909122213051901.
- (133) Aly, A. A. M.; Walfort, B.; Lang, H. Z. *Krist.* **2004**, *219*, 489-491.
- (134) Nilsson, K.; Oskarsson, A. *Acta Chem. Scand. A* **1984**, *38*, 79-85.
- (135) Ahmad, R.; Hardie, M. J. *Cryst. Growth Design* **2003**, *3*, 493-499.
- (136) Tsang, C.-W.; Sun, J.; Xie, Z. *J. Organomet. Chem.* **2000**, *613*, 99-104.
- (137) Ang, H.-G.; Fraenk, W.; Karaghiosoff, K.; Klapotke, T. M.; Mayer, P.; Noth, H.; Sprott, J.; Warehold, M. Z. *Anorg. Allg. Chem.* **2002**, *628*, 2894-2900.
- (138) Knapp, C.; Schulz, C. *Chem. Commun.* **2009**, 4991-4993.

- (139) Jabor, J. K.; Stosser, R.; Thong, N. H.; Ziemer, B.; Meisel, M. *Angew. Chem. Int. Ed.* **2007**, *46*, 6354-6356.
- (140) Li, S. L.; Lan, Y. Q.; Ma, J. F.; Yang, J.; Wang, X. H.; Su, Z. M. *Inorg. Chem.* **2007**, *46*, 8283-8290.
- (141) Zhang, Y. M.; Santos, A. M.; Herdtweck, E.; Mink, J.; Kuhn, F. E. *New J. Chem.* **2005**, *29*, 366-370.
- (142) Newbound, T. D.; Colman, M. R.; Miller, M. M.; Wulfsberg, G. P.; Anderson, O. P.; Strauss, S. H. *Journal of the American Chemical Society* **1989**, *111*, 3762-3764.
- (143) Colman, M. R.; Newbound, T. D.; Marshall, L. J.; Noirot, M. D.; Miller, M. M.; Wulfsberg, G. P.; Frye, J. S.; Anderson, O. P.; Strauss, S. H. *Journal of the American Chemical Society* **1990**, *112*, 2349-2362.
- (144) Decken, A.; Knapp, C.; Nikiforov, G. B.; Passmore, J.; Rautiainen, J. M.; Wang, X. P.; Zeng, X. Q. *Chem. Eur. J.* **2009**, *15*, 6504-6517.
- (145) Krossing, I. *Chemistry-Eur. J.* **2001**, *7*, 490-502.
- (146) Van Seggen, D. M.; Hurlburt, P. K.; Anderson, O. P.; Strauss, S. H. *J. Am. Chem. Soc.* **1992**, *114*, 10995-10997.
- (147) Reisinger, A.; Trapp, N.; Knapp, C.; Himmel, D.; Breher, F.; Ruegger, H.; Krossing, I. *Chem. Eur. J.* **2009**, *15*, 9505-9520.
- (148) Bihlmeier, A.; Gonsior, M.; Raabe, I.; Trapp, N.; Krossing, I. *Chem. Eur. J.* **2004**, *10*, 5041-5051.
- (149) Hurlburt, P. K.; Rack, J. J.; Luck, J. S.; Dec, S. F.; Webb, J. D.; Anderson, O. P.; Strauss, S. H. *J. Am. Chem. Soc.* **1994**, *116*, 10003-10014.
- (150) Bernhardt, E.; Henkel, G.; Willner, H.; Pawelke, G.; Burger, H. *Chem. Eur. J.* **2001**, *7*, 4696-4705.
- (151) Hadjiivanov, K.; Knozinger, H. *Surface Sci.* **2009**, *603*, 1629-1636.
- (152) Bolis, V.; Barbaglia, A.; Bordiga, S.; Lamberti, C.; Zecchina, A. *J. Phys. Chem. B* **2004**, *108*, 9970-9983.

- (153) Rasika-Dias, H. V.; Fianchini, M. *Comments Inorg. Chem.* **2007**, *28*, 73-92.
- (154) Hadjiivanov, K.; Knozinger, H. *J. Phys. Chem. B* **1998**, *102*, 10936-10940.
- (155) Lupinetti, A. J.; Strauss, S. H.; Frenking, G. *Prog. Inorg. Chem.* **2001**, *49*, 1-112.
- (156) Czako, G.; Matyus, E.; Simmonett, A. C.; Csaszar, A. G.; Schaefer III, H. F.; Allen, W. D. *J. Chem. Theory Comp.* **2008**, *4*, 1220-1229.
- (157) Avelar, A.; Tham, F. S.; Reed, C. A. *Angew. Chem. Int. Ed.* **2009**, *48*, 3491-3493.
- (158) Geis, V.; Guttsche, K.; Knapp, C.; Scherer, H.; Uzun, R. *Dalton Trans.* **2009**, 2687-2694.
- (159) Derendorf, J.; Kessler, M.; Knapp, C.; Ruhle, M.; Schulz, C. *Dalton Trans.* **2010**, *39*, 8671-8678.
- (160) Finze, M.; Bernhardt, E.; Willner, H.; Lehmann, C. W.; Aubke, F. *Inorg. Chem.* **2005**, *44*, 4206-4214.
- (161) Bernhardt, E.; Bach, C.; Bley, B.; Wartchow, R.; Westphal, U.; Sham, I. H. T.; von Ahsen, B.; Wang, C. Q.; Willner, H.; Thompson, R. C.; Aubke, F. *Inorg. Chem.* **2005**, *44*, 4189-4205.
- (162) Willner, H.; Bodenbinder, M.; Brochler, R.; Hwang, G.; Rettig, S. J.; Trotter, J.; von Ahsen, B.; Westphal, U.; Jonas, V.; Thiel, W.; Aubke, F. *J. Amer. Chem. Soc.* **2001**, *123*, 588-602.
- (163) Guichela, M.; Vanhest, J. A. M.; Reedijk, J. *Inorg. Nucl. Chem. Lett.* **1974**, *10*, 999-1004.
- (164) Gobbels, D.; Meyer, G. *Z. Anorg. Allg. Chem.* **2002**, *628*, 1799-1805.
- (165) Dance, I. *CrystEngComm* **2003**, *5*, 208-221.
- (166) Nikolova, D.; Georgiev, M. *J. Therm. Anal. Calor.* **2009**, *95*, 319-321.
- (167) Ivanova, S. M.; Nolan, B. G.; Kobayashi, Y.; Miller, S. M.; Anderson, O. P.; Strauss, S. H. *Chem. Eur. J.* **2001**, *7*, 503-510.

- (168)Rach, S. F.; Kühn, F. E. *Chem. Rev.* **2009**, *109*, 2061-2080.
- (169)Lee, J.; Farha, O. K.; Roberts, J.; Scheidt, K. A.; Nguyen, S.; Hupp, J. T. *Chem. Soc. Rev.* **2009**, *38*, 1450-1459.
- (170)Czaja, A. U.; Trukhan, N.; Müller, U. *Chem. Soc. Rev.* **2009**, *38*, 1284-1293.
- (171)Hurd, J. A.; Vaidhyanathan, R.; Thangadurai, V.; Ratcliffe, C. I.; Moudrakovski, I. L.; Shimizu, G. K. H. *Nature Chem.* **2009**, *1*, 705-710.
- (172)Pérez-Ramírez, J.; Christensen, C. H.; Egeblad, K.; Christensen, C. H.; Groen, J. C. *Chem. Soc. Rev.* **2008**, *37*, 2530-2542.
- (173)Stöcker, M. *Microporous Mesoporous Mater.* **2005**, *82*, 257-292.
- (174)Becke, A. D. *Phys. Rev. A* **1998**, *38*, 3098-3100.
- (175)Lee, C.; Yang, W.; Parr, R. G. *Phys. Rev. B* **1988**, *37*, 785-789.
- (176)Grimme, S. *J. Chem. Phys.* **2006**, *124*, 034108.
- (177)Neese, F.; Schwabe, T.; Grimme, S. *J. Chem. Phys.* **2007**, *126*, 124115.
- (178)Kendall, R. A.; Dunning, J., T. H.; Harrison, R. J. *J. Chem. Phys.* **1992**, *96*, 6796.
- (179)Finch, G. J.; Fordham, S. *Proc. Phys. Soc.* **1936**, *48*, 85-94.
- (180)Zintl, E.; Harder, A.; Dauth, B. *Z. Elektrochem. Angew. Phys. Chem.* **1934**, *40*, 588-593.
- (181)Mitani, M.; Yoshioka, Y. *J. Mol. Struct. THEOCHEM* **2009**, *915*, 160-169.
- (182)Searles, S. K.; Kebarle, P. *Can. J. Chem.* **1969**, *47*, 2619-2627.
- (183)Džidic, I.; Kebarle, P. *J. Phys. Chem.* **1970**, *74*, 1466-1474.
- (184)Haynes, D. R.; Tro, N. J.; George, S. M. *J. Phys. Chem.* **1992**, *96*, 8502-8509.

- (185) Streltsov, V. A.; Tsirelson, V. G.; Ozerov, R. P.; Golovanov, O. A. *Kristallografiya* **1988**, *33*, 90-97.
- (186) David, W. I. F.; Jones, M. O.; Gregory, D. H.; Jewell, C. M.; Johnson, S. R.; Walton, A.; Edwards, P. P. *J. Am. Chem. Soc.* **2007**, *129*, 1594-1601.
- (187) Mazej, Z.; Goresnik, E. *Eur. J. Inorg. Chem.* **2008**, 1795-1812.
- (188) Ahmed, I. A.; Kastner, G.; Reuter, H.; Schultze, D. *J. Organomet. Chem.* **2002**, *649*, 147-151.
- (189) Balters, S.; Bernhardt, E.; Willner, H.; Berends, T. *Z. Anorg. Allg. Chem.* **2004**, *630*, 257-267.
- (190) Itoh, J.; Kusaka, R.; Yamagata, Y.; Kiriya, R.; Ibamoto, H. *J. Phys. Soc. Japan* **1953**, *8*, 293-301.
- (191) Aurivillius, K.; Stalhandske, C. *Acta Chem. Scand.* **1973**, *27*, 1086-1088.
- (192) Beurskens, G.; Jeffrey, G. A. *J. Chem. Phys.* **1964**, *41*, 917-923.
- (193) Herzberg, G. *Molecular Spectra and Molecular Structure II. Infrared and Raman Spectra of Polyatomic Molecules*; Kreiger: Malabar, FL, 1991.
- (194) Vaden, T. D.; Weinheimer, C. J.; Lisy, J. M. *J. Chem. Phys.* **2004**, *121*, 3102-3107.
- (195) Falk, M.; Huang, C.-H.; Knop, O. *Can. J. Chem.* **1974**, *52*, 2380-2388.
- (196) Falk, M.; Knop, O. *Can. J. Chem.* **1977**, *55*, 1736-1744.
- (197) Flaud, J. M.; Camy-Peyret, C. *J. Mol. Spectr.* **1974**, *51*, 142-150.
- (198) Toth, R. A. *J. Opt. Soc. Am. B* **1993**, *10*, 1526-1544.
- (199) Toth, R. A. *J. Mol. Spectr.* **1999**, *195*, 73-97.
- (200) Vyazovkin, S.; Wight, C. A. *Annu. Rev. Phys. Chem.* **1997**, *48*, 125-149.

- (201)L'vov, B. L. *Spectrochim. Acta Part B* **1998**, 53, 809-820.
- (202)Khawam, A.; Flanagan, D. R. *Thermochim. Acta* **2005**, 429, 92-102.
- (203)Khawam, A.; Flanagan, D. R. *J. Phys. Chem. B* **2006**, 110, 17315-17328.
- (204)Galway, A. K. *J. Therm. Anal. Calor.* **2008**, 92, 967-983.
- (205)Sheth, A. R.; Zhou, D.; Muller, F. X.; Grant, D. J. W. *J. Pharm. Sci.* **2004**, 93, 3013-3026.
- (206)Vlaev, L.; Nedelchev, N.; Gyurova, K.; Zagorcheva, M. *J. Anal. Appl. Pyrolysis* **2008**, 81, 253-262.
- (207)Boonchom, B.; Kongtaweelert, S. *J. Therm. Anal. Calorim.* **2010**, 99, 531-538.
- (208)Nerád, I.; Proks, I.; Šaušová, S. *Chem. Papers* **1991**, 45, 721-730.
- (209)Miletich, R.; Zemann, J.; Nowak, M. *Phys. Chem. Minerals* **1997**, 24, 411-422.
- (210)Paulik, F.; Paulik, J.; Arnold, M. *Thermochim. Acta* **1992**, 200, 195-204.
- (211)Magin, R. L.; Mangum, B. W.; Statler, J. A.; Thornton, D. D. *J. Res. Natl. Bur. Stand. (U.S.)* **1980**, 86, 181-192.
- (212)*Handbook of Chemistry and Physics 73rd Edition*; Lide, D. R., Ed.; CRC Press: Boca Raton, FL, 1992-1993.
- (213)Uchida, S.; Kawamoto, R.; Akatsuka, T.; Hikichi, S.; Mizuno, N. *Chem. Mater.* **2005**, 17, 1367-1375, and references therein.
- (214)Greenspan, L. *J. Res. Natl. Bur. Stand. A* **1977**, 81, 89-96.
- (215)Carling, S. G.; Day, P.; Visser, D. *Inorg. Chem.* **1995**, 34, 3917-3927.
- (216)de Kozak, A.; Gredin, P.; Pierrard, A.; Renaudin, J. *J. Fluorine Chem.* **1996**, 77, 39-44.

(217)Hoyos, D.; Paillaud, J.-L.; Simon-Masseron, A.; Guth, J.-L. *Solid State Sci.* **2005**, *7*, 616-621.

(218)Franklin, M. L.; Flanagan, T. B. *J. Phys. Chem.* **1971**, *75*, 1272-1278.

(219)Moreira da Silva, A. M.; Steiner, T.; Saenger, W.; Empis, J.; Teixeira-Dias, J. J. C. *Chem. Commun.* **1997**, 465-466.

(220)Peryshkov, D. V.; Strauss, S. H. *J. Fluorine Chem.* **2010**, *131*, 1252-1256.

(221)Spek, A. L. *Acta Crystallogr.* **2009**, *D65*, 148-155.